Cross sections for single and double ionization of atomic helium under impact by fast multiply charged ions

A. B. Voĭtkiv

Institute of Electronics, Uzbekistan Academy of Sciences, 700143 Tashkent, Uzbekistan
(Submitted June 5, 1996; resubmitted January 31, 1997)
Zh. Tekh. Fiz. **68**, 1–7 (March 1998)

Expressions for the cross sections for single and double ionization of atomic helium in collisions with fast multiply charged ions are obtained in the collision parameter range $v^2 \gg Z \gtrsim v$, $v_0 \ll v < c$, where Z and v are, respectively, the ion charge and ion velocity, v_0 is the characteristic velocity of electrons in the atomic helium ground state, and c is the velocity of light.
 [S1063-7842(98)01703-6]

1. INTRODUCTION

Different aspects of collisions of fast multiply charged ions (MCIs) with helium atoms have been discussed in a large number of works.[1–13] In a number of experiments[2–5] single and double ionization of helium by fast MCIs in the parameter range $Z \gtrsim v \gg v_0$ and $v^2/c^2 \ll 1$ (Z and v are the charge and velocity of the MCI, v_0 is the characteristic velocity of the electrons in the atomic helium ground state, $c = 137$ is the velocity of light; here and below, unless otherwise stated, atomic units are used). There are a number of approaches,[4,6–13] falling outside the range of first-order perturbation theory in the interaction with the field of the MCI and giving reasonable agreement with experimental data on helium ionization cross sections, for calculating the impact ionization cross sections of helium in the range $Z \gtrsim v \gg v_0$, where the Born approximation is inapplicable. Since, however, in contradistinction to the Bethe-Born approach (see, for example, Ref. 14) these approaches, as a rule, do not lead to simple final formulas for the cross sections, empirical scalings are quite widely used[3,5,15] to describe experimental results. Moreover, real calculations of the cross sections are ordinarily limited to relatively small charges of the fast ions.

In the experiment of Ref. 15 (see also Refs. 2 and 5) the ionization of helium atoms by collisions with uranium ions U^{90+}, whose velocities approach relativistic values (right up to $v/c = 0.72$), was studied. At the same time the charges of these ions are so high that $Z \sim v \sim c$.

In the present paper we shall study collisions of fast (including relativistic) MCIs with helium atoms for $v^2 \gg Z \gtrsim v$, $v_0 \ll v \ll c$ and we shall obtain for the single- and double-ionization cross sections of helium simple expressions that describe all experimental data known to us in the parameter range studied. We note that even though the collision velocities considered in the present paper are high these collisions cannot be referred to the so-called ''high-velocity limit,'' where not only $v \gg v_0$ but $Z \ll v$ must hold also (see, for example, Ref. 16).

2. BASIC RELATIONS

Two basic difficulties arise in the theoretical description of the ionization of helium in collisions with fast MCIs: a) Generally speaking, perturbation theory should not be used to take account of the influence of the field of a fast MCI on the atomic electrons and b) the two-electron states of the helium atom must be described with adequate accuracy. However, these difficulties apparently ''compete'' with one another to a large degree. It is most important that the interelectron interaction be taken into account exactly in the high collision velocity limit (especially in calculations of two-electron ionization cross sections), where $Z \ll v$ and perturbation theory can be used to describe the effect of the field of the fast particle. On the other hand, when the ion charge is very high, the electronic correlations become relatively less important. It is known (see, for example, Ref. 17) that in this case the atom ionizes mainly by the so-called direct mechanism, where the ionization process can be described in the independent-electron approximation, which we shall employ below to find the helium ionization cross sections for $Z \gtrsim v \gg v_0$. In this approximation the probability W_n that n electrons are removed simultaneously from an atomic shell containing N electrons is determined by the expression[17]

$$W_n(b) = \binom{N}{n} w^n (1-w)^{N-n}, \tag{1}$$

where $w(b)$ is the probability of a single-electron (ionization) transition, b is the impact parameter, and $\binom{N}{n}$ are binomial coefficients.

To calculate $w(b)$ it is assumed that an electron in an atom moves in a mean field. Following Ref. 11, we shall assume that the probability $w(b)$ depends on the charge state of the recoil ion $w = w_n(b)$. Then we have for the single- and double-ionization cross sections of helium

$$\sigma_i^{(1+)} = 4\pi \int_0^\infty w_1(b)(1-w_1(b))\, b\, db, \tag{2}$$

$$\sigma_i^{(2+)} = 2\pi \int_0^\infty w_2^2(b)\, b\, db. \tag{3}$$

We shall assume below that $w_1(b)$ and $w_2(b)$ can be approximately described as the probabilities of single-electron ionization from the $1s$ state of hydrogen-like ions with nuclear charges z_1 and z_2. In the corresponding Cou-

lomb units the probabilities $w_1(b)$ and $w_2(b)$ become simply the hydrogen ionization probability. It should be noted that despite its simplicity such an approach often gives good agreement with the experimental data.[4,11,17]

In Ref. 18 simple approach was proposed for finding the ionization cross section of hydrogen atoms (and hydrogenlike ions) in collisions with fast MCIs in the parameter range $v^2 \gg Z \gtrsim v$, $v_0 \ll v$. It is convenient for what follows to present here the basic features and results of this approach. The approach is based on dividing the entire impact parameter range $0 \leqslant b < \infty$ into subregions: 1) $b \ll v\tau$ ($\tau \simeq 1$—the characteristic atomic time) and 2) $b \gg Z/v$. In the region $b \gg Z/v$, where the ionization probability is low, first-order perturbation theory in the interaction of the electron with the field of the MCI was used to calculate the ionization probability. To find the ionization probability in the region $b \ll v\tau$ (where the effective collision time $T \sim b/v$ is short), the zeroth-order sudden-perturbation approximation[19] in the interaction of the electron with the field of the MCI was used and the interaction itself was taken in the dipole approximation. Of course, the dipole expansion for the electron–MCI interaction, which is valid for $b > 1$, is inapplicable for $b < 1$. Here, however, it is important to note the following. Comparing with more accurate calculations in this range of values of b (for example, the method of classical Monte-Carlo trajectories[20]) shows that for $Z \gtrsim v \gg v_0$ using for $b < 1$ the formally inapplicable dipole expansion for this interaction in the sudden-perturbation approximation does not introduce a significant error in the ionization probability and for this reason the value $b = 0$ was taken in Ref. 18 as the lower limit of the region 1. It is important to note that according to the calculations such an approximation is inapplicable for fast low-charge ($Z \ll v$) particles. For $Z/v^2 \ll 1$ the regions 1 and 2 overlap, and in the overlap region both approximations give identical ionization probabilities. On account of this, the ionization cross section, being a sum of contributions from both regions, does not depend on the choice of ''limit'' point between them. Thus, the results of Ref. 17 (and, correspondingly, of the present work, which makes substantial use of them) are applicable for $v^2 \gg Z \gtrsim v \gg v_0$. In Ref. 18 the ionization cross section of a hydrogenlike ion with not too high nuclear (core) charge z_i (from the condition $v_0 \ll v$ follows $z_i \ll v$) was found as

$$\sigma_i = 8\pi 0.283 \frac{Z^2}{v^2 z_i^2} \ln\left(\frac{5v^2}{Z z_i}\right). \tag{4}$$

In Ref. 21 this approach was extended to the case of relativistic collisions with $v^2 \gg Z \gtrsim v$ and $v_0 \ll v < c$

$$\sigma_i = 8\pi 0.283 \frac{Z^2}{v^2 z_i^2} \left(\ln\left(\frac{5v^2}{Z z_i}\gamma\right) - \frac{v^2}{2c^2}\right), \tag{5}$$

where $\gamma = (1 - v^2/c^2)^{-1/2}$.

Let us return to the ionization cross sections of helium atoms. The integral $4\pi\int_0^\infty (b) b db$ appearing in the expression (2) equals the average ionization cross section (5) of a hydrogen-like ion taken with $z_i = z_1$. To calculate the integrals $\int_0^\infty w_{1,2}^2(b) b db$ appearing in Eqs. (2) and (3) we proceed as follows. The integrand in these integrals decreases quite rapidly with increasing impact parameter already in the region $Z v^{-1} z_{1,2}^{-1} \ll b \ll \gamma v \tau z_{1,2}^{-2}$ ($b w_{1,2}^2 \sim b^{-2}$), where the sudden-perturbation approximation is applicable. For this reason, to calculate these integrals we shall use in the entire range of impact parameters $0 \leqslant b < \infty$ the probabilities $w_{1,2}(b)$ found in this approximation. Of course, for impact parameters $b \geqslant \gamma v \tau z_{1,2}^{-2}$, where for the atom the field of the MCI is not only weak but also slowly varying in time, the ionization probability decreases not as a powe law but exponentially.[22] However, even the quantities $w_{1,2}^2$ calculated in the sudden-perturbation approximation are already so small for such values of b that their use for calculating these integrals in the entire range of impact parameters $0 \leqslant b < \infty$ does not introduce an appreciable error (estimated to be in order of magnitude $Z^4 \gamma^{-2} v^{-6}$). In what follows we shall neglect this error. Using this approximation we have

$$\int_0^\infty dbb w_{1,2}^2 = \frac{4Z^2}{v^2 z_{1,2}^2} \int_0^\infty \frac{dq}{q^3} p^2(q), \tag{6}$$

where $\mathbf{q} = 2Z\mathbf{b}/(b^2/v)$ is the average momentum transferred to an electron in a collision with a fast particle;[18]

$$p(q) = p(\mathbf{q}) = \int d\mathbf{k} |\langle \varphi_{\mathbf{k}} | \exp(-i\mathbf{q}\cdot\mathbf{r}) | \varphi_{1s} \rangle|^2$$

is the ionization probability of a hydrogen atom accompanying sudden transfer of momentum q to an atomic electron[18] (φ_{1s} and $\varphi_{\mathbf{k}}$ are, respectively, the ground state and a state in the continuum of the hydrogen atom).

The integrand in the expression on the right-hand side of Eq. (6) no longer depends on Z, v, and $z_{1,2}$ and can be calculated numerically by substituting an exlicit expression for $p(q)$ (see, for example, Ref. 23). The result is

$$\int_0^\infty dbb w_{1,2}^2 = \frac{4Z^2}{v^2 z_{1,2}^2}\ 0.374. \tag{7}$$

Using Eqs. (2), (5), and (7) we find for the single-ionization cross section of helium

$$\sigma_i^{(1+)} = 16\pi \frac{0.283}{z_1^2} \frac{Z^2}{v^2} \left[\ln\left(\frac{\beta_i v^2 \gamma}{Z}\right) - \frac{v^2}{2c^2}\right], \tag{8}$$

where

$$\beta_i = \frac{5}{z_1} \exp\left[\frac{1}{0.283} \int_0^\infty p^2(q) q^{-3} dq\right] = \frac{1.33}{z_1}.$$

The sum of the squared moduli of the dipole-transition matrix elements from the ground state into a state in the ''single-electron'' continuum of the helium atom is determined in the present approach as $2 \cdot 0.283/z_1^2$ and equals 0.489 (see, for example, Ref. 24). From the equality $2 \cdot 0.283/z_1^2 = 0.489$ follows $z_1 = 1.11$, and we obtain for the cross section

$$\sigma_i^{(1+)} = 12.289 \frac{Z^2}{v^2} \left(\ln\left(\frac{1.2v^2}{Z}\gamma\right) - \frac{v^2}{2c^2}\right). \tag{9}$$

The expression

$$\sigma_{BB}^{(1+)} = 12.289 \frac{Z^2}{v^2} \left(\ln(2.08 v\gamma) - \frac{v^2}{2c^2}\right) \tag{10}$$

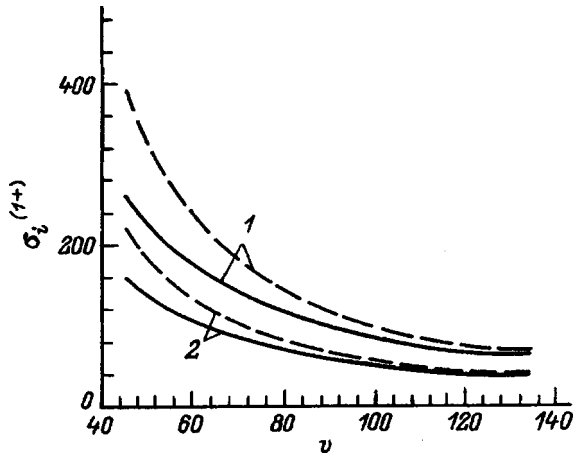

FIG. 1. Single-ionization cross sections for helium calculated from Eq. (9) (solid curve) and (10) (dashed curve). Z: *1*—120, *2*—90; $45<v<135$.

describes the single-ionization cross section of helium in the Bethe-Born approach.

The computational results obtained with Eqs. (9) and (10) are compared in Figs. 1 and 4.

In the ultrarelativisitic limit $\gamma \gg 1$ the results obtained with Eqs. (9) and (10) are very close to one another, even when $Z \simeq c$ (Fig. 1). The physical reason for such a small difference between the results (9) and (10) lies in the following. Since in the limit $\gamma \gg 1$ the field of a fast charged particle is ''flattened'' in the direction of motion of the particle, a collision with the particle is sudden for the atom right up to very large values of the parameter $b \sim c\gamma$, and the region $b \gg Z/v$, where perturbation theory is applicable, in this case makes an overwhelming contribution to the single-ionization cross section.

In Fig. 2a the computational results obtained with Eq. (9) (solid line) are compared to the experimental data (circles) from Ref. 15 on single-ionization of helium by uranium ions U^{+90} (60, 120, 420 MeV/amu and, respectively, $v/c = 0.34$, 0.46, and 0.72). The figure also displays the results obtained with the McKenzie–Olson approximation formula (dashed line).[8] On account of the large uncertainty in the experimentally measured values of the cross sections it can be concluded only that our computational results are consistent with these data. The expression (9), just as the McKenzie–Olson approximation formula, predicts a monotonic decrease of the cross sections with increasing collision velocity for the parameter range studied in Ref. 15. This seems obvious for $Z \sim v \gg v_0$, where charge transfer is negligibly weak compared with direct ionization and at the same time relativistic effects are small ($\gamma \leqslant 1.4$). The equation (9) give much higher single-ionization cross sections than the McKenzie–Olson scaling, which approximates the numerical results obtained by the classical Monte-Carlo trajectories method.[9] This discrepancy arises for the following reasons. According to classical mechanics, collisions with quite large impact parameters, for which the (classically computed) energy transferred to the atom is less than the ionization potential of the atom, do not make an appreciable contribution to the ionization cross section (the contribution of the region of

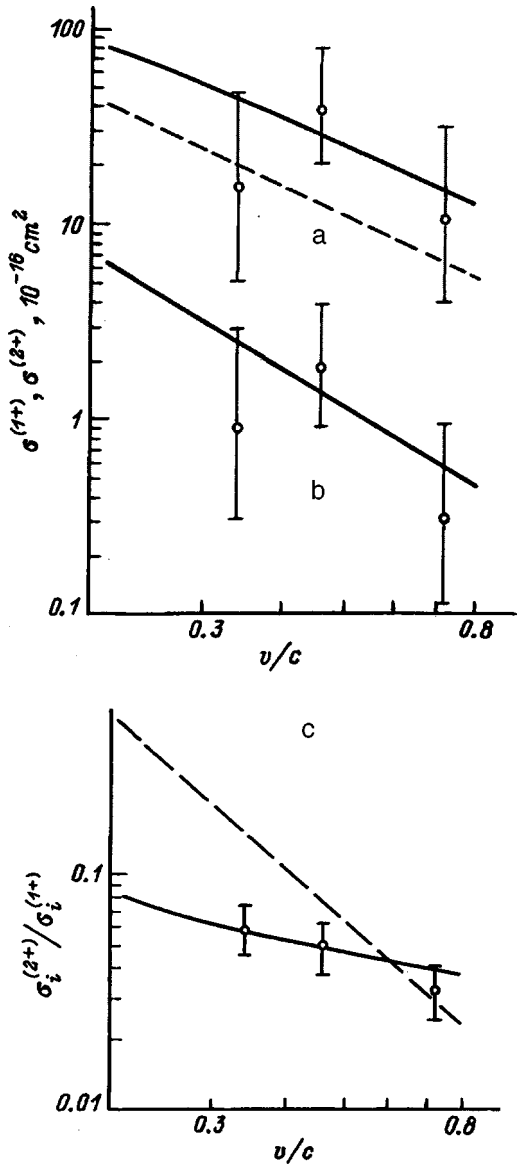

FIG. 2. Ionization cross sections for helium in collisions with U^{+90}. a—Single ionization, b—double ionization, c—ratio of ionization cross sections $\sigma_i^{(2+)}/\sigma_i^{(1+)}$.

large impact parameters is ''classically suppressed'' [25]). On the other hand, in a quantum-mechanical analysis this region of impact parameters makes the main contribution to the ionization cross section when $v \gg v_0$. This difference leads to different asymptotic behavior of the single-ionization cross sections in the region $v \gg v_0$: $\sigma''_{\rm cl} v^{-2}$;[26] $\sigma''_{\rm q}(\text{const}_1 + \ln v)v^{-2}$ $(v \gg v_0, Z)$;[14,24] $\sigma_{\rm q} \sim (\text{const}_2 + \ln(v^2/Z))v^{-2}$ $(Z \sim v \gg v_0)$,[1,18] i.e., a calculation on the basis of classical mechanics in the Z and v range considered should give too low values of the single-ionization cross sections.

Figure 3 compares our computational results with the experimental data (squares) of Ref. 5 on single ionization of helium by fast MCIs with $8 \leqslant Z \leqslant 54$ in the collision energy range $1 \leqslant E \leqslant 11.4$ MeV/amu, where relativistic effects in the cross section disappear virtually completely.

In Fig. 4 the computational results obtained with Eqs. (9) (solid curve) and (10) (dashed curve) are compared to the

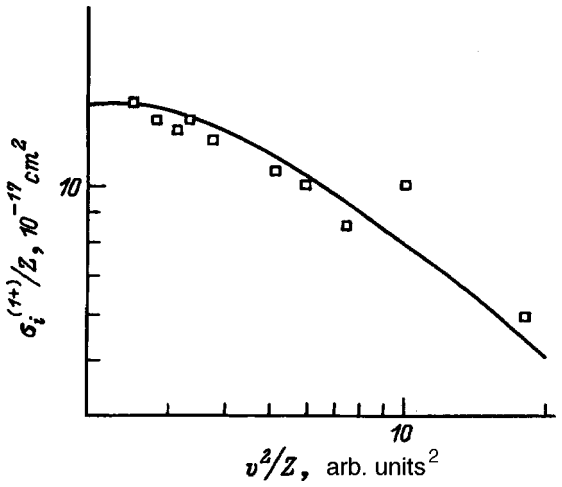

FIG. 3. Single-ionization cross sections for $v^2/c^2 \ll 1$.

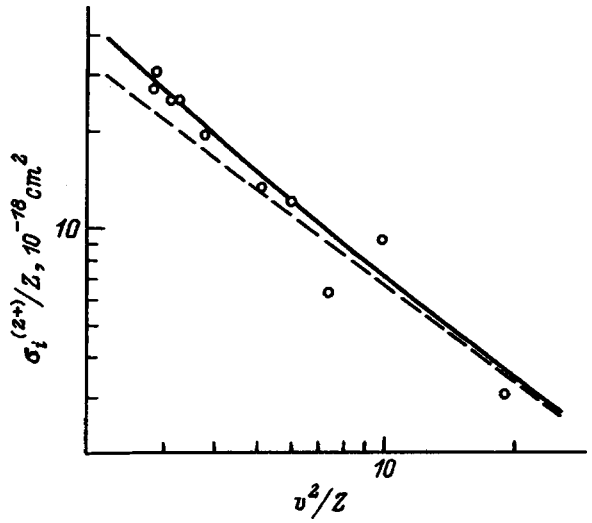

FIG. 5. Double-ionization cross sections for $v^2/c^2 \ll 1$.

experimental data (circles) from Ref. 5 on the ionization at fixed collision enegy $E=3.6$ MeV/amu with the charge of the MCI varying from $Z=24$ up to 54. We note that our calculation reproduces the experimentally observed deviation of the single-ionization cross sections from the relation $\sigma_i^{(1+)} \sim Z^2$, which follows from the Born–Bethe approximation.

From Eqs., (3) and (7) we find for the double-ionization cross section of helium

$$\sigma_i^{(2+)} = \frac{9.39}{z_2^2} \frac{Z^2}{v^2}. \tag{11}$$

On the basis of the standard perturbation theory one would expect that $\sigma_i^{(2+)} \sim Z^4 v^{-4}$ should appear for the two-step ionization mechanism.[3,4,15] However, in the case at hand the perturbation theory is inapplicable for small impact parameters, where the ionization probability ''saturates'' and is very close to 1, while the approach studied in the present paper preserves unitarity and gives for the single-electron ionization probability a reasonable value for $Z \gtrsim v \gg v_0$ and small b, and we arrive at a qualitatively different relation $\sigma_i^{(2+)} \sim Z^2 v^{-2}$.

The effective charge z_2 evidently must lie in the range $1.69 < z_2 < 2$, the uncertainty being relatively small. We shall treat z_2 as an adjustable parameter and we shall determine it by comparing with the experimental data on double ionization of helium by fast (but $v^2/c^2 \to 0$) MCIs with $Z \sim v \gg v_0$.[3–5] This gives $z_2 \sim 2$ and

$$\sigma_i^{(2+)} = 2.35 \frac{Z^2}{v^2}. \tag{12}$$

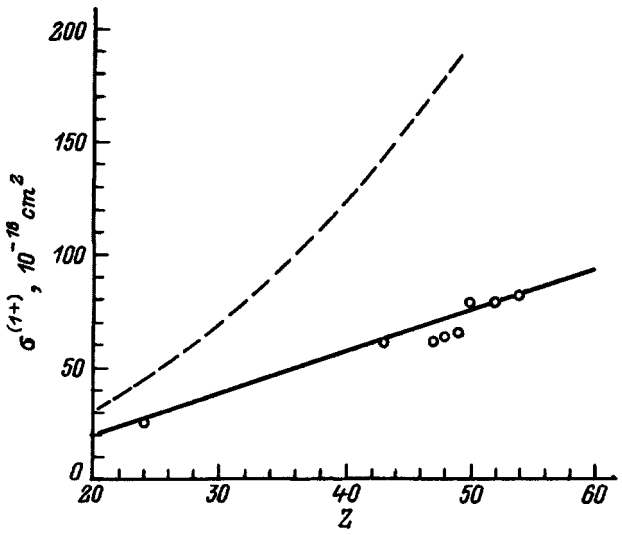

FIG. 4. Single-ionization cross sections for $E=3.6$ MeV/amu and $24 \leqslant Z \leqslant 54$.

In Fig. 2b the cross sections calculated with Eq. (12) (solid curve) are compared to the experimental data (circles) from Ref. 15 on double ionization of helium atoms by uranium ions U^{+90} (60, 120, and 420 MeV/amu). Figure 2c displays the experimental results of Ref. 15 and the computational results obtained with Eqs. (9) and (12) for the ratio of the double-ionization cross section to the single-ionization cross section (solid line). The figure also shows the computational results (dashed curve) obtained using the empirical scaling proposed in Ref. 3 (see also Refs. 5 and 15). As one can see from the figure, our computational results are in good agreement with the experimental data, whose accuracy is estimated by the authors to be 25–30%, on the ratio of the cross sections.

In Fig. 5 the calculations performed with Eqs. (12) (dashed curve) and (14) (solid curve) are compared to the experimental data (circles) from Refs. 2–5 on the double ionization of helium by fast MCIs ($8 \leqslant Z \leqslant 54$, 1 MeV/amu $\leqslant E \leqslant 11.4$ MeV/amu). Figure 6 displays the experimental data from Ref. 2 (circles) on the double ionization of helium at fixed collision energy $E=3.6$ MeV/amu, where the charge of MCI varies from $Z=24$ up to 54, as well as the computational results obtained with Eqs. (12) (dashed line) and (14) (solid line). It is evident from this figure that as the ratio Z/v^2 increases, the computational results obtained with Eq.

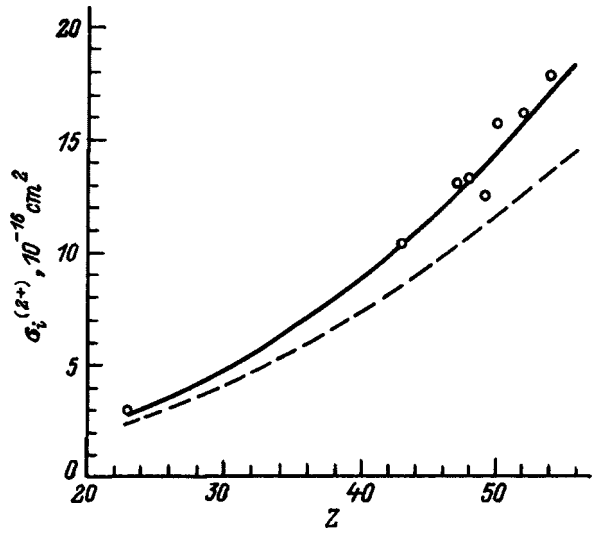

FIG. 6. Double-ionization cross section for $E=3.6$ MeV/amu and $24\leqslant Z\leqslant 54$.

(12) fall substantially below the experimentally observed values. For example, $(\sigma_{\exp}^{(2+)}-\sigma_i^{(2+)})/\sigma_{\exp}^{(2+)}\simeq 0.3$ for $Z=54$ $(Z/v^2\simeq 0.38)$.

Let us endeavor to improvement the agreement with the experimental data on the double-ionization cross sections at follows. In our derivation of the expression for the ionization probability for impact parameters in a range where the sudden-perturbation approximation was used, we neglected the spatial displacement of the electron during the effective collision time $T\sim b(\gamma v)$ (in the zeroth-order in the sudden-perturbation approximation the position of the electron is assumed to be ''frozen'' during the collision). This displacement, whose magnitude can be estimated as $\delta\sim q(b)T(b)\sim Z/v^2$, can be quite important for double ionization, since the range of impact parameters $b\ll v z_2^{-2}$, where the sudden-perturbation approximation is applicable, makes an overwhelming contribution to the double-ionization cross section (this is not so for single ionization because of the term $(1-w_1)$ and the fact that impact parameters $b\sim v z_1^{-2}$, where the sudden-perturbation approximation is inapplicable, make a substantial contribution to the integral $\int_0^\infty dbbw_1(b)$).

In Ref. 28 it was shown that for $b\ll v$ the wave function of the atomic electron after a collision can be represented as

$$\varphi_{1s}(\mathbf{r}-\boldsymbol{\delta})\exp(i\mathbf{q}\cdot\mathbf{r}),$$

where $\varphi_{1s}(\mathbf{r})$ is the wave function of the initial state and $\boldsymbol{\delta}\sim Z\mathbf{b}/v^2 b$.

In order for the approach employed in the present paper to be applicable the spatial displacement δ must be small compared with the characteristic atomic size $r_0\sim 1$ and we can write

$$\varphi_{1s}(\mathbf{r}-\boldsymbol{\delta})\simeq\varphi_{1s}(\mathbf{r})-\boldsymbol{\delta}\cdot\frac{\partial\varphi_{1s}(\mathbf{r})}{\partial\rho}\sim\varphi_{1s}(\mathbf{r})-\delta\frac{\partial\varphi_{1s}(\mathbf{r})}{\partial\rho}.$$

Approximating the derivative as[1)] $\partial\varphi_{1s}/\partial\rho\sim(-\varphi_{1s}/r_0)$ (Ref. 29) and using the expressions (3) and (6) we have

$$\sigma_i^{(2+)}\simeq\frac{9.39}{z_2^2}\frac{Z^2}{v^2}(1+\alpha_1 Z/v^2), \tag{13}$$

where $\alpha_1>0$ is independent of Z and v.

There is one other possibility for the cross section to increase as a result of the spatial displacement δ. When (during a displacement) the position of the electron wave packets changes (without a large change in their initial shape[28]), the screening of the helium nucleus for each atomic electron can also change. Electrons moving in a free atom ''strive'' to maximize their distance from one another because of their mutual repulsion. During the short interaction time $T(b)$ the strong field of the MCI displaces the electron packets from their initial positions in approximately the same direction. The effect of this is to decrease the ratio of the average interelectron distance to the average distance between the electrons and the helium nucleus and, correspondingly, the electrons increase the screening of the atomic nucleus for one another. Thus, it can be conjectured that the effective charge of the atomic core should decrease when the electrons are displaced. Assuming the effective charge z_2 to be a function of this displacment (i.e., a function of the ratio Z/v^2) and using for small Z/v^2 the simple expansion

$$z_2^{-2}\simeq z_2^{-2}(0)(1+\alpha_2 Z/v^2),$$

where $\alpha_2>0$ is independent of Z and v and $z_2(0)$ $z_2(0)\simeq z_2(v^{-1})\sim z_2(Z=v)\simeq 2$, we obtain from Eqs. (12) and (13)

$$\sigma_i^{(2+)}\simeq 2.35\frac{Z^2}{v^2}(1+\alpha Z/v^2), \tag{14}$$

where $\alpha=\alpha_1+\alpha_2$.

We note that terms of order Z^3/v^4 can still be taken into account in the cross section in the approximation employed, where the term of order Z^4/v^6, which is much less than Z^3/v^4 for $Z/v^2\ll 1$, is dropped. Comparing with the experimental data from Refs. 2–5 gives $\alpha=0.5$. The results obtained with Eq. (14) are presented in Figs. 5 and 6 (solid curves). For the collision parameters Z and v in Fig. 2 the Eqs. (12) and (14) give virtually identical results for the cross sections.

In many works[3,5,15] a great deal of attention was devoted to the ratio of the cross sections $R=\sigma_i^{(2+)}/\sigma_i^{(1+)}$. For this ratio we have from Eqs. (9) and (14)

$$R=0.19(1+0.5Z/v^2)\left(\ln\left(\frac{1.2v^2}{Z}\gamma\right)-\frac{v^2}{2c^2}\right)^{-1}. \tag{15}$$

The authors of the experiment of Ref. 15 pointed out that their data on R as a function of v/Z for recations with participation of U^{+90} (60, 120, 420 MeV/amu) do not fall on a ''universal'' curve. In our view, these data from Ref. 15 do not stand alone as compared with other data on the ionization of helium by fast ions with high charges (specifically, this follows from Fig. 8b of Ref. 5 of the same authors as those of Ref. 15). The ''universal'' curve for R, proposed in Ref. 3 for relatively small charges of the incident particles, is not, in our opinion, universal for collisions with the participation of ions with large charges. Moreover, it seems to us that in the

collision parameter range $Z \gtrsim v \gg v_0$ it is more natural to plot R as a function of v^2/Z (and not v/Z, in any case while the Lorentz factor γ is not too large $\gamma \ll v^2/Z$), bearing in mind the known scaling for the cross section for ionization by fast (but nonrelativistic) MCIs $\sigma/Z = f(v^2/Z)$.[1] On such a scale all data on R which are known to us for fast MCIs follow well the curve described by the expression (15).

3. CONCLUSIONS

We have proposed simple formulas for the single- and double-ionization cross sections of helium atoms in collisions with fast ions with very large charges. These formulas are applicable in a quite wide range of collision parameters: $v^2 \gg Z \gtrsim v$, $v_0 \ll v < c$. Up to now these cross sections have been studied quite systematically experimentally for $v^2/c^2 \ll 1$. At the same time, for $Z \sim v \sim c$ only isolated experimental data are available (and only for small values of γ). In our opinion it would be of definite interest to perform systematic investigations of the cross sections for the ionization of helium by heavy ions at relativistic collision velocities, where γ is substantially greater than 1.

[1)] In our approach the quantity δ can be estimated only qualitatively. For this reason it is pointless to calculate $\partial\varphi_{1s}/\partial\rho$ (and the corresponding integrals over the variable **r** and **b**).

[1] L. P. Presnyakov, V. P. Shevel'ko, and R. K. Yanev, *Elementary Processes with Participation of Multiply Charged Ions* [in Russian], Énergoatomizdat, Moscow (1986), 200 pp.
[2] H. Berg, *Doctoral Dissertation*, Universitat Frankfurt, 1993.
[3] H. Knudsen, L. H. Andersen, P. Hvelplund *et al.*, J. Phys. B **17**, 3545 (1984).
[4] J. H. McGuire, A. Mueller, B. Shuch *et al.*, Phys. Rev. A **35**, 2479 (1987).
[5] H. Berg, J. Ullrich, E. Bernstein *et al.*, J. Phys. B **25**, 3655 (1992).
[6] R. K. Janev and L. P. Presnyakov, J. Phys. B **13**, 4233 (1980).
[7] R. K. Janev, Phys. Lett. A **83**, 5 (1981).
[8] M. L. McKenzie and R. E. Olson, Phys. Rev. A **35**, 2863 (1987).
[9] A. Salin, Phys. Rev. A **36**, 5471 (1987).
[10] J. F. Reading and A. L. Ford, Phys. Rev. Lett. **58**, 543 (1987); J. Phys. B **20**, 3747 (1987).
[11] V. S. Nikolaev and V. A. Sidorovich, Nucl. Instrum. Methods **36**, 239 (1989).
[12] P. D. Fainstein, V. H. Ponce, and R. D. Rivarola, J. Phys. B **24**, 3091 (1991).
[13] L. P. Presnyakov, H. Tawara, I. Yu. Tolstikhina, and D. B. Uskov, J. Phys. B **28**, 785 (1995).
[14] N. Mott and H. Massey, *The Theory of Atomic Collisions* [Clarendon Press, Oxford, 1965 (3rd edition); Nauka, Moscow, 1969].
[15] H. Berg, M. D. DuBois, O. Jagutzki *et al.*, Phys. Rev. A **46**, 5539 (1992).
[16] J. Ullrich, R. Moshammer, H. Berg *et al.*, Phys. Rev. Lett. **71**, 1697 (1993).
[17] J. H. McGuire, Adv. At. Mol. and Opt. Phys. **29**, 217 (1992).
[18] A. B. Voĭtkiv and A. V. Koval', Zh. Tekh. Fiz. **64**, 188 (1994) [Tech. Phys. **39**, 335 (1994)].
[19] A. M. Dykhne and G. L. Yudin, Usp. Fiz. Nauk **125**, 377 (1978) [Sov. Phys. Usp. **21**, 549 (1978)].
[20] C. O. Reinhold, C. A. Falcon, and J. E. Miraglia, J. Phys. B **20**, 3737 (1987).
[21] A. B. Voĭtkiv and V. I. Matveev, Zh. Tekh. Fiz. **65**, 12 (1995) [Tech. Phys. **40**, 6 (1995)].
[22] E. L. Duman, L. I. Menshikov, and B. M. Smirnov, Zh. Éksp. Teor. Fiz. **76**, 516 (1979) [Sov. Phys. JETP **49**, 260 (1979)].
[23] A. R. Holt, J. Phys. B **2**, 1209 (1969).
[24] M. Inokuti, Rev. Mod. Phys. **43**, 297 (1971); *ibid.* **50**, 23 (1978).
[25] C. Reinhold and J. Burgdorfer, J. Phys. B **26**, 3101 (1993).
[26] J. J. Thompson, Philos. Mag. **23**, 449 (1912).
[27] S. L. Willis, G. Peach, M. R. C. McDowell, and J. Banerji, J. Phys. B **18**, 3921 (1985).
[28] A. B. Voitkiv and V. A. Pazdzersky, J. Phys. B **21**, 3369 (1988).
[29] A. B. Migdal and V. P. Kraĭnov, *Approximation Methods in Quantum Mechanics*, Benjamin, N. Y., 1969 [Russian original, Nauka, Moscow, 1966].

Translated by M. E. Alferieff

Laser-induced spatial structures in a chemically active gas-phase medium illuminated by annular diffracting beams

O. A. Gunaze and V. A. Trofimov

M. V. Lomonosov Moscow State University, 119899 Moscow, Russia
(Submitted April 18, 1996; resubmitted November 26, 1996)
Zh. Tekh. Fiz. **68**, 8–14 (March 1998)

The laws governing the propagation of diffracting beams in a two-component gaseous mixture are investigated on the basis of a computer simulation. It is discovered that several regions with high concentrations of the reaction product form. It is also found that the beam focus can move both in the direction of beam propagation and in the counter direction, and the change in its position can occur abruptly. It is shown that as time goes on, a high concentration of the reaction product is achieved in the central unilluminated region of the medium near the entrance cross section on account of diffusion (i.e., a diffusional concentration growth occurs). This leads to the formation of a dynamic concentration maximum in this region of the medium. © *1998 American Institute of Physics.* [S1063-7842(98)00103-2]

INTRODUCTION

One of the effective methods for controlling the rate of chemical reactions utilizes the action of laser radiation and the selective absorption of its energy by one of the components of a gas mixture.[1–8] Under certain conditions the nonequilibrium and local contribution of the light energy produces a complex spatial distribution of the reaction product (or of the original substance) in the medium, which is a consequence, in particular, of the multivalued (usually bistable) dependence of the concentration of each substance on intensity of the optical radiation entering the medium.

The diversity of the physicochemical processes taking place when laser radiation acts on a chemically active gas mixture partly accounts for the steady interest of various investigators in this problem. This interest is also due to the numerous practical applications of the results obtained from such research, as well as the possibility of realizing various nonlinear-optical self-organization processes, which belong to a rapidly developing area of laser physics known as nonlinear-optical dynamics.

In the present work, which continues the work in Ref. 8, the effectiveness of the action of a diffracting light pulse with an annular intensity distribution at the entrance to a cell containing a gas mixture is analyzed. It should be stressed that, as will be shown below, the diffraction of optical radiation fundamentally alters the spatial distribution of the concentration of the reaction product in comparison to the case of weakly diffracting beams. Therefore, diffraction must be taken into account in order to obtain results that faithfully describe the physical experiment in the case when the diffraction length of the beam is approximately equal to the longitudinal dimension of the cell.

STATEMENT OF THE PROBLEM

The distribution of a laser beam along the z coordinate in a chemically active, two-component gas mixture in the presence of a buffer gas with the absorption of optical energy by the reaction product under the assumption of local binding of the components of the gas mixture (one consequence of this is the equality between the diffusion coefficients of the original substance and the reaction product) is described by the system of dimensionless equations

$$\frac{\partial A}{\partial z}+iD\Delta_{\perp}A+i\varepsilon_{\mathrm{nl}}A+\delta_0 NA=0, \quad 0<z\leqslant 1,$$

$$\varepsilon\,\frac{\partial T}{\partial t}=\chi\Delta_{\perp}T+qN|A|^2+\gamma f, \quad t>0,$$

$$\frac{\partial N}{\partial t}=D_N\Delta_{\perp}N+f, \quad \Delta_{\perp}=\frac{\partial^2}{\partial x^2},$$

$$f=(1-N)\exp\left(-\frac{1}{T}\right)-kN\,\exp\left(-\frac{T_c}{T}\right),$$

$$\varepsilon_{\mathrm{nl}}=\alpha T+\beta(N-N_0) \tag{1}$$

with the initial and boundary conditions

$$A|_{z=0}=A_0(x)\sqrt{I_0(t)},$$

$$A|_{x=0,L_x}=0, \quad T|_{t=0}=T_0, \quad f|_{t=0}=0,$$

$$\left.\frac{\partial N}{\partial x}\right|_{x=0,L_x}=0, \quad \chi\left.\frac{\partial T}{\partial x}\right|_{x=0,L_x}=\pm\eta(T-T_0). \tag{2}$$

In (1) and (2) the complex amplitude $A(z,x,t)$ is normalized to its maximum entrance value; $N(z,x,t)$ is the concentration of the reaction product; $T(z,x,t)$ is the temperature of the medium normalized to the activation energy of the forward reaction expressed in temperature units; z is measured in units of the diffraction length $I_d=2\kappa a_0^2$, where κ is the wave number, a_0 is the initial radius of the beam, and the transverse coordinate x is measured in units of a_0; D is a coefficient, which is equal to unity under the normalization selected but has been left in (1) for convenience in analyzing the influence of diffraction of the beam on the spatial distri-

bution of the temperature, the concentration, and the intensity of the light beam. The parameter δ_0 characterizes the amplitude of the absorption coefficient of all the molecules belonging to the reaction product. The time t is measured in units of the characteristic reaction time. The parameter ε characterizes the rate of variation of the temperature relative to the rate of variation of the composition of the gas mixture. The coefficients χ and D_N are equal, respectively, to the ratios of the characteristic reaction time to the characteristic heat-conduction and diffusion times. The parameter q is the ratio of the initial beam power to the power expended to change the composition of the mixture from the original gas to the reaction product. The parameter γ, which is proportional to (T_c-1), characterizes the thermal effect of the reaction, T_c is the ratio of the activation energies of the reverse and forward reactions, and k is the ratio of the preexponential factors of the reverse and forward reactions.

The self-effect of the optical radiation is described by the term with ε_{nl} in (1), in which α is the ratio between the entrance power P_0 of the beam to the power of the thermal self-effect ($\alpha<0$ corresponds to defocusing of the beam) and β is proportional to the difference between the refractive indices of the reaction product and the original substance. It is positive if the original substance is less dense than the reaction product, and is negative in the opposite situation, L_x is the boundary of the region along the x axis, and $I_0(t)$ describes the shape of the optical radiation pulse. In numerical experiments it is chosen in the form

$$I_0(t)=(1-\exp(-t/\tau))^2, \quad \tau=0.1 \tag{3}$$

and corresponds to the rapid achievement of a stationary level by the pulse.

We note that the boundary conditions pertaining to the concentration of the reaction product correspond to a cell that is closed with respect to mass transfer. On the other hand, heat exchange with the surrounding medium, whose temperature is T_0, takes place through the lateral surface. The heat-transfer rate is specified by the dimensionless constant η.

In accordance with the purpose of the present work, the initial beam profile was selected in the form

$$A_0(x)=\frac{(x-L_x/2)^2}{a^2}\exp\left(-\frac{(x-L_x/2)^2}{a^2}\right). \tag{4}$$

Two comments should be made regarding Eq. (4). First, the dimensionless parameter a has been introduced into (4) for convenience in representing the results obtained in the numerical experiments. It can be eliminated by making the replacements $D\to D/a^2$, $\chi\to\chi/a^2$, $D_N\to D_N/a^2$, and $L_x\to L_x/a^2$, which corresponds to the normalization chosen. Second, the term ''annular beam,'' which was introduced in the title of this paper, refers below to optical radiation whose initial intensity distribution has a dip on the axis. As we know, approximation (4) is valid if the beam radii along the transverse coordinates differ significantly. The need to analyze the distributions (4) is also dictated by the fact that it is difficult to simulate nonstationary nonlinear processes described by system (1) in a space of three variables because of the large time interval (several tens or hundreds of dimensionless units) during which the processes under investigation develop.

CALCULATION RESULTS

Taking into account the results in Ref. 8, we fix several parameters below:

$$T_c=0.375, \quad k=0.5, \quad T_0=0.125,$$
$$\eta=2, \quad \varepsilon=1, \quad L_x=2,$$
$$D_N=\chi=10^{-5}, \quad D=0.001, \quad q=5, \quad a=0.1. \tag{5}$$

We note that these choices of the values of D_N and χ stem from an analysis of the influence of purely diffraction effects on the kinetics of chemical reactions. In practice, all other conditions being equal, these values of the dimensionless coefficients can be ensured by adjusting both the initial beam radius and the duration of the optical illumination. The ratio $D/a^2=1$, which corresponds to a manifestation of the influence of diffraction on the cell length.

We stress that the effective diffusivity and thermal conductivity are specified by the ratios D_N/a^2 and χ/a^2 and are equal to 0.001, since a is the characteristic dimension of the spatial inhomogeneities induced by a Gaussian beam. In the case of the propagation of annular beams analyzed in the present work, the characteristic scale of the inhomogeneities induced by them is even smaller (by a factor of four, at least). Therefore, the influence of the diffusion is even stronger than in the case of Gaussian beams. In addition, because of the absorption of light energy and the frequently realized division of a light beam into subbeams in a medium as a result of diffraction effects, further enhancement of the influence of the diffusion and heat conduction of the medium on the temperature and concentration profiles is possible.

The numerical experiments performed reveal the following general laws governing the interaction of a diffracting beam with a chemically active gas mixture in the case of weak diffusion of its components. First of all, it should be stressed that diffraction of the beam transforms its intensity profile into a distribution having a maximum on the axis as the beam propagates along the z axis (Fig. 1). The nature of this transformation is governed by the interference of two subbeams. As we know, a similar picture appears when optical radiation is diffracted by two slits. In our case the transition into the region of the geometric shadow of the beam occurs smoothly; therefore, the intensity does not vanish between the subbeams, as it does in the intensity distribution after the passage of optical radiation through two slits.

Several stages can be clearly identified in the dynamics of the interaction of laser radiation with a chemical mixture. As in the case of illumination by wide-aperture beams, the process includes an initial slow stage, in which the concentration of the reaction product increases, a rapid increase in its concentration during a certain time interval, and then a slow decrease. The intensity of the beam varies in a similar manner. However, an increase in concentration corresponds to a decrease in the intensity of the optical radiation. Also, the rate of variation of the concentration is determined by the

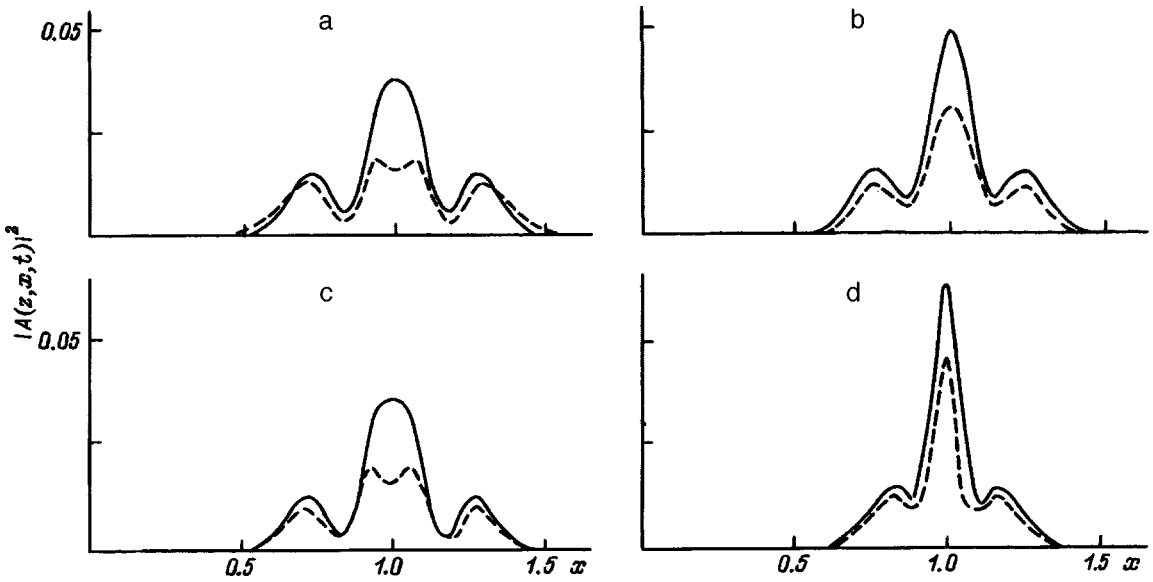

FIG. 1. Intensity distribution in the $z=0.5$ cross section at the times $t=25$ (solid curve) and 30 (dashed curve). $\delta_0=4$, $\gamma=0$; $\alpha=-5$, $\beta=0$ (a); $\alpha=\beta=0$ (b); $\alpha=0$, $\beta=-10$ (c); $\alpha=0$, $\beta=10$ (d).

coordinates of the point considered in the cell. It is significant that the spatial redistribution of the concentration of the reaction product is a result of two factors: diffusion and transformation of the beam profile due to diffraction.

The diffraction of optical radiation leads to inhomogeneous variation of the concentration of the reaction product along the longitudinal coordinate on the beam axis. For example, for wide-aperture beams there would be a monotonic decrease in N with increasing distance from the entrance side of the cell as a result of the diffusion of the mixture components in the $x=L_x/2$ plane (the center of the beam). In the case investigated here, i.e., the stimulation of chemical reactions by narrow-aperture beams, the situation is fundamentally different on account of the transformation of the intensity profile (Fig. 1). The maximum value of the concentration on the beam axis is achieved at first in the z_m cross section, which is specified by the diffraction of the beam in the transparent medium (in the initial stage there is little absorption). Then, z_m decreases with time and tends toward the entrance cross section of the cell. This occurs for two reasons: transformation of the beam profile into a Gaussian distribution over a shorter path at the beginning of the interaction (because of the decrease in its dimensions, for example, as a result of absorption), and diffusion of the gas components later on, when sufficiently high values of N are achieved (the rate of thermal diffusion plays an appreciable role here). With the passage of time, the concentration of the reaction product increases near the entrance cross section, and its value becomes equal to the maximum concentration value at the point where the peak intensity is achieved. This is a new (fourth) stage in the in the interaction of annular beams with a chemically active gas mixture. This regime was not previously obtained for wide-aperture beams in Ref. 5, because the interaction of the laser beam with the chemically active medium was analyzed both over a shorter time interval and for higher diffusivity and thermal conductivity values.

The laws described are valid for all the relations between the parameters considered ($\alpha=0,-5$; $\beta=0,\pm10$; $\gamma=0,-2$; $\delta_0=4,8$); but each specific case has its own differences, which will be discussed below.

Propagation of light beams under weak-interaction conditions. This type of interaction ($\alpha=\beta=0$) is realized if the cell length is much shorter than the characteristic nonlinear thermal defocusing and refraction lengths due to alteration of the composition of the mixture. Let us, first of all, consider the case in which the influence of the thermal effect is insignificant ($\gamma=0$). The structure of three subbeams with a bright central maximum formed in the initial moment of propagation (a linear precursor) persists over the entire interval considered ($t\leqslant150$) (Fig. 1b). However, with the passage of time, the intensities at the maxima even off to the same value. The concentration profile of the reaction product also has a spatial distribution with three maxima; however, as the time increases, the values of N in the central part of the region achieve significantly higher values than do the lateral maxima. To illustrate this, Fig. 2a presents the evolution of the concentration N (solid curve *1*) and the intensity of the beam (dashed curve *1*) in the $z=0.5$ cross section on the beam axis ($x=L_x/2$), as well as the positions of their maxima on the beam axis (curves *2* in Fig. 2b) along z. We note that the time interval in which the interaction acquires the features of a process that is stationary with respect to the value of the peak intensity and the maximum concentration of the reaction product is confined to about 50 units.

When the influence of the thermal effect of the reaction on the evolution of the interaction process is appreciable (for example, when $\gamma=-2$), the main features of the preceding case persist. However, the rate of variation of the temperature and the concentration of the reaction product decreases, and the value of the concentration at the end of the cell decreases.

In analyzing the transformation of the complex spatial distribution of the concentration N along z (Fig. 3) it is important to stress an interesting detail. Initially, N has a

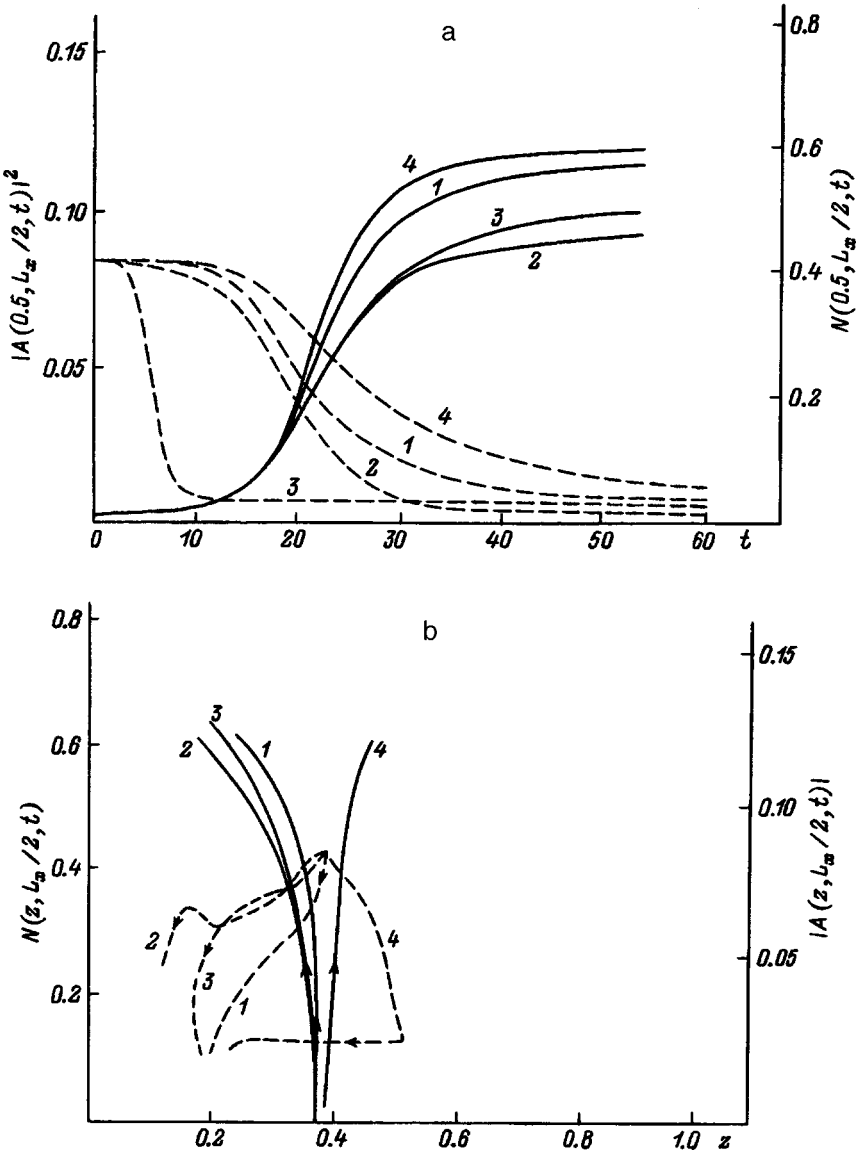

FIG. 2. a—Evolution of the light intensity (dashed curves, left-hand vertical axis) and the concentration of the reaction product (solid curves, right-hand vertical axis) on the beam axis: $\delta_0=4$, $\gamma=0$; *1*—$\alpha=\beta=0$; *2*—$\alpha=-5$, $\beta=0$; *3*—$\alpha=0$, $\beta=-10$; *4*—$\alpha=0$, $\beta=10$; b—temporal variation of the longitudinal coordinate of the intensity maximum (dashed curves, right-hand vertical axis) and of the concentration of the reaction product (solid curves, left-hand vertical axes) and their values on the beam axis for the interaction parameters corresponding to Fig. 1a (the arrow indicates the direction of variation).

smaller value on the beam axis near $z=0$ than at neighboring points along z. Then, with the passage of time, its value increases more rapidly than in the region located near the principal maximum along z, and the concentration profile transforms into a distribution with two local maxima along z, which were observed in all the cases analyzed. Then the concentration of the reaction product on the beam axis near the entrance cross section increases slowly, achieving a value practically equal to its value at the original maximum along z. Such a distribution is subsequently observed for a long time.

The formation and realization of a distribution of the concentration of the reaction product with several local maxima depends on the ratio between the characteristic diffusion times of the reaction product, the thermal conductivity, and the rates of the forward and reverse reactions. It is significant that the reaction rates are exponentially dependent on the temperature. As a result, the difference between the pre-exponential factors of the reactions is manifested at a fairly high temperature, at which the exponential factor becomes of the order of unity.

Therefore, several stages of development can be identified in the formation of the spatial structure presented in Fig. 3. At first, the reaction proceeds efficiently within the beam. As a result of diffusion and heat conduction, the concentra-

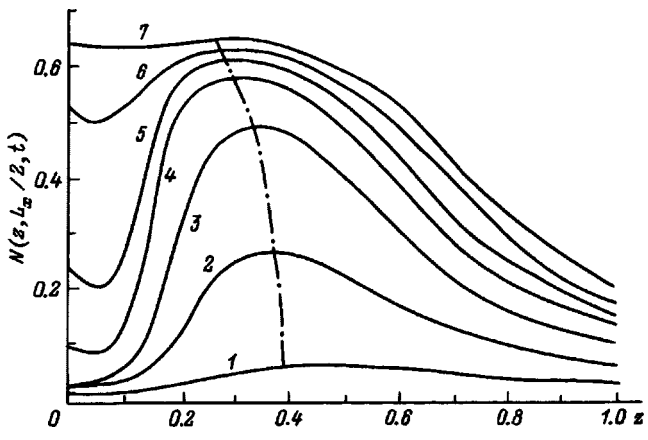

FIG. 3.

tion wave of the reaction product propagates into a region not occupied by the optical radiation, particularly near the center of the beam. This initially leads to increases in the concentration and temperature near the beam region. As a result of further diffusion, the concentration of the reaction product continues to increase at the center of the cell near $z=0$. However, the temperature here remains low for the following reason. Near the region illuminated by the optical radiation the temperature of the medium initially increases with resultant activation of the reverse reaction and the absorption of heat for the forward reaction (since $\gamma<0$). This results in termination of the propagation of the temperature wave along the transverse coordinate, practically complete cessation of the reverse reaction on the beam axis, and the appearance of an additional region with a high concentration at the entrance cross section.

This distribution is observed for a long time and is maintained by diffusion of the reaction product from the region illuminated by the optical radiation. This diffusion is also the reason for the formation of a homogeneous distribution of the concentration of the reaction product along z near the entrance end of the cell. In summation, we can refer to the process taking place as the diffusion-controlled stimulation of a reversible chemical reaction by laser radiation.

If the lateral surface of the cell is at a distance of the order of the distance from the maximum of the annular beam to its center, similar processes will take place in that direction. Therefore, generally speaking, the application of annular beams to a chemically active gas mixture opens up the possibility of forming a practically homogeneous distribution of the concentration of the reaction product along the transverse coordinate within a part of the region of the region along the propagation axis, which is determined by the initial beam power.

Summarizing this section, we can conclude that the kinetics of the stimulation of reversible chemical reactions by diffracting laser radiation are fundamentally altered in the case of comparable contributions to the variation of the temperature from the thermal effect of the reaction and the heating due to the optical radiation from the situation in the case of wide-aperture beams.

Influence of the self-effect of the light beam on the reaction kinetics. If the length of the cell is comparable to the characteristic self-effect length, the nonlinear refraction of the beam must be taken into account. We note that the thermal self-effect is manifested in the form of defocusing of the optical radiation and that the refraction due to the variation of the properties of the mixture can have the sign of either a focusing lens or a defocusing lens, depending on the optical properties of the medium. As will be shown below, the self-effect of the optical radiation can fundamentally alter both the dynamics of the interaction between the medium and the beam and the resultant spatial distribution of the concentration of the reaction product.

a) Thermal defocusing ($\alpha=-5$, $\beta=\gamma=0$). Let us first consider the effect of thermal defocusing. It is manifested, in particular, in the transformation of the spatial distribution of the beam: beginning at a certain moment in time the central (diffraction, i.e., formed in the initial, practically linear stage of the interaction at $t<25$) intensity maximum of the beam acquires an annular structure due to thermal defocusing, for example, in the $z=0.25$ cross section (Fig 1a). Consequently, the intensity profile of the optical radiation has only two maxima at the exit from the cell (the central diffraction maximum is absent).

This process is illustrated by Fig. 2 (curve *2*). A comparison of the evolution of the intensity of the beam on its axis ($x=L_x/2$) in the $z=0.5$ cross section for the cases of $\alpha=0$ and -5 shows that the light intensity decreases with increasing time because of the increase in the strength of the defocusing lens. The main drop in intensity occurs specifically in the time interval with an increase in the reaction rate. The redistribution of the intensity of the optical radiation in the transverse cross section also leads to lowering of the concentration of the reaction product on the beam axis (Fig. 2, curve *2*).

Thermal defocusing leads to twofold lowering of the concentration of the reaction product near the exit cross section of the cell. The coordinate at which the longitudinal maximum in the $x=L_x/2$ plane is achieved shifts toward the entrance cross section of the cell (Fig. 2b, solid curve *2*). This attests to focusing of the optical radiation over a shorter path than in the case of a weak self-effect. We note that the main mechanism maintaining a sufficiently high concentration of the reaction product on the axis in this case is diffusion. A fairly high concentration of the reaction product is maintained in the portion of the cell at $z>0.4$ in the interval that we considered specifically because of the low rates of heat removal and diffusion.

To conclude this section, we turn to an analysis of the evolution of the intensity of the beam on its axis (at $x=L_x/2$) along z. In Fig. 2b dashed curve *2* shows the temporal variation of the longitudinal coordinate of the maximum intensity. A segment corresponding to rapid displacement of the position of the maximum along the z axis can be singled out here. The strength of the thermal lens increases in this time interval. As a result, there is an abrupt shift of the intensity maximum in the center of the region, and even its height increases here (Fig. 2).

b) Defocusing of the beam due to variation of the composition of the mixture ($\alpha=\gamma=0$, $\beta=-10$). Defocusing of the beam due to variation of the composition of the mixture generally leads to results that are similar to the case of the thermal self-effect (Fig. 1c), but its influence is weaker. This is confirmed by solid curve *3* in Fig. 2b and by solid curve *3* and dashed curve *3* in Fig. 2a. However, there are also significant differences in the evolution of the beam intensity profile in comparison with thermal defocusing. For example, the time interval during which a dip in the intensity distribution forms on the beam axis in the $z=0.5$ cross section is followed by the formation of a central maximum in this cross section. As a result, a structure consisting of four subbeams of approximately equal intensity forms at the exit from the medium (instead of the three appearing for $\alpha=\beta=0$ and the two appearing in the preceding case).

The longitudinal coordinate of the intensity maximum in the $x=L_x/2$ cross section also varies with the passage of time according to a new scenario (Fig. 2b, dashed curve *3*). For

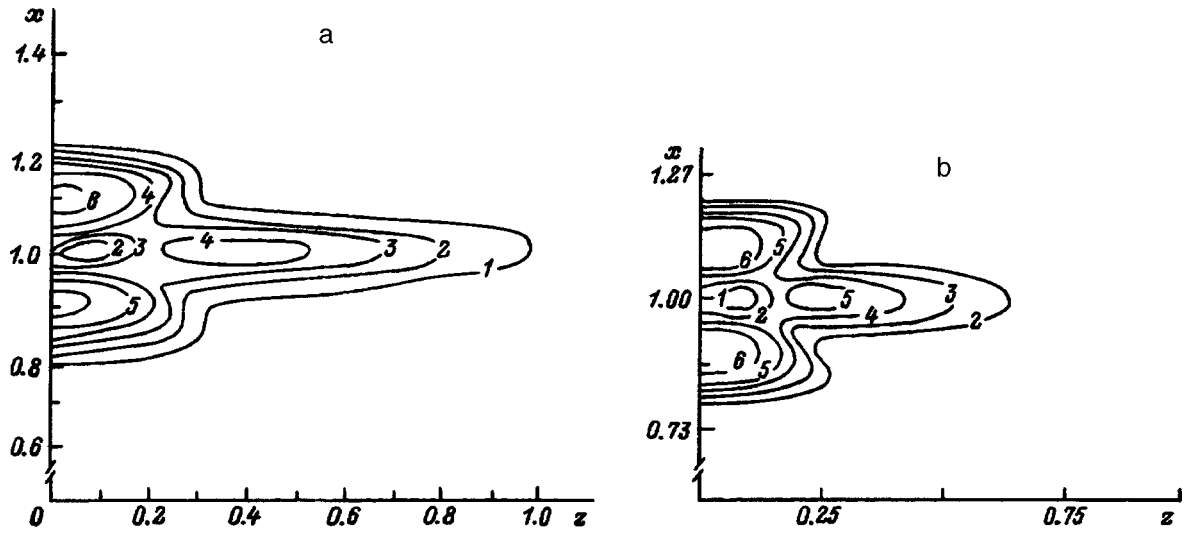

FIG. 4. Level lines of the concentration of the reaction product. $\delta_0=8$, $\alpha=0$; $\beta=10$ (a), -10 (b); $\gamma=0$; N: *1*—0.1, *2*—0.2, *3*—0.3, *4*—0.4, *5*—0.5, *6*—0.6.

example, while at first it shifts toward the entrance end of the cell, it subsequently moves in the opposite direction. The value of the intensity at this point decreases monotonically (in contrast to the case of thermal defocusing).

c) Self-focusing of the beam caused by variation of the composition of the mixture ($\alpha=\gamma=0$, $\beta=10$). Self-focusing of the light beam leads to an increase in the value of the intensity on the beam axis (for example, in the $z=0.5$ cross section; Figs. 1a and 2a, dashed curve *4*) and to a more rapid increase in the concentration of the reaction product in that region (Fig. 2a, solid curve *4*) in comparison to the case of a weak self-effect. The maximum concentration of the reaction product (Fig. 2b, solid curve *4*) is achieved farther from the entrance cross section of the cell and, in contrast to the preceding cases, shifts with time along the propagation direction of the optical radiation. In the steady-state regime a high value of the concentration of the reaction product is achieved within the beam over a more extensive portion of the propagation path.

The longitudinal coordinate of the intensity maximum in the $x=L_x/2$ cross section also evolves in a complicated manner. At first its value increases with time (the focus move along the z axis). Then there is a moment in time when the maximum intensity value is achieved over a certain range along z, after which there is a rapid decrease in the value of the coordinate of the intensity maximum. It subsequently remains practically constant. Such temporal evolution of the coordinate is due to the self-focusing of the beam, which increases in the initial stage of the interaction due to the increase in the concentration and then decreases because of the absorption of the radiated power by the reaction product.

The phenomenon which we discussed above can be called a jumping focus, where the beam focus is displaced over a distance of the order of $0.6ka_0^2$ during a very short time interval. In contrast to the familiar mechanism of a moving focus, as the entrance intensity of a pulse with a Gaussian spatial profile is increased in the present case, the displacement of the focus is antiparallel to the propagation direction of the optical radiation.

In conclusion, let us discuss one more phenomenon, which is observed for either sign of the self-effect (and in its absence): the existence of small-domain structures. Since their appearance is caused by diffraction of a beam on two slits, we shall call them multidomain diffraction structures. To illustrate this, we present Fig. 4, which shows level lines of the concentration of the reaction product at the time $t=50$ for $\delta_0=8$, $\beta=10$ (a) and -10 (b), and $\alpha=\gamma=0$. The figure clearly reveals for the formation of three transverse and two longitudinal high-concentration regions. We stress once again that such structures form regardless of the sign of the self-effect and are therefore of a diffractional nature.

CONCLUSIONS

In the present work we have investigated the influence of the diffraction and nonlinear refraction of optical radiation on the stimulation of reversible chemical reactions in gas mixtures. It has been shown that diffraction of the beam can fundamentally alter the spatiotemporal evolution of a region with a high concentration of the reaction product and, in particular, can lead to the formation of several domains of high absorption and a diffusional regime for stimulating reversible chemical reactions by laser radiation in a region not illuminated by it. We note that similar processes take place in other optically bistable systems based on increasing absorption, for example, in systems based on semiconductors. In our opinion, this research can be assigned to a new area within the study of optically bistable systems: the diffraction optics of cavityless, optically bistable systems. The results of the present work show that the refraction of light beams fundamentally alters the propagation of optical radiation and the shaping of the regions of high absorption in comparison to the case of the action of wide-aperture beams on a medium.

This work was performed with support from the Russian Fund for Fundamental Research (Grant No. 95-02-0448-a).

[1] A. M. Bonch-Bruevich and M. N. Libenson, Izv. Akad. Nauk SSSR Ser. Fiz. **46**, 1104 (1982) [Bull. Acad. Sci. USSR, Phys. Ser. **46**(6), 82 (1982)].

[2] F. V. Bunkin, N. A. Kirichenko, and B. S. Luk'yanchuk, Izv. Akad. Nauk SSSR Ser. Fiz. **46** 1150 (1982) [Bull. Acad. Sci. USSR, Phys. Ser. **46**(6), 122 (1982)].
[3] M. I. Kalinichenko and V. A. Trofimov, Zh. Tekh. Fiz. **63**(9), 99 (1993) [Tech. Phys. **38**, 786 (1993)].
[4] M. I. Kalinichenko and V. A. Trofimov, Zh. Tekh. Fiz. **63**(8), 195 (1993) [Tech. Phys. **38**, 732 (1993)].
[5] M. I. Kalinichenko and V. A. Trofimov, Khim. Fiz. **9**, 901 (1990).
[6] O. A. Gunaze and V. A. Trofimov, Bull. Russ. Acad. Sci. Phys., Suppl. Phys. Vib. **57**, 193 (1993).
[7] V. A. Trofimov and V. V. Troshin, Comput. Math. Model. **1**, 251 (1990).
[8] O. A. Gunaze and V. A. Trofimov, Izv. Ross. Akad. Nauk, Ser. Fiz. **60** No. 6, (1996) (in press).

Translated by P. Shelnitz

Combined modes of a two-layer fluid and a solid block in an infinite waveguide

A. K. Abramyan, V. V. Alekseev, and D. A. Indeĭtsev

Institute of Mechanical-Engineering Problems, Russian Academy of Sciences, 199178 St. Petersburg, Russia
(Submitted May 28, 1996; resubmitted December 27, 1996)
Zh. Tekh. Fiz. **68**, 15–19 (March 1998)

It is shown that a waveguide in the form of a channel of infinite length filled by a two-layer heavy fluid with a free surface can have nonpropagating waves (trapped vibrational modes) along with traveling waves. These waves are localized in the region of a dynamic inclusion, i.e., a solid block (massive die) on the bottom of the channel. The appearance of such waves is due to the presence of a real discrete frequency spectrum of eigenmodes, which is located on the axis of the continuous spectrum corresponding to the divergent waves in the fluid. A relation between the geometric parameters of the channel and the characteristics of the fluid and the solid block for which such a spectrum exists is found for cases with fluids of similar density in the waveguide. © *1998 American Institute of Physics.* [S1063-7842(98)00203-7]

INTRODUCTION

The resonant properties of elastic systems of finite dimensions are well known. They include, first of all, the discrete and positive character of the frequency spectrum of eigenmodes. In the case of bodies having at least one boundary of infinite extent, regions of a continuous spectrum, whose boundaries are called cutoff frequencies in acoustics, appear. The existence of a mixed spectrum of eigenfrequencies was discovered in problems in the mechanics of a deformable solid by Vorovich and Babeshko. The resonant modes of a solid block on an elastic strip were considered in Refs. 1 and 2. The modes of a block in a channel filled by a heavy compressible fluid were considered in Ref. 3. The existence of nonpropagating modes (the existence of a discrete spectrum) in a channel containing a heavy compressible fluid with a free surface and a solid block on the bottom as an inclusion was established in Ref. 4. It was shown that the existence of both acoustic modes, which are specified by the compressibility of the fluid, and gravitational waves, which are caused by the presence of a free surface on the fluid, is possible in the system.

The present work demonstrates the existence of standing waves in a waveguide filled by a two-layer fluid with a free surface. An analytical solution indicating localization of the wave process in the region of a block, which is located on the bottom of the channel and undergoes small oscillations, is obtained for the case of fluids of similar densities. Such a case is of great practical importance in questions concerning oceanology and hydraulic engineering.

MODES OF A HEAVY TWO-LAYER FLUID IN A PLANAR CHANNEL WITH AN INCLUSION

A planar channel of infinite length and height H is filled by an incompressible nonviscous fluid consisting of two layers. The density and thickness of the upper layer of the fluid are ρ_1 and h_1, and those of the lower layer are ρ_2 and h_2 ($\rho_2 > \rho_1$). The x,y plane is chosen in the plane of the interface between the two fluids in equilibrium, and the z axis is directed vertically upward. The upper fluid layer ($z=h_1$) has a free surface, and the lower layer ($z=-h_2$) is bounded by a stationary horizontal plane. On the bottom of the channel there is a block of mass M and width $2a$, which undergoes small vertical oscillations according to the harmonic law $w=w_0 \exp(-i\omega t)$ with the frequency ω and the displacement amplitude w_0. The z axis passes through the middle of the block.

Gravitational waves, which propagate simultaneously along the free surface and along the interface between the fluids, are excited under the action of the oscillations of the block. The motion of the fluid is assumed to be potential motion with a velocity potential φ_j and is described by the Laplace equation $\nabla^2 \varphi_j = 0$ (here and below the variables corresponding to the upper layer have the label $j=1$, and those for the other layer have the label $j=2$). The motion of the fluid satisfies the boundary conditions

$$\frac{\partial \varphi_1}{\partial z} + \frac{1}{g}\frac{\partial^2 \varphi_1}{\partial t^2} = 0, \quad z = h_1, \tag{1}$$

$$\frac{\partial \varphi_1}{\partial z} = \frac{\partial \varphi_2}{\partial z}, \quad z = 0, \tag{2}$$

$$\frac{\partial \varphi_2}{\partial z} = \begin{cases} 0, & |x| > a \\ \partial w/\partial t, & |x| \leqslant a, \end{cases} \quad z = -h_2, \tag{3}$$

where g is the acceleration of gravity and w is the coordinate of the surface of the block.

Condition (1) is the usual condition on a free surface. Condition (2) expresses the condition of equality between the velocities of the two fluids at the interface. Condition (3) expresses the condition of equality between the velocities of the fluid particles and the block at the contact surface, as well as the condition of impenetrability of the solid boundaries of the channel.

The pressures acting in the fluids are

$$p_1(z) = -\rho_1 \frac{\partial \varphi_1}{\partial z} - \rho_1 g z, \quad p_2(z) = -\rho_2 \frac{\partial \varphi_2}{\partial z} - \rho_2 g z.$$

On the interface between the fluids, i.e., $\eta(x,t)$, the pressure should be continuous, i.e., $p_1(\eta)=p_2(\eta)$. According to Ref. 5, this condition together with (2) leads to the relation

$$g(\rho_2-\rho_1)\frac{\partial\varphi_1}{\partial z}=\rho_1\frac{\partial^2\varphi_1}{\partial t^2}-\rho_2\frac{\partial^2\varphi_2}{\partial t^2},\quad z=0. \tag{4}$$

To formulate the boundary condition at $x\to\pm\infty$, we utilize the familiar radiation condition.[6]

The motion of the block is described by the equation

$$M\frac{d^2w}{dt^2}=-\int_{-a}^{a}p_2(x,-h_2,t)dx. \tag{5}$$

The pressure on the bottom of the channel $p_2(x,-h_2,t)$ is specified by the relation

$$p_2|_{z=-h_2}=-\rho_2\left.\frac{\partial\varphi_2}{\partial t}\right|_{z=-h_2}-\rho_2 g\begin{cases}0, & |x|>a,\\ w, & |x|\leqslant a.\end{cases} \tag{6}$$

All the variables characterizing the flow of the fluid are assumed to be proportional to the multiplier $\exp(-i\omega t)$, as is done in the investigation of steady oscillations, only the real part having physical meaning.

Performing Fourier transformation with respect to the coordinate x in the system of equations and boundary conditions (1)–(4) and separating out the temporal multiplier $\exp(-i\omega t)$, we obtain

$$\frac{\partial^2\hat\varphi_j}{\partial z^2}-k^2\hat\varphi_j=0, \tag{7}$$

$$\frac{\partial\hat\varphi_1}{\partial z}-\frac{\omega^2}{g}\hat\varphi_1=0,\quad z=h_1,$$

$$\frac{\partial\hat\varphi_1}{\partial z}=\frac{\partial\hat\varphi_2}{\partial z}, \tag{8}$$

$$g(\rho_2-\rho_1)\frac{\partial\hat\varphi_1}{\partial z}=-\omega^2(\rho_1\hat\varphi_1-\rho_2\hat\varphi_2),\quad z=0, \tag{9}$$

$$\frac{\partial\hat\varphi_2}{\partial z}=-2i\omega w_0\frac{\sin ka}{k},\quad z=-h_2, \tag{10}$$

where $\hat\varphi(z,k)=\int_{-\infty}^{\infty}\varphi\exp(-ikx)dx$.

The solution of Eqs. (7) has the form

$$\hat\varphi_1(z,k)=A_1\sinh kz+B_1\cosh kz,$$

$$\hat\varphi_2(z,k)=A_2\sinh kz+B_2\cosh kz,$$

where the constants A_1, B_1, A_2, and B_2 are determined from boundary conditions (8)–(10).

Then the solution is ultimately written in the form

$$\hat\varphi_1(z,k)=-\frac{2i\omega w_0}{\cosh kh_2\Delta(k,\omega)}\frac{\sin ka}{k^2}\times[\omega^2(gk\tanh kh_1-\omega^2)\sinh kz-\omega^2\times(gk-\omega^2\tanh kh_1)\cosh kz],$$

$$\hat\varphi_2(z,k)=-\frac{2i\omega w_0}{\Delta(k,\omega)\cosh kh_2}\frac{\sin ka}{k^2}\times\left\{\omega^2(gk\tanh kh_1-\omega^2)\times\sinh kz-\left[\omega^2\frac{\rho_1}{\rho_2}(gk-\omega^2\tanh kh_1)-gk\frac{\Delta\rho}{\rho_2}(gk\tanh kh_1-\omega^2)\right]\cosh kz\right\},$$

where we have introduced the notation $\Delta\rho=\rho_2-\rho_1$,

$$\Delta(k,\omega)=-\omega^4\left(1+\frac{\rho_1}{\rho_2}\tanh kh_1\tanh kh_2\right)+\omega^2gk(\tanh kh_1+\tanh kh_2)-g^2k^2\frac{\Delta\rho}{\rho_2}\tanh kh_1\tanh kh_2. \tag{11}$$

Studying combined modes of the fluid and the block requires an expression for the pressure on the bottom of the channel like (6), which contains the quantity $\varphi_2(x,-h_2)$. Therefore, we present the final form of the streaming potential only for the lower layer of the fluid. Performing the inverse Fourier transformation of $\hat\varphi_2(z,k)$ for $z=-h_2$ using the properties of the convolution, we obtain

$$\varphi_2(x,-h_2)=-i\omega w_0\int_{-a}^{a}G(|x-\xi|,\omega)d\xi, \tag{12}$$

where $G(|x-\xi|,\omega)$ is the Green's function of the original problem.

The Green's function $G(x,\omega)$ is represented in the form

$$G(x,\omega)=\frac{1}{2\pi}\int_{-\infty}^{\infty}\frac{1}{k}\frac{\Delta_1(k,\omega)}{\Delta(k,\omega)}\exp(ikx)dk. \tag{13}$$

Here the denominator in the integrand is defined by Eq. (11), and the numerator has the form

$$\Delta_1(k,\omega)=\omega^4\left(\frac{\rho_1}{\rho_2}\tanh kh_1+\tanh kh_2\right)-\omega^2gk(1+\tanh kh_1\tanh kh_2)+g^2k^2\frac{\Delta\rho}{\rho_2}\tanh kh_1.$$

The dispersion relation $\Delta(k,\omega)=0$ has real roots of the form

$$\omega_{1,2}^2=\frac{gk(\tanh kh_1+\tanh kh_2)}{2[1+(\rho_1/\rho_2)\tanh kh_1\ \tanh kh_2]}\left\{1\pm\sqrt{1-4\frac{\Delta\rho}{\rho_2}\frac{[1+(\rho_1/\rho_2)\tanh kh_1\ \tanh kh_2]\tanh kh_1\ \tanh kh_2}{(\tanh kh_1+\tanh kh_2)^2}}\right\}. \quad (14)$$

It can be shown that the expression under the radical sign is never less than zero. Therefore, the relation $\Delta(k,\omega)=0$ contains two branches of the dispersion curves. One branch, $\omega_1^2(k)$, specifies the surface wave in the layer, and the other branch, $\omega_2^2(k)$, specifies the wave on the interface between the two media.

Let us find the explicit form of the Green's function. The integration in (13) is performed on the complex plane using the residue theorem. The integrand in (13), where k is now complex, has the poles $\pm k_0^{(1)}$ and $\pm k_0^{(2)}$ on the real axis and the poles $\pm ik_n^{(1)}$ and $\pm ik_n^{(2)}$ $(n=1,2,\ldots)$ on the imaginary axis, which are specified by Eq. (14). The superscripts 1 and 2 in the notation for the poles correspond to waves of the surface layer and waves on the interface between the two media.

The integral in (13) should be calculated with consideration of the radiation condition, which was mentioned in the formulation of the problem and states that only outgoing waves exist at $x\to\pm\infty$. This can be realized using the principle of limiting absorption by formally adding the term $\varepsilon\partial\varphi_1/\partial t$, which characterizes damped waves, where ε is a small parameter, to the right-hand side of Eq. (1). Then, in (8)–(10) the frequency ω will be a complex quantity with an imaginary part that is proportional to ε. This leads to displacement of the poles $k_0^{(1)}$ and $k_0^{(2)}$ from the real axis by an amount proportional to ε. In this case the integration in (13) is performed over a contour that does not enclose singularities on the real axis, and this eliminates the indeterminacy of the result. After calculating the integral in (13) and letting ε tend to zero, we have a solution that does not contain waves arriving from infinity.

Because of the symmetry of the flow pattern relative to $x=0$, we perform the integration in (13) for $x>0$. Then the integration contour will not contain the poles $-k_0^{(1)}$, $-k_0^{(2)}$, $ik_n^{(1)}$, and $-ik_n^{(2)}$ within it, and after the parameter ε is allowed to tend to zero, the Green's function is represented in the form

$$G(x,\omega)=iA(k_0^{(1)})\exp(ik_0^{(1)}x)+iA(k_0^{(2)})\exp(ik_0^{(2)}x)+i\sum_{n=1}^{\infty}A(k_n^{(1)})\exp(-k_n^{(1)}x)+i\sum_{n=1}^{\infty}A(k_n^{(2)})\exp(-k_n^{(2)}x), \quad (15)$$

where $A(k)$ is defined by the expression

$$A(k)=\Delta_1(k,\omega)\left\{\frac{d}{dk}[k\Delta,(k,\omega)]\right\}^{-1}.$$

In accordance with (12) and (6), in which the multiplier $\exp(-i\omega t)$ was separated out, the pressure on the bottom of the channel has the form

$$p_2(x,-h_2)=p_2\omega^2w_0\int_{-a}^{a}G|x-\xi|,\omega)d\xi-\rho_2g\begin{cases}0, & |x|>a,\\ w_0, & |x|<a.\end{cases} \quad (16)$$

In calculating the integral in (16) it should be borne in mind that the Green's function at $-\infty<x<\infty$ is also given by (15), except that the variable x must be replaced by $|x|$ in the exponents.

NONPROPAGATING MODES OF A TWO-LAYER FLUID IN A CHANNEL WITH AN INCLUSION

The combined modes of the two-layer fluid and the solid block will be studied for the case in which the densities of the fluids are approximately equal, i.e., $\rho_1\approx\rho_2$. In an approximation the dispersion relation (11) has the form

$$\omega^4(1+\tanh kh_1\ \tanh kh_2)+\omega^2gk(\tanh kh_1+\tanh kh_2)-g^2k^2\frac{\Delta\rho}{\rho_2}\tanh kh_1\ \tanh kh_2=0.$$

It has the roots

$$\omega_{1,2}^2=\frac{gk\ \tanh k(h_1+h_2)}{2}\times\left[1\pm\sqrt{1-4\frac{\Delta\rho}{\rho_2}\frac{\coth k(h_1+h_2)}{\coth kh_1+\coth kh_2}}\right].$$

Expanding the square root into a Taylor series, we obtain

$$\omega_1^2=gk\ \tanh k(h_1+h_2),$$

$$\omega_2^2=\frac{\Delta\rho}{\rho_2}gk(\coth kh_1+\coth kh_2)^{-1}, \quad (17)$$

where $\omega_1^2(k_0^{(1)})$ is a surface wave in a layer of thickness h_1+h_2, and $\omega_2^2(k_0^{(2)})$ is an internal wave on the interface between the fluids with consideration of the boundaries at $z=h_1$ and $z=-h_2$.

We write the Green's function at $-\infty<x<\infty$ in the form

$$G(x,\omega)=iA_1(k_0^{(1)})\exp(ik_0^{(1)}|x|)+iA_2(k_0^{(2)})\exp(ik_0^{(2)}|x|)+\sum_{n=1}^{\infty}B_1(k_n^{(1)})\exp(-k_n^{(1)}|x|)+\sum_{n=1}^{\infty}B_2(k_n^{(2)})\exp(-k_n^{(2)}|x|),$$

where $k_0^{(1)}$ and $k_0^{(2)}$ are defined by (17), and $k_n^{(1)}$ and $k_n^{(2)}$ are defined, respectively, by the relations

$$\omega_1^2=-gk_n^{(1)}\tan[k_n^{(1)}(h_1+h_2)],$$

$$\omega_2^2 = -\frac{\Delta\rho}{\rho_2} g k_n^{(2)} (\cot k_n^{(2)} h_1 + \cot k_n^{(2)} h_2)^{-1}. \tag{18}$$

The coefficients $A_1(k_0^{(1)})$, $A_2(k_0^{(2)})$, $B_1(k_n^{(1)})$, and $B_2(k_n^{(2)})$ are not presented because of their cumbersome nature. Performing the integration of the Green's function in (16), we obtain the expression for the pressure on the bottom of the channel at $|x|<a$

$$\begin{aligned} p_2(x,-h_2) = 2\rho_2\omega^2 w_0 & \times \left\{ \frac{A_1(k_0^{(1)})}{k_0^{(1)}} [\exp(ik_0^{(1)}a)\cos(k_0^{(1)}x) - 1] \right. \\ & + \frac{A_2(k_0^{(2)}}{k_0^{(2)}} [\exp(ik_0^{(2)}a)\cos(k_0^{(2)}x) - 1] \\ & + \sum_{n=1}^{\infty} \frac{B_1(k_n^{(1)})}{k_n^{(1)}} [1 - \exp(-k_n^{(1)}a)\cosh(k_n^{(1)}x)] \\ & + \sum_{n=1}^{\infty} \frac{B_2(k_n^{(2)})}{k_n^{(2)}} [1 - \exp(-k_n^{(2)}a) \\ & \left. \times \cosh(k_n^{(2)}x)] \right\} - \rho_2 g w_0, \end{aligned} \tag{19}$$

and at $|x|>a$ we obtain

$$\begin{aligned} p_2(x,-h_2) = 2\rho_2\omega^2 w_0 & \left[i\frac{A_1(k_0^{(1)})}{k_0^{(1)}} \exp(ik_0^{(1)}x)\sin(k_0^{(1)}a) \right. \\ & + i\frac{A_2(k_0^{(2)}}{k_0^{(2)}} \exp(ik_0^{(2)}x)\sin(k_0^{(2)}a) \\ & + \sum_{n=1}^{\infty} \frac{B_1(k_n^{(1)})}{k_n^{(1)}} \exp(-k_n^{(1)}x)\sinh(k_n^{(1)}a) \\ & \left. + \sum_{n=1}^{\infty} \frac{B_2(k_n^{(2)})}{k_n^{(2)}} \exp(-k_n^{(2)}x)\sinh(k_n^{(2)}a) \right]. \end{aligned} \tag{20}$$

The presence of the imaginary multipliers in the expression for the pressure at $|x|>a$ physically signifies that the energy of the oscillating block is transported by surface and internal waves to infinity.

The existence of a discrete spectrum of modes in the infinite waveguide under consideration can be ensured only in the absence of waves which transport energy to infinity. Then, the terms specifying the transport of energy in the solution obtained must be set equal to zero. The corresponding terms in the expression (20) for the pressure at $|x|>a$ are the ones which contain $\exp(ik_0^{(1)}x)$ and $\exp(ik_0^{(2)}x)$. To eliminate them we require fulfillment of the equalities $\sin(k_0^{(1)}a)=0$ and $\sin(k_0^{(2)}a)=0$. This is ensured under the conditions $k_0^{(1)}=(\pi/a)l$ and $k_0^{(2)}=(\pi/a)m$ $(l,m=1,2,\ldots)$. Let us ascertain when the fulfillment of these conditions is possible. The existence of combined modes in the fluid requires equality between the frequencies of the surface and internal waves defined by (17). Equating expressions (17), we have

$$\begin{aligned} & \frac{\Delta\rho}{\rho_2} \frac{\tanh(k_0^{(2)}h_1)\tanh(k_0^{(2)}h_2)}{\tanh(k_0^{(2)}h_1)+\tanh(k_0^{(2)}h_2)} \\ & \times \frac{1+\tanh(k_0^{(1)}h_1)\tanh(k_0^{(1)}h_2)}{\tanh(k_0^{(1)}h_1)+\tanh(k_0^{(1)}h_2)} = \frac{k_0^{(1)}}{k_0^{(2)}} = \frac{l}{m}. \end{aligned} \tag{21}$$

For the limiting cases of deep and shallow water, from (21) we find in an approximation

$$\begin{aligned} & \text{for } h_1, h_2 \gg a (\text{deep water}) \; l/m = \Delta\rho/(2\rho_2), \\ & \text{for } h_1 \approx h_2 \ll a (\text{shallow water}) \; l/m = [\Delta\rho/(4\rho_2)]^{1/2}. \end{aligned} \tag{22}$$

We note that the numbers l and m characterize the number of crests on the standing surface and internal waves appearing over a block of length $2a$, i.e., in the absence of waves which transport energy to infinity the energy of the oscillating block and the fluid is localized within the length of the block. In addition, the number of standing surface waves must be smaller than the number of internal waves in the ratio specified by (22).

We define the force exerted by the fluid on the oscillating block using the expressions for the pressure (19):

$$\begin{aligned} Q = & -\int_{-a}^{a} p_2(x,-h_2)\,dx \\ = & -4\rho_2\omega^2 w_0 \left\{ \frac{A_1(k_0^{(1)})}{k_0^{(1)}} \left[\exp(ik_0^{(1)}a)\, \frac{\sin(k_0^{(1)}a)}{k_0^{(1)}} - a \right] \right. \\ & + \frac{A_2(k_0^{(2)})}{k_0^{(2)}} \left[\exp(ik_0^{(2)}a)\, \frac{\sin(k_0^{(2)}a)}{k_0^{(2)}} - a \right] \\ & + \sum_{n=1}^{\infty} \frac{B_1(k_n^{(1)})}{k_n^{(1)}} \left[a - \exp(-k_n^{(1)}a)\, \frac{\sinh(k_n^{(1)}a)}{k_n^{(1)}} \right] \\ & \left. + \sum_{n=1}^{\infty} \frac{B_2(k_n^{(2)})}{k_n^{(2)}} \left[a - \exp(-k_n^{(2)}a)\, \frac{\sinh(k_n^{(2)}a)}{k_n^{(2)}} \right] \right\} \\ & + 2a\rho_2 g w_0. \end{aligned}$$

To determine the steady oscillations of the fluid and the block, we substitute the force found Q into Eq. (5), which defines the motion of the block. We also take into account that the equalities $\sin(k_0^{(1)}a)=0$ and $\sin(k_0^{(2)}a)=0$, which eliminate the transport of energy to infinity, must be satisfied for the steady oscillations. We then obtain the equation of motion of the block in the form

$$\begin{aligned} -M\omega^2 w_0 = 4\rho_2\omega^2 w_0 & \left\{ \frac{A_1(k_0^{(1)})}{k_0^{(1)}} a + \frac{A_2(k_0^{(2)})}{k_0^{(2)}} a \right. \\ & - \sum_{n=1}^{\infty} \frac{B_1(k_n^{(1)})}{(k_n^{(1)})^2} [ak_n^{(1)} \\ & - \exp(-k_n^{(1)}a)\sinh(k_n^{(1)}a)] \\ & \left. - \sum_{n=1}^{\infty} \frac{B_2(k_n^{(2)})}{(k_n^{(2)})^2} [ak_n^{(2)} \right. \end{aligned}$$

$$-\exp(-k_n^{(2)}a)\sinh(k_n^{(2)}a)]\Bigg\}+2a\rho_2 g w_0.$$

It is seen that Eq. (23) describes the steady oscillations of the fluid and the block only when the right-hand side is negative. Otherwise, the equation does not have any physical meaning.

Let us estimate the orders of magnitude of the terms appearing on the right-hand side of Eq. (23). We perform the calculation for the case of shallow water, setting $h_1=h_2=h\ll a$ and $H=2h$. In addition, we assume that there is one standing wave on the surface of the fluid, i.e., $l=1$. Then, in an approximation we have

$$A_1(k_0^{(1)})\approx-\frac{1}{2k_0^{(1)}H},\quad A_2(k_0^{(2)})\approx-\frac{1}{2k_0^{(2)}H}.$$

It can be shown that the roots of expressions (18) lie in the ranges $-\pi/2+\pi n<k_n^{(1)}H<\pi n$ and $-\pi/2+\pi n<k_n^{(2)}h<\pi n$ $(n=1,2,\ldots)$. When $\Delta\rho/\rho_2$ is small, we set

$$B_1(k_n^{(1)})=-[0.5\ \sin(2k_n^{(1)}H)+k_n^{(1)}H]^{-1},$$

$$B_2(k_n^{(2)})=-[0.5\ \sin(2k_n^{(2)}H)+k_n^{(2)}H]^{-1}.$$

Then Eq. (23) can be written in the form

$$-M\omega^2 w_0=2\rho_2\omega^2 w_0\Bigg\{-\frac{aH}{(k_0^{(1)}H)^2}-\frac{aH}{(k_0^{(2)}H)^2}+\sum_{n=1}^{\infty}\frac{2k_n^{(1)}a-1+\exp(-2k_n^{(1)}a)}{(k_n^{(1)})^2[0.5\ \sin(2k_n^{(1)}H)+k_n^{(1)}H]}+\sum_{n=1}^{\infty}\frac{2k_n^{(2)}a-1+\exp(-2k_n^{(2)}a)}{(k_n^{(2)})^2[0.5\ \sin(2k_n^{(2)}H)+k_n^{(2)}H]}+\frac{a}{\omega^2}g\Bigg\}. \tag{24}$$

In evaluating the series appearing in (24) we neglect the exponential term, which is small, and the sine, which is negative, and assume that $k_n^{(1)}H=\pi n$ and $k_n^{(2)}H=2\pi n$. Then the series obtained can be summed. We transform the last term in the brackets in (24) using the relation $\omega^2=g(k_0^{(1)})^2H$, which holds in the shallow-water approximation. Then we ultimately have the equation

$$-M\omega^2 w_0=2\rho_2\omega^2 w_0\Bigg[-\frac{aH}{(k_0^{(1)}H)^2}-\frac{aH}{(k_0^{(2)}H)^2}+\frac{aH}{3}+\frac{aH}{12}+\frac{aH}{(k_0^{(1)}H)^2}\Bigg]. \tag{25}$$

It is seen in this equation that the first and last terms in the brackets in Eq. (25) cancel each other out, and, since $k_0^{(2)}<1$ (the shallow-water approximation), that the right-hand side of the equation is negative. Therefore, it can be concluded that Eq. (25) describes the steady oscillations in the two-layer fluid with the formation of standing waves over the block. We note that if the fluid were a one-layer system, the second and fourth terms in the brackets in Eq. (25) would not be present, and the right-hand side would be positive. It must then be acknowledged that the formation of standing waves in a one-layer fluid is impossible. The interface between the two fluids is an accumulating layer, which transforms and redistributes the energy of the oscillating system with the formation of standing waves.

We note that to simplify the calculations the estimates of the sums in Eqs. (23) were approximate. The exact determination and calculation of $A_1(k_0^{(1)})$ and $A_2(k_0^{(2)})$ require more detailed calculations. This also applies to the case in which there is more than one standing wave on the surface of the fluid, since it cannot be assumed categorically in (21) that $k_0^{(2)}H<1$. The present approximate calculation demonstrates the possibility, in principle, of forming nonpropagating localized waves, which would lead to undamped oscillations of a block in a system, such as an infinite waveguide filled by a two-layer fluid. When there is an external source of oscillations at the eigenfrequencies found, resonant oscillations can arise.

This work was performed with support from the Russian Fund for Fundamental Research (Grant No. 96-01-01153a).

[1] V. A. Babeshko, I. I. Vorovich, and I. F. Obraztsov, Izv. Akad. Nauk SSSR Mekh. Tverd. Tela, No. 3, 74 (1990).
[2] V. A. Babeshko, B. V. Glushkov, and N. F. Vinchenko, *Dynamics of Inhomogeneous Linearly Elastic Media* [in Russian], Nauka, Moscow (1989).
[3] A. K. Abramyan, V. L. Andreev, and D. A. Indeĭtsev, Model. Mekh. **6**, 34 (1992).
[4] A. K. Abramian and D. A. Indejtchev, in *Proceedings of the 3rd International Congress on Air and Structure-Borne Sound and Vibration*, Montreal (1994), Vol. 3, p. 1817.
[5] L. D. Landau and E. M. Lifshitz, *Fluid Mechanics*, 2nd ed., Pergamon Press, Oxford (1987) [cited Russian original: Nauka, Moscow, 1988].
[6] A. N. Tikhonov and A. A. Samarskii, *Equations of Mathematical Physics*, Pergamon Press, Oxford (1964) [cited Russian original: Nauka, Moscow, 1977].

Translated by P. Shelnitz

Some laws governing the settling and accumulation of an industrial aerosol over a region

A. I. Grigor'ev and T. I. Sidorova

Yaroslavl State University, 150000 Yaroslavl, Russia
(Submitted September 9, 1996)
Zh. Tekh. Fiz. **68**, 20–24 (March 1998)

The content of such typical ecologically hazardous chemical elements as Pb, Ni, Cu, Sr, and Zn in soil and plant ash from the vicinity of an industrial center is measured. Since the main sources of these elements are smoke aerosols of industrial origin, the dependence of the concentrations of these elements on the distance from highly profuse, continually operating sources of emission is measured to a distance of ~10 km. It is shown that the laws governing the variation of the concentration of different chemical elements in soil with the distance from the source of emission into the atmosphere are determined by the conditions of their gravity settling with consideration of the electrical interaction of the aerosol with the ground electric field and that the laws in plant ash are determined by the accumulation of highly dispersed, charged aerosol on the surface of plant leaves polarized in the ground electric field.
 [S1063-7842(98)00303-1]

Smoke aerosols of industrial origin containing heavy metals and their toxic chemical compounds are one of the main sources of soil, water, and air pollution in both urbanized regions and mountainous and marine areas that are very far from industrial centers.[1–3] For this reason it would be of interest to investigate the physical laws governing the settling of aerosols of industrial origin on the ground and their accumulation in the near-surface layer.

1. The concentrations of various chemical elements in soil and plants were measured in systematic ecological investigations to a distance of ~10 km from an industrial center along the prevalent wind direction. The microelement composition of the soil and plant ash was measured using a DFS-13 spectrograph by stationary emission spectrographic analysis with vaporization from the channel in a carbon electrode.

During the investigations it became clear that the decisive contribution to the soil pollution is made by 28 chemical elements, of which lead, zinc, arsenic, copper, and mercury are characterized by the highest values. Their content in the soil exceeded the mean values characteristic of the region considered by tens of fold. Furthermore, of the 37 elements determined in plants, 17 were detected. Among them, 10 were detected with a concentration exceeding the normal values of the generalized data for many plant species. The concentrations of barium, manganese, molybdenum, and strontium in the plant samples are characterized by values exceeding the generalized data by 3–6 fold. Copper, manganese, molybdenum, strontium, and zinc were the most widely encountered elements and were present in all the samples. The results of the measurements of the concentrations (in atomic units) of Pb, Ni, Cu, Zn, and Sr for soils (curves *2*) and plant ash (curves *1*) are presented in Figs. 1a–1e as a function of the distance.

2. It is seen from Fig. 1 that the variation of the concentrations of all the chemical elements cited in the soil samples (curves *2*) has a qualitatively similar form: as the distance from the source of emission of the smoke aerosol into the atmosphere increases, the soil concentrations of all the elements analyzed increase, reach a maximum at a distance of about 1–2 km from the beginning of the route, and then rapidly decrease to an approximately constant level. However, the disparity between the positions of the concentration maxima of different elements on the plots presented is striking. This finding is, generally speaking, unexpected, since it indirectly indicates, through the laws governing the settling of an aerosol on the ground, differences in the physicochemical properties of smoke of the same origin. Several physical mechanisms capable of producing such an effect were discussed in Refs. 4 and 5.

For convenience in comparing the plots of the dependence of the percentage content of different chemical elements in the soil on the distance with one another, the measurement results can be approximated (using the least-squares method) by the analytical expression

$$Y = \alpha X \exp(-\beta X). \tag{1}$$

The results of such a treatment, i.e., the values of α and β for Ni, Cu, Zn, Sr, Ba, Co, Zr, and Pb are presented in Table I. The last column lists the values of the correlation coefficients between the respective analytical dependence and the measurement results. As we see, in all cases the correlation coefficients are close to unity.

We note that the position of the maximum X_m on a plot of Eq. (1) is determined by β: $X_m = 1/\beta$. This parameter also determines the curvature of the curve (the rate of descent on both sides of the maximum), which increases with increasing β.

It is not difficult to see from the data presented in Table I that different elements naturally separate into two groups

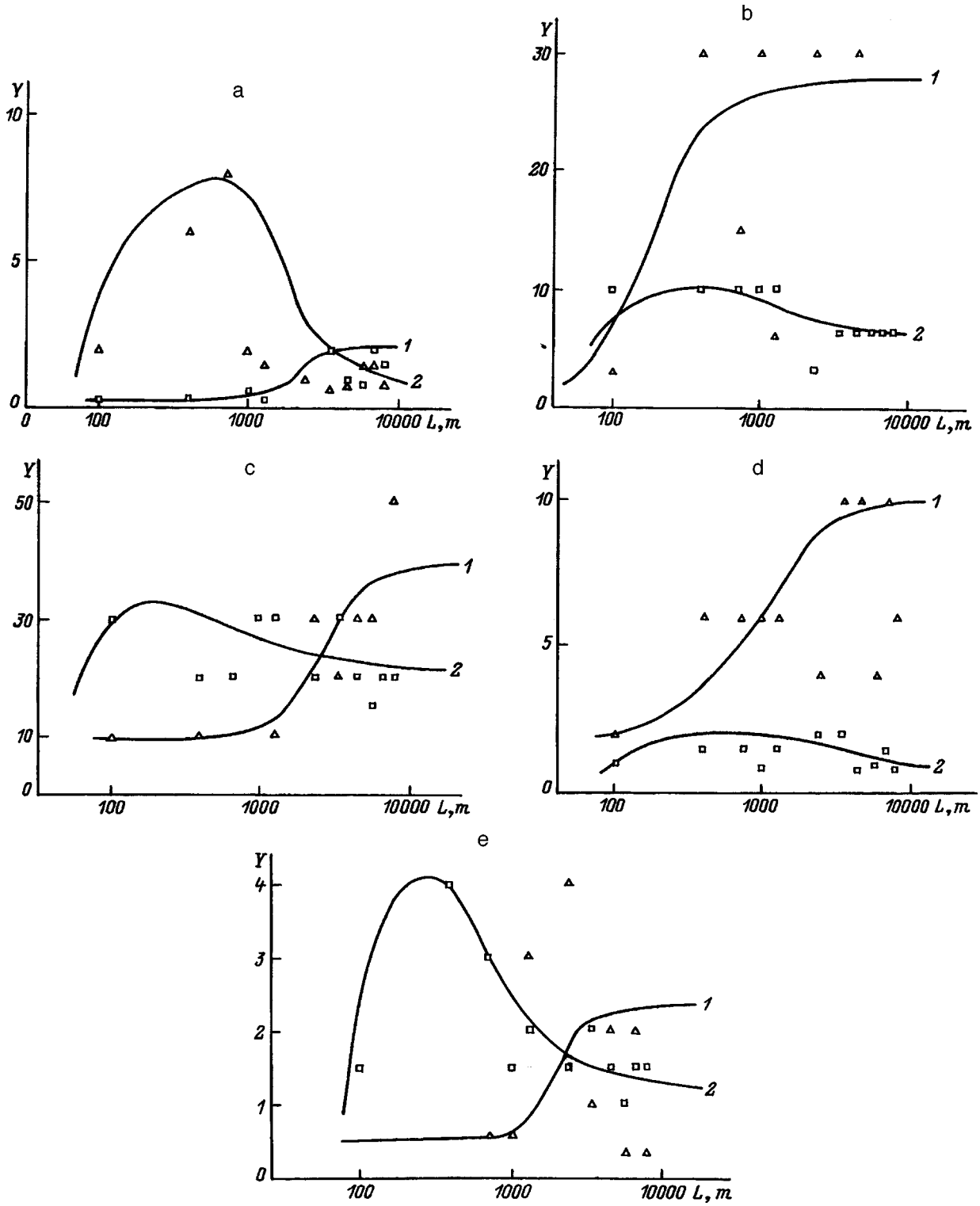

FIG. 1. Dependence of the relative concentrations of various elements in plant ash (*1*) and in soil (*2*) on the distance from the site of emission into the atmosphere: a—Pb, b—Zn, c—Sr, d—Cu, e—Ni.

according to the positions of the maxima of the curves. One group contains Ni, Cu, Zn, Sr, and Ba, and the other group contains Co, Zr, and Pb. The positions of the maxima for the elements of the former group can be regarded as coinciding within the range of the measurement error and as corresponding to a distance from the aerosol emission site equal to about 2 km. The concentration maximum of Co in the soil is at approximately half of this distance. The positions of the concentration maxima of lead and zirconium in the soil are also markedly separated. These data directly indicate that different elements entering the atmosphere in smoke are represented inhomogeneously in it.

We note that the appearance of particles with different physicochemical properties in smoke aerosols when fuels of

TABLE I. Values found by the least-squares method for the constants in Eq. (1), which approximates data from natural measurements.

Chemical element	α, arb. units/m	$\beta\times10^4$, m^{-1}	Correlation coefficient
Cu	31	4.7	0.91
Sr	589	4.8	0.89
Zn	204	5.1	0.87
Ni	51	5.1	0.90
Ba	1085	5.2	0.92
Zr	422	5.5	0.83
Pb	65	6.1	0.86
Co	187	8.6	0.97

complex chemical composition are burned is not surprising, since the chemical composition of a specific particle is determined by all of its history: the site of nucleation in the burner, as well as the chemical composition and temperature of the surrounding vapors and combustion products. Let us assume in an initial idealization that the formation of a smoke particle takes place as a result of the condensation of vapors on a nucleus in accordance with Maxwell's equation, according to which the flux of the condensing vapor of a certain substance on a particle is proportional to the difference between the partial vapor pressures of that substance in the surrounding medium and on the surface of the particle, where the vapor can be considered saturated.[6] If it is taken into account that the saturated vapor pressure varies exponentially with the temperature, it is not difficult to see that the smoke particles located at the center of a flame and on its periphery will be surrounded by gaseous combustion products with temperatures differing by several hundred degrees. In such a situation the mass fluxes of the condensing vapors impinging on particles in these two cases will differ in both intensity and chemical composition. As a result, the spread of the values of the physicochemical characteristics of the material in different smoke particles can be very large.

The further evolution of a smoke aerosol formed during burning is associated with its charging as a result of thermionic emission processes and interactions with electrons and ions in the weakly ionized plasma comprising the flame.[7] However, this initial charging of smoke particles hardly plays a significant role in their subsequent fate. Before entering the atmosphere, a smoke aerosol passes through the plasma of the corona discharge in an electrostatic precipitator, which retains a considerable portion of the particles and imparts electric charges to the smoke particles passing through it. For the most part, smoke particles with a resistivity ranging from 10^4 to 10^{10} $\Omega\cdot$cm are retained in an electrostatic precipitator.[8] Smoke particles with good electrical conductivity, whose resistivity is less than 10^4 $\Omega\cdot$cm, are rapidly recharged on the collecting electrode of the electrostatic precipitator. As a result, they are repelled from it, sent back into the gas flow, and carried by the latter into the atmosphere. The substances of interest to us in the investigation conducted have an electrical conductivity greater than 10^{-4} S/cm and therefore enter the atmosphere in the form of charged particles. At the same time, the oxides of lead and cobalt have electrical conductivities that are three to four orders of magnitude greater than those of the oxides of Ba, Sr, Zn, Ni, and Cu. Ultimately, as a result, the smoke particles consisting predominantly of PbO and CoO will have greater charges at the outlet to the atmosphere than the smoke particles consisting mainly of the oxides of Ba, Zn, Sr, Ni, and Cu.

3. However, let us consider the laws governing the settling of a spherical aerosol particle having a charge q, a radius r, and a mass m on the ground. We assume that the charge and mass of a particle remain unchanged during the observation period. Then the equation of motion of such a particle in an air flow with a velocity **U** in its vicinity, which entrains it, can be written in the form[6]

$$m\frac{d\mathbf{V}}{dt}=6\pi\mu r(\mathbf{U}-\mathbf{V})-mg\mathbf{n}_z+qE\mathbf{n}_z, \tag{2}$$

where **V** is the velocity of the center of gravity of the particle, **E** is the electric field strength, g is the acceleration of free fall ($\mathbf{E}\|\mathbf{n}_z$), $\mathbf{n}_z$ is the vertical unit vector ($\mathbf{g}\|-\mathbf{n}_z$), and μ is the dynamic viscosity of air.

We rewrite (2) in a form that is more convenient for our further arguments, introducing the characteristic relaxation time of the velocity of the aerosol particle $\tau=m/6\pi\mu r$:[6]

$$\tau\frac{d\mathbf{V}}{dt}+\mathbf{V}=\mathbf{U}_0,$$

$$\mathbf{U}_0=\mathbf{U}+\tau\left(\frac{q}{m}E-g\right)\mathbf{n}_z. \tag{2a}$$

Because motions along the vertical and horizontal axes are independent, it is not difficult to show that the settling velocity of a particle onto the ground (the rate of motion along the vertical axis) at any moment in time has the form

$$V_z=\tau\left(\frac{q}{m}E-g\right)+\left[V_{0z}-\tau\left(\frac{q}{m}E-g\right)\right]\exp(-t/\tau), \tag{3}$$

where V_{0z} is the vertical component of the velocity of the aerosol particle with which it drops with the air flow into the free atmosphere, which has the meaning of the initial velocity in Eq. (2a).

It is seen from Eq. (3) that at $t\gg\tau$ the second term, which is proportional to the exponential function, can be neglected, and the settling velocity of the particle becomes stationary [if the weak dependence of $E=E(z)$ is neglected]. The magnitude of the stationary settling velocity is determined by the relationship between the gravitational force acting on the particle and the force of its interaction with the electric field (which is directed toward the ground in clear weather[9,10]). It is easy to see that when $qE=mg$, the stationary settling velocity of the particle vanishes. It follows from elementary estimates that such suspension of the particles in the atmosphere occurs, for example, when $r\approx0.25$ μm, $\rho=1$ g/cm^3, $q\sim100e$ (where e is the charge of an electron), and $E\approx1$ V/cm.[10] The value of the particle charge taken in the estimate corresponds to the conditions of natural charging in the plasma of a corona discharge for a smoke particle of the assigned radius.[11] Here it would be appropriate to address the question of what happens to a particle as its

charge and radius deviate from the values presented above. To answer this question we must take into account the conditions under which the particle is charged. If a particle acquires a charge in the field of a corona discharge, then, according to Ref. 11, it receives a charge of the order of the maximum charge for shock charging by a stream of ions

$$q_* = \frac{3\varepsilon}{\varepsilon+2} E_* r^2,$$

where ε is the dielectric constant of the particle and E_* is the external electric field strength in its vicinity.

For the investigation performed it is important that the charge of the particle varies with the radius as $\sim r^2$, while its mass varies as $\sim r^3$. As a result, we find that, as the radius of the particle increases, the influence of the interaction of the electric charge with the ground electric field on the settling velocity of the particle decreases rapidly. Already when $r > 3\ \mu$m, this interaction is negligibly small compared with the influence of the gravitational force.

If smoke particles which are highly conductive acquire their charge when they are recharged on the collecting electrode, the charge of the particles is specified by the relation $q \approx \varphi \times r$, where φ is the potential of the collecting electrode. In this case the influence of the variation of the particle radius and the interaction of its charge with the electric field on the laws governing its settling on the ground will be qualitatively the same as in the case considered above of the charging of particles in a corona discharge plasma, except that it must be taken into account that the particle charge thus acquired will have a sign which is opposite to the sign of the charge of a particle charged in a corona discharge. The influence of the charge on the laws governing the settling of smoke particles on the ground becomes small as soon as $r > 1\ \mu$m, since the increase in the charge of a particle as its radius increases then becomes weaker: $q \sim r$.

Two hypotheses can be advanced to interpret the measurement data: smoke particles consisting predominantly of the oxides of Pb, Zr, and Co settle more rapidly than do the other particles, because 1) they have larger radii and 2) their charge is opposite in sign to the charge of particles consisting of the other oxides.

4. The law found for the dependence of the percentage content of the elements analyzed in plant ash on the distance is interesting. It is seen from Fig. 1 (curves *1*) that the concentrations of the elements analyzed gradually increase with increasing distance from the site of emission of the aerosol into the atmosphere and reach stationary values at distances exceeding the positions of the maxima on the curves characterizing the concentrations of the same elements in the soil. Furthermore, as can be seen from Fig. 1, the content of the elements analyzed in the plant ash is significantly higher than in the soil. This points out the accumulating role of vegetation with respect to an aerosol settling from the atmosphere. The accumulation of aerosol particles on vegetation is associated with its very large surface area per unit of mass in comparison with soil. The only thing remaining is to analyze the physical mechanisms underlying the ability of plants to collect a settling aerosol from the atmosphere.

The qualitative course of curves *1* in Fig. 1 and the arguments presented above regarding some of the laws governing the settling of a metal-containing aerosol from the atmosphere indicate that a very fine aerosol accumulates on vegetation. In fact, the metal content in the plant ash from the area where the most coarsely dispersed aerosol settles (in the immediate vicinity of the site of emission of the smoke aerosol into the atmosphere), whose particles are easily washed from leaf surfaces by rain, is small. At large distances from the smoke source, where only the finely dispersed aerosol fraction ($r < 1\ \mu$m) remains in the suspended state, the particles settling on vegetation can be held on the leaves by forces of molecular adhesion, and the concentrations of all the metals in the plant ash increase.

The ability of plants to accumulate a highly dispersed charged aerosol can be attributed to the intensification of the ground electric field in the vicinity of the tips of leaves and blades of grass as a consequence of the polarization of the atmosphere in the near-surface layer of the atmosphere. This situation, which seems incredible at first glance, has been adequately confirmed by observations and measurements.[12,13] For example, according to the data from the natural measurements in Ref. 12, when the ground electric field strength increases in prestorm weather by about an order of magnitude in comparison to the field in clear weather (up to 10 V/cm), a weak corona discharge is ignited in the vicinity of the tips of leaves, but because of the large number of leaves the total current in the cloud reaches a value of ≈ 3 A. In clear weather the ground electric field strength is ~ 1 V/cm.[10] However, in the vicinity of the tips of leaves and blades of grass the electric field strength increases many fold and has an appreciable orienting influence on the trajectory of motion of settling, positively charged, highly dispersed aerosol particles (we note that in clear weather the vector of the ground electric field strength is directed away from the earth's surface, which has a negative charge). The fact that at large distances from the site of emission into the atmosphere the highly dispersed aerosol fraction remaining in the suspended state has a positive charge is associated with ''aging'' of the aerosol.[1] This phenomenon is manifested by the fact that the charges of the individual particles in a smoke aerosol do not remain unchanged, regardless of their history. A weak ion current continually flows in the atmosphere between the ionosphere and the ground. Therefore, the charges of smoke particles vary in both magnitude and sign with the passage of time due to diffusive charging. This phenomenon is also called aerosol ''aging.'' The characteristic ''aging'' time is of the order of several hours.[1] In the situation under consideration this means that negatively charged smoke particles ultimately acquire positive charges.

We note, in conclusion, that the accumulation of a charged aerosol by vegetation not only is known, but is also utilized in the electrohydrodynamic spraying of insecticides,[14] whose theory and practice have been thoroughly developed.[15]

[1] H. L. Green and W. R. Lane, *Particulate Clouds: Dusts, Smokes and Mists*, 2nd ed., Van Nostrand, Princeton (1964); Khimiya, Leningrad (1969).
[2] V. K. Arguchintsev, Yu. S. Kusner, and V. L. Makukhin, Zh. Tekh. Fiz. **63**, 1 (1993) [Tech. Phys. **38**, 633 (1993)].
[3] C. Migon and B. Gentili, J. Atmos. Chem. **16**, 277 (1993).
[4] T. I. Sidorova and A. I. Grigor'ev, Pis'ma Zh. Tekh. Fiz. **19**(4), 34 (1993) [Tech. Phys. **19**(2), 105 (1993)].
[5] T. I. Sidorova and A. I. Grigor'ev, Elektron. Obrab. Mater. (5), 44 (1993).
[6] P. C. Reist, *Introduction to Aerosol Science*, Macmillan, New York; Collier Macmillan, London (1984); Mir, Moscow (1987).
[7] D. I. Zhukhovitskiĭ, A. K. Khrapak, and I. T. Yakubov, *Plasma Chemistry*, No. 11 [in Russian], Energoatomizdat, Moscow (1984), pp. 130–170.
[8] I. P. Vereshchagin, V. I. Levitov, G. Z. Mirzabekyan, and M. M. Pashin, *Principles of the Elecrtrogasdynamics of Disperse Systems* [in Russian], Énergiya, Moscow (1974).
[9] *The Oxide Handbook*, G. V. Samsonov (Ed.), Plenum Press, New York (1973).
[10] Ya. I. Frenkel', *Theory of Atmospheric Electricity* [in Russian], Gostekhteorizdat, Leningrad–Moscow (1949).
[11] E. P. Emets, V. A. Kashcheev, and P. P. Poluéktov *et al.*, Preprint of the ''Atominform'' Central Scientific-Research Institute, No. 2(136) (1991).
[12] B. F. J. Schonland, *The Flight of Thunderbolts*, 2nd ed. Clarendon Press, Oxford (1964) [Russ. transl., Gidrometeoizdat, Moscow (1970)].
[13] A. K. Kamra and D. V. Ahire, J. Clim. Appl. Meteorol. **22**, 509 (1983).
[14] S. O. Cooper and S. E. Law, IEEE Trans. Ind. Appl. **IA-23**, 217 (1987).
[15] S. I. Shevchenko, A. I. Grigor'ev, and S. O. Shiryaeva, Nauchn. Priborostroenie **1**(4), 3 (1991).

Translated by P. Shelnitz

Trapped and free electrons in the near-anode region of a striated discharge

Yu. B. Golubovskiĭ, V. S. Nekuchaev, and N. S. Ponomarev

Scientific-Research Institute of Physics, St. Petersburg State University, 198904 St. Petersburg, Russia
(Submitted September 19, 1996)
Zh. Tekh. Fiz. **68**, 25–32 (March 1998)

Spatial potential profiles and electron energy distribution functions are measured in the near-anode region of a striated neon glow discharge. It is discovered that potential wells of small depth adjacent to the anode appear on the spatial potential profiles at certain moments in time. The distribution functions measured in the potential wells have a pronounced maximum of slow electrons, which sharply distinguishes them from the distribution functions in the striation phases where there are no wells. The mechanism which shapes the electron distribution function for electrons trapped in a potential well is analyzed. A perturbing effect of the anode on the electron distribution function as the anode is approached is discovered experimentally, and an interpretation of this effect is given. © *1998 American Institute of Physics.* [S1063-7842(98)00403-6]

The shaping of the electron distribution function in the positive column of a striated discharge in inert gases at low pressures (up to a few Torr) and small currents (up to a few tens of milliamperes) has been investigated in several theoretical and experimental studies.[1–7] A comparison of the results of experiments and calculations of electron distribution functions on the basis of nonlocal electron kinetics[2] in spatially periodic potential fields revealed the main factors shaping the electron distribution functions in S and P striations.[6,7] Under the discharge conditions considered the potential drop over the thickness of a striation is determined by the loss of electron energy in elastic and inelastic collisions. There is an electron bunching effect,[2] which results in the appearance of a specific maximum on the distribution function, which migrates along the energy axis and the coordinate. In the case of S striations this maximum is associated with one resonant trajectory, to which the electrons are drawn as a result of bunching. The energy gained by electrons on this resonant trajectory in one period exceeds the excitation threshold ε_1 by the magnitude of the mean elastic losses $\Delta\varepsilon$, the potential drop on an S striation is equal to $\varepsilon_s=\varepsilon_1+\Delta\varepsilon$, and the thickness of an S striation equals $L_s=\varepsilon_s/eE_0$, where E_0 is the mean value of the field. In the case of P striations, it was found experimentally that the potential drop on a single striation ε_p and the striation thickness L_p are two times smaller than those for an S striation. Since ε_p is appreciably smaller than ε_1, electrons must traverse two spatial periods in order to gain the energy needed for excitation. This case corresponds to two resonant trajectories and, accordingly, two maxima on the distribution function separated by a distance equal to the potential drop on a P striation. The results of experimental measurements of the electron distribution functions in S and P striations in the positive column of a neon discharge have been interpreted from this standpoint.[6,7]

The object of the present work is to investigate the mechanisms which shape the electron distribution functions in S and P striations in the near-anode region of the quasineutral plasma of a striated neon discharge. Experiments were performed to measure the spatial potential profiles and the distribution functions for S and P striations near the anode and in the unperturbed positive column. The form of the electron distribution function in the presence and absence of potential wells on the spatial potential profile is analyzed on the basis of a kinetic equation.

MEASUREMENTS OF THE ELECTRON DISTRIBUTION FUNCTION IN THE PRESENCE OF POTENTIAL WELLS NEAR THE ANODE

The experiments were performed in a neon discharge at $p=1-2$ Torr and $i=10-20$ mA. A tube of radius $R=1.4$ cm had a flat anode filling the entire cross section of the discharge and a mobile probe, which permits the performance of measurements of the electron distribution function and the plasma potential at different distances from the anode with a spacing of 2 mm on the discharge axis. At each fixed position of the probe, the electron distribution functions were measured with a temporal resolution of 10 μs in 12 striation phases. The procedure for correctly measuring spatial potential profiles in the presence of oscillations of the plasma potential was described in Ref. 7.

The results of the measurements of the spatial potential profiles for S and P striations in the near-anode region at different moments in time are presented in Figs. 1a–1c. Figure 1a corresponds to S striations, which are observed for small currents at $pR>25$ Torr·cm, Fig. 1b corresponds to P-striations with a large electric field modulation depth, and Fig. 1c corresponds to P striations near the lower current boundary for the existence of striations and to nearly sinusoidal modulation of the electric field. It is seen from Fig. 1 that the axial distribution of the potential can be represented in the form of the superposition of a potential wave, oscillations of the plasma potential as a whole, a potential which decays linearly toward the cathode, and an anode fall adjacent to the anode. In addition, the magnitude and sign of the

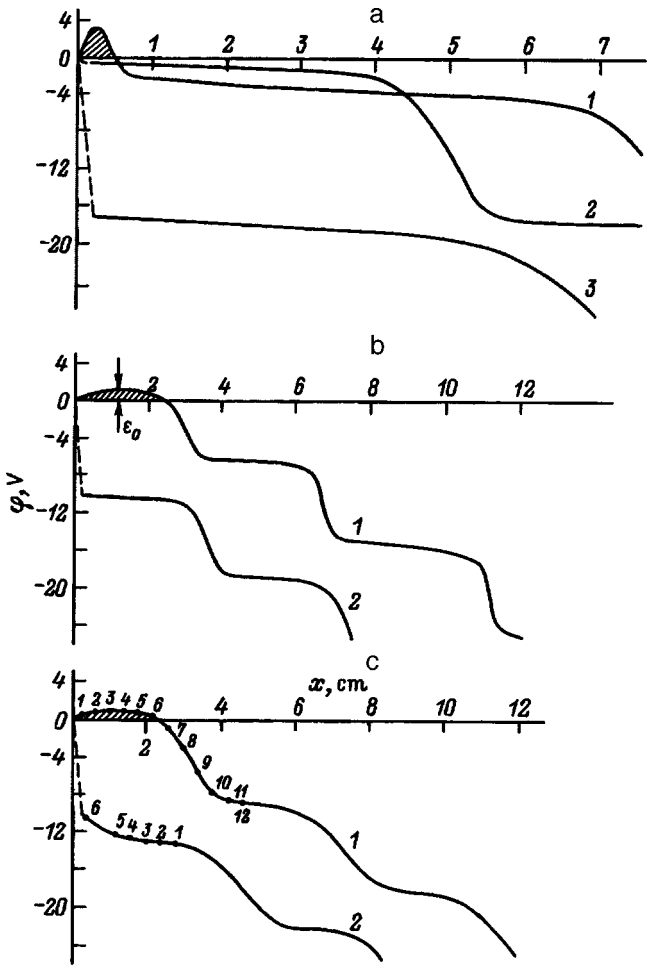

FIG. 1. Spatial potential profiles in *S* (a) and *P* (b, c) striations measured at various moments in time, μs: *1*—270, *2*—95, *3*—370. The dashed lines connect the zero potential of the grounded anode with the plasma potential measured at a distance of $\sim$2 mm. Anode oscillations should develop in this region. pR, Torr: a—2.7, b—2.24, c—1; i/R, mA/cm: a—13, b—10, c—14; a—I_s=7 cm, ε_s=18 eV; b—L_p=4.5 cm, ε_p=10 eV; c—L_p=4.2 cm, ε_p=9.1 eV.

anode fall vary with time in such a manner that at certain moments in time the plasma potential near the anode becomes positive and a potential well which traps electrons forms (the hatched regions in Fig. 1). The distribution functions measured in the potential wells are sharply distinguished from the electron distribution functions measured outside the potential wells by the presence of a pronounced peak of slow electrons with energies of $\sim$0.2–0.5 eV. Figure 2 presents electron distribution functions measured for an *S* striation at a distance of 2 mm from the anode (approximately at the center of the potential well) at different moments in time during a striation period. A sharp peak of slow electrons is observed in an interval lasting $\sim$30 μs (260–290 μs). Curve *1* in Fig. 1a exhibits a potential well corresponding to 270 μs on the time axis of Fig. 2. As is seen from the figure, the peak of slow electrons appears in the striation phases in which potential wells are observed.

A similar picture is observed for the measurements of the electron distribution function in *P* striations in the presence of potential wells. Figure 3 presents electron distribution functions measured in *P* striations. It is clearly seen that the electron distribution function is shifted toward small energies $\leqslant$1 eV within a potential well and that the amplitude of the peak of slow electrons increases with increasing distance from the anode, reaches a maximum at the midpoint of the potential well, and then drops. As it passes through the

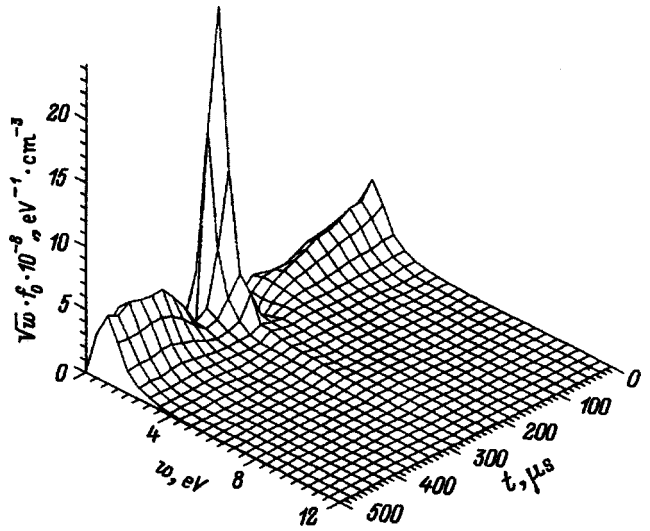

FIG. 2. Electron distribution functions measured for an *S* striation at a distance of 2 mm from the anode at various moments in time.

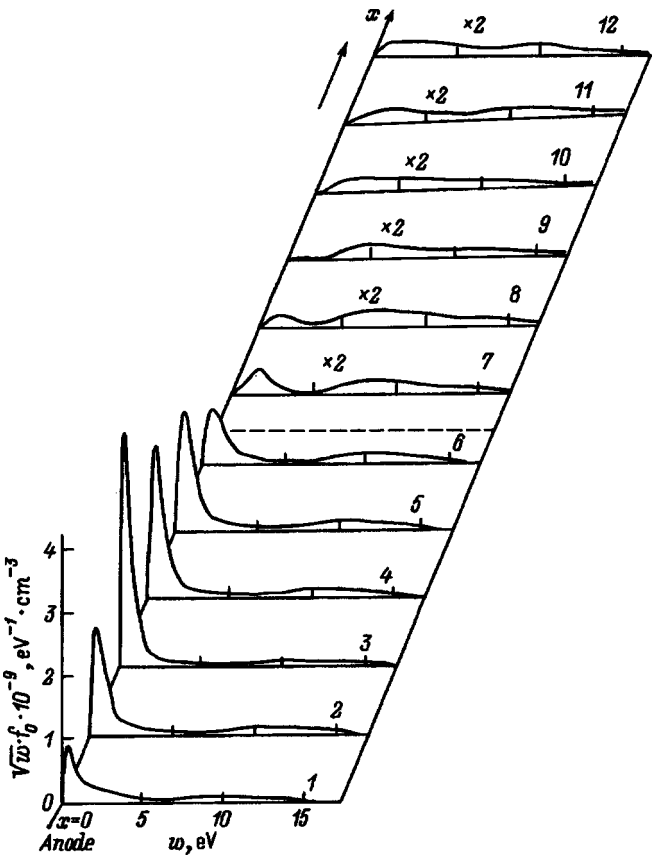

FIG. 3. Electron distribution functions measured for a *P* striation at the time corresponding to curve *1* in Fig. 1c and at various distances from the anode at the 12 points marked on that curve. The boundary of the potential well is indicated by hatching.

boundary of the well, the form of the electron distribution function changes drastically, its amplitude drops appreciably, the peak of slow electrons vanishes, and the electron distribution function acquires the form characteristic of a P striation in the column. Thus, the most interesting effect is the appearance of a clearly expressed group of slow electrons on the distribution function with energies smaller than the depth of the potential well on the spatial potential profile. These electrons make the major contribution to the total concentration.

The appearance of slow electrons on the distribution function was observed in Ref. 8 for negative anode falls in an unstriated neon discharge at appreciably lower pressures ($pR=0.1$–0.05 Torr·cm).

KINETICS OF TRAPPED ELECTRONS

Questions concerning the shaping of the distribution function in the presence of trapped electrons in potential wells were analyzed in Refs. 9 and 10. The effect observed in the present work can be interpreted on the basis of a one-dimensional kinetic equation, which is conveniently written in the following variables: the total energy $\varepsilon=w+e\varphi(x)$ and the coordinate x [w is the kinetic energy and $e\varphi(x)$ is the potential energy].

Assuming that the time for the formation of the electron distribution function is appreciably shorter than the striation period, we can use the steady-state approximation and write the kinetic equation in the form

$$\frac{\partial}{\partial x}\frac{2w^{3/2}}{3m\nu}\frac{\partial f_0}{\partial x}+\frac{\partial}{\partial\varepsilon}\left[2\frac{m}{M}\nu w^{3/2}\left(f_0+T_a\frac{\partial f_0}{\partial\varepsilon}\right)\right]+\frac{\partial}{\partial\varepsilon}\left[2\nu_e w^{3/2}\left(A_1 f_0+A_2\frac{\partial f_0}{\partial\varepsilon}\right)\right]=S^*, \tag{1}$$

where $f_0(\varepsilon,x)$ is the isotropic part of the distribution function, $\nu(v)$ is the transport frequency of the elastic collisions,

$$\nu_e=\frac{4\pi\cdot e^4 n}{m^2 v^3}\ln\Lambda$$

is the frequency of interelectronic collisions, $\ln\lambda$ is the Coulomb logarithm, T_a is the temperature of the Maxwellian distribution of neutral atoms, m and M are the masses of an electron and an atom,

$$A_1=\frac{1}{n}\int_0^{\varepsilon} f_0(\varepsilon)\sqrt{\varepsilon}\,d\varepsilon,$$

$$A_2=\frac{2}{3n}\left[\int_0^{\varepsilon}\varepsilon^{3/2}f_0(\varepsilon)d\varepsilon+\varepsilon^{3/2}\int_{\varepsilon}^{\infty}f_0(\varepsilon)d\varepsilon\right]. \tag{2}$$

The first term in (1) describes diffusion along the x coordinate in the ε, x phase plane (heating in the electric field), the second term describes the energy losses in elastic collisions, as well as the heating in collisions with atoms, and the third term describes the exchange of energy in interelectronic collisions. The right-hand side is the inelastic-collision operator, which can be represented in an approximation in the form

$$S^*=\sqrt{w}\,\nu^*(w)f_0(\varepsilon,x)-\sqrt{w'}\,\nu^*(w')f_0(\varepsilon',x), \tag{3}$$

where $\nu'(w)$ is the total transport frequency of the inelastic collisions with the excitation threshold ε_1.

Here $\varepsilon'=\varepsilon+\varepsilon_1$ and $w'=w+\varepsilon_1$. As was shown in Ref. 9, when there is a potential well, the electrons can be separated into two weakly correlated groups: electrons trapped in the well ($\varepsilon<\varepsilon_0$) and free electrons ($\varepsilon>\varepsilon_0$), where ε_0 is the depth of the well. If the energy relaxation distance with respect to the elastic and interelectronic collisions appreciably exceeds the width of the well, it can be assumed that electrons move within the well with conservation of the total energy. The distribution function in the well does not depend explicitly on the coordinate and is a function of the total energy $f_0^t(\varepsilon)$. In this case averaging of the kinetic equation (1) with respect to the coordinate can be performed for the trapped electrons, and the result can be written in the form

$$\frac{\partial}{\partial\varepsilon}\left[\overline{V}_\varepsilon f_0^t(\varepsilon)+\overline{D}_\varepsilon\frac{\partial f_0^t(\varepsilon)}{\partial\varepsilon}\right]=q(\varepsilon), \tag{4}$$

where

$$\overline{V}_\varepsilon=\frac{1}{L}\int_{x^-(\varepsilon)}^{x^+(\varepsilon)}2w^{3/2}\left(\frac{m}{M}\nu+A_1\right)dx,$$

$$\overline{D}_\varepsilon=\frac{1}{L}\int_{x^-(\varepsilon)}^{x^+(\varepsilon)}2w^{3/2}\left(A_2\nu_e+\frac{m}{M}\nu T_a\right)dx,$$

L is the width of the well, and $x^-(\varepsilon)$ and $x^+(\varepsilon)$ are the turning points for electrons with the energy ε.

If the well is nearly rectangular, the averaging procedure is simplified by replacing the kinetic energy by the total energy. If the profile of the well is nonrectangular, the averaging result has a numerical multiplier (for example, the multiplier for a parabolic profile is ~1.5). The sources $q(\varepsilon)$ of electrons in the well are associated with the appearance of slow electrons as a result of inelastic collisions of free electrons with energies exceeding the excitation threshold [the second term on the right-hand side of (3)]. Assuming that the electron distribution function after the excitation threshold $f_0^i(\varepsilon)$ is known, we can write the expression for $q(\varepsilon)$ in the form

$$q(\varepsilon)=\frac{1}{L}\int_{x^-(\varepsilon)}^{x^+(\varepsilon)}\sqrt{w+\varepsilon_1}\cdot\nu^*(w+\varepsilon_1)f_0^i(\varepsilon+\varepsilon_1)dx. \tag{5}$$

Equation (4) has the physical meaning of the continuity equation for the flux, which is the sum of diffusion with the coefficient $\overline{D}_\varepsilon$ and drift with the velocity $\overline{V}_\varepsilon$ in the presence of the source $q(\varepsilon)$. As the experimental data (Fig. 3) show, the characteristic energy of the trapped electrons (~0.2 eV) is appreciably smaller than the depth of the well (~1 eV), permitting construction of the electron distribution function of the trapped electrons with a zero boundary condition at $\varepsilon=\varepsilon_0$. The solution of Eq. (4) in this approximation has the form

$$f_0^t(\varepsilon)=\int_{\varepsilon}^{\varepsilon_0}\frac{Q(\varepsilon')}{\overline{D}_{\varepsilon'}}\exp\left\{\int_{\varepsilon}^{\varepsilon'}\frac{\overline{V}_{\varepsilon''}}{\overline{D}_{\varepsilon''}}d\varepsilon''\right\}d\varepsilon', \tag{6}$$

where

$$Q(\varepsilon')=\int_0^{\varepsilon'} q(\varepsilon)d\varepsilon.$$

The limiting transition to a Maxwellian distribution function for electrons with energies $\varepsilon<\varepsilon_0$ can easily be seen from Eq. (6). In the case where interelectronic collisions predominate [$\nu_e \gg (m/M)\nu$] the ratio $\overline{D}_{\varepsilon''}/\overline{V}_{\varepsilon''}$ equals T_e, and for $f_0^t(\varepsilon)$ we obtain

$$f_0^t(\varepsilon)\approx \frac{Q(\varepsilon_0)}{\overline{D}_{\varepsilon_0}} T_e(e^{\varepsilon_0-\varepsilon/T_e}-1)\approx \text{const}\cdot e^{-\varepsilon/T_e}. \tag{7}$$

If the interelectronic collisions do not play a decisive role, the distribution function will be determined by the temperature of the atoms T_d.

To determine the mean energy (the temperature) of the distribution function (6) we must consider the energy balance of the trapped electrons, which can be obtained by multiplying Eqs. (1)–(3) by the energy and integrating over the energy in the range $0-\varepsilon_0$ and over the coordinate within the well. For trapped electrons both the particle flux and the energy flux along the coordinate are equal to zero outside the well, allowing us to discard the first term of Eq. (1) in the energy balance.

The integration of the second term in Eq. (1) describes the exchange of energy between the trapped electrons and atoms in elastic collisions:

$$\begin{aligned} H_a &= \frac{1}{L}\int_0^{\varepsilon_0} d\varepsilon \int_{x^-(\varepsilon)}^{x^+(\varepsilon)} w \frac{\partial}{\partial\varepsilon} 2\frac{m}{M}\varepsilon^{3/2}\nu \\ &\quad\times\left(f_0^t(\varepsilon)+T_a\frac{\partial f_0^t(\varepsilon)}{\partial\varepsilon}\right)dx \\ &\approx 2\frac{m}{M}\nu T_a\varepsilon^{5/2}\frac{\partial f_0^t(\varepsilon)}{\partial\varepsilon}\bigg|_{\varepsilon=\varepsilon_0} - 2\frac{m}{M}n^t\left(1-\frac{T_a}{T_e}\right)\langle \nu w\rangle \\ &= -H_a^d - H_a^V, \end{aligned} \tag{8}$$

where n^t is the concentration of trapped electrons, the first term H_a^d on the right-hand side of (8) describes the electron energy flux outside the well due to collisions with atoms having a nonzero temperature (diffusive cooling), and the second term H_a^V describes energy exchange with atoms within of the well.

There is special interest in the exchange of energy between the trapped and free electrons due to interelectronic collisions [the third term in Eq. (1)]

$$\begin{aligned} H_e &= \frac{1}{L}\int_0^{\varepsilon_0} d\varepsilon \int_{x^-(\varepsilon)}^{x^+(\varepsilon)} w\,\frac{\partial}{\partial\varepsilon} 2w^{3/2}\nu_e\left(A_1 f_0 + A_2\frac{\partial f_0}{\partial\varepsilon}\right)dx \\ &\approx 2\nu_e A_2(\varepsilon_0)\varepsilon_0^{5/2}\frac{\partial f_0}{\partial\varepsilon}\bigg|_{\varepsilon=\varepsilon_0} - 2\int_0^{\varepsilon_0} w^{3/2}\nu_e\left[A_1-\frac{\partial A_2}{\partial\varepsilon}\right]f_0 d\varepsilon \\ &= -H_e^d - H_e^*. \end{aligned} \tag{9}$$

The first term H_e^d on the right-hand side of (9) describes the diffusive cooling of the trapped electrons due to interelectronic collisions in the well. As is seen from (2), the quantity $A_2(\varepsilon_0)$ for the trapped electrons has a value of $\sim(2/3)\langle\varepsilon\rangle \sim T_e$. After the substitution of the expressions for A_1 and $(\partial A_2)/(\partial\varepsilon)$ from (2), the second term H_e^* in (9) can be written in the form

$$\begin{aligned} H_e^* = -2\frac{\nu_e\varepsilon^{3/2}}{n}\Bigg\{ &\int_0^{\varepsilon_0} f_0(\varepsilon)d\varepsilon\int_0^{\varepsilon} f_0(\varepsilon')\sqrt{\varepsilon'}d\varepsilon' \\ &- \int_0^{\varepsilon_0} f_0(\varepsilon)\sqrt{\varepsilon}d\varepsilon\int_{\varepsilon}^{\infty} f_0(\varepsilon')d\varepsilon'\Bigg\}. \end{aligned}$$

The second term in the curly brackets can be transformed by dividing the integration range of the internal integral into $\varepsilon-\varepsilon_0$ and $\varepsilon_0-\infty$. By changing the order of integration in the first of the two terms obtained, we can see that this term cancels out with the first term in the curly brackets. Physically, this means that the exchange of the energy of the electrons within the well leads to compensation of the cooling and heating. For H_e^* we ultimately obtain

$$H_e^* = 2\nu_e\varepsilon^{3/2}\frac{1}{n}\int_0^{\varepsilon_0} f_0(\varepsilon)\sqrt{\varepsilon}d\varepsilon\int_{\varepsilon_0}^{\infty} f_0(\varepsilon)d\varepsilon. \tag{10}$$

This term describes the transfer of energy from free electrons ($\varepsilon>\varepsilon_0$) to trapped electrons ($\varepsilon<\varepsilon_0$). The first integral in (1) gives the concentration of trapped electrons m^*. The second integral in (1) can be estimated in order of magnitude as $n^i/\sqrt{\varepsilon^i}$, where n' is the concentration of free electrons and ε' is the mean energy of the free electrons. Thus, the heating of trapped electrons due to the cooling of free electrons in interelectronic collisions equals

$$H_e^* \cong 2\nu_e(\varepsilon^i)\varepsilon^i\frac{n^t n^i}{n}. \tag{11}$$

A similar expression was presented in Ref. 9 for the case of $n^t\approx n$.

The heating of trapped electrons can be caused by inelastic collisions of free electrons with an energy $\varepsilon>\varepsilon_1$ due to the appearance of slow electrons with an energy $\varepsilon-\varepsilon_1$. The magnitude of this heating can be obtained by averaging the second term of the operator of inelastic collisions (3) multiplied by the energy over the well:

$$\begin{aligned} H_a^* &= \frac{1}{L}\int_0^{\varepsilon_0} d\varepsilon\int_{x^-(\varepsilon)}^{x^+(\varepsilon)} w\sqrt{w+\varepsilon_1}\cdot\nu^*(w+\varepsilon_1) \\ &\quad\times f_0^i(\varepsilon+\varepsilon_1)dx \approx \frac{1}{3}\nu_0^*\varepsilon_1^{5/2}\left(\frac{\varepsilon_0}{\varepsilon_1}\right)^3 f_0^i(\varepsilon_1). \end{aligned} \tag{12}$$

In calculating (12) we used the approximation of the frequency of inelastic collisions in the form

$$\nu^* = \nu_0^*\left(\frac{w}{\varepsilon_1}-1\right).$$

In the framework of the model considered the mean energy (the temperature T_e) of the trapped electrons can be calculated from the energy balance in the form

$$H_a^* + H_e^* - H_a^d - H_e^d - H_a^V = 0. \tag{13}$$

The diffusive cooling in balance equation (13) $H_a^d+H_e^d$ can be reduced to a form similar to (12) in Eqs. (8) and (9). In fact, from (6) we can obtain

$$\left.\frac{\partial f_0^t}{\partial \varepsilon}\right|_{\varepsilon=\varepsilon_0} = -\frac{Q(\varepsilon_0)}{\overline{D}_{\varepsilon_0}}.$$

Substituting this expression for the derivative into the expression for $H_a^d+H_e^d$, we obtain

$$H_a^d+H_e^d=\varepsilon_0\int_0^{\varepsilon_0} q(\varepsilon)d\varepsilon=\frac{1}{2}\nu_0^*\varepsilon_1^{5/2}\left(\frac{\varepsilon_0}{\varepsilon_1}\right)^3 f_0^i(\varepsilon_1).$$

Ultimately, the equation which should be used to find the mean energy (the temperature T_e) has the form

$$2\nu_e(\varepsilon^i)\varepsilon^i\frac{n^t n^i}{n}-\frac{1}{6}\nu_0^*\varepsilon_1^{5/2}\left(\frac{\varepsilon_0}{\varepsilon_1}\right)^3 f_0^i(\varepsilon_1)-3\frac{m}{M}\times\left(1-\frac{T_a}{T_e}\right)\nu(T_e)T_e n^t=0. \quad (14)$$

The calculation of T_a using (14) requires knowledge of the concentration of trapped electrons n^t, the concentration of free electrons n^i, ε^i, and $f_0^i(\varepsilon_1)$ for electrons outside the potential well. For concrete calculations we used the following values, which were obtained from experimental measurements: $\varepsilon^i\approx 4$ eV, $n\approx 3\times 10^9$ cm^{-3}, $n^t\approx 2\times 10^9$ cm^{-3}, $n^i\approx 10^9$ cm^{-3}, $\nu_e(\varepsilon^i)\approx 13\times 10^4$ s^{-1}, $\nu_0^*\approx 2\times 10^8$ s^{-1}, $\nu(T_e)=2.2\times 10^9\sqrt{T_e/\varepsilon_1}$, $\varepsilon_0\approx 1$ eV, $\varepsilon_1=16.6$ eV, and $T_e\approx 0.026$ eV. The solution of Eq. (14) is critical with respect to the value of the electron energy distribution function at the excitation threshold, $f_0^i(\varepsilon_1)$. This value can be obtained by matching the distribution functions from the elastic and inelastic regions at the point ε_1 according to their slopes.[11] As a result, we obtain

$$f_0^i(\varepsilon_1)\approx\frac{9}{4}\frac{n^i}{\varepsilon_1^{3/2}}\left(\frac{4}{3}\right)^{1/3}\left(\frac{T_1}{\varepsilon_1}\right)^{2/3}\left.\frac{z^{1/3}K_{1/3}(z)}{\Gamma(2/3)}\right|_{z=0}$$
$$\approx\frac{9}{4}\frac{n^i}{\varepsilon_1^{3/2}}\left(\frac{T^*}{\varepsilon_1}\right)\frac{2^{2/3}}{3}\frac{\Gamma(1/3)}{\Gamma(2/3)}$$
$$\approx 4.6\times 10^6\ \text{eV}^{-3/2}\text{cm}^{-3}, \quad (15)$$

where

$$T_1=\frac{1}{\sqrt{3}}\sqrt{\frac{\nu_0}{\nu_0^*}}\cdot eE_0\lambda;\quad T^*=\left(\frac{3}{2}\right)^{2/3}\left(\frac{T_1}{\varepsilon_1}\right)^{2/3}.$$

This value of $f_0^i(\varepsilon_1)$ correlates satisfactorily with the experimental data. The calculations using (14) give the value $T\approx 0.25$ eV, which agrees closely with the position of the peak of slow electrons on the experimental curve (Fig. 3).

It is noteworthy that in the energy balance (14) the diffusive cooling markedly surpasses the cooling due to elastic collisions and basically compensates the heating due to interelectronic collisions. Within the model describing the shaping of the electron distribution function of the trapped electrons considered here (a black-wall condition at $\varepsilon=\varepsilon_0$), the flux of particles entering the well due to inelastic collisions is equal to the flux of particles leaving the well, mainly as a result of interelectronic collisions (followed by escape). The corresponding fluxes do not compensate one another in the energy balance, since electrons having the energy ε_0 escape, while electrons having a spectrum in the range $0-\varepsilon_0$ enter the well.

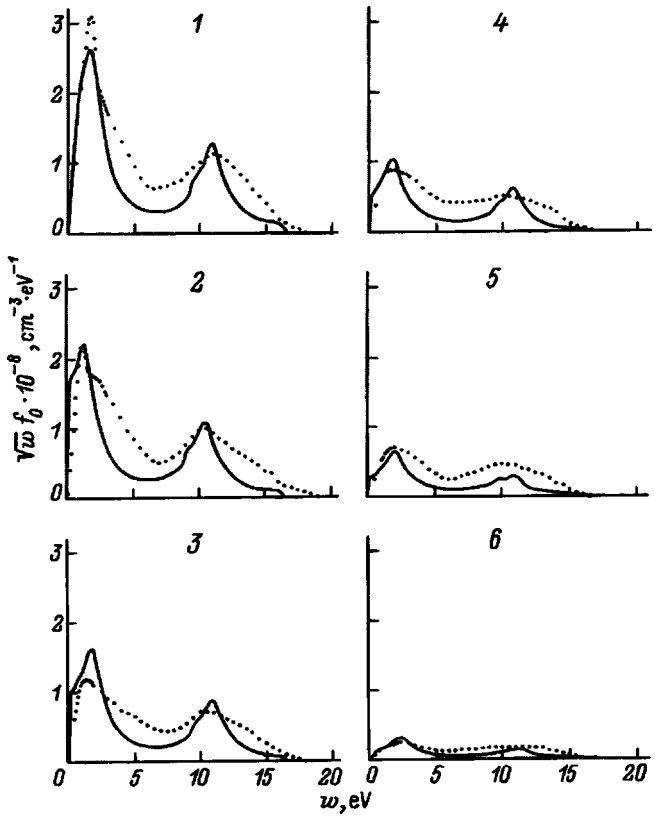

FIG. 4. Measured (points) and calculated (solid curves) electron distribution functions at various distances from the anode in *P* striations. The numbers *1–6* correspond to points *1–6* on potential curve *2* in Fig. 1c.

INFLUENCE OF THE DRAINAGE OF ELECTRONS TO THE ANODE ON THE ELECTRON DISTRIBUTION FUNCTIONS IN STRIATIONS

As the experimental results show, spatial potential profiles without potential wells and reversed fields appear at definite moments in time. It would be of definite interest to ascertain the reasons for the differences between the electron distribution functions in striations near the anode and the functions in striations of the positive column. Figure 4 presents the electron distribution functions measured at distances of 0 to 3 cm from the anode for potential curve *2* in Fig. 1c. The figure exhibits a drop in the amplitude of the electron distribution function in the near-anode region as the anode is approached. At first there is a decrease in the number of slow electrons, and then the depletion of the electron distribution function affects increasingly faster electrons. At a distance of ~ 2 mm from the anode the electron concentration is diminished by more than an order of magnitude. The distribution functions measured in a striated positive column far from the anode do not exhibit a similar drop in the am-

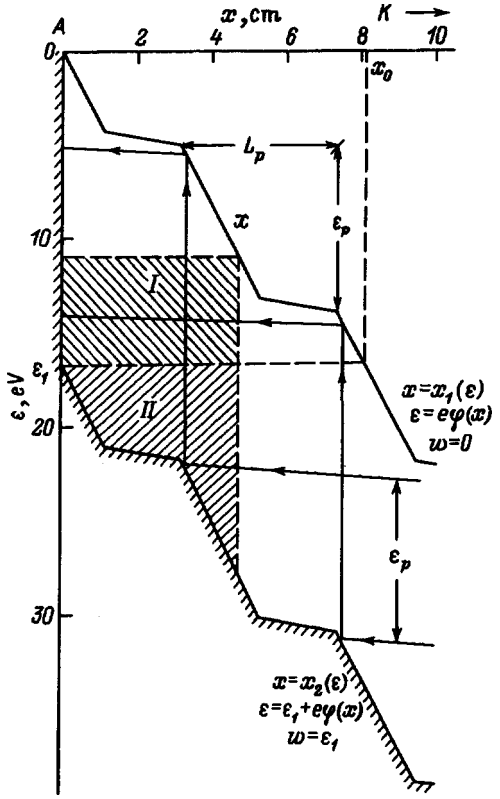

FIG. 5. Representation of the ε,x plane, in which the solution of kinetic equation (16) is analyzed.

plitude of the electron distribution function and are faithfully reproduced from striation to striation as the distance from the anode increases.

An interpretation of the experimental results can be given on the basis of the conception of nonlocal electron kinetics. Calculations of the electron distribution function in the near-anode region of 1an unstriated neon discharge were performed in Ref. 12. The presence of the anode, which is taken into account in the theory by introducing a zero boundary condition at the anode,[13] leads to distortion of the electron distribution function at a distance of the order of the energy relaxation distance. As the analysis performed shows,[12,13] draining of the slow electrons occurs at first, and the draining involves increasingly faster electrons as the anode is approached.

A theory for the near-anode region of a striated discharge can be devised on the basis of similar arguments. Figure 5 presents the ε,x plane, which shows an approximation of the measured potential profile for a P striation (curve *2* in Fig. 1c). The point $x_0=x_1(\varepsilon_1)$ in this figure separates the region of the positive column not perturbed by the anode ($x>x_0$) from the near-anode region ($x<x_0$), in which the perturbing effect of the anode on the distribution function is manifested. In fact, in certain approximations (small energy losses in elastic collisions and a zero boundary condition at the excitation threshold ε_1) the electron distribution function can be represented in the form[2]

$$f_0(\varepsilon,x)=\Phi(\varepsilon)\int_{x_2(\varepsilon)}^{x(\varepsilon)}\frac{\nu(\varepsilon,x')}{v^3(\varepsilon,x')}dx'=\Phi(\varepsilon)\cdot F_0(\varepsilon,x), \tag{16}$$

where $\Phi(\varepsilon)$ is the amplitude of the distribution function, and $F_0(\varepsilon,x)$ is the electron distribution function which would be formed in the potential field $\varphi(x)$ without energy losses in elastic collisions.

At $\varepsilon>\varepsilon_1$ the $x_1(\varepsilon)$ curve is the curve on which the kinetic energy of the electrons is equal to the excitation threshold ε_1. For energies in the range $0<\varepsilon<\varepsilon_1$ the lower integration limit in (16) $x_1(\varepsilon)=0$, which corresponds to the zero boundary condition for the electron distribution function at the anode. For $x>x_0$ the calculation of the integral $F_0(\varepsilon,x)$ in (16) for energies in the range $e\varphi(x)<\varepsilon<\varepsilon_1+e\varphi(x)$ does not depend on the presence of the anode, since the lower integration limit $x_2(\varepsilon)$ does not reach the anode. The electron distribution function corresponds to the positive column not perturbed by the anode and is periodic with the spatial period L_p. Similar electron distribution functions were calculated in Ref. 7 for potential curve *2* in Fig. 1b. For $x<x_0$ the lower integration limit in (16) is equal to zero for energies in the range $e\varphi(x)<\varepsilon<\varepsilon_1$ (integration region I in Fig. 5) and to $x_2(\varepsilon)$ for energies in the range $\varepsilon_1<\varepsilon<\varepsilon_1+e\varphi(x)$ (integration region *II* in Fig. 5). This permits calculation of $F_0(\varepsilon,x)$ in (16) in the near-anode region, and at the anode $F_0(\varepsilon,x)|_{x=0}=0$. The amplitude of the electron distribution function $\Phi(\varepsilon)$ for P striations was calculated in Ref. 7, and in the energy range $0-\varepsilon_1$ it was found that there are two maxima separated along the energy scale by ε_p (the potential drop on a P striation). These maxima are caused by bunching due to constriction of the electron distribution function toward two resonant trajectories when the electrons traverse a certain number of periods in a resonant spatially periodic potential. It can be assumed that the amplitude $\Phi(\varepsilon)$ in the last spatial period, which is adjacent to the anode, is the same as in the column. In the present work we performed calculations of the electron distribution function for curve *2* in Fig. 1c both in a striated positive column far from the anode and in the near-anode region. The results of the calculations of $\sqrt{w}f_0(\varepsilon_1,x)$ in the near-anode region in a potential field (Fig. 5) are compared with the experimental data at the distance from the anode in Fig. 4. It is seen from the figure that the theory faithfully describes the experimentally observed decay of the electron distribution function as the anode is approached.

CALCULATION OF THE ELECTRODE DISTRIBUTION FUNCTION IN THE PRESENCE OF TRAPPED AND FREE ELECTRONS

The electron distribution function can be constructed over the entire range of energies on the basis of a solution of the kinetic equation averaged over the well for trapped electrons in form (6) and the kinetic equation for free electrons in form (16). The idea that the electrons separate into two weakly correlated groups that can be described by Eqs. (6) and (16) enables us to find the parameters of these two groups: n^t and T_e for the trapped electrons and n^i and ε^i for the free electrons. The question of the temperature and con-

centration of the trapped electrons can be solved on the basis of a combined solution of the energy balance equation and the particle balance equation in the potential well. The energy balance of the electrons was previously discussed in Ref. 14. The particle balance can be obtained by integrating the kinetic equations (1)–(3) over the energy in the range from 0 to ε_0 and over the coordinate within the well

$$\overline{D}_{\varepsilon_0}\frac{\partial f_0}{\partial \varepsilon}\bigg|_{\varepsilon_0}=\frac{1}{L}\int_0^{\varepsilon_0}d\varepsilon\int_{x^-(\varepsilon)}^{x^+(\varepsilon)}w\sqrt{w+\varepsilon_1}\cdot\nu^*(w+\varepsilon_1)\times f_0(\varepsilon+\varepsilon_1)dx\approx\frac{1}{2}\nu_0^*\varepsilon_1^{3/2}\left(\frac{\varepsilon_0}{\varepsilon_1}\right)^2 f_0(\varepsilon_1), \tag{17}$$

where

$$\overline{D}_{\varepsilon_0}=\frac{2}{3n}\left[\int_0^{\varepsilon_0}\varepsilon^{3/2}f_0(\varepsilon)d\varepsilon+\varepsilon_0^{3/2}\int_{\varepsilon_0}^{\infty}f_0(\varepsilon)d\varepsilon\right]\nu_e(\varepsilon_0)\varepsilon^{3/2}$$

$$\approx\left(\frac{n^t}{n}T_e+\frac{2}{3}\frac{\varepsilon_0^{3/2}}{\sqrt{\varepsilon^i}}\frac{n^i}{n}\right)\nu_e(\varepsilon_0)\varepsilon_0^{3/2},$$

$$\frac{df_0}{d\varepsilon}\bigg|_{\varepsilon_0}=\frac{2}{\sqrt{\pi}}n^t\mathrm{e}^{-\varepsilon_0/T_e}\frac{1}{T_e^{5/2}}.$$

The system of particle and energy balance equations (17) and (14) for determining the parameters of the electron distribution functions of the trapped electrons n^t and T_e in terms of the parameters of the free electrons n^i and ε^i can be brought into a form convenient for calculations

$$\frac{n^t}{n^t+n^i}\left(\frac{n^t}{n^i}\frac{T_e\sqrt{\varepsilon^i}}{\varepsilon_0^{3/2}}+1\right)\frac{\varepsilon_0\varepsilon_0^3}{T_e^{5/2}\sqrt{\varepsilon^i}T^*}\frac{\nu_e(\varepsilon_0)}{\nu_0^*}\mathrm{e}^{-\varepsilon_0/T_e}=\frac{3\cdot 2^{2/3}\sqrt{\pi}}{16}\cdot\frac{\Gamma(1/3)}{\Gamma(2/3)}=1.044, \tag{18}$$

$$\frac{n^t}{n^t+n^i}\left(\frac{\varepsilon_1}{\varepsilon_0}\right)^3\frac{\nu_e(\varepsilon^i)}{\nu_0^*}\frac{\varepsilon^i}{T^*}-\frac{3}{2}\frac{n^t}{n^i}\frac{m}{M}\times\left(1-\frac{T_a}{T_e}\right)\frac{\nu(T_e)}{\nu_0^*}\left(\frac{\varepsilon_1}{\varepsilon_0}\right)^3\frac{T_e}{T^*}=\frac{2^{2/3}}{16}\frac{\Gamma(1/3)}{\Gamma(2/3)}=0.196. \tag{19}$$

The parameters $n^t/n^i=26$ and $T_e=0.3$ eV obtained from the solution of the system of equations (18) and (19) agree satisfactorily with the experimental data.

Figure 6 compares the distribution function calculated from Eq. (6) for the trapped electrons and Eq. (16) for the free electrons with the experimental data. It is seen from the figure that the theoretical model discussed in this paper qualitatively describes the shaping of the electron distribution function in the presence of a potential well. The assumptions underlying the theoretical model (the black-wall condition for the trapped electrons at $\varepsilon=\varepsilon_0$ and the presence of two weakly correlated groups of electrons) lead to a discontinuity on the electron distribution function at $\varepsilon=\varepsilon_0$. The behavior of the electron distribution function near ε_0 requires a more rigorous analysis of the kinetic equation in this energy range. Nevertheless, the model considered provides a graphic representation of the physical picture of the shaping of the electron distribution function and the relationship between the concentrations and mean energies of the trapped and free electrons.

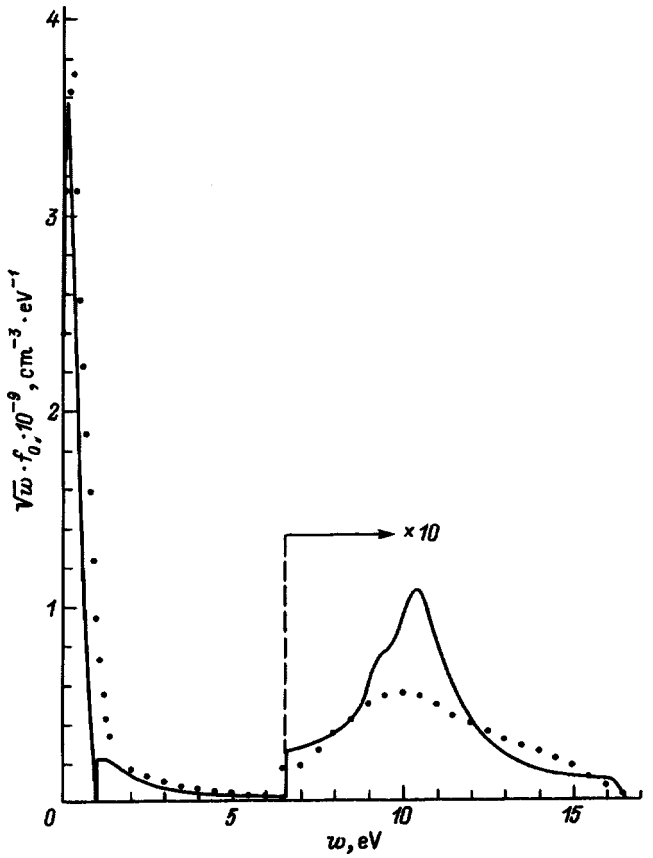

FIG. 6. Comparison of the experimental (points) and calculated (solid curve) results for the electron distribution functions in *P* striations in the presence of a potential well. The electron distribution function in the range of energies exceeding 6.5 eV has been magnified 10× for clarity.

CONCLUSIONS

In a low-pressure striated discharge the magnitude and sign of the anode fall vary with time, and spatial potential profiles with potential wells adjacent to the anode having a depth of ~1 eV can appear at definite moments in time. At other moments in time the spatial potential profiles do not exhibit potential wells. The measured distribution functions in wells are sharply distinguished from the distribution functions outside the wells by the presence of a clearly expressed peak of slow electrons with energies amounting to tenths of an electron volt. The distribution functions measured at points corresponding to a potential well on the spatial potential profile separate along the energy scale into two weakly correlated groups of trapped and free electrons. The trapped electrons are heated as a result of the entry of electrons which have undergone an inelastic collision into the well, as well as upon the transfer of energy from free electrons to

trapped electrons in interelectronic collisions. The cooling of the trapped electrons is associated with diffusive cooling upon the escape of electrons bearing an amount of energy equal to the depth of the well and with energy losses in elastic collisions. The mean energy is determined by the balance between the heating and cooling processes.

The idea that there are two weakly correlated groups of trapped and free electrons makes it possible to find the concentration and temperature of the trapped electrons in terms of the concentration and mean energy of the free electrons from the solution of a system of particle and energy balance equations. The calculated electron distribution function qualitatively describes the observed experimental data.

When a striation passes through the near-anode region, a characteristic distortion of the distribution function associated with the draining of electrons to the anode is observed.

[1] T. Ruzicka and K. Rohlena, Czech. J. Phys. **22**, 906 (1972).
[2] L. D. Tsendin, Fiz. Plazmy **8**, 400 (1982) [Sov. J. Plasma Phys. **8**, 228 (1982)].
[3] V. A. Shveĭgert, Fiz. Plazmy **15**, 1230 (1989) [Sov. J. Plasma Phys. **15**, 714 (1989)].
[4] K. F. Bessonova, O. N. Oreshak, E. P. Ostapchenko, and V. A. Stepanov, Zh. Tekh. Fiz. **41**, 979 (1971) [Sov. Phys. Tech. Phys. **16**, 770 (1971)].
[5] B. M. Kagan, N. B. Kolokolov, T. N. Krylova, and V. M. Milenin, Zh. Tekh. Fiz. **41**, 120 (1971) [Sov. Phys. Tech. Phys. **16**, 88 (1971)].
[6] Yu. B. Golubovskiĭ and S. U. Nisimov, Zh. Tekh. Fiz. **66**(7), 20 (1996) [Tech. Phys. **41**, 645 (1996)].
[7] B. B. Golubovskiĭ, V. O. Nekuchaev, N. S. Ponomarev, and I. A. Porokhova, Zh. Tekh. Fiz. **67**(9), 14 (1997) [Tech. Phys. **42**, 997 (1997)].
[8] V. G. Belov, V. A. Ivanov, and N. V. Musaeva, in *Abstracts of Reports to the 8th All-Union Conference on the Physics of Low-Temperature Plasmas* [in Russian], Minsk, (1991), Part 1, pp. 80–81.
[9] V. I. Kolobov and L. D. Tsendin, Phys. Rev. A **46**, 7837 (1992).
[10] V. A. Schweigert and I. V. Schweigert, Fiz. Plazmy **14**, 347 (1988) [Sov. J. Plasma Phys. **14**, 204 (1988)].
[11] Yu. B. Golubovskiĭ, S. U. Nisimov, and I. A. Porokhova, Zh. Tekh. Fiz. **67**(2), 24 (1997) [Tech. Phys. **42**, 145 (1997)].
[12] Yu. B. Golubovskiĭ, S. H. al Hawat, and L. D. Tsendin, Zh. Tekh. Fiz. **57**, 1285 (1987) [Sov. Phys. Tech. Phys. **32**, 760 (1987)].
[13] L. D. Tsendin, Zh. Tekh. Fiz. **56**, 278 (1986) [Sov. Phys. Tech. Phys. **31**, 169 (1986)].
[14] Yu. B. Golubovskiĭ and S. H. al Hawat, Zh. Tekh. Fiz. **57**, 44 (1987) [Sov. Phys. Tech. Phys. **32**, 25 (1987)].

Translated by P. Shelnitz

Open discharges: structure, development, and role of photoemission

A. R. Sorokin

Institute of Semiconductor Physics, Russian Academy of Sciences, Siberian Branch, 630090 Novosibirsk, Russia

(Submitted October 9, 1996)
Zh. Tekh. Fiz. **68**, 33–38 (March 1998)

The research reported in three preceding papers is summarized. The photoelectron mechanism for the formation of electron beams in an open discharge with a grid anode is revised. Revision of the discharge mechanism also requires revision of the optimal conditions for its excitation. A new method for pumping lasers by beams of fast atoms formed in an open discharge with an inverted voltage is proposed. © *1998 American Institute of Physics.* [S1063-7842(98)00503-0]

INTRODUCTION

The so-called[1] ''open discharge,'' a modification of the hindered discharge, was proposed in Ref. 2 in connection with the development of new pumping sources for pulsed gas lasers.[3] In an open discharge the bulk of the discharge energy is carried off by an electron beam through a grid anode into a drift space, from which additional photoillumination of the cathode is provided and into which the electric field from the discharge gap ''sags'' through the holes in the grid. These features of an open discharge are responsible for its high stability and permit the achievement of large currents, up to 100 A/cm^2, in the voltage range from several to 70 kV without the discharge becoming an arc discharge.[4] The existence of continuous electron beams was noted in Ref. 1, and such a regime was investigated for an open discharge in Refs. 5 and 6. As it turned out, a continuous open discharge had actually been known beforehand[7] and was used to pump continuous lasers. A hollow-anode discharge (the special case of an open discharge with a ''grid'' having one opening),[8,9] as well as various modifications of it, for which there is further information in Ref. 10, can also be classified as open discharges. Here we shall confine ourselves to an examination of an open discharge with a multiple-hole grid.

In contrast to all the known forms of glow discharges, where photoemission from the cathode does not play a decisive role, in an open discharge, as was assumed in Refs. 1, 5, and 11–15, the formation of the discharge, the mechanism sustaining it, and the principal source of beam electrons are provided by photoemission from the cathode. Adopting such an assumption, we can consider many properties of an open discharge without taking into account the ionization processes in the gap. However, these processes are important when a cathode fall appears and the concentrating of the field at the cathode can lead to sparking of the discharge. The qualitative treatment in Ref. 1, as well as the direct experiments using grid probes in Ref. 15, showed that a cathode fall can be present in an open discharge while a high electron-beam generation efficiency is maintained. There is also an opposing opinion.[11,12]

A new approach to the study of the processes in an open discharge was described in our preceding publications,[16–18] where, particularly in Ref. 18, the role of photoillumination from the drift space was reduced to ensuring the uniform emission of electrons from the cathode in the prebreakdown stage of the discharge. It was also confirmed in Ref. 16 that a high electron-beam generation efficiency is also maintained in the presence of a cathode fall. To reinforce the conclusions in Refs. 16–18, the structure and development of open discharges and the role of photoemission are considered in this summary paper with reference to additional experimental data, including data taken from the work of other investigators.

To avoid confusion in the terminology we shall call a discharge simply a high-voltage discharge when the field in the gap is distorted by the charges, but there is no clearly expressed cathode fall, and call it an anomalous discharge when the length of the cathode-fall region is shorter than the length of the discharge gap $l_c < d$. If we use the terminology in Ref. 19, both these types of discharges fall under the general heading of a ''dense discharge.''

LONGITUDINAL STRUCTURE OF A DISCHARGE

The structure was investigated as in Ref. 16 by analyzing the spectral-temporal characteristics of the spontaneous emission along the discharge. A flat movable cathode and a similar collector made from Duralumin were used in the experiments. The anode, whose central portion had a working diameter of 16.4 mm, had the form of a grid with an area $S = 1$ cm^2, a characteristic hole diameter equal to 0.4 mm, and a geometric transparency $\mu = 60\%$, so that the total transparency of the anode was $\mu' = 28\%$. Such a design made it possible to monitor the appearance of the discharge on the solid part of the anode.

It was shown in Ref. 16 that the character of the glow in the cathode layer of an open discharge is determined practically completely by the excitation of atoms by fast atoms (including ionized atoms). We present some additional evidence from experiments with a backward electron beam. Such a beam forms in the region into which the potential is transported by positive ions from the gap when the polarity

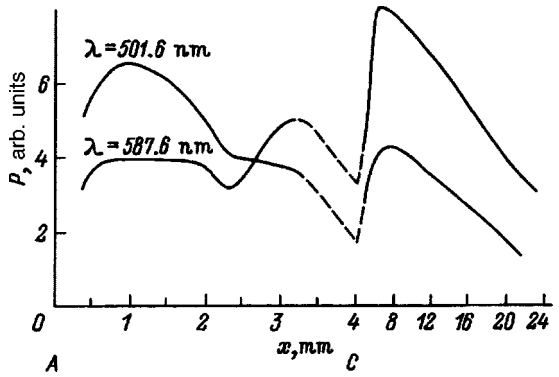

FIG. 1. Distribution of the intensity P of spontaneous emission lines along the x axis of a discharge. The scale for x has been altered after $x=4$ mm, $p_{\mathrm{He}}=220$ Pa; A—anode, C—cathode.

of the voltage supplied is reversed.[1] In the drift space there is, in addition to the electron beam, a beam of fast atoms formed in charge-transfer processes. As in Ref. 16, two lines were investigated in detail: 587.6 and 501.6 nm. The upper level of the former line is not optically coupled with the ground state (the function describing the excitation of the line by electrons has a maximum at 27 eV followed by an abrupt descent), while the latter line is so coupled (a maximum at 100 eV with a gently sloping descent).

Atoms excite the line at $\lambda=587.6$ nm with greatest efficiency.[16] Near the cathode the drop in the field toward the anode is accompanied by a decrease in the velocity of the fast atoms, which leads to a drop in the radiated intensity P (Fig. 1). At small x there is a small increase in P, which is a result of an increase in the excitation efficiency in the residual field of the negative-glow region. The main contribution to excitation of the line is still made here by the electron beam propagating toward the anode, i.e., the slower electrons on the tailing edge of U. Therefore, there is a delay of the radiation maximum relative to the current maximum, and its decay with time is slower at $x=1$ mm (Fig. 2) than at $x=3$ mm. Unlike an ordinary open discharge,[16] near the anode there is a break on the leading edge of the radiation oscillogram ($x=1$ mm) due to the difference between excitation of the line by the electron beam and excitation by the beam of atoms which is formed in the near-cathode region on the drift-space side of the grid and moves toward the anode.

An estimate of the length of the cathode-fall region (Fig. 1) gives $l_c\approx 2$ mm. We note that the cathode fall in the discharge stream is in the formation stage. If the radiation is detected at a definite moment in time on the leading or tailing edge of a current maximum, more of the distribution of the measured intensity P along the discharge is found on the leading edge of I than on the tailing edge.

In the drift space the intensity of the line at 587.6 nm is higher than that of the line at 501.6 nm (Fig. 1), in contrast to Ref. 16. As the distance from the grid increases, the rapid increase in the radiated intensity slows due to the slower velocity of the atoms exciting the line in comparison to the beam electrons (Fig. 2). The contribution of the fast atoms to the excitation of the line at 501.6 nm is smaller, but is still

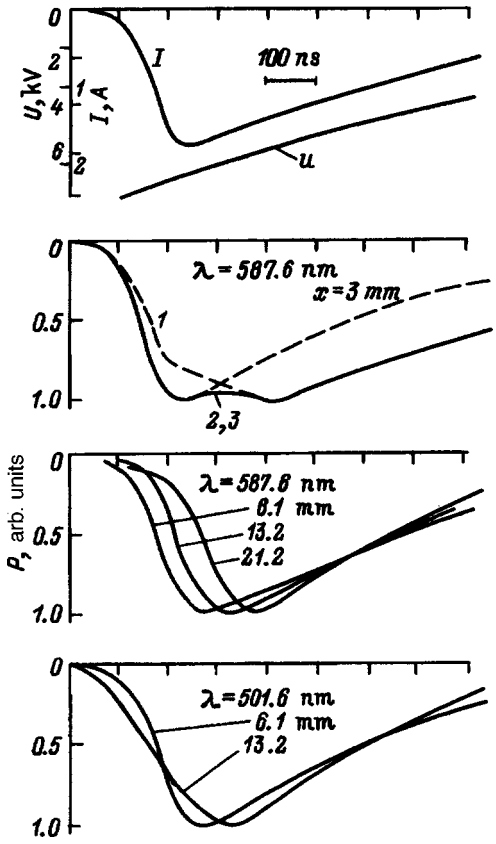

FIG. 2. Oscillograms of the current I, the voltage U, and the radiated intensity P at various distances x from the anode.

noticeable, as is evidenced by the displacement of the maximum of P as the distance from the grid increases (Fig. 2, $x=6.1$, 13.2 mm). If the current is decreased to 25 mA ($U=3.5$ kV, $l_c=3$ mm), the value of P near the grid becomes 3 times higher at 587.6 nm than at 501.6 nm, but at $x=25$ mm it becomes, conversely, 2 times lower because of the decrease in the penetration depth of the atomic beam.

The results presented in Fig. 3 for an ordinary open discharge in neon can be interpreted in analogy to the above material as well as Ref. 16. Here the fast atoms efficiently excite the neon line at 640.2 nm (P').

When $p_{\mathrm{Ne}}=230$ Pa, there is no discharge on the solid part of the anode, and there is no cathode fall in the gap. There is still appreciable distortion of the field by the charges, i.e., the maximum of P' is located closer to the cathode than is the maximum of P. Excitation of the line at 640.2 nm by fast atoms is dominant across the entire gap (t' increases sharply in the drift region). If d is increased at fixed values of U and p_{Ne}, we can determine l_c, which is found to be equal to 0.7 mm. When $p_{\mathrm{Ne}}=600$ Pa, a discharge is also observed on the solid part of the anode. Although there is no clearly expressed minimum for P', as in Fig. 1 for the line at 587.6 nm in helium, l_c can be determined from the behavior of t': $l_c\approx 0.3$ mm.

Thus, lines can be selected in any gas, and the length of the cathode fall can be determined from the behavior of the radiation characteristics along the discharge. Since the radiation of a discharge in the cathode-fall region integrated over

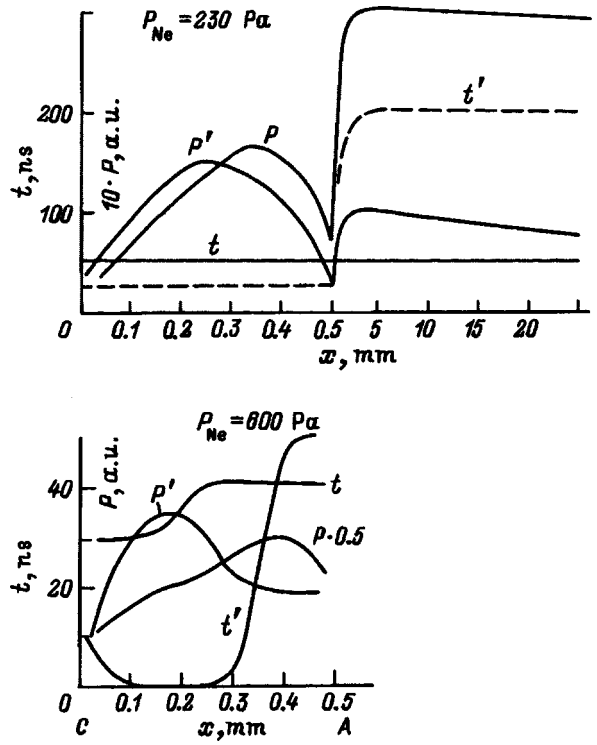

FIG. 3. Distribution of the intensities P and P' and variation of the delays t and t' between the maxima of the total current I and the spontaneous emission along the x axis. The amplitude values for $p_{Ne}=230$ Pa are $U=8.8$ kV and $I=5.8$ A; and the corresponding values for $p_{Ne}=600$ Pa are 4 kV and 6.4 A; $d=0.5$ mm. The values marked with a prime refer to $\lambda=640.2$ nm, and those without a prime refer to $k\lambda=587.2$ nm.

the spectrum behaves similarly to the radiation in lines that are efficiently excited by the fast atoms, the character of the glow in the cathode layer is determined practically completely by the excitation of atoms by the fast heavy particles. Let us dwell on the use of the inverted-voltage regime of an open discharge to pump lasers. It was noted in Ref. 1 that when the polarity of the voltage supplied is reversed in a coaxial design, greater radiated power is generated in several laser transitions, and the distribution of the laser radiation over the cross section of the beam becomes homogeneous (under ordinary polarity it decreases sharply from the center toward the edges of the tube). For example, for a mixture with He:Xe=100:1, $p=1.6$ kPa, and a current equal to 4.5 A the peak laser power at $\lambda=2.03$ μm was close to saturation and amounted to 1 W. When only the polarity of the voltage supplied was reversed, it took a value of 9 W, and the current increased by a factor of 2. In accordance with Ref. 1, under these conditions the parameters of the forward and backward electron beams are about the same. It is clear that even in the best case the power could increase by a factor of 2 as a result of the absence of the grid ($\mu=50\%$) on the path of the backward electron beam and not by a factor of 9. No explanation for this finding was given in Ref. 1.

Although the upper level of a laser transition is resonant and requires fast electrons to efficiently excite it, owing to the considerable cross section for excitation by electrons near the excitation threshold this transition is very intense in a high-pressure laser[20,21] when low values of E/p are achieved. Hence, in accordance with the material presented in this section, it should be theorized that when the polarity of the voltage supplied is reversed, population inversion is formed in the laser transition mainly as a result of excitation by the beam of fast atoms, rather than by the electron beam. It is difficult to find another explanation for the observed effect.

Thus, not only the electron beams, but also the atomic beams of open discharges can be used to excite lasers. We note that the conditions for the efficient generation of atom and electron beams do not always coincide.[1] This expands the possibilities for selecting the optimum excitation conditions for specific laser transitions.

DEVELOPMENT OF A DISCHARGE. ROLE OF PHOTOEMISSION

In a recently published paper Kolbychev *et al.*[13] drew the following conclusion, which reflects a widely accepted opinion: ''The ignition and development of a glow discharge from the entire cathode surface, which efficiently generates a beam of runaway electrons, is initiated and maintained by the UV illumination from the beam plasma in the trans-anode region. Its ignition occurs at a voltage which is 2–3 times lower than the voltage necessary for a self-sustaining breakdown of the gap, and in this sense the discharge is non-self-maintained.'' They added, ''Since the mechanism for the ignition and development of a glow discharge is predominantly photoelectric, while the breakdown of the gap depends solely on the ionization of the gas..., these two processes develop practically independently of each other. (Kolbychev *et al.* construe breakdown to be the transformation of an open discharge into a spark).

A different opinion was advanced in Refs. 7 and 8. According to Ref. 18, the development of an open discharge can be divided into five stages.

The first is the prebreakdown stage ($I<10^{-4}$ A/cm^2). The conditions in it, especially the intensity of the photoillumination of the cathode, determine the subsequent evolution of the discharge: its uniformity and the magnitude and stability of the breakdown delay.

The second stage is a pre-high-voltage discharge (usually $I<0.1$ A/cm^2), which is sustained by ionization of the gas in the weak field sagging through the openings in the anode grid. There is practically no discharge on the grid wires; therefore, the electron-beam generation efficiency does not depend on μ, but is determined directly by the processes in the discharge and can have a value close to 100%. In this stage the current can be increased to the level usually achieved in an open discharge by adjusting the conditions ($l_c>d$, increasing the field in the holes of the grid). No perceptible influence of photoillumination on this stage or on the subsequent stage was discovered.

The next two stages are high-voltage and anomalous discharges. The electric field in the gap is still distorted by space charges. The conditions for ionization in the weakened field of the near-anode region are improved, a discharge forms on the grid wires, and a cathode fall appears. Now part

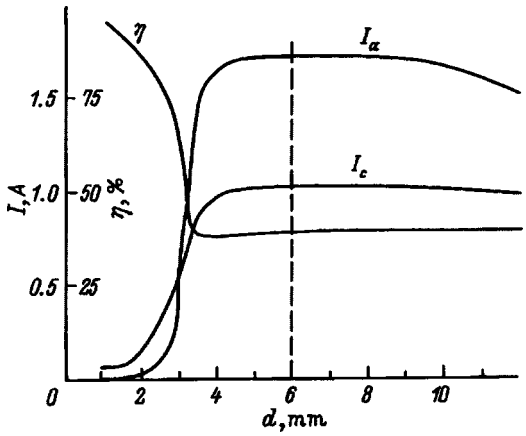

FIG. 4. Dependence of the collector current I_c, the anode current I_a, and the electron-beam generation efficiency $\eta = I_c(I_a + I_c)^{-1}$ on d. The amplitude value is $U = 10.8$ kV, the length of the drift space $L = 30$ mm, and $p_{He} = 290$ Pa. Dashed line—length of the cathode-fall region in a normal glow discharge. The excitation pulse repetition frequency $f = 240$ Hz with a decay time constant $\tau = 15$ μs.

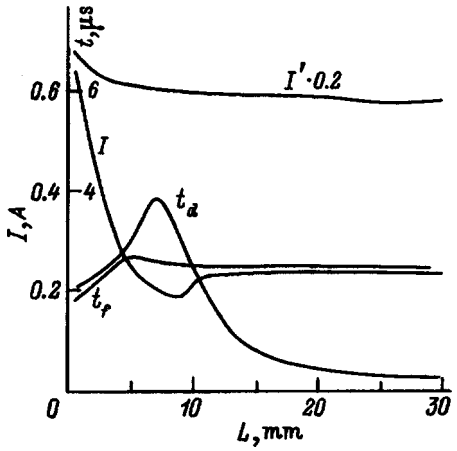

FIG. 6. Variation of the total current $I = I_a + I_c$, the breakdown delay time t_a, and the pulse rise time t_f as functions of L. $p_{He} = 280$ Pa, $U = 8.6$ kV, $f = 240$ Hz, $\tau = 15$ μs, $d = 1.5$ mm; I'—for $d = 4$ mm.

of the electron beam is intercepted by the grid, and the transmission efficiency of the electron beam gradually decreases down to a value close to the geometric transparency of the grid. The anomalous stage of an open discharge was thoroughly investigated in Ref. 22, where it was shown on the basis of known experimental data that an open discharge can be described within the concept of an ordinary anomalous discharge. Obviously, such correspondence is impossible in the case of a photoelectron open discharge.

The last stage is an arc discharge. It is the result of the ordinary transformation (which was investigated in detail in Ref. 13) of an anomalous discharge into an arc discharge.

The development of an open discharge can be stopped in any of the stages just enumerated by adjusting the conditions. The first four stages are easily traced as d (Fig. 4) or U (Fig. 5) increase. The minimum efficiency $\eta = 38\%$ (Fig. 4) is somewhat higher than the total geometric transparency of the anode $\mu' = 28\%$ and is naturally associated with the small current density on the solid part of the anode.

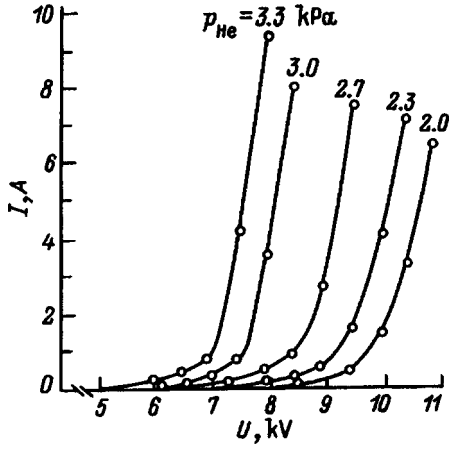

FIG. 5. Dependence of the current on the initial voltage. $d = 0.5$ mm, $S = 1$ cm^2, $\mu = 80\%$, $f = 400$ Hz, and $\tau = 3.1$ μs.

Figure 5 was taken from Ref. 13, where it was noted that the break on the $I(U)$ curves does not have an unequivocal explanation and one of the possible causes of the break was called ''additional UV illumination of the cathode by the discharge appearing in the beam-plasma body in the drift region.'' It is clear from the foregoing that the breaks on both $I(d)$ (Fig. 4) and $I(U)$ (Fig. 5) are caused by ''switching'' to a discharge process involving the entire gap, including the regions corresponding to the grid wires and the solid part of the anode, and are associated with the formation of a cathode fall.

For a photoelectron onset of an open discharge the photoillumination must ensure an electron multiplication factor $k > 1$, which must be maintained in the subsequent stages. Then the amplitude value of I_c need not depend on d, as in Fig. 4, and its absolute value, like the absolute value for I in Fig. 5, should be much greater. For the fairly long pulses with which we are dealing, I is determined by the familiar 3/2 power law. For example, for $U = 6$ kV and $d = 0.5$ mm we have $I = 2.34 \times 10^{-6} d^{-2} \cdot U^{3/2} = 440$ A/cm^2, rather than ~ 0.1 A/cm^2, as in the case of the curve for $p_{He} = 3.3$ kPa in Fig. 5.

One of the arguments in favor of the photoelectron character of the development of an open discharge in Ref. 13 is the absence of the breakdown characteristic of an ordinary discharge on oscillograms of I and U and the smooth initial course of the $I(U)$ curves in Fig. 5, which do not visibly cross the horizontal axis. In reality, such breakdown occurs and is clearly seen on the oscillograms illustrating a pre-high-voltage discharge, such as those in Ref. 18, but at smaller current densities equal to $\sim 10^{-3}$ A/cm^2. We were unable to obtain a smooth increase in the current without characteristic breakdown under any conditions. This is evidence that even the breakdown stage appears as a result of ionization processes and the movement of charges.

Let us examine the influence of the processes in the drift space on a discharge in greater detail. We make a comparison in two discharge stages, viz., the pre-high-voltage and anomalous stages ($d = 1.5$ and 4 mm, Fig. 4). For $d = 1.5$ mm (Fig. 6) a decrease in the size of the photoillu-

mination region leads to an increase in the breakdown delay time t_d. The current I and its development time t_f scarcely vary. When beam electrons reflected from the collector additionally ionize the gas in the grid holes, the value of t_d decreases and I increases only in the immediate vicinity of the grid anode. When $L \lesssim 1$ mm, sparking appears.

The transition to $d=4$ mm is accompanied by an increase in I by an order of magnitude, from 0.2 to 3 A, while the value $I=3$ A is maintained as L varies (Fig. 6). The value $t_f=140$ ns is totally independent of L. The breakdown delay time t_d remains stable and equal to 200 ns as L decreases to 15 mm. As L decreases further, an instability in the value of t_d appears, which grows and leads to the variation of t_d in the range 0.2–1 μs near the grid.

The results presented are totally inconsistent with a photoelectron open discharge from the moment of breakdown, after which the further development of the discharge (the duration of the increase in t_f and the value of I) is determined by processes in the gap itself and in the holes in the anode grid. The fact that, if a cathode fall does not form, the usual working currents of an open discharge can be achieved by increasing the field in the grid holes attests to the decisive role of the ionization processes in the weakened field in the multiplication of charges. This same is true for a region of weakened field when a cathode fall forms and the influence of the field in the grid holes is small.

The electric field beyond the cathode fall in Ref. 23 ($d=1.9$ mm, $p_{\mathrm{He}}=15$ Torr, $U=3.1$ kV) is very strong: $E(x>l_c=0.6\ \mathrm{mm})=10^4$ V/cm [at the cathode $E(x=0)=6\times10^4$ V/cm]. It is even significantly stronger than the critical field $E_{\mathrm{cr}}=2.2\times10^3$ V/cm needed for the onset of the continuous acceleration of electrons.[24] Apparently, it is also strong under the conditions of our experiments. The lines (for He at 501.6 nm and for Ne at 587.6 nm) with slow decay of the functions for excitation by electrons primarily sense the decrease in E in the near-anode plasma, as is manifested by the increase in P (Figs. 1 and 3). However, even for them the maxima of P shift with time toward smaller values of U in this region, and the decay of P is slower than in the case of I. Similar behavior was also discovered for the He II line at 468.5 nm. The weakened, but still fairly strong field outside the cathode-fall region leads to the appearance of an appreciable group of electrons with energies $<eU$. This is manifested by the appearance of a maximum on the radiation distribution near the grid on the drift-space side. In Ref. 16 the appearance of the maximum was hypothetically attributed to neutralizion currents.

Thus, in an open discharge the near-anode plasma is the main source of the ions which bombard the cathode and sustain the current in the open discharge. In the initial breakdown stage it is created in the region of the weakened field sagging through the holes in the anode grid. During the formation of the cathode fall, the region of the weakened field expands, and the role of the field in the grid holes decreases. When the cathode fall is completely formed, the influence of the field in the grid holes can become negligibly small.

Although conditions with small $U<10$ kV are typical of open discharges, they can employ significantly larger values of U, at which ionization by fast atoms can become the main source for the formation of charged particles.[25] For example, if we take $l_c=1.5$ mm and a charge-transfer cross section $\sigma_{\mathrm{ct}}\sim10^{-15}$ cm^2 under the conditions in Ref. 4 ($d=10$ mm, $p_{\mathrm{Ne}}=150$ Pa, and $U=70$ kV), for the mean free path of the ions we obtain $\lambda_{\mathrm{ct}}=(N\sigma_{\mathrm{ct}})^{-1}=0.25$ mm, and for the energy of the fast atoms we have $W\sim l\lambda_i U l_c^{-1}=12$ keV. For such an energy of, for example, He atoms the ionization cross section $\sigma_{\mathrm{ia}}\sim10^{-16}$ cm^2 (Ref. 26), which even exceeds the largest cross section for ionization by electrons $\sigma_{\mathrm{ie}}=3.4\times10^{-17}$ cm^2.

In the present work we examined only the influence of photoelectron emission on a discharge in detail. The principal mechanism of emission in different types of high-voltage discharges with an anode plasma and, therefore, in open discharges is, as is generally assumed, emission under the action of the flux of fast heavy particles. The efficiency of this mechanism depends on the charge-transfer processes and other factors: the material and state of the cathode (the degree of contamination and the cleanliness of the treatment), the distribution of the field E in the gap, the cathode sputtering rate, the initial purity and kind of gas and its contamination by the sputtering products, and the release of gases from structural elements of the discharge chamber. These factors were analyzed in detail in Ref. 10. Because of the difficulty in taking them into account simultaneously, the general picture is very complicated.

The emission processes must be closely related to the length of the cathode-fall region. In a strongly anomalous discharge l_c depends weakly on the current, and as I increases, it tends to its lower limit[27] $(l_c)_{\min}=0.37\times(pl_c)_n p^{-1}$, where the value of $(pl_c)_n$ is taken for a normal glow discharge. For example, for an aluminum cathode under the conditions in Fig. 3 $(l_c)_{\min}=1.3$ and 0.5, and for $p_{\mathrm{He}}=15$ Torr it equals 0.33 mm.

When the current exceeds a certain value in experiments with two grid electrodes, the penetration depths of the oppositely directed electron beams become comparable.[1] This is possible only when the potential is completely transported beyond the cathode grid by ions from the gap. For this to occur, the ions must move in the cathode-fall region without perceptible energy losses. Therefore, the condition $l_c \lesssim \lambda_{\mathrm{ct}}$ must be satisfied,[1] or in our examples we must have $\lambda_{\mathrm{ct}}=0.2$, 0.07, and 0.02 mm, which are significantly less than $(l_c)_{\min}$.

It was postulated in Ref. 11 that the potentials can also be completely withdrawn by impurity ions that interact weakly with the main gas when $l_c=d$. The measured values of l_c (0.7, 0.3, and 0.6 mm) for low pressures ($p_{\mathrm{Ne}}=230$ and 600 Pa) are appreciably smaller than $(l_c)_{\min}$, but significantly greater than λ_{ct}. In accordance with Ref. 15, the relation $l_c\sim\lambda_{\mathrm{ct}}$ is established when $I\geqslant16$ A/cm^2 ($p_{\mathrm{Ne}}=600$ Pa), but there are definite doubts[16] regarding the correctness of this estimate. The design of our discharge cell did not allow us to achieve such currents due to the appearance of parasitic breakdown on the walls of the tube, and the fact that $l_c<(l_c)_{\min}$ can be attributed, for example, to contamination of the cathode. Under the conditions considered the value of l_c is possibly influenced by ionization by heavy particles in the cathode-fall region, which was not taken into

account in the derivation of the formula for $(l_c)_{\min}$ in Ref. 27.

Thus, elucidation of the real picture requires a set of additional investigations, including not only measurements of l_c, but also a mass-energy analysis of the ions.[28] It was discovered in Ref. 28 that the situation $l_c \sim \lambda_{ct}$ is possible in a glow discharge. In an open discharge such a situation complicates finding an explanation for the high emission of electrons from the cathode even more.

CONCLUSIONS

The investigations performed in this work demonstrated the following.

1. The length of the cathode-fall region can be determined by analyzing the spectral-temporal characteristics of the radiation along a discharge. A fairly strong field can remain after the cathode-fall region. The character of the glow in the cathode layer of an open discharge is determined practically completely by the excitation of atoms by fast heavy particles. The great difference between the excitation efficiencies of individual atomic states by beam electrons and fast atoms opens up prospects for creating lasers pumped by beams of atoms formed in an open discharge with an inverted voltage.

2. An open discharge is a certain type of glow discharge. Thus, the disputed question of the presence or absence of a cathode fall in an open discharge can be considered resolved.

3. Photoillumination from the drift space influences only the development of the prebreakdown discharge stage and, together with the field in the holes of the anode grid, determines the magnitude and stability of the breakdown delay. Its influence on the subsequent stages also begins in the prebreakdown stage as a result of the creation of a large number of emission centers on the cathode, which provide for the stability of the discharge.

4. After the moment of breakdown, the development of the discharge is determined by the processes in the gap itself and in the holes of the anode grid, the near-anode plasma becoming the main source of ions that sustain the current and the open discharge and bombard (together with atoms) the cathode. At high field intensities the role of field emission should increase, and ionization by fast atoms can become the main source of ions.

5. The revision of the mechanism for the generation of an electron beam in an open discharge also requires revision of the conditions for the appearance of an open discharge. For example, to increase the current, the ion flux should be increased by expanding the region of the near-anode plasma. In a pre-high-voltage discharge the geometric transparency of the grid must be increased to maintain a high electron-beam generation efficiency, and a grid with large holes should be chosen to increase the current in it.

[1] P. A. Bokhan and A. R. Sorokin, Zh. Tekh. Fiz. **55**, 88 (1985) [Sov. Phys. Tech. Phys. **30**, 50 (1985)].
[2] P. A. Bokhan and G. V. Kolbychev, Pis'ma Zh. Tekh. Fiz. **6**, 418 (1980) [Sov. Phys. Tech. Phys. **6**, 180 (1980)].
[3] P. A. Bokhan and A. R. Sorokin, Opt. Quantum Electron. **23**, 523 (1991).
[4] A. R. Sorokin and P. A. Bokhan, Pis'ma Zh. Tekh. Fiz. **20**(17), 86 (1994) [Tech. Phys. Lett. **20**(9), 720 (1994)].
[5] A. S. Kovalev, Yu. A. Mankelevich, E. A. Muratov *et al.*, Fiz. Plazmy **18**, 1076 (1992) [Sov. J. Plasma Phys. **18**, 561 (1992)].
[6] A. R. Sorokin, Zh. Tekh. Fiz. **65**, 189 (1995) [Tech. Phys. **40**, 517 (1995)].
[7] K. Rózsa, M. Jánossy, L. Scillag *et al.*, Opt. Commun. **23**, 162 (1977).
[8] G. G. Isaacs, Electron. Lett. **4**, 405 (1968).
[9] J. J. Rossa, J. D. Meyer, M. R. Farrell, and G. J. Collins, J. Appl. Phys. **56**, 790 (1984).
[10] M. A. Zav'yalov, Yu. E. Kreĭndel', and A. A. Ṇovikov, *Plasma Processes in Industrial Electron Guns* [in Russian], Énergoatomizdat, Moscow (1989).
[11] G. V. Kolbychev and I. V. Ptashnik, Zh. Tekh. Fiz. **59**, 104 (1989) [Sov. Phys. Tech. Phys. **34**, 1018 (1989)].
[12] G. V. Kolbychev, Opt. Atmos. Okeana **6**, 635 (1993).
[13] G. V. Kolbychev, P. D. Kolbycheva, and I. V. Ptashnik, Zh. Tekh. Fiz. **66**, 59 (1996) [Tech. Phys. **41**, 144 (1996)].
[14] S. V. Arlantsev, B. L. Borovich, V. V. Buchanov *et al.*, J. Russ. Laser Res. **16**, 99 (1995).
[15] P. A. Bokhan, Zh. Tekh. Fiz. **61**, 61 (1991) [Sov. Phys. Tech. Phys. **36**, 620 (1991)].
[16] A. R. Sorokin, Pis'ma Zh. Tekh. Fiz. **21**(17), 33 (1995) [Tech. Phys. Lett. **21**(9), 692 (1995)].
[17] A. R. Sorokin, Pis'ma Zh. Tekh. Fiz. **21**(20), 37 (1995) [Tech. Phys. Lett. **21**(10), 832 (1995)].
[18] A. R. Sorokin, Pis'ma Zh. Tekh. Fiz. **22**(13), 17 (1996) [Tech. Phys. Lett. **22**(7), 526 (1996)].
[19] B. N. Klyarfel'd, L. G. Guseva, and A. S. Pokrovskaya-Soboleva, Zh. Tekh. Fiz. **36**, 704 (1966) [Sov. Phys. Tech. Phys. **11**, 520 (1966)].
[20] A. R. Sorokin, Zh. Tekh. Fiz. **49**, 1673 (1979) [Sov. Phys. Tech. Phys. **24**, 932 (1979)].
[21] A. R. Sorokin, Kvantovaya Elektron. **10**, 308 (1983) [Sov. J. Quantum Electron. **13**, 165 (1983)].
[22] K. A. Klimenko and Yu. D. Korolev, Zh. Tekh. Fiz. **60**, 138 (1990) [Sov. Phys. Tech. Phys. **35**, 1084 (1990)].
[23] V. P. Demkin, B. V. Korolev, and S. V. Mel'nichuk, Fiz. Plazmy **21**, 81 (1995) [Plasma Phys. Rep. **21**, 76 (1995)].
[24] Yu. D. Korolev and G. A. Mesyats, *Physics of the Pulsed Breakdown of Gases* [in Russian], Nauka, Moscow (1991).
[25] K. N. Ul'yanov and V. V. Chulkov, Zh. Tekh. Fiz. **58**, 328 (1988) [Sov. Phys. Tech. Phys. **33**, 201 (1988)].
[26] H. C. Hayden and N. G. Utterback, Phys. Rev. **135**, 1575 (1964).
[27] Yu. P. Raizer, *Gas Discharge Physics*, Springer-Verlag, Berlin–New York (1991) [Russian original: Nauka, Moscow, 1987].
[28] A. V. Bondarenko, Zh. Tekh. Fiz. **46**, 2535 (1976) [Sov. Phys. Tech. Phys. **21**, 1497 (1976)].

Translated by P. Shelnitz

Stability of the superconducting state of a multiconductor current-carrying element during the induction of current in it

V. R. Romanovskiĭ

Kurchatov Institute Russian Science Center, 123182, Moscow, Russia
(Submitted February 2, 1996)
Zh. Tekh. Fiz. **68**, 39–44 (March 1998)

A model which permits estimation of the temporal variation of the temperature and the current in the components of a superconducting cable is proposed. The permissible currents which can be induced in a six-strand current-carrying element without destroying its superconducting properties are determined. It is shown that in the presence of inductive coupling between the conductors, the position of the cable component in which instability is initiated is not a regular function of the current induction rate if there is a spread in the nonlinearity parameters of the current–voltage characteristics of the components. © *1998 American Institute of Physics.* [S1063-7842(98)00603-5]

The stable operation of superconducting magnetic systems requires maintenance of conditions which ensure the stability of the superconducting state of their current-carrying elements. The stability problem has been investigated most thoroughly for current-carrying elements in the form of a solitary composite conductor,[1–4] which is a structure that is ordered in some manner and consists of a large number of thin superconducting filaments in a normally conducting matrix. However, large magnets often utilize current-conducting elements consisting of transposed conductors. They have a number of advantages over monolithic current-carrying elements.[3] For example, the use of a superconducting cable with insulated conductors lowers the level of cooperative losses. At the same time, the presence of a large number of conductors in a current-carrying element can modify the conditions for the appearance and development of the numerous instabilities that appear when a superconducting magnet operates (see, for example, Refs. 5–12). In particular, one of the probable causes of the premature transition of a superconducting winding to the normal state during the induction of current can be thermomagnetic instability.[2–4] Nevertheless, the use of the existing theory, which was developed for a monolithic composite superconductor, has a restricted range of application in analyzing the stable states of superconducting cables. In addition, it should also be noted that the theoretical models of the transition processes in superconducting cables that have been formulated are based on *a priori* assignment of the region which initiates the transition of the entire composite to the normal state. The self-consistent variation of the current and the temperature in each component of a cable preceding the appearance of instability is disregarded. Since these processes are decisive for such important characteristics of superconducting systems as the current-carrying capacity and the restriction of the current induction rate, the existing models lead to very simplified results, and the methods used do not provide exhaustive information on the stability of multiconductor superconducting cables.

To completely understand the processes occurring in superconducting cables, we must take into account both the local and macroscopic properties of the entire structure. This requires departure from the model of a continuous medium and consideration of collective effects. For this reason, the model proposed below is based on a more general conception, which takes into account the interrelated dynamics of the temperature and current in all the elements of the composite over the course of the entire current-induction process.

Let us consider the very simple problem of determining the current-carrying capacity of a cooled superconducting cable. Let the current in the circuit be initially equal to zero, and then let the current begin to increase linearly at a constant rate. To simplify the analysis performed we assume that the cable is a set of inductively coupled straight composites based on hard superconductors with a small transverse dimension that are insulated from one another, that the superconductor is evenly distributed over the cross section of each conductor and thus its thermo- and electrophysical parameters can be described by the continuous-medium model, that the variation of the longitudinal magnetic field within each conductor is small, that the cable is initially cooled to the temperature of the coolant and the external surface of each conductor is cooled with an assigned heat-transfer coefficient, and that the current–voltage characteristic of the superconductor is described by a model exponential dependence.[13] Within the assumptions just formulated the temperature distribution in each component of the superconducting cable, which does not depend on the longitudinal and azimuthal coordinates, is described by the equations

$$c_k \frac{\partial T_k}{\partial t} = \frac{1}{r} \frac{\partial}{\partial r} \left(\lambda_k r \frac{\partial T_k}{\partial r} \right) + E_k J_k, \quad k = \overline{1, N}, \tag{1}$$

in which the electric field strength E_k, the magnetic field induction B_k, and the current density J_k satisfy the system of Maxwell's equations

$$\frac{1}{r} \frac{\partial (r B_k)}{\partial r} = \mu_0 J_k, \quad \frac{\partial E_k}{\partial r} = \frac{\partial B_k}{\partial t}, \quad k = \overline{1, N}. \tag{2}$$

Here c_k is the specific heat of the kth conductor in the cable, λ_k is its thermal conductivity, and N is the number of conductors in the cable. The problem defined by (1) and (2) enables us to investigate the stability of the superconducting state of each component of the cable under appropriate initial and boundary conditions. However, its solution is associated with definite mathematical difficulties. Let us go from the general system consisting of (1) and (2) to a simplified system that does not require a formidable number of calculations. We integrate Eq. (1) over the radius. Taking into account the occurrence of heat exchange with the coolant, we have

$$c_k\int_0^a \frac{\partial T_k}{\partial t} r dr = -h_k a(T_k - T_0) + \int_0^a E_k J_k r dr.$$

Neglecting the nonuniformity of the temperature field in the plane of a transverse section for thin conductors, we bring this equation into the form

$$c_k \frac{\partial T_k}{\partial t} = -\frac{2h_k}{a}(T_k - T_0) + \frac{2}{a^2}\int_0^a E_k J_k r dr. \tag{3}$$

To calculate the ohmic losses, we utilize the approximate formula

$$\int_0^a E_k J_k r dr = \eta_k [J_c(T_k) - \Delta J_k]\int_0^a E_k r dr. \tag{4}$$

It is, first, a consequence of the assumption that the temperature is uniform in a cross section of the kth conductor, and, second, it holds, because the superconducting component of the current density is significantly greater than the corresponding normal component, which can be neglected. In this expression η_k is the superconductor volume fraction in the kth conductor; $J_C(T)$ is the dependence of the critical current density on the temperature in a given magnetic field, which is assigned for a superconductor with an ideal current–voltage characteristics; and ΔJ_k is the degradation component of the current-carrying capacity due to the nonlinearity of its current–voltage characteristic. It can be determined by considering the limiting case of the induction of current at an infinitely slow rate. For superconducting composites with an exponential current–voltage characteristic and a nonlinearity parameter δ_k it is not difficult to obtain[14]

$$\Delta J_k = J_C(T_{q,k}) - J_{C0} i_{q,k}, \quad T_{q,k} = T_0 + \tau_{q,k}(T_{CB} - T_0),$$

where

$$i_{q,k} = 1 - \delta_k\left\{1 + \ln\left[r_k\left(\frac{\alpha i_{q,k} - 1}{\delta_k} i_{q,k} - 1\right)\right]\right\},$$

$$\tau_{q,k} = \alpha i_{q,k}\left(\frac{i_{q,k}}{2} - \left(\frac{i_{q,k}^2}{4} - \frac{i_{q,k}\delta_k}{\alpha i_{q,k} - 1}\right)^{1/2}\right).$$

Here, according to Ref. 15,

$$\delta_k = \frac{J_\delta}{J_{C0}}, \quad r_k = \frac{(1-\eta_k)\rho_s}{\eta_k \rho_m},$$

$$\alpha = \frac{J_{C0}^2 \eta_k^2 \rho_m S_k}{(1-\eta_k) h_k p_k (T_{CB} - T_0)},$$

S_k is the cross-sectional area of the kth conductor, p_k is the cooled perimeter, h_k is the heat-transfer coefficient to the coolant, T_0 is the temperature of the coolant, T_{CB} and J_{C0} are the critical parameters of the superconductor in a given magnetic field, J_δ is the current nonlinearity parameter of the current–voltage characteristic, and ρ_s and ρ_m are the resistivities of the superconductor and the matrix, respectively.

The electric field strength within a conductor of round cross section with a radius a is found after Ref. 4 from the simplified solution of system (2)

$$E_k(r,t) = \frac{\mu_0}{2\pi}\frac{dI_k}{dt}\ln\frac{r}{r_{p,k}(t)}, \tag{5}$$

where dI_k/dt is the rate of variation of the current in the conductor, and $r_{p,k}(t)$ is the magnetic-flux penetration depth, which is related to the current flowing in the conductor by the expression

$$I_k = S_k \eta_k [J_C(T_k) - \Delta I_k]\left[1 - \left(\frac{r_{p,k}}{a}\right)^2\right]. \tag{6}$$

We determine the distribution of the currents in the circuit formed by the cable components from the solution of a system of Kirchhoff's equations of the form

$$\sum_{j=1}^N M_{k,j}\frac{dI_i}{dt} + I_k R_k\left(\frac{dI_k}{dt}, T_k\right) = U, \quad k = \overline{1, N},$$

$$\sum_{k=1}^N \frac{dI_k}{dt} = \frac{dI}{dt}. \tag{7}$$

Here dI/dt is the rate of variation of the current in the general circuit, $\{M_{k,j}\}$ is the assigned inductance matrix of the composite, and $R_k(dI_k/dt, T_k)$ is the electrical resistance of the kth conductor due to the variation of the current in it. We define it for a conductor of round cross section and length l according to Ohm's law as

$$R_k\left(\frac{dI_k}{dt}, T_k\right) = \frac{2l}{I_k a^2}\int_{r_{p,k}}^a E_k r dr.$$

The solution of system (3)–(7) under the initial conditions

$$T_k(0) = T_0, \quad I_k(0) = 0, \quad k = \overline{1, N}$$

was based on the Runge–Kutta method. It permits the calculation of the averaged values of the temperature and the current in each component of a multiconductor current-carrying element before the irreversible destruction of its superconducting state. To determine the time of the onset of the development of instability, we utilize the conclusions formulated in Ref. 14, according to which the destruction of the superconducting properties of a solitary composite is a consequence of the nonisothermal dynamics of the magnetic flux within the superconductor. As a result of this process, the permissible increase in the temperature of the composite is bounded from above by a nontrivial value, which depends on the magnetic-flux penetration conditions. The numerical experiments performed in Ref. 14 for superconducting conductors with current–voltage characteristics having nonlinearity parameters varying in the range $1 \leqslant \delta_k \leqslant 5\%$ show that for

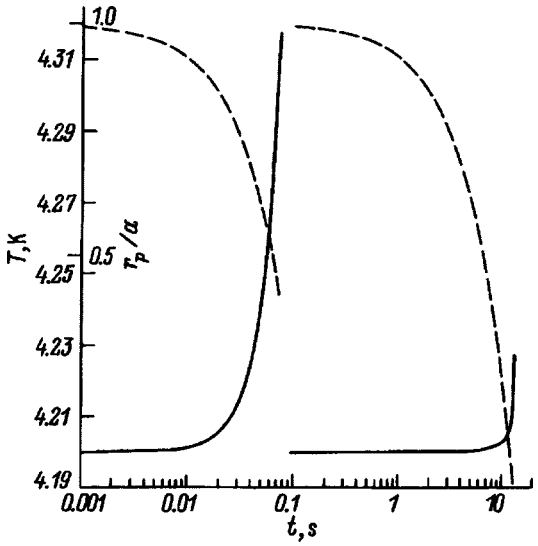

FIG. 1. Temporal variation of the temperature of the composite (—) and the magnetic-flux penetration depth (----) before the appearance of instability in the case of the complete and partial filling of the transverse section of the conductor by the current.

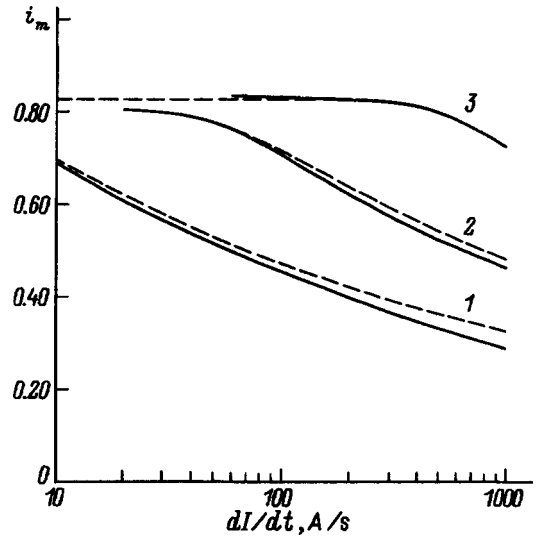

FIG. 2. Dependence of the dimensionless critical current induced in a solitary superconducting composite ($a=5\times10^{-4}$ m) on the current induction rate for various values of the heat-transfer coefficient. h, W/m^2·K: *1*—10, *2*—100, *3*—1000.

states in which the magnetic flux does not completely fill the cross section of the conductor, the appearance of instability can be described by an inequality of the form

$$T_k(t)>T_{\max,k}=T_{q,k}+(T_{CB}-T_0)\left(1-\sqrt{\frac{I_k}{\eta_k S_k J_{C0} i_{q,k}}}\right)^3,$$

$$t>0, \quad k=\overline{1,N}.$$

Within model (3)–(7) the limiting case $r_{p,k}\to 0$ signifies an irreversible transition to the normal state of the respective component when its transverse section is completely filled by the current.

To illustrate the efficacy of the stability criteria used in the present work, Fig. 1 presents plots, which describe the temporal variation of the temperature of a niobium-titanium superconductor in a copper matrix and the corresponding values of the magnetic-flux penetration depth for two characteristic values of the current induction rate, at which instability develops with incomplete ($dI/dt=10^4$ A/s) and complete ($dI/dt=10^2$ A/s) filling of the transverse section of the conductor by the current. In the former case the destruction of the superconducting properties of the composite is a result of an increase in the temperature of the conductor to a level above the permissible value, and in the latter case it is a consequence of complete penetration of the magnetic flux into the composite. The starting parameters taken for the calculations were

$$l=10 \text{ m}, \quad a=5\times10^{-4} \text{ m}, \quad c=10^3\frac{\text{J}}{\text{m}^3\text{K}},$$

$$\eta=0.5, \quad h=1000\frac{\text{W}}{\text{m}^2\text{K}},$$

$$J_C(T)=J_{C0}\frac{T_{CB}-T}{T_{CB}-T_0}, \quad J_{C0}=4\times10^9\frac{\text{A}}{\text{m}^2},$$

$$T_{CB}=9 \text{ K}, \quad T_0=4.2 \text{ K},$$

$$\rho_m=2\times10^{-10} \ \Omega\cdot\text{m}, \quad \rho_s=5\times10^{-7} \ \Omega\cdot\text{m},$$

$$\delta=0.01.$$

To test the proposed model we determined the boundaries of the stable states of a solitary superconducting composite when current is induced in it. They were compared with a previously performed analysis of the critical currents based on a solution of a complete system of Fourier and Maxwell equations.[14] Figures 2 and 3 present the results of calculations of the dimensionless values of the critical currents [$i_m=I_m/(\eta S J_{C0})$] in the ''simplified'' (solid curves) and ''exact'' (dashed curves) models for various values of the heat-transfer coefficient and radius of the conductor.

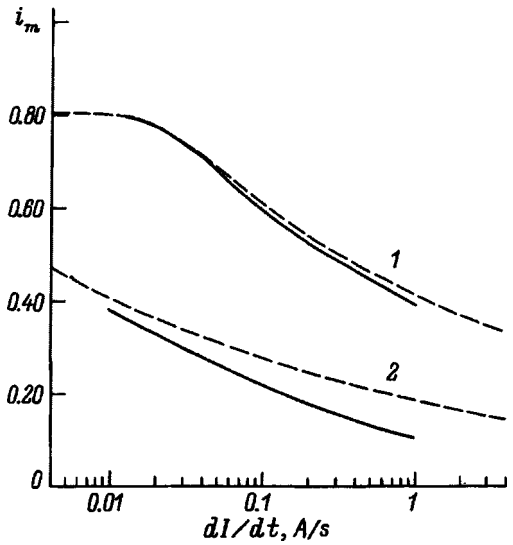

FIG. 3. Dependence of the dimensionless critical current induced in a solitary superconducting composite ($h=1000$ W/m^2·K) on the current induction rate for various values of the conductor radius. ϕ, mm: *1*—1, *2*—10.

They graphically demonstrate the satisfactory agreement of both models. However, it should be noted that the accuracy of the determination of I_m in the ''simplified'' model can be improved by refining the formula written down above for calculating $T_{\max,k}$. However, this requires additional calculations, which we intend to perform later on. At the same time, since the ''simplified'' model contains characteristic physical features that describe the appearance of instability in a superconducting composite, it can be employed with acceptable accuracy as an initial approximation for estimating the stability of the superconducting state of multiconductor structures [otherwise, as we have already noted, the solution of the complete system of equations (1) and (2) is required].

Figure 4 presents the results of a calculation of the permissible currents $i_m = I_m/(N\eta_k S_k J_C(T_0))$, which can be induced in a superconducting cable with maintenance of the superconducting state by all of its components. The cable consists of six conductors symmetrically arranged relative to one another around a common center.[8] According to Ref. 8, the original parameters of the conductors were assigned the values

$$l = 20 \text{ m}, \quad a = 7.6\times 10^{-5} \text{ m}, \quad \eta_k = 0.256,$$

$$h_k = 1000\ \frac{\text{W}}{\text{m}^2\text{K}},$$

$$\rho_m = 1.4\times 10^{-7}\ \Omega\cdot\text{m}, \quad \rho_s = 4.5\times 10^{-7}\ \Omega\cdot\text{m},$$

$$T_{CB} = 9.2 \text{ K}, \quad T_0 = 4.2 \text{ K},$$

$$c_k = \eta_k c_s + (1-\eta_k)c_m,$$

$$c_s = 50.55T^3 + 69.88T\left[\frac{\text{J}}{\text{m}^3\text{K}}\right],$$

$$c_m = \begin{cases} 85.5T^{1.78}, & 4 < T \leqslant 5 \text{ K} \\ 30.5T^{2.42}, & 5 < T \leqslant 10 \text{ K} \end{cases}\left(\left[\frac{\text{J}}{\text{m}^3\text{K}}\right]\right), \tag{8}$$

and the critical properties of the superconductor immersed in the assigned external magnetic field $B_e = 1$ T were described by the relations

$$J_C(T) = \frac{\alpha B_{C2}^3(T)}{\sqrt{B_e}}\left[1 - \frac{B_e}{B_{C2}(T)}\right],$$

$$B_{C2}(T) = B_C\left[1 - \left(\frac{T}{T_{CB}}\right)^2\right],$$

$$B_C = 12.63T, \quad \alpha = 10.76\times 10^8\ \frac{\text{A}}{\text{m}^2\cdot\text{T}^3}.$$

In addition, it was assumed that the current–voltage characteristics of the individual conductors can differ from one another because of possible imperfections in their fabrication process. It was also assumed with no loss of generality that the spread of the values of δ_k does not exceed 10% and that the nonlinearity parameters of the current–voltage characteristic of the cable components take the minimum value for $k = 1$ and the maximum value for $k = 2$.

Dimensionless plots of the dependence of the permissible currents on the current induction rate have been constructed in Fig. 4a in the range of variation of dI/dt corresponding to the strongest influence of the nonlinearity parameter of the current–voltage characteristic. Curve *1* corresponds to the currents which can be induced in a solitary conductor with the nonlinearity parameter $\delta = 0.01$. For the starting parameters given, the collapse current in the limiting case of $dI/dt \to 0$ equals 147 A. In the experiment in Ref. 8

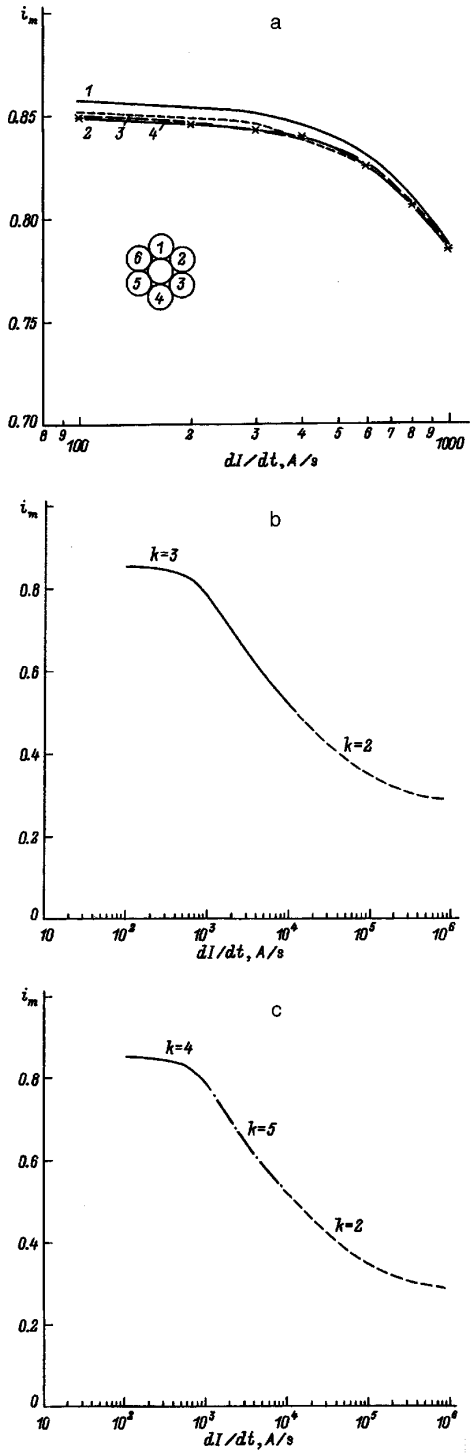

FIG. 4. Dependence of the dimensionless permissible currents induced in a six-strand superconducting cable having a spread of nonlinearity parameters of the current–voltage characteristics on the current induction rate for various types of inductive coupling between the conductors.

the corresponding value was 144 A. Because of the symmetric arrangement of the conductors in the cable, the same curve corresponds to the dependence of $i_m(dI/dt)$ for a six-strand cable provided the nonlinearity parameters of all the conductors are identical ($\delta_k=0.01$). Curve *2* was calculated for a composite in which there is no inductive coupling between the conductors, whose nonlinearity parameters differ from one another:

$$\delta_1=0.010,\quad \delta_2=0.011,\quad \delta_3=0.0109,$$
$$\delta_4=0.0108,\quad \delta_5=0.0107,\quad \delta_6=0.0106. \tag{9}$$

In this case the presence of conductors with different values of δ_k in the cable can not only lower the value of i_m, but can also alter the site in the cable where the instability is initiated as the current induction rate is increased. For example, at small current induction rates (when $dI/dt<350$ A/s for the parameters given) the transition to the normal state begins in the conductor with the largest value of δ_k ($k=2$). At large values of dI/dt the collapse of current induction is a consequence of the destruction of the superconducting properties of the conductor with the smallest nonlinearity parameter ($k=1$). These features are dictated by the following circumstances. At relatively ''small'' values of the current induction rate instability develops after the transverse section of the conductor is completely filled by the current. Therefore, in these cases the conductor having the highest instability parameter passes into the normal state first, since it is filled most quickly by the current. As dI/dt increases, the redistribution of the current in the circuit formed by the electrical resistances of each conductor should be taken into account. In this case the smaller is δ_k, the smaller is the corresponding value of $R_k(dI_k/dt,T_k)$ owing to the smaller spreading of the current profile within the conductor. Consequently, the time-dependent values of the current and, thus, of the temperature are higher in the conductor with the smallest value of δ_k than in the other conductors. Therefore, instability appears because of the great excessive heating in the conductor with the smallest value of δ_k.

It follows from the foregoing that consideration of the inductance matrix of a real multiconductor cable can alter the calculated values of the critical currents. The corresponding dependences of the permissible currents for inductively coupled conductors with different nonlinearity parameters are plotted in Fig. 4a. The parameters for curve *3* were described by the relations (9), the values for curve *4* were set equal to

$$\delta_1=0.010,\quad \delta_2=0.011,\quad \delta_3=0.0101,$$
$$\delta_4=0.0108,\quad \delta_5=0.0107,\quad \delta_6=0.0106, \tag{10}$$

and the inductance matrix was calculated using the formulas presented in Ref. 8.

The calculations performed show that the collapse of current induction can begin in any of the components of a multiconductor cable, since in this case the variation of the temperature of each conductor depends on the corresponding redistribution of the current in the $R=\{M_{k,j}\}$ circuit formed by all the cable components. As a consequence of this flow of current, situations are possible in which only the position of the conductor in the cable in which its transition to the normal state is initiated varies in an irregular manner as only the current induction rate is increased. For example, for a cable with the nonlinearity parameters (9) instability is initiated in the $k=3$ conductor in the range of variation of the current induction rate up to 10^4 A/s. As dI/dt is increased further (Fig. 4b), the transition to the normal state begins in the $k=2$ conductor. At the same time, for a composite with the nonlinearity parameters (10) there is a different sequence of numbers of the conductors in which instability is initiated (Fig. 4c). In this case the initial segment of the $i_m(Dt/dt)$ curve is dictated by its appearance in the $k=4$ conductor, then the onset of the collapse of current induction occurs in the $k=5$ conductor, and at large current induction rates it takes place in the $k=2$ conductor.

Thus, a ''simplified'' model has been proposed for calculating the time-dependent distribution of the temperature and the current in a superconducting multiconductor cable with an arbitrary number of components. This model permits taking into account the diversity of the designs of superconducting cables. The analysis of the stability of the superconducting state of a six-strand cable with conductors arranged symmetrically relative to a common center have been analyzed on its basis. The permissible currents which can be induced in a cable at an assigned rate without destroying the superconducting properties of all of its components have been determined for this design. The calculation performed with consideration of the inductive coupling between the conductors and different nonlinearity parameters of the current–voltage characteristics for each conductor demonstrates the existence of an irregular sequence of the conductors which initiate the possible transition of a cable to the normal state.

This work was performed with the support of the Russian Fund for Fundamental Research (Project No 95-02-03527a).

[1] H. Brechna, *Superconducting Magnet Systems*, Springer-Verlag, Berlin (1973); Mir, Moscow (1976).
[2] V. A. Al'tov, V. B. Zenkevich, M. G. Kremlev, and V. V. Sychev, *Stabilization of Superconducting Magnetic Systems*, Plenum Press, New York (1977) [cited Russian original: Energoatomizdat, Moscow (1984)].
[3] M. N. Wilson, *Superconducting Magnets*, Oxford University Press, London (1983); Mir, Moscow (1985).
[4] A. V. Gurevich, R. G. Mints, and A. L. Rakhmanov, *The Physics of Composite Superconductors*, CRC Press, Boca Raton, Fla. (1995).
[5] R. I. Schermer and B. P. Turck, Adv. Cryog. Eng. **26**, 599 (1980).
[6] G. Ries, Cryogenics **20**, 513 (1980).
[7] G. Reiter, Cryogenics **22**, 451 (1982).
[8] M. Iwakuma, H. Kanetaka, K. Tasaki, K. Funaki, M. Takeo, and K. Yamafuji, Cryogenics **30**, 686 (1990).
[9] N. Amemiya, I. Hlasnik, and O. Tsukamoto, Cryogenics **33**, 889 (1993).
[10] T. Shimada, Y. Takada, K. Okazaki, M. Tsuda, and A. Ishiyama, Cryogenics **34**, 555 (1995).
[11] L. Krempasky and C. Schmidt, Appl. Phys. Lett. **66**, 1545 (1995).
[12] T. Verhaege, P. Estop, J. P. Tavergnier *et al.*, IEEE Trans. Magn. **MAG-30**, 1911 (1994).
[13] G. L. Dorofejev, A. B. Imenitov, and E. Yu. Klimenko, Cryogenics **20**, 307 (1980).
[14] V. E. Keilin and V. R. Romanovskii, Cryogenics **33**, 986 (1993).
[15] E. Yu. Klimenko, N. N. Martovetskiĭ, and S. I. Novikov, Dokl. Akad. Nauk SSSR **261**, 1350 (1981) [Sov. Phys. Dokl. **26**, 1180 (1981)].

Translated by P. Shelnitz

Influence of local nonequilibrium on the rapid solidification of binary alloys

S. L. Sobolev

Institute of Chemical Physics, Russian Academy of Sciences, 142432 Chernogolovka, Moscow District, Russia

(Submitted April 22, 1996)
Zh. Tekh. Fiz. **68**, 45–52 (March 1998)

A local-nonequilibrium model of the diffusion of a solute during the rapid solidification of a binary alloy is considered. The model has two characteristic parameters: the diffusion velocity through the interface V_{Di} and the diffusion velocity in the bulk of the liquid phase V_D. The influence of local nonequilibrium on the separation of an impurity, the stability of the interface, and the dependence of the temperature of the interface on the velocity of the solidification front is investigated. A comparison with experiment is made. © *1998 American Institute of Physics.* [S1063-7842(98)00703-X]

INTRODUCTION

Special interest has recently been aroused by the rapid solidification of binary alloys initiated by deep undercooling of the phase-transformation surface.[1–18] Such undercooling can be achieved in the solidification of a melt obtained as a result of the pulsed action of a high-intensity energy source (for example, laser radiation) on the surface of a solid or as a result of deep undercooling of an initial melt. Under such conditions the solidification process takes place with a large deviation from local equilibrium, which influences the shaping of the micro- and macrostructure of the solid phase, its physicochemical properties, and the distribution of impurities and possible defects.

The existing theories regarding the solidification of binary alloys (see Refs. 1 and 2 and the references therein) take into account only the deviation from thermodynamic equilibrium at the interface by introducing the impurity partition coefficient K, which depends on the interface velocity V. However, it is then assumed that local thermodynamic equilibrium exists in the bulk of both phases and that the heat- and mass-transport processes in them can be described by classical local-equilibrium transport equations of the parabolic type. Such an approximation is valid only for relatively low interface velocities $V \ll V^*$, where V^* is a characteristic velocity, whose physical meaning will be discussed below. In the opposite case, i.e., when $V \sim V^*$, the state of the system exhibits an appreciable deviation from local equilibrium, which can have a significant influence on the heat- and mass-transport processes near the interface.[12,19,20]

The main parameter which describes the relaxation of a system to local equilibrium is the characteristic time τ needed for the system to pass from a local-nonequilibrium state to a local-equilibrium state, i.e., the relaxation time. For simple systems, such as mixtures of ideal gases, the characteristic time for diffusion-controlled relaxation τ_D, i.e., the time for the establishment of the local-equilibrium values of the concentration of the diffusing component, coincides with the characteristic thermal relaxation time τ_T, i.e., the time for the establishment of the local-equilibrium temperature values. However, in systems with a more complicated structure,[19] particularly in melts of metals,[11,12] $\tau_D \gg \tau_T$ In such systems thermal equilibrium is established first, and only then is diffusional equilibrium established. Each of these stages of the establishment of local equilibrium has its own characteristic speed V^*: the diffusion velocity $V_D = (D/\tau_D)^{1/2}$ and the thermal-wave speed $V_T = (a/\tau_T)^{1/2}$, where D is the diffusion coefficient and a is the thermal diffusivity. For melts $V_D \sim 1-10$ m/s, and $V_T \sim 10^3-10^4$ m/s, i.e., $V_D \ll V_T$ (V_T is of the order of the velocity of sound in a liquid phase). Thus, over the fairly broad range of variation of the velocity of the solidification front $V = 1-100$ m/s, which is of practical interest,[1–10] a phase-transformation process takes place with local-nonequilibrium diffusion of the solute in the liquid phase ($V \sim V_D$) and local-equilibrium heat transfer ($V \ll V_T$). The main purpose of the present work is to further develop the local-nonequilibrium model of the solidification of binary alloys,[12] which is based on the general theory of traveling waves under local-nonequilibrium conditions.[19,20]

1. THE MODEL

According to extended irreversible thermodynamics,[21–23] under local-nonequilibrium conditions the diffusion flux $\mathbf{J}$ obeys the Maxwell–Cattaneo law

$$\mathbf{J} + \tau_D \frac{\partial \mathbf{J}}{\partial t} = -D \nabla C, \tag{1}$$

where τ_D is the time for the relaxation of $\mathbf{J}$ to its local-equilibrium value, D is the diffusion coefficient in the liquid phase, and C is the concentration of the solute.

The local-nonequilibrium Maxwell–Cattaneo law (1) is distinguished from the classical local-equilibrium Fick's law by the presence of an additional term on the left-hand side of (1), which takes into account the relaxation of the diffusion field to local equilibrium. Taking into account the mass conservation law, we find that Eq. (1) leads to a diffusion equation of the hyperbolic type

$$\frac{\partial C}{\partial t}+\tau_D\frac{\partial^2 C}{\partial t^2}=D\nabla^2 C. \quad (2)$$

The characteristics $X\pm V_D t=\text{const}$ of the hyperbolic equation (2), which describes the local-nonequilibrium diffusion of the solute, indicate that the strong discontinuity appearing in the medium as a result of the concentration jump, propagates with a finite speed V_D. In other words, V_D can be regarded as the propagation rate of diffusive perturbations or the maximum mass-transport speed.

The boundary condition which expresses the mass conservation law at the interface has the form[12]

$$(V+\tau_D\dot{V})(C_l-C_S)+\tau_D V\left(\frac{\partial C_l}{\partial t}-\frac{\partial C_S}{\partial t}\right)=-D\nabla C, \quad (3)$$

where C_l and C_S are the concentrations of the impurity at the interface in the liquid and solid phases, respectively, and $\dot{V}$ is the acceleration of the interface.

It is noteworthy that the local-nonequilibrium boundary condition (3) differs significantly from the classical boundary condition. First, it contains not only the values of C_l and C_S at the interface, but also their derivatives with respect to time. Second, (3) contains the acceleration of the interface $\dot{V}$ along with its velocity. The presence of these additional terms is stipulated by the relaxation of the mass flux **J** [see Eq. (1)].

Thus, the local-nonequilibrium diffusion of the solute in the liquid phase observed at high interface velocities $V\sim V_D$ (or in the initial stages of a solidification process at $t\sim\tau_D$), is described by the hyperbolic mass-transport equation (2) with the boundary condition (3). When $V\ll V_D$ (or $t\gg\tau_D$), the system of equations (2) and (3) reduces to the classical local-equilibrium diffusion equation of the parabolic type with the corresponding boundary condition.

2. STATIONARY REGIME

In the stationary regime, i.e., when $V=\text{const}$, Eqs. (2) and (3) take the following form:

$$D(1-V^2/V_D^2)\frac{d^2C}{dX^2}+V\frac{dC}{dX}=0, \quad (4)$$

$$V(C_l-C_S)=-D(1-V^2/V_D^2)\frac{dC}{dX}. \quad (5)$$

The solution of Eq. (4) with consideration of (5) gives the distribution of the impurity concentration $C(X)$ in the liquid phase at $X>0$

$$C(X)=\begin{cases}(C_l-C_S)\exp[-VX/D(1-V^2/V_D^2)]+C_\infty; & V<V_D,\\ C_\infty; & V>V_D,\end{cases} \quad (6)$$

where C_∞ is the initial $(X\to\infty)$ concentration and C_l is the concentration of the impurity in the liquid phase at the interface $(X=0)$.

The concentration distribution (6) corresponds to the characteristic depth d of the diffusion layer:

$$d=\begin{cases}D(1-V^2/V_D^2)/V; & V<V_D,\\ 0; & V>V_D.\end{cases} \quad (7)$$

It follows from (6) and (7) that V_D is the decisive parameter, on which the character of the diffusion of the solute in the liquid phase depends. In the local-equilibrium limit, where $V\ll V_D$, concentration distribution (6) coincides with the classical distribution and does not depend on V_D. As V increases, the depth of the diffusion layer d varies with a rate considerably higher than the one predicted by the classical theory [see (7)]. When V passes through the critical point $V=V_D$, a qualitative change in the character of the diffusion process takes place. At this point the diffusion layer vanishes, and at $V\geqslant V_D$ the concentration of the impurity in the liquid phase is identically equal to the initial concentration $C(X)=C_\infty$, i.e., when $V\geqslant V_D$, there is no diffusion in front of the solidification front. This phenomenon is fully understood from the physical standpoint: perturbations from a source (the phase boundary in our case) which moves in the medium with a velocity exceeding the maximum possible propagation rate of the perturbations cannot propagate in its direction of motion (there is an analogous phenomenon in hydrodynamics, viz., ultrasound). Thus, the local-nonequilibrium model predicts qualitative modification of the mechanism of the solidification of a binary alloy when $V=V_D$. While at $V<V_D$ the solidification mechanism and its principal laws are determined mainly by diffusion of the solute, at $V>V_D$ diffusion is absent, and consequently the solidification process is controlled only by the thermal effects. Such a transition from a diffusion mechanism of solidification to a thermal mechanism as the interface velocity increases was observed in the experiments in Refs. 1, 3–5, 7, and 8. Moreover, in cases where it was possible to evaluate V_D the change in the solidification mechanism was observed specifically at $V=V_D$.[1,3–5]

The form of the local-nonequilibrium model for the stationary regimes (4) and (5) and the behavior of its solution (6) permit the introduction of an effective diffusion coefficient D^* (Ref. 12)

$$D^*=\begin{cases}D(1-V^2/V_D^2); & V<V_D,\\ 0; & V>V_D.\end{cases} \quad (8)$$

The effective diffusion coefficient (8) takes into account the decrease in the impurity concentration gradient in the liquid phase caused by the deviation from local equilibrium, which is proportional to the ratio V/V_D. Using (8), we can expand the range of applicability of several classical results of the local-equilibrium theory of binary alloys by replacing D by D^*.

3. PARTITION COEFFICIENT OF THE IMPURITY

In the local-equilibrium approximation the partition coefficient of the impurity, which is equal to the ratio between its concentration in the liquid and solid phases at the interface, has the form[6]

$$K(V)=(K_E+V/V_{Di})/(1+V/V_{Di}), \quad (9)$$

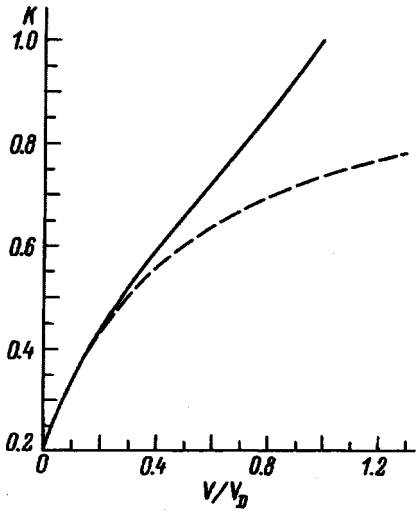

FIG. 1. Dependence of the partition coefficient of the impurity on the dimensionless solidification front velocity V/V_D. Solid curve—local-nonequilibrium model (10), dashed line—local-equilibrium model (9).

where K_E is the equilibrium partition coefficient, and V_{Di} is a characteristic speed, which is equal to the ratio of the diffusion coefficient of the impurity through the interface D_i to the interatomic distance λ.

It should be stressed that D_i is the mean value of the diffusion coefficient of the impurity through the interface, which can be regarded in the general case as a two-phase zone containing both a liquid phase and a solid phase. Therefore, the value of D_i should be somewhere between the diffusion coefficient in the liquid phase D and the diffusion coefficient in the solid phase $D_S \approx 0$, i.e., $D_i < D$. Molecular-dynamics calculations show that D_i can be 5–10 times smaller than D.[16] Taking into account that $\tau_D = \lambda/V_D$, we obtain

$$V_D = D/\lambda.$$

Thus, the diffusion velocity V_D, which is the propagation rate of the diffusive perturbations in the bulk of the liquid phase, can be 5–10 times greater than V_{Di}, which is the mean diffusion velocity through the two-phase zone separating the liquid and solid phases. For a narrow phase-transformation zone of the order of one atomic layer it is natural to assume that $V_{Di} = (V_D + V_S)/2$ and $D_i = (D + D_S)/2$, where V_S and D_S are the diffusion velocity and the diffusion coefficient in the solid phase. Since $V_S \approx 0$ and $D_S \approx 0$, we have $V_{Di} \approx V_D/2$ and $D_i \approx D/2$. In the case of a diffuse interface, where the phase transition takes place over a distance of several atomic layers, the values of V_{Di} and D_i are even smaller.

Substituting the effective diffusion coefficient (8) into (9), we obtain the local-nonequilibrium partition coefficient K^*, which depends on both V_D and V_{Di},

$$K^* = \begin{cases} \dfrac{K_E(1 - V^2/V_D^2) + V/V_{Di}}{1 - V^2/V_D^2 + V/V_{Di}}; & V < V_D, \\ 1; & V > V_D. \end{cases} \tag{10}$$

Figure 1 presents K [Eq. (9)] and K^* [Eq. (10)] as functions of the dimensionless velocity V/V_D for $V_{Di} = V_D/2$. At the relatively low velocities $V \sim V_{Di} < V_D$, where the local-nonequilibrium effects of the diffusion of the impurity in the liquid phase can be neglected, K and K^* practically coincide, and the rate-limiting step in the process of the separation of the impurity is its diffusion through the interface with the characteristic speed V_{Di} [see Eq. (9)]. When $V \sim V_D$, the local-nonequilibrium effects lead to a significant decrease in the effective diffusion coefficient (8). In this case the rate-limiting step in the separation of the impurity is its diffusion in the liquid phase, and K^* differs appreciably from K. When $V \geqslant V_D$, K^* does not depend on V and is identically equal to unity, while K increases monotonically to $K = 1$ as $V \to \infty$. Thus, the local-nonequilibrium model, which describes the diffusion of a solute with consideration of the relaxation of the diffusion flux, predicts a transition to diffusionless ($D^* = 0$) and separationless ($K^* = 1$) solidification for $V \geqslant V_D$. It should be noted that the result $K^* = 1$ for $V \geqslant V_D$ does not depend on the mechanism of separation of the impurity at the interface, since it is determined by purely diffusional effects. Therefore, it is also maintained in other models of the separation of an impurity differing from (9). Any other mechanism which influences the distribution of the impurity in the liquid phase and is not taken into account in the present work, for example, thermal diffusion, can lead to the variation of K at $V \sim V_D$. An investigation of the influence of thermal diffusion on the partition coefficient of the impurity upon the solidification of binary alloys is planned for subsequent studies.

4. STABILITY OF THE PHASE BOUNDARY

According to the classical theory of stability,[13] the destabilizing influence of the diffusion of an impurity at an interface is compensated by the surface energy, and the absolute stability criterion has the form

$$C_0 = \frac{K T_m \Gamma V_a}{m D (1 - K)}, \tag{11}$$

where C_0 is the critical concentration of the solute, T_m is the melting point of the pure substance, m is the slope of the liquidus line, Γ is the Gibbs-Thomson coefficient, and V_a is the velocity at which absolute stability of a planar solidification front is achieved.

The stability criterion (11) was originally obtained for the equilibrium values of m and K. However, it was found that this criterion is also valid when equilibrium does not exist at the interface and K and m depend on V.[14,15] This makes it possible to assume that the criterion (11) is also valid under local-nonequilibrium conditions, as long as the local-equilibrium values $K(V)$ and D are replaced by the local-nonequilibrium analogs $K^*(V)$ and $D^*(V)$. For simplicity, we assume that m does not depend on V, since $m(V)$ is a weak function V in comparison to $K^*(V)$ and $D^*(V)$. Figure 2 presents plots of the dependence of C_0 on V_a, which were calculated from Eq. (11) in the local-equilibrium case with $K(V)$ [Eq. (9)] and $D = \text{const}$ and in the local-nonequilibrium case with $K^*(V)$ [Eq. (10)] and $D^*(V)$ [Eq. (8)] for Si–Sn alloys.[15] As expected, these curves differ sig-

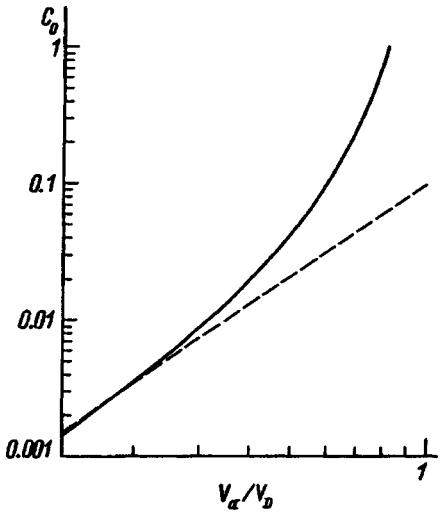

FIG. 2. Dependence of the critical concentration C_0 on the dimensionless velocity corresponding to absolute stability V_a/V_D [Eq. (11)]. $K^*(V)$, $D^*(V)$—solid curve; $K(V)$, $D=\text{const}$—dashed curve.

nificantly at $V\sim V_D$. In fact, the local-nonequilibrium effects at $V\sim V_D$ lead to an appreciable decrease in the effective diffusion coefficient $D^*(V)$, which weakens the destabilizing influence of diffusion. Therefore, equilibrium with a stabilizing influence of the surface energy is achieved at velocities of the solidification front that are considerably smaller than those predicted by the classical theory, and, therefore, $V_a<V_a'$ at the same value of C_0, where V_a' is the local-equilibrium value of the velocity corresponding to absolute stability (Fig. 2). In addition, if $V\to V_D$, then $D^*(V)\to 0$ and $C_0\to\infty$. This means that the stability of a planar solidification front is always achieved when $V_a<V_D$. It follows from (11) that $V_a=V_a'(1-V_a^2/V_D^2)$, whence it is not difficult to obtain the following estimate for V_a

$$V_a=V_a'(1-(V_a'/2V_D)^2).$$

Thus, the local-nonequilibrium effects have a stabilizing influence on the solidification front of a binary alloy and impose a fundamental restriction on the value of V_a, which is always less than V_D. The criterion (11) and all the ensuing arguments are valid in the case of directed solidification. When undercooled melts solidify, a transition occurs at $V=V_D$ to purely thermal regimes of dendritic growth, for which V_a is of the order of the speed of sound.[1]

5. TEMPERATURE OF A PLANAR INTERFACE

When a planar interface propagates in a binary alloy, its temperature T_i has the following form:[2]

$$T_i=T_S+\left(\frac{m(V)}{K(V)}-\frac{m}{K_E}\right)C_\infty-V/\mu, \tag{12}$$

where T_S is the equilibrium solidus temperature, m is the equilibrium slope of the liquidus line, $m(V)$ is the slope of the liquidus line under nonequilibrium conditions, and μ is a kinetic coefficient.

The effective slope of the liquidus line is determined by the degree of separation of the impurity[2]

$$m(V)=m\left(\frac{1-K(V)+K(V)\ln(K(V)/K_E)}{1-K_E}\right). \tag{13}$$

Under equilibrium conditions $T_i=T_S$; however, when there is a deviation from equilibrium, i.e., when V increases, T_i increases because of the increase in the effective solidus temperature T_S^*, which is equal to the sum of the first two terms on the right-hand side of (12). If $V=V_D$, T_S^* reaches its maximum value $T_{S\,\max}^*$:

$$T_{S\,\max}^*=T_S+\left(\frac{K_E-1-K_E\ln K_E}{K_E(1-K_E)}\right)mC_\infty. \tag{14}$$

When $V>V_D$, the effective slope of the liquidus line (13) does not vary further, and $T_S^*\equiv T_{S\,\max}^*$. In this case the liquidus and solidus lines coincide, and the interface temperature, according to thermodynamic conceptions, is determined by the equality between the free energies of the liquid and solid phases at the same value of $C(T_0)$, i.e., when $V\geqslant V_D$, $T_{S\,\max}^*=T_0$. We note that the real interface temperature T_i is smaller than T_0 by the value of the kinetic correction V/μ [see Eq. (12)].

If $V\geqslant V_D$, it follows from (12)–(14) that

$$T_i=T_{S\,\max}^*-V/\mu. \tag{15}$$

Thus, at the point of the transition from a diffusive solidification regime to a thermal regime, i.e, at $V=V_D$, a change in the form of $T_i(V)$ also occurs. While at $V<V_D$ the interface temperature T_i increases as a result of the increase in the effective solidus temperature T_S^*, at $V>V_D$ it decreases linearly with V owing to the kinetic undercooling [the last term in (12) and (15)].

6. TEMPERATURE OF THE INTERFACE IN THE CASE OF DENDRITIC GROWTH

According to the theory of dendritic growth,[2] the undercooling of the interface $\Delta T(V)$ has the form

$$\Delta T(V)=\Delta T_t(V)+\Delta T_S(V)+\Delta T_R(V)+\Delta T_K(V)+\Delta T_{ne}(V),$$

where ΔT_t, ΔT_S, and ΔT_K are the thermal, concentration (diffusive), and kinetic undercoolings, and ΔT_R is the undercooling associated with the curvature of the surface.

The last term

$$\Delta T_{ne}=[m-m(V)]C_\infty \tag{16}$$

appears as a consequence of the difference between the slopes m and $m(V)$ of the equilibrium and nonequilibrium liquidus lines, respectively. Replacing D in the expression for $\Delta T_S(V)$ by D^*, we obtain the local-nonequilibrium diffusive undercooling $\Delta T_S^*(V)$

$$\Delta T_S^*=m(V)C_\infty\left[1-\frac{1}{1-(1-K^*(V))\mathrm{I_v}(P_C^*)}\right], \tag{17}$$

where $\mathrm{I_v}$ is an Ivantsov function expressed in terms of the local-nonequilibrium Peclet number $P_C^*=VR/2D^*$, where R is the radius of a dendrite.

If $V \to V_D$, then $D^* \to 0$, $K^* \to 1$, $P_C^* \to \infty$, and $I_v \to 1$. This means that the diffusive undercooling $\Delta T_S^* \equiv 0$ at $V \geqslant V_D$ [see (17)]. In this case ΔT_{ne} achieves its maximum value

$$\Delta T_{ne}^{\max} = mC_\infty \left(\frac{1 - K_E + \ln K_E}{1 - K_E} \right) \tag{18}$$

and remains constant, i.e., $\Delta T_{ne} = \Delta T_{ne}^{\max}$, at $V > V_D$. Thus, just as in the case of a planar solidification front, the character of the $\Delta T(V)$ curve undergoes a qualitative change at $V = V_D$. At $V < V_D$ the dependence of ΔT on T is determined mainly by the diffusion terms ΔT_S^* and ΔT_{ne}, since they depend significantly on $K^*(V)$ and $m(V)$. If $V > V_D$, then $\Delta T_S^* = 0$ and $\Delta T_{ne} = \Delta T_{ne}^{\max} = \text{const}$. In this case the total undercooling does not depend on diffusion, and solidification takes place in a purely thermal regime with $D^* = 0$ and $K^* = 1$. At $V \geqslant V_D$ the total undercooling has the form

$$\Delta T(V) = \Delta T_t(V) + \Delta T_R(V) + \Delta T_K(V) + \Delta T_{ne}^{\max}. \tag{19}$$

The dendrite radius R can also be calculated by replacing D in the classical theory[2] by D^*. It should be expected that the value of R will increase sharply upon passage through the critical point $V = V_D$ and that it will be determined only by heat-conduction effects (there will be a ''thermal dendrite'') at $V > V_D$.

We note that the results obtained in the present section are based on the assumption that the shape of the dendrite and the functional dependences of $\Delta T(V)$ are maintained when there is a deviation from local equilibrium. Strictly speaking, the change in the character of the diffusion of the impurity at high interface propagation rates leads to distortion of the shape of the dendrite. Moreover, the value of $K(V)$ varies along the surface of the dendrite, since the normal velocity, which determines $K(V)$, decreases with increasing distance from the dendrite tip. Thus, the exact formulation of the problem of the shaping and propagation of a dendritic solidification surface of a binary alloy requires a combined solution of the local-nonequilibrium (hyperbolic) diffusion equation and the classical (parabolic) heat-conduction equation with consideration of the alteration of the boundary conditions on the interface because of the variable angle between the normal and the velocity vector.

7. DISCUSSION OF RESULTS AND COMPARISON WITH EXPERIMENT

The local-nonequilibrium model of the diffusion of a solute predicts that a change in the solidification mechanism of a binary alloy will occur at the critical point $V = V_D$ from a diffusive mechanism at $V < V_D$ to a purely thermal mechanism at $V > V_D$. This transition, as well as other manifestations of local nonequilibrium, can be described by the effective diffusion coefficient D^*, whose value depends on the degree of deviation from local equilibrium, which is proportional to the value of V/V_D. At the point $V = V_D$ separationless solidification with $K^* = 1$ is also achieved, and with consideration of a kinetic correction the temperature of the interface corresponds to T_0. The transition from a diffusive solidification mechanism to a thermal mechanism was observed in Ag–Cu (Ref. 7) and Ti–Ni (Ref. 8) alloys when the temperature of the interface dropped below T_0. In addition, such a transition was also observed during the solidification of Cu–Ni (Ref. 3) and Ni–B (Ref. 4) alloys, but here it was shown that the critical parameter evoking the sharp change in the solidification mechanism is the interface velocity, which is approximately equal to V_D, rather than the undercooling. Thus, the results of the experiments in Refs. 3–5, 7, and 8 are consistent with the predictions of the local-nonequilibrium model, which regards the diffusion velocity V_D as the critical parameter describing the transition to purely thermal solidification regimes with a zero effective diffusion coefficient (i.e., diffusionless solidification).

In addition, the local-nonequilibrium model predicts that separationless solidification with $K^* = 1$ is also achieved at $V = V_D$, rather than at $V \to \infty$, as would follow from the classical theory (9). This result is consistent with the experiments on the laser melting of Si with B, P, and As impurities in Ref. 18, where $K = 1$ was observed for $V = 2.7$–4.5 m/s. The molecular-dynamics calculations in Ref. 16 showed that $K = 1$ for a stationary interface velocity $V = 4$ m/s. Cook and Clancy also noted that this result, i.e., separationless solidification, cannot be explained within the existing theories that lead to expressions for K like (9).

In the general case the interface can be regarded as a two-phase zone consisting of both a solid phase and a liquid phase. Hence it follows that the mean values of the diffusion coefficient D_i and the diffusion velocity V_{Di} in this two-phase zone should satisfy the inequalities $D_S < D_i < D$ and $V_{DS} < V_{Di} < V_D$, where V_{DS} is the diffusion velocity in the solid phase. As we have already noted above in the case of a sharp phase boundary consisting of one atomic layer, it can be assumed that $D_i = (D + D_S)/2$ and $V_{Di} = (V_D + V_{DS})/2$. If this assumption is used to analyze a diffusive interface consisting of n atomic layers and it is also assumed that the diffusion coefficient D_k in the kth layer is equal to the arithmetic mean of the values of the diffusion coefficients in the neighboring $(k-1)$th and $(k+1)$th layers, i.e., $D_k = (D_{k+1} + D_{k-1})/2$, the mean value of the diffusion coefficient in the two-phase zone takes the form $D_i = g(n)D$, where g is a coefficient, whose values are listed in Table I. When $n > 6$, it can be assumed in an approximation that $g(n) = 1/n$. The mean diffusion velocity through the interface $V_{Di} = g(n)V_D$ can be obtained in a similar manner. Thus, V_{Di} can be represented in the form $V_{Di} = D_i/\lambda = D/L$, where $L = \lambda/g(n)$ is the effective width of the interfacial zone. An exact determination of the diffusion velocities in the liquid phase (V_D) and in the two-phase zone (V_{Di}) is needed to compare the theoretical value of K^* with the experimental data.

Figure 3 compares the calculation of the partition coefficient of the impurity as defined by formulas (9) and (10) with the results of the experiment on the laser melting of Ge–Si alloys in Ref. 10. At relatively low values of the solidification front velocity V the local-equilibrium model (9) faithfully describes the experimental results for $K_E = 0.4$ and $V_{Di} = 2$ m/s.[10] The local-nonequilibrium model (10) gives better agreement over the entire range of variation of V for the same values of K_E and V_{Di} and $V_D = 4.9$ m/s. This value practically coincides with the value $V_D = 5$ m/s, which

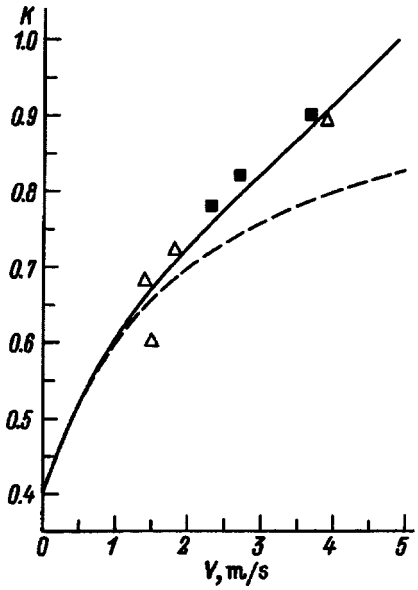

FIG. 3. Dependence of the partition coefficient of the impurity on the solidification front velocity V for Ge–Si alloys. △, ■—experiment in Ref. 10, solid and dashed curves—same as in Fig. 1.

was obtained in Ref. 17 by dividing the diffusion coefficient in the liquid phase by the interatomic distance. We stress that it is the diffusion velocity in the liquid, i.e, V_D, rather than the diffusion velocity at the interface V_{Di}.

Figure 4 presents plots of $K(V)$ and $K^*(V)$ together with experimental data obtained for the solidification of Si–As alloys.[9] The local-equilibrium model (9) gives the best agreement with experiment for $V_{Di}=0.46$ m/s.[9] However, in this case it predicts overestimated values of K at low V and underestimated values at high V (Fig. 4). The local-nonequilibrium model gives better agreement with experiment over the entire range of variation of V for $V_{Di}=0.75$ m/s and $V_D=2.6$ m/s.

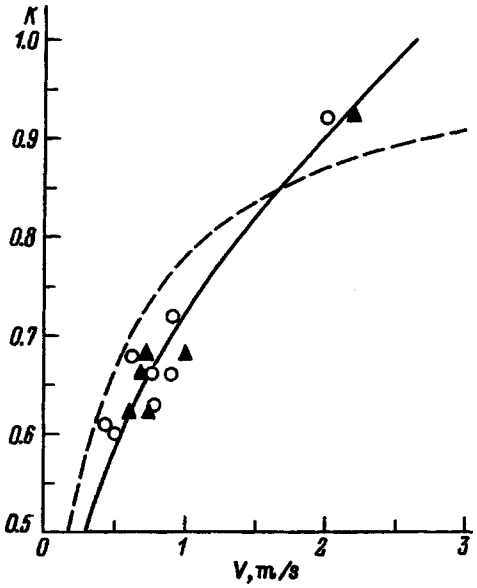

FIG. 4. Dependence of the partition coefficient of the impurity on the solidification front velocity V for Si–As alloys. ○, ▲—experiment in Ref. 9, solid and dashed curves—same as in Fig. 1.

TABLE I.

n	$g(n)$
1	0.5
2	0.37
3	0.33
4	0.29
5	0.26

We note that $V_{Di}/V_D=0.4$ for Ge–Si alloys and that $V_{Di}/V_D=0.28$ for Si–As alloys, i.e., $V_{Di}<V_D$. This is consistent with the conception of a two-phase zone having values of D_i and V_{Di} that are smaller than D and V_D, respectively. The relation between V_{Di} and V_D for Ge–Si alloys corresponds to a two-phase zone consisting of $n=2$ atomic layers (see Table I), which is close to the estimate $n=3$ obtained on the basis of molecular-dynamics calculations.[17]

Measurements of the $V(\Delta T)$ curves for Ag–Cu and Ti–Ni alloys revealed a sharp increase in the velocity of the solidification front V when the temperature of the interface corresponded to T_0.[7,8] To account for such behavior of the $V(\Delta T)$ curve, Walder and Ryder[7] introduced an additional term into the kinetic undercooling, which ensures the approach of the liquidus and solidus lines to the T_0 curve as $V\to\infty$. In Ref. 8 this additional term was modified using the effective diffusion coefficient (8), which depends on the velocity V of the solidification front,[12] to ensure better agreement between the theoretical plot of $V(\Delta T)$ and the experimental results.

We note that the empirical term in the kinetic undercooling introduced by Walder and Ryder[7,8] corresponds to ΔT_{ne} [Eq. (16)]. This undercooling, which takes into account the variation of the slope of the liquidus line with V, also ensures its fit with the T_0 curve as $V\to V_D$ (see also Sec. 5). Thus, the relations (12), (14), and (15) for a planar surface and (16)–(18) for dendritic growth can be used for a detailed calculation of the $V(\Delta T)$ curve with consideration of the local-nonequilibrium diffusion of the impurity, which is manifested by the appearance of a dependence of the effective diffusion coefficient (8) on the velocity of the solidification front V.

8. CONCLUSIONS

The characteristic rates of the solidification of binary alloys, viz., the diffusion velocity at the interface V_{Di}, the diffusion velocity in the bulk of the liquid phase V_D, and the thermal-wave speed V_T, permit the establishment of a hierarchical sequence of deviations of the state of the system from equilibrium, which corresponds to increases in the solidification front velocity V ($V_{Di}<V_D<V_T$).

1. $V=0$. Complete equilibrium.

2. $V<V_{Di}$. The system deviates from equilibrium as a whole, but there is local equilibrium both at the interface and in the bulk of each phase, i.e., $K=K_E=\text{const}$.

3. $V \sim V_{Di}$. There is a deviation from local equilibrium at the interface. The rate-limiting step in the separation of the impurity is its diffusion through the interface, and K depends on V with the characteristic parameter V_{Di} [see Eq. (9)].

4. $V \sim V_D$. The diffusion of the impurity in the liquid phase deviates from local equilibrium. The distribution of the impurity concentration obeys the local-nonequilibrium hyperbolic diffusion equation (2). In stationary solidification regimes the deviations from local equilibrium can be described by the effective diffusion coefficient D^*, which depends on the solidification front velocity V [see (8)]. The rate-limiting step in the separation of the impurity is its diffusion in the bulk of the liquid phase, and K^* depends on both V_{Di} and V_D. If $V \to V_D$, then $D^* \to 0$. This has a stabilizing effect on the interface, leading to a decrease in the limiting velocity corresponding to absolute stability V_a, which has an upper bound at V_D. The function $V(\Delta T)$ is specified by both diffusional and thermal effects.

5. $V > V_D$. In this case $D^* = 0$, and $K^* = 1$. These equalities signify a diffusionless solidification regime and the absence of separation of the impurity at the interface. Here the diffusive undercooling is equal to zero, and the effective liquidus and solidus lines coincide with the T_0 curve. The function $V(\Delta T)$ is specified only by thermal effects.

6. $V \sim V_T$. At such high solidification velocities both the diffusion process and heat conduction take place under local-nonequilibrium conditions. In this case the distribution of the temperature in the system is also described by an equation of the hyperbolic type.[19–22]

[1] D. M. Herlach, Mater. Sci. Eng. **R12**, 177 (1994).
[2] R. Trivedi and W. Kurz, Int. Mat. Rev. **39**, 49 (1994).
[3] R. Willnecker, D. M. Herlach, and B. Feuerbacher, Phys. Rev. Lett. **62**, 2707 (1989); Appl. Phys. Lett. **56**, 324 (1990).
[4] K. Eckler, R. F. Cochrane, D. M. Herlach, and B. Feuerbacher, Phys. Rev. B **45**, 5019 (1992).
[5] K. Eckler, D. M. Herlach, and M. J. Aziz, Acta Metall. Mater. **42**, 975 (1994).
[6] M. J. Aziz and T. Kaplan, Acta Metall. **36**, 2335 (1988).
[7] S. Walder and P. L. Ryder, J. Appl. Phys. **74**, 6100 (1993); Acta Metall. Mater. **43**, 4007 (1995).
[8] S. Walder, J. Appl. Phys. (accepted for publication).
[9] J. A. Kittl, M. J. Aziz, D. P. Brunco, and M. O. Thompson, J. Cryst. Growth **148**, 172 (1995).
[10] D. P. Brunco, M. O. Thompson, D. E. Hoglung *et al.*, J. Appl. Phys. **78**, 1575 (1995).
[11] P. K. Galenko, Zh. Tekh. Fiz. **65**(11), 110 (1995) [Tech. Phys. **40**, 1149 (1995)].
[12] S. L. Sobolev, Phys. Lett. A **199**, 383 (1995).
[13] W. W. Mullins and R. F. Sekerka, J. Appl. Phys. **35**, 444 (1964).
[14] G. J. Merchant and S. H. Davis, Acta Metall. Mater. **38**, 2683 (1990).
[15] D. E. Hoglund and M. J. Aziz, Mater. Res. Soc. Symp. Proc. **205**, 325 (1992).
[16] S. J. Cook and P. Clancy, J. Chem. Phys. **99**, 2175 (1993).
[17] Q. Yu and P. Clancy, J. Cryst. Growth **149**, 45 (1995).
[18] C. W. White, *Laser and Electron-Beam Interactions with Solids*, B. R. Appleton and G. K. Celler (eds.), North–Holland (1982), pp. 109–120.
[19] S. L. Sobolev, Usp. Fiz. Nauk **161**(3), 5 (1991) [Sov. Phys. Usp. **34**, 217 (1991)].
[20] S. L. Sobolev, Zh. Tekh. Fiz. **59**(10), 170 (1989) [Sov. Phys. Tech. Phys. **34**, 1196 (1989)]; Zh. Tekh. Fiz. **60**(3), 16 (1990) [Sov. Phys. Tech. Phys. **35**, 284 (1990)].
[21] D. Jou, J. Casas-Vazquez, and G. Lebon, Rep. Prog. Phys. **51**, 1105 (1988).
[22] R. E. Nettleton and S. L. Sobolev, J. Non-Equilib. Thermodyn. **20**, 205 (1995).
[23] D. Jou, J. Camacho, and M. Grmela, Macromolecules **24**, 3597 (1991).

Translated by P. Shelnitz

Semiconductor–metal phase transition under a strain induced by a spherical indenter

V. V. Kaminskiĭ

A. F. Ioffe Physicotechnical Institute, Russian Academy of Sciences, 194021 St. Petersburg, Russia

S. Lanyi

Institute of Physics, Slovak Academy of Sciences, 84228 Bratislava, Slovakia
(Submitted August 13, 1996)
Zh. Tekh. Fiz. **68**, 53–57 (March 1998)

A semiconductor–metal phase transition is produced in samarium monosulfide under the action of the pressure of a spherical indenter in the region of quasiuniaxial compression of the sample material under the indenter and investigated. It is shown that the phase transition occurs when the decrease in the volume of SmS under the action of the applied field reaches a critical value of 4–5% at $T=300$ K. The temperature dependence of the critical volume decrease is recorded in the range 280–440 K. © *1998 American Institute of Physics.* [S1063-7842(98)00803-4]

INTRODUCTION

Samarium monosulfide is known to undergo a first-order isostructural (NaCl–NaCl) semiconductor–metal phase transition when a sample is uniformly compressed and, in a subsurface layer, when its surface is polished.[1] A similar phase transition was discovered in $Sm_{1-x}Gd_xS$ and $Sm_{1-x}Y_xS$ solid solutions when samples were subjected to uniaxial compression;[2] however, the semiconductor phase was a very strongly degenerate semiconductor with a free-carrier concentration $n\sim10^{21}$ cm^{-3} in this case. Attempts to produce semiconductor–metal phase transitions by uniaxial compression in SmS of stoichiometric composition, which is a nondegenerate material with clearly expressed semiconductor properties ($n\sim10^{19}$ cm^{-3}), were unsuccessful, because the possibility of applying a sufficiently high pressure by uniaxial compression was restricted by the ultimate strength of SmS single crystals.[3] This effect has likewise not yet been produced in other semiconductors. The purpose of the present work was to attempt to produce a semiconductor–metal phase transition using deformation by uniaxial compression.

EXPERIMENT

An indenter with a spherically rounded tip (needle) was employed to create the system of strains corresponding to the strains which appear under uniaxial compression in a SmS single crystal. The strain distribution appearing in the bulk of a sample when a pressure is applied to its surface by such an indenter has a fairly complicated character. However, in a small part of the volume located under the center of the contact surface the strains can be described by fairly simple relations. These strains were calculated from the solution of the contact problem of the theory of elasticity for contact between two bodies under a load. Its results, which have bearing on the present case, were presented in Ref. 4.

The SmS single crystal measured $3\times4\times1$ and was cut along the {100}, {010}, and {001} cleavage planes. The force F was applied to a steel tip with a radius of curvature $R=36$ μm in a direction perpendicular to the sample surface. The tip makes contact with the sample on a surface which can be assumed in an approximation to be round with a radius

$$a=(RFD)^{1/3}, \tag{1}$$

and the maximum pressure is exerted at the center of this region and equals

$$P=\frac{3}{2}\frac{F^{1/3}}{\pi(RD)^{2/3}}. \tag{2}$$

Here

$$D=\frac{3}{4}\left(\frac{1-\sigma^2}{E}+\frac{1-\sigma'^2}{E'}\right)=0.945\times10^{-5}\ \text{MPa}^{-1}, \tag{3}$$

where σ and E are the Poisson's ratio and Young's modulus of SmS in the [100] crystallographic direction, which are equal to 0.085 and 1.2×10^5 MPa, respectively,[1)] and σ' and E' are the same parameters for steel.

If the coordinate axes are parallel to the axes of the crystal (Fig. 1), then, on the basis of Ref. 4, for $0\leqslant z\leqslant0.4a$ and $\sqrt{x^2+y^2}\leqslant0.2a$ we have

$$\varepsilon_{zz}=(0.65-0.85)P/E,\quad \varepsilon_{xx}=\varepsilon_{yy}\approx-0.1\varepsilon_{zz}. \tag{4}$$

It is significant that SmS has an extremely small value for σ (the usual values for other materials are ~0.3), which is close to the values of ε_{xx} and ε_{yy}. Thus, in the small volume indicated we have a strain distribution for SmS that corresponds approximately to uniaxial compression.

The phase transition was detected by capacitance spectroscopy, which permits monitoring of the relaxation of the capacitance under the contact area.[6] It provides information on the space charge in the portion of the sample located directly under its contact surface with the indenter, i.e., in the region where SmS undergoes quasiuniaxial deformation. The experiments were initially performed on the metal-insulator-

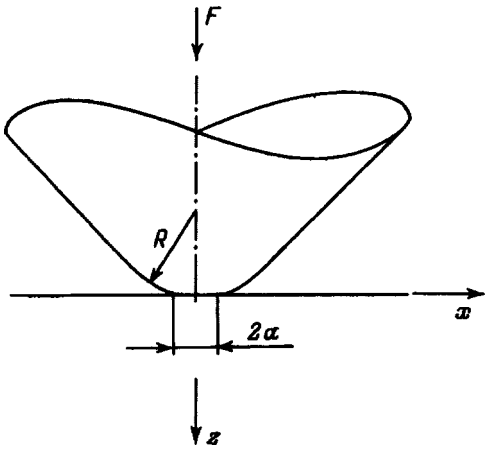

FIG. 1. Pressure of the spherical indenter on a SmS single crystal. The x, y, and z axes are parallel to the [001], [010], and [100] crystallographic directions.

semiconductor structures that we employed in Ref. 6. The pressure of the tip was applied to an aluminum contact pad with an area of 0.34 mm^2, which was separated from the SmS surface by a layer of Al_2O_3 or a polyimide. Subsequently, the indenter was pressed directly against an insulating layer of Al_2O_3 with a thickness of 50–100 nm. Spectra of the variation of the capacitance were recorded in the temperature range from 77 to 440 K at various fixed values of F. The phase transition was manifested as a sharp peak or abrupt variation in the spectrum.[6] It was discovered during the experiments that a contact of SmS with iron has adequate blocking properties for ensuring the possibility of performing measurements without an insulating layer (Fig. 2), whose presence decreases the capacitance and, accordingly, leads to a decrease in the sensitivity of the method.

In the measurements with an insulating layer, a bias voltage from -0.5 to -1 V and exciting rectangular pulses with a height of 0.4 V were supplied to the input (the aluminum contact pad or the indenter). In the measurements on a metal–semiconductor contact the bias was -0.3 or -0.4 V, and the pulse height was 0.3 V. The pulse duration ranged

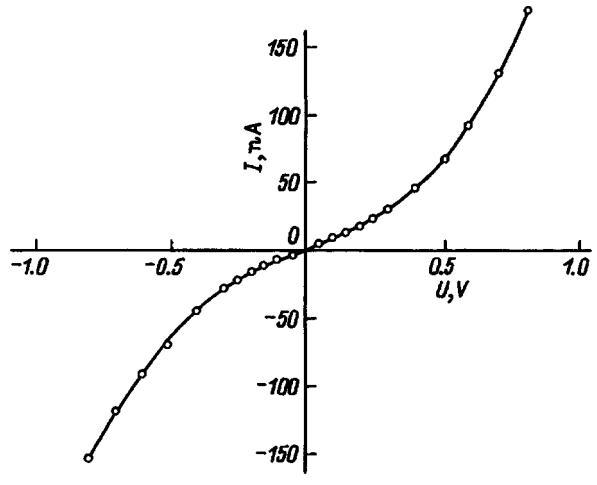

FIG. 2. Current–voltage characteristic of the contact formed by the steel indenter with the surface of a SmS single crystal.

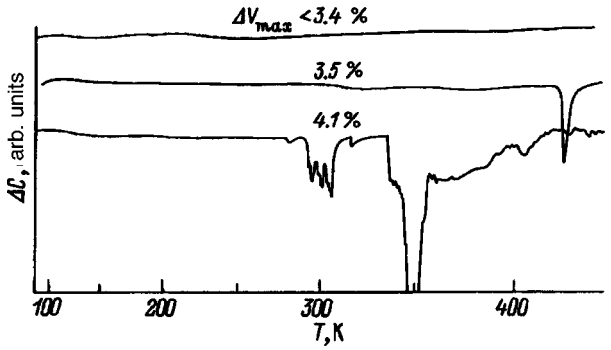

FIG. 3. Temperature spectrum of the variation of the capacitance under the indenter, $\Delta C = C(t_1) - C(t_2)$. The values of ΔV_{max} correspond to the fixed load values $F = 0.23$, 0.25, and 0.40 N.

from 2 to 10 μs. The output signal from the capacitance analyzer was used to record the temperature spectrum of ΔC, which is the difference between two quantities: the signal proportional to the capacitance (C) at the time t_1, which is measured 1–10 μs after the exciting pulse ends, and the signal at the time t_2, which is 4–10 μs later than t_1. In the measurements without an insulating layer it was found that as a result of the transition of SmS from the semiconductor phase to the metallic phase, the initially blocking iron–SmS contact becomes an Ohmic contact (an iron–metallic SmS–semiconducting SmS structure). This allowed us to detect the phase transition by a simple method based on measurements of the constant current flowing through the iron–SmS contact under the action of the bias voltage (-0.3 V). Such a method was used in experiments where F increased smoothly and then decreased at a constant temperature.

RESULTS

Figure 3 presents typical spectra of the variation of the capacitance recorded on SmS samples at various fixed values of F. The point of the phase transition to the metallic state corresponds to the beginning of the chaotic oscillations on the curves. This point also corresponds to a sharp change in the character of the capacitance relaxation processes obtained on the oscillograph, which is similar to the change described in Ref. 6. As the load on the indenter is increased, the temperature of the phase transition decreases (Fig. 4). Figure 5 shows the behavior of the reverse current of an iron–SmS Schottky diode as F is gradually raised from 0 to ~ 0.9 N and then F is lowered at $T = 300$ K. A difference between the results obtained in the first loading cycle and after the performance of several cycles is observed. In the first cycle the current jump accompanying the phase transition is preceded by a broad region of current instability, in which the current appears for a short time and then vanishes (the vertical lines in Fig. 5a). After several cycles the dependence takes the form shown in Fig. 5b. Visual inspection of the indenter imprints remaining on the surface of the sample after the experiments revealed spots of a metallic phase of SmS, which did not differ in appearance from the metallic phase appearing on the surface of the SmS samples after mechanical polishing by a diamond paste.

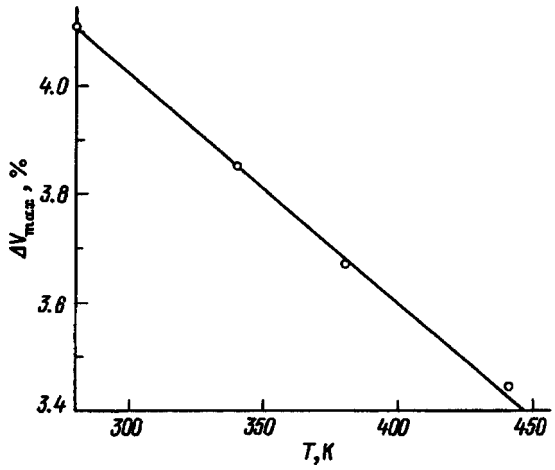

FIG. 4. Dependence of the temperature of the semiconductor–metal phase transition on the volume change in the region of the SmS single crystal quasiuniaxially deformed by the indenter.

DISCUSSION

To account for the experimental data obtained we start out from the assumption that the mechanism of the semiconductor–metal phase transition in SmS under uniaxial compression has much in common with the mechanism of the analogous transition under uniform compression of the sample. At the same time, the following facts should be noted: 1) the mechanism of the transition of SmS to the metallic state has a concentration-dependent character, and its appearance requires the accumulation of a certain critical electron concentration equal to $\sim 10^{20}$ cm^{-3} in the conduction band;[7] 2) the change in the concentration of conduction electrons in SmS resulting from mechanical treatment of the sample is stipulated by the volume change and does not depend on the nature of the stressed state that led to the change;[8] 3) the phase transition observed in response to uniform compression occurs after the volume of the sample has been diminished by $\sim 6\%$.[9]

Thus, as the sample is heated, the value of n increases, and a smaller value of F is required for the transition to the metallic state, as we observe in Fig. 3. The phase transition in the bulk of the sample investigated should begin at the moment when the critical stressed state is achieved at some point in it. On the basis of Eq. (4), each value of F can be mapped to a definite maximum decrease in the volume of the substance, which takes place at the center of the deformed region and equals

$$\Delta V_{\max} = \varepsilon_{zz} + \varepsilon_{xx} + \varepsilon_{yy} \approx 0.8\varepsilon_{zz} = 0.68P/E. \tag{5}$$

In such a case the curve in Fig. 4 is a segment of the phase diagram of the semiconductor–metal phase transition in SmS in $T - \Delta V_{\max}$ coordinates. If we convert the values of F into values of $\Delta V_{\max}$ in such a manner, we should have jumps in the current (I) in Fig. 5 when the critical values of the decrease in the volume of the region of the sample investigated are achieved. The dependence presented in Fig. 5a is typical of the dependences that we recorded in the first loading cycle. The jump at $\Delta V_{\max} \sim 5\%$ can be attributed to a phase transition in the entire region investigated. The value of the critical volume change agrees satisfactorily with the value obtained for uniform compression ($\sim 6\%$). The remaining spikes of I, which begin at $\Delta V_{\max} > 3\%$, can be associated with the appearance of foci of the metallic phase of SmS. The vanishing of I immediately after its appearance is attributed to the fact that the transition is accompanied by a decrease in the volume of the portion of SmS which has undergone the transition to the metallic state by $\sim 15\%$ (Ref. 9) and this portion of the material ceases to be in contact with the indentor. It should be noted that measurements of the resistivity ρ of SmS under the effect of uniform compression also revealed some instability of ρ at pressures 100–200

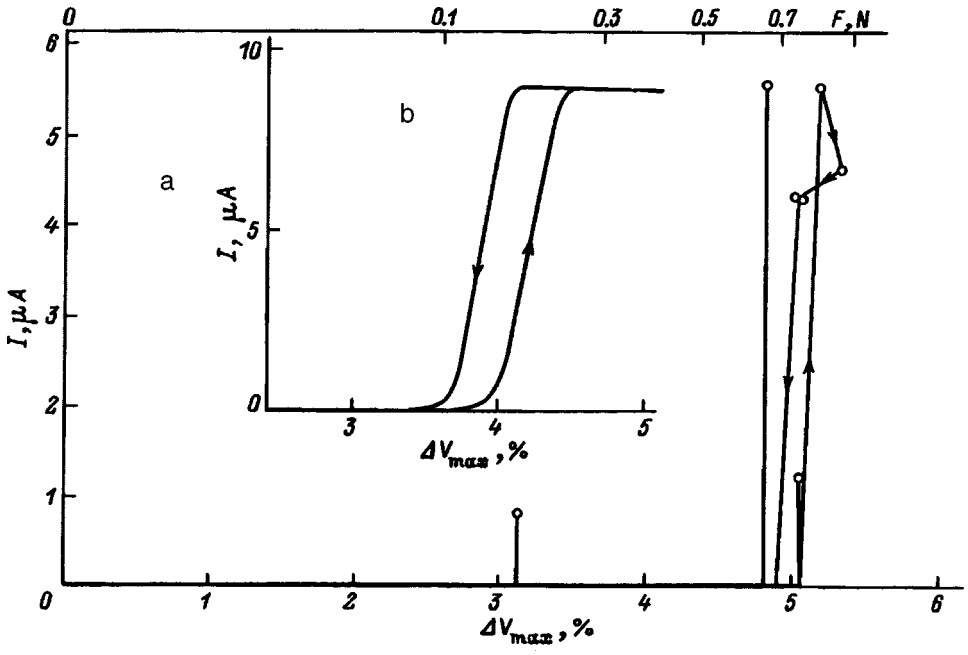

FIG. 5. Dependence of the current flowing through the iron–SmS contact on the load on the indenter. a—First loading cycle, b—after several cycles.

MPa smaller than the phase transition pressure, but the total abrupt change in ρ occurring at ~ 650 MPa in the first loading cycle is taken as the transition pressure.[2)] The decrease in I immediately after the phase transition can be attributed to cracking of the sample due to the asynchronous nature of the transition over the region investigated. After several loading cycles are performed, the picture of the transition changes (Fig. 5b): the maximum of I at the moment of the semiconductor–metal transition and the spikes of I preceding the transition disappear. In addition, a region where two phases coexist, which is located at approximately the same values of $\Delta V_{\max}$ as the spikes of I in the first cycle and is characterized by a gradual increase in the current as the load is increased. The same region is observed in the reverse transition with $\sim 0.5\%$ hysteresis. This conditioning of the phase transition can be attributed to the formation of a system of misfit dislocations on the boundary between the metallic and semiconductor phases of SmS. According to Ref. 10, such dislocations immobilize the metallic phase on the surface of the semiconductor phase. The occurrence of immobilization of the metallic phase of SmS is not questionable, since spots of metallic SmS of yellowish gold color are clearly observed in the indenter imprints after experiments are performed. The size of the imprints corresponds to the calculated value to within $\sim 10\%$, which also characterizes the accuracy of the determination of the other calculated parameters.

With respect to the mechanism of the phase transition in SmS under quasiuniaxial compression, there is an impression that it differs somewhat from the mechanism of the transition under uniform compression and that the smaller critical values of ΔV are not simply a consequence of experimental error. This is consistent with the data in Ref. 3, where a possible value for the pressure of the phase transition in SmS under uniaxial compression was obtained by extrapolating the data obtained under the simultaneous effects of uniform and uniaxial compression, as well as with the data in Ref. 2 for the solid solution $Sm_{0.85}Gd_{0.15}S$. In both of these cases conversion of the uniaxial compressive pressures into volumes gives values that are smaller than in the case of uniform compression. A possible reason for this disparity is that the elastic constants of SmS depend on the electron density in the conduction band and values obtained under normal conditions are used to calculate ΔV, although this is not entirely correct near a phase transition point.

CONCLUSIONS

1. A semiconductor–metal phase transition has been produced in SmS under the action of a stress applied by an indenter, which creates the same strain distribution in the semiconductor as does the stress appearing when a samarium monosulfide sample is subjected to uniaxial compression. Such a stressed state can be considered nominally equivalent to uniaxial compression (quasiuniaxial stressing).

2. The phase transition in SmS occurs when there is a critical decrease in the volume of the semiconductor phase under the action of the applied stress, which is equal to 4–5% at $T = 300$ K.

3. The mechanism of the semiconductor–metal phase transition in SmS under quasiuniaxial compression is similar in general terms to the mechanism of the phase transition under uniform compression.[11]

We thank A. V. Golubkov for supplying the samarium monosulfide single crystals.

[1)] The values of σ and E were calculated from the elastic constants measured in Ref. 5.

[2)] The sample generally fails (cracks) during the reverse transition as the pressure is removed, and subsequent cycles are not carried out.

[1] I. A. Smirnov and V. S. Oskotskiĭ, Usp. Fiz. Nauk **124**, 241 (1978) [Sov. Phys. Usp. **21**, 117 (1978)].
[2] V. V. Kaminskiĭ, A. A. Vinogradov, N. N. Stepanov *et al.*, Pis'ma Zh. Tekh. Fiz. **9**, 624 (1983) [Sov. Tech. Phys. Lett. **9**, 269 (1983)].
[3] G. L. Akimov, A. V. Ryabov, B. I. Smirnov *et al.*, Fiz. Tverd. Tela (Leningrad) **25**, 1328 (1983) [Sov. Phys. Solid State **25**, 763 (1983)].
[4] A. L. Polyakova, *Deformation of Semiconductors and Semiconductor Devices* [in Russian], Énergiya, Moscow (1979).
[5] P. D. Dernier, W. Weber, and L. D. Longinotti, Phys. Rev. B **14**, 3635 (1976).
[6] Sh. Lani, V. V. Kaminskiĭ, and A. V. Golubkov, Zh. Tekh. Fiz. **58**, 1201 (1988) [Sov. Phys. Tech. Phys. **33**, 709 (1988)].
[7] S. I. Grebinskiĭ, V. V. Kaminskiĭ, A. V. Ryabov *et al.*, Fiz. Tverd. Tela (Leningrad) **24**, 1874 (1982) [Sov. Phys. Solid State **24**, 1069 (1982)].
[8] V. V. Kaminskiĭ, A. V. Ryabov, and N. N. Stepanov, Fiz. Tverd. Tela (Leningrad) **23**, 1805 (1981) [Sov. Phys. Solid State **23**, 1052 (1981)].
[9] A. Chaterjee, A. Jayaraman, S. Ramaseshan *et al.*, Acta Crystallogr. **28A**, S243 (1972).
[10] A. V. Ryabov, B. I. Smirnov, S. G. Shul'man *et al.*, Fiz. Tverd. Tela (Leningrad) **19**, 2699 (1977) [Sov. Phys. Solid State **19**, 1580 (1977)].
[11] V. V. Kaminskiĭ, V. A. Kapustin, and I. A. Smirnov, Fiz. Tverd. Tela (Leningrad) **22**, 3568 (1980) [Sov. Phys. Solid State **22**, 2091 (1980)].

Translated by P. Shelnitz

Influence of successive electron and laser irradiation on the photoluminescence of porous silicon

B. M. Kostishko and A. M. Orlov

Ulyanovsk State University, 432700 Ulyanovsk, Russia
(Submitted September 9, 1996; resubmitted January 9, 1997)
Zh. Tekh. Fiz. **68**, 58–63 (March 1998)

The influence of electron irradiation on the light-emitting properties of p- and n-type porous silicon prepared by electrochemical etching is investigated. The dose and energy dependences of the electron-stimulated quenching of the photoluminescence (PL) are determined. It is shown that electron treatment of a porous silicon surface followed by prolonged storage in air can be used to stabilize the PL. The excitation of photoluminescence by a UV laser acting on sections of porous silicon samples subjected to preliminary electron treatment is discovered for the first time. The influence of the electron energy and the power of the laser beam on this process is investigated. The results presented are attributed to variation in the number of radiative recombination centers as a result of the dissociation and restoration of hydrogen-containing groups on the pore surface. © *1998 American Institute of Physics.* [S1063-7842(98)00903-9]

The discovery of the light-emitting properties of porous silicon[1] aroused great interest in this substance as a promising material for optoelectronics. Researchers have devoted a great deal of attention to the variation of the photoluminescence (PL) intensity of porous silicon under continuous and pulsed laser irradiation.[2–4] The aftereffects of the irradiation of a porous silicon surface by α particles, γ quanta, ions, and electrons have been studied to a considerably lesser extent.[5–7] Furthermore, the influence of electrons on the light-emitting properties of porous silicon are represented in the literature only qualitatively, since there is no information on the dependence of the PL intensity on the electron dose and energy for porous silicon having different types of conduction, doping levels, and formation conditions. Despite the abundant experimental material, a general theory, which describes both the mechanism and kinetics of the variation of the PL intensity of porous silicon under different types of treatment, has hitherto not been developed.

This paper is devoted to an investigation of the dose and energy dependence of the degradation of the PL of p- and n-type porous silicon when its surface is irradiated by kiloelectron-volt electrons. It presents results showing how the photoluminescence of porous silicon preliminarily treated with electrons evolves as the material is subjected to continuous laser irradiation.

The starting material used to obtain p-type porous silicon consisted of boron-doped silicon wafers with the (111) orientation and a resistivity $\rho = 10\ \Omega \cdot \mathrm{cm}$ ($N_a = 2.5 \times 10^{15}\ \mathrm{cm}^{-3}$). The n-type samples were obtained from phosphorous-doped wafers with the (100) orientation and $\rho = 2.4\ \Omega \cdot \mathrm{cm}$ ($N_d = 2.5 \times 10^{15}\ \mathrm{cm}^{-3}$). Porous silicon was formed according to a standard technology involving electrochemical etching in an electrolyte consisting of 48% hydrofluoric acid (HF) and ethyl alcohol in a 1:1 ratio. The electrochemical etching time was $t_{\mathrm{etch}} = 30$ min at a current density $j = 10\ \mathrm{mA/cm}^2$ for the p-type samples and $t_{\mathrm{etch}} = 40$ min at $j = 10\ \mathrm{mA/cm}^2$ for n-type porous silicon. Each sample was checked to determine its initial PL intensity and its homogeneity at the surface.

An analysis of the variation of the integrated PL intensity (I_l) showed that the photostimulated quenching effect can be neglected, if an OI-18A illuminator with a UFS6 ultraviolet filter is employed as the light source. In this case the intensity of the UV light did not exceed $1\ \mathrm{mW/cm}^2$. It was noted that even in this case there is a 5–10% decrease in the PL intensity after 4 min of exposure. For this reason, the total irradiation time for the preliminary measurements was restricted to 1 min.

Electron irradiation was carried out in the ultrahigh-vacuum chamber of an O9IOS10-005 Auger spectroscopy with a residual pressure in the chamber equal to 10^{-7} Pa in a regime with scanning of the electron beam over the raster. This permitted variation of the irradiation dose in the range $D = 10^{15} - 6 \times 10^{16}\ \mathrm{cm}^{-2}$. A series of up to 12 sections (Fig. 1) with different dose values was formed on a single sample with an area of $1\ \mathrm{cm}^2$. The intensity of their luminescence under the illuminator with the UV filter was different and depended strongly on the electron irradiation dose.

Plots of the quantitative dependence of I_l on the dose D and the electron energy E_p were obtained from the initial intensity values for irradiation of the porous silicon surface by an LGN-409 He-Cd laser ($\lambda = 325$ nm, $P = 10 - 50\ \mathrm{mW/cm}^2$). An FÉU-64 photomultiplier, which was adapted for use with an INFRAM-I ocular microscope, served as a detector. The region from which the integrated PL intensity was analyzed was 1.5–2 times smaller than the dimensions of a single electron-irradiated section.

The results of the measurements of the integrated photoluminescence intensity of the samples are shown as points in Figs. 2a and 2b. As we see, regardless of their type of con-

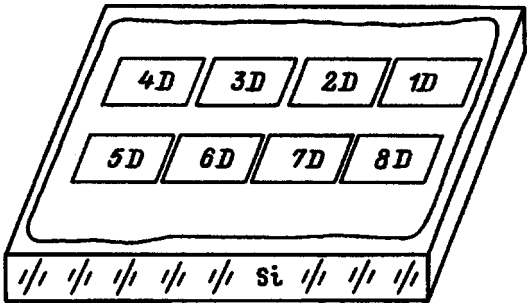

FIG. 1. Sample of porous silicon with sections irradiated by electrons. The sections are arranged in order of increasing dose.

duction, an exponential decay of $I_l(D)$ followed by the achievement of a saturation value I_S at large doses $D>D_S$ is observed (the values of the saturation dose D_S exceed 6×10^{15} cm^{-2}). An increase in the beam energy E_p leads to an appreciable increase in the degradation rate and a decrease in I_S.

It was found that the influence of electron irradiation on the PL of porous silicon decreases when the sample is stored in a dark place in air as the time interval between the electron and UV irradiations is increased. In fact, after porous silicon is stored for 1–2 months under such conditions, the photoluminescence of the surface becomes practically uniform. It should also be noted that the sections subjected to irradiation by electrons of lower energy recover more rapidly. This effect is not observed at all in samples stored for the same time in an ultrahigh-vacuum chamber with a residual pressure $p=10^{-5}-10^{-7}$ Pa. Therefore, the significant degradation of the PL is most probably not attributable to the accumulation of electric charge on the surface discovered in Ref. 8.

It is interesting that the recovered sections do not exhibit any appreciable variation of the PL intensity after repeated electron irradiation. Such electron ''tempering,'' i.e., irradiation to complete quenching followed by recovery in air can probably be used to stabilize the light-emitting properties of porous silicon.

The degradation of the PL under the action of electrons followed by its recovery in air cannot be attributed to structural changes in the near-surface layer of porous silicon. In

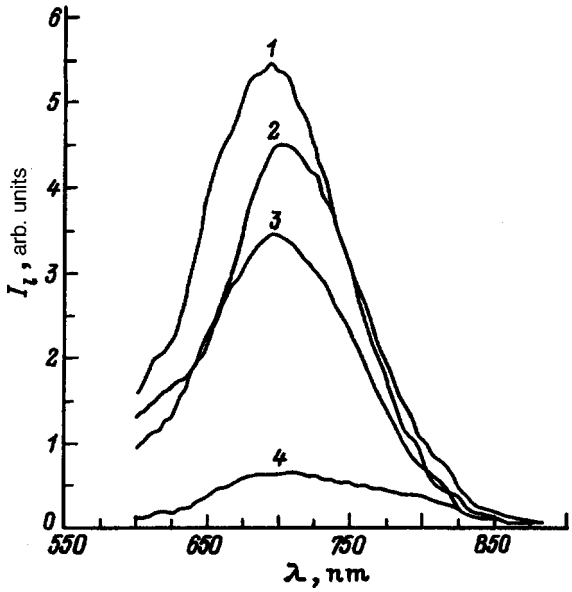

FIG. 3. Photoluminescence spectrum of p-type porous silicon after irradiation by electrons. Electron energy, keV: *1*—2, *2*—3, *3*—4, *4*—5.

fact, the threshold energies for the displacement of atoms in silicon by electrons amount to 10–30 eV, which are achieved during irradiation by particles accelerated to 250 keV.[9] Consequently, electron-stimulated defect formation does not occur in the bulk of the quantum wires in the range of doses and energies used. Therefore, the observed effect can be associated only with alteration of the composition, the atoms passivating the surface of the quantum wires, and the number of dangling bonds. A correlation between the decrease in the PL intensity and the appearance of a large number of dangling bonds (5.5×10^{17} cm^{-3}) on the internal pore surface following annealing in a vacuum was discovered in Ref. 10. Additional confirmation of the desorption nature of the electron-stimulated alteration of the PL can be provided by the fact that the spectral intensity maximum ($\lambda=697\pm8$ nm) scarcely moves as the electron energy is increased (Fig. 3), as well as by the vigorous evolution of gases in hydrofluoric acid only on the sections which have undergone irradiation and recovery in air.

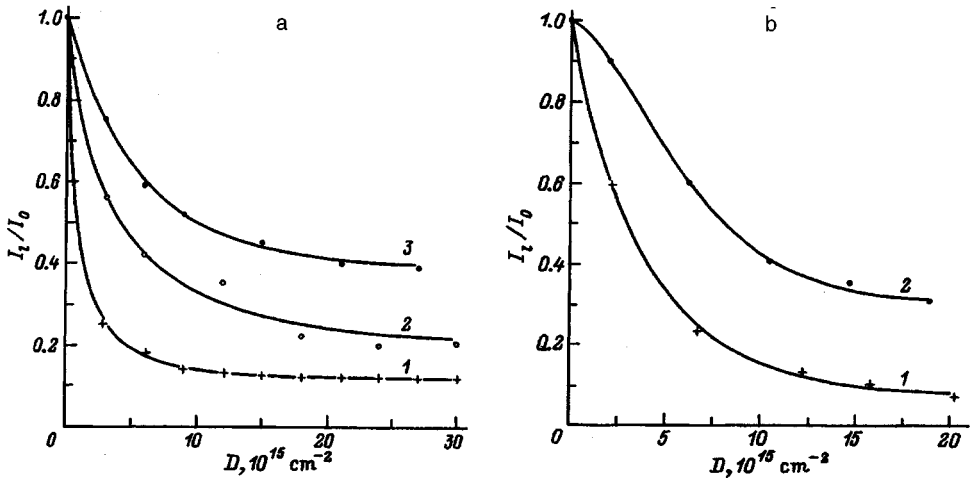

FIG. 2. Dependence of normalized integrated PL intensity on the electron irradiation dose for p- (a) and n-type (b) porous silicon. Points—experimental values; lines—results calculated from Eq. (6). Electron energy, keV: *1*—4, *2*—3, *3*—2.

For these reasons the mechanism of the electron-stimulated degradation of the PL of porous silicon can be described in the following manner. The surface of freshly prepared porous silicon is passivated mainly by hydrogen atoms[11,12] in the form of SiH and SiH_2 groups, whose role in the light-emitting properties of porous silicon has been determined in numerous studies.[12,13] The presence of SiH_2 groups on the pore surface creates luminescent centers. In the case of only radiative electron-hole recombination, the PL intensity at a sufficiently high excitation level can be described by the formula[14]

$$I_l^r = A^r N_l^r \frac{C_n^l C_p^l}{C_n^l/p_S + C_p^l/n_S}, \tag{1}$$

where N_l^r is the concentration of radiative recombination centers, C_p^l and C_n^l are the cross sections for the trapping of holes and electrons by these centers, respectively, n_S and p_S are the photoinduced concentrations of free electrons and holes, and A^r is a dimensional constant.

If we take into account the large exciton ionization energies in porous silicon ($E_{ex}=0.11$–0.39 eV)[15] and the consequent high probability of their radiative annihilation even at room temperature, it becomes necessary to take into account another component of the PL

$$I_l^{ex} = A^{ex} \beta N_l^{ex} n_{ex}, \tag{2}$$

where N_l^{ex} is the concentration of radiative exciton-annihilation centers, which are associated with neutral surface states of adsorbed atoms, n_{ex} is the exciton concentration, β is the probability of radiative annihilation, and A^{ex} is a dimensional constant. To be specific, we shall henceforth consider only the exciton mechanism of the PL of porous silicon.

As can be seen from Eqs. (1) and (2), the PL intensity is directly proportional to the concentration of luminescent centers, which can vary during the desorption of hydrogen from porous silicon when it is irradiated by electrons of sufficient energy. Then, it can be postulated on the basis of the experimental data obtained that the dose dependence of the concentration of SiH_2 groups and, accordingly, of luminescent centers at the maximum electron penetration depth h, which is commensurate with the thickness of the light-emitting layer h_0, can be written in the form

$$N_l(D) = N_0 \exp(-(D/D_0)^\alpha), \tag{3}$$

where N_0 is the initial concentration of luminescent centers in the sample, D_0 is the characteristic electron dose, at which the concentration of hydrogen-passivated bonds in porous silicon decreases by a factor of e, and α is an empirical parameter.

When sufficiently large values of $D > D_S$ are achieved, all the luminescent centers in a layer of thickness h are practically completely removed, and the PL intensity is determined only by the radiative annihilation centers located at a depth $h < x < h_0$. With consideration of (3) the mean concentration of luminescent centers in porous silicon after electron irradiation is specified by the expression

$$N_l^{ex}(D) = N_0[1-(h/h_0)(1-\exp(-(D/D_0)^\alpha))]. \tag{4}$$

TABLE I. Parameters of the model of the electron-stimulated quenching of the PL of porous silicon.

Type of conduction	E_p, keV	D_0, 10^{15} cm^{-2}	α	h/h_0
p	4	1.1	0.58	0.88
	3	4.3	0.71	0.8
	2	5.7	0.95	0.61
n	4	3.9	0.95	0.93
	3	6.9	1.53	0.7

Substituting Eq. (4) into (2), we obtain the PL intensity

$$I_l^{ex} = I_l(D) = A^{ex} \beta n_{ex} N_0[1-(h/h_0)(1-\exp(-(D/D_0)^\alpha))]. \tag{5}$$

To eliminate the constants that cannot be determined under the conditions of the experiment, the data in Fig. 2 are represented in a normalized form, i.e., as values of I_l/I_0, where $I_0 = A^{ex}\beta n_{ex} N_0$ is the PL intensity before electron treatment. Lines calculated using the equation

$$I_l(D)/I_0 = 1-(h/h_0)(1-\exp(-(D/D_0)^\alpha)) \tag{6}$$

are plotted through the experimental points.

The parameters used in the calculation for different samples and electron energies are presented in Table I. As we see, the calculated lines faithfully describe the experimental results.

Several laws associated with the experimental dependence of D_0, h/h_0, and α on the energy and the type of conduction in the sample should be noted. First, there is a characteristic increase in D_0 as the electron energy decreases. In accordance with (6), it is attributed to a decrease in the maximum electron penetration depth h. Information on the energy dependence of the ratio h/h_0 permitted determination of the depth of the luminescent layer in porous silicon. In fact, electrons penetrate to a depth equal to h_0 already at $E_p = 4.5$ keV for p-type porous silicon and $E_p = 4.1$ keV for n-type porous silicon, and complete photoluminescence quenching occurs when sufficiently large doses are achieved. On this basis, the specific electron energy losses in silicon[16] were used to obtain an estimate of the thickness of the light-emitting layer in p-type porous silicon $h_0 \approx 0.5$ μm, which is in satisfactory agreement with the literature values (1–2 μm).[7] The thickness of the light-emitting layer in a sample with n-type conduction is somewhat smaller: $h_0 \approx 0.45$ μm.

Another characteristic feature is the decrease in the empirical parameter α with increasing electron energies, which is apparently due to the hindered removal of the desorbed hydrogen atoms when the electron penetration depth increases. Thus, the larger values of α for an n-type sample should be associated with its smaller porosity. Indirect confirmation of this is provided by the data from an Auger electron spectroscopic (AES) study of the surface of porous silicon. The silicon $L_{23}VV$ Auger peak ($E = 91$ eV) was not detected on a p-type sample because of the considerable charging of the surface, while the silicon Auger line was detected fairly steadily on n-type porous silicon. According to the results in Ref. 17, the concentration of charge carriers

in a sample of porous silicon with a high porosity can decrease to the intrinsic level as a result of depletion of the dopant from the thin layer in the quantum wires. Thus, the AES data point out the insignificance of this depletion and the comparatively large diameter of the pores in n-type porous silicon, which, in turn, signify better conditions for the removal of the desorption products and larger values of α than in a p-type sample.

The further investigations were devoted to determining the photostimulated evolution of the PL of porous silicon that has undergone preliminary electron treatment. In Figs. 4a and 4b the points describe the experimental dependence of I_l on the irradiation time ($t<2$ min) by an LGN-409 UV laser with $P=15$ mW/cm^2 for p- and n-type samples, respectively. The samples were irradiated by electrons with the energy $E_p=4$ keV.

As we see, regardless of the type of conduction, a change in the law of variation of the PL intensity is observed: quenching on the sections with a small electron irradiation dose and excitation on the section where the dose exceeds a certain critical value D_e. This is attributed to the fact that in air the dissociation of the hydrogen-containing groups under the action of laser irradiation should be accompanied by their restoration. According to the kinetic model presented in Ref. 18, the variation of the concentration of luminescent centers during short laser treatment times is described by the following equation:

$$dN_l/dt=-k_dN_l+k_c(N_0^a-N_l), \tag{7}$$

where N_0^a is the concentration of adsorption centers, and k_d and k_c are the rate constants of the dissociation and restoration of the hydrogen-containing groups, respectively.

The restoration constant is usually written in the form[14]

$$k_c=\frac{PKS}{\sqrt{2\pi MkT}}, \tag{8}$$

where P is the partial pressure of the gas, K is the probability that a hydrogen molecule which has reached an adsorption center on the surface will become attached to it, and S and M are the effective area of a molecule and its mass.

The photodissociation constant can be defined in the following manner:

$$k_d=Fj_F\sigma, \tag{9}$$

where j_F is the number of photons impinging on a unit area of the porous silicon surface per unit time, σ is the cross section for the absorption of photons by hydrogen-containing groups, and F is the quantum yield, i.e., the probability of the desorption of a hydrogen atom upon the absorption of a photon by an adsorption-center/hydrogen-atom system.

In writing Eq. (7) it was assumed that k_d and k_c do not depend on the depth. This assumption is based on the ''bleaching'' effect in porous silicon, in which the absorption coefficient is approximately an order of magnitude smaller than in c-Si (Refs. 19 and 20). This bleaching leads to insignificant variation of the intensity of the exciting UV light within a region of thickness $h=0.5$ μm. In addition, it was assumed that the electron processes which transform the neutral radiative annihilation centers into charged nonradiative states can be neglected in comparison with the adsorption and desorption mechanisms.

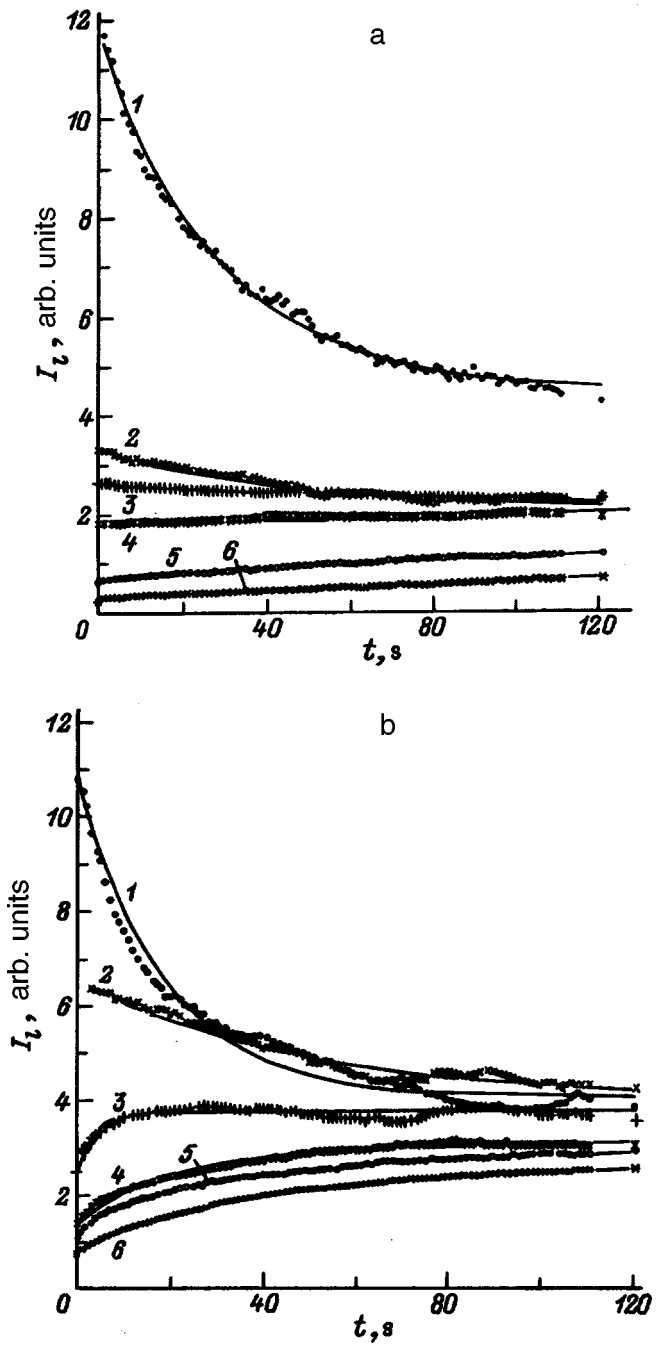

FIG. 4. Dependence of the photoluminescence intensity of porous silicon on the electron irradiation time. a: Preliminary electron treatment dose for p-type porous silicon, cm^{-2}: *1*—0, *2*—4.2×10^{15}, *3*—8.4×10^{15}, *4*—16.8×10^{15}, *5*—25.2×10^{15}, *6*—33.6×10^{15}; b: for n-type porous silicon, cm^{-2}: *1*—0, *2*—2.25×10^{15}, *3*—6.75×10^{15}, *4*—11.75×10^{15}, *5*—15.75×10^{15}, *6*—20.25×10^{15}.

The solution of Eq. (7) with initial condition (4) gives the analytical expression

$$N_l(t)=\frac{N_0^ak_c}{k_c+k_d}+\left\{N_0[1-(h/h_0)(1-\exp(-(D/D_0)^\alpha))]\right.$$

$$-\frac{N_0^a k_c}{k_c+k_d}\Bigg\}\exp(-(k_d+k_c)t). \quad (10)$$

According to (10), the PL intensity of porous silicon varies with the laser irradiation time according to an exponential law. The character of its evolution is determined by the pre-exponential factor in the curly brackets. At small irradiation doses the desorption rate of hydrogen exceeds the adsorption rate, the number of radiative annihilation centers decreases, and the PL is quenched. Conversely, if the doses exceed a certain value, the photoluminescence intensity begins to increase as a result of the predominant chemisorption of hydrogen atoms. On the basis of Eq. (10), the value of the critical electron irradiation dose equals

$$D_e = D_0\alpha\ \sqrt{\ln\frac{N_0 h/h_0}{N_0^a k_c/(k_c+k_d)+N_0(h/h_0-1)}}. \quad (11)$$

The solid curves in Figs. 4a and 4b are plots of $I_l(t)$ calculated from Eq. (10). The critical doses D_e are equal to 6.75×10^{15} cm^{-2} for an n-type sample and 25.2×10^{15} cm^{-2} for a p-type sample.

A decrease in the electron energy in the preliminary treatment of porous silicon leads to an appreciable increase in the critical dose for the change in the mechanism of the evolution of the PL (in the case of an n-type sample $D_e=14.7\times10^{15}$ cm^{-2} for $E_p=3$ keV and $D_e=22\times10^{15}$ cm^{-2} for $E_p=2$ keV). Within the proposed adsorption model this is attributed to a decrease in the electron penetration depth in porous silicon and, accordingly, to the need to achieve larger doses in order to reverse the sign of the pre-exponential factor in (10).

The intensity of the laser radiation also has an influence on the character of the photostimulated evolution of the PL of porous silicon. To determine this dependence, an n-type sample that had been treated with electrons ($E_p=3$ keV) was irradiated by a laser with an intensity equal to 10, 15, and 35 mW/cm^2. These investigations showed that the excitation of PL does not occur when $P=35$ mW/cm^2 even on the sections with a dose $D=30\times10^{15}$ cm^{-2}, while intensities equal to 10 and 15 mW/cm^2 permit the observation of the excitation of PL at doses greater than 8.8×10^{15} and 14.7×10^{15} cm^{-2}, respectively. An increase in the intensity of the laser radiation clearly leads to an increase in the dissociation coefficient of the hydrogen bonds k_d (9) and a decrease in the second term of the pre-exponential factor in Eq. (10). Thus, large photon fluxes cause predominant dissociation of the hydrogen-containing groups even in the case of a fairly large number of free adsorption centers.

CONCLUSIONS

The dependences of the integrated PL intensity of porous silicon with p- and n-type conduction on the electron irradiation dose and energy have been obtained in this work. The experimental results have been attributed to a decrease in the number of radiative exciton-annihilation centers as a result of the electron-stimulated cleavage of hydrogen bonds on the surface of the quantum wires. The thickness of the layer for effective photoluminescence in the samples investigated has been estimated.

It has been discovered for the first time that preliminary electron treatment can lead not only to the quenching of the PL, as occurs on the original sample of porous silicon, but also to excitation under the action of continuous laser irradiation. The influence of the electron energy and the laser intensity on the value of the critical electron dose at which the UV-induced increase in the PL intensity begins has been demonstrated. The observed effect has been attributed to the presence of two competing channels for altering the number of luminescent centers, viz., photostimulated desorption and chemisorption of hydrogen on the internal pore surface. The use of electron irradiation permits modification of the relation between the rates of these processes. Although the observed effects have been attributed here to variation of the number of hydrogen-containing groups, the activation role of the oxygen present in the pores cannot be ruled out completely.

We thank S. N. Mikov for assisting in the determination of the spectral characteristics of the photoluminescence of porous silicon.

[1] L. T. Canham, Appl. Phys. Lett. **57**, 1046 (1990).
[2] K. S. Zhuravlev, N. P. Stepina, E. S. Shamirzaev *et al.*, Fiz. Tekh. Poluprovodn. **28**, 483 (1994) [Semiconductors **28**, 295 (1994)].
[3] P. D. Stevens, Appl. Phys. Lett. **63**, 803 (1993).
[4] V. B. Pikulev, S. N. Kuznetsov, and A. M. Il'in, Zh. Tekh. Fiz. **65**, 170 (1995) [Tech. Phys. **40**, 1068 (1995)].
[5] E. V. Astrova, R. F. Vitman, V. V. Emtsev *et al.*, Fiz. Tekh. Poluprovodn. **30**, 507 (1996) [Semiconductors **30**, 279 (1996)].
[6] S. Migazaki, K. Shiba, K. Sakamoto *et al.*, Optoelectron.—Devices Technol. **7**, 95 (1992).
[7] V. G. Baru, T. P. Kolmakova, A. B. Ormont *et al.*, Pis'ma Zh. Tekh. Fiz. **20**(20), 62 (1994) [Tech. Phys. Lett. **20**(11), 838 (1994)].
[8] A. V. Petrov and A. G. Petrukhin, Fiz. Tekh. Poluprovodn. **28**, 82 (1994) [Semiconductors **28**, 49 (1994)].
[9] T. D. Dzhafarov, *Radiation-Stimulated Diffusion in Semiconductors* [in Russian], Énergoizdat, Moscow (1991).
[10] E. A. Konstantinova, V. Yu. Timoshenko, and P. K. Kashkarov, Poverkhnost', No. 2, 32 (1996).
[11] H. D. Fuchs, M. Stutzmann, M. S. Brandt *et al.*, Phys. Rev. B **48**, 8172 (1993).
[12] C. Tsai, K.-H. Li, J. Sarathz *et al.*, Appl. Phys. Lett. **59**, 2814 (1991).
[13] B. M. Kostishko, A. M. Orlov, S. N. Mikov *et al.*, Izv. Akad. Nauk SSSR, Neorg. Mater. **31**, 444 (1995).
[14] T. Wolkenstein, *Electronic Processes on Semiconductor Surfaces during Chemisorption* [Consultants Bureau, New York (1991); Nauka, Moscow (1987)].
[15] G. D. Sanders and Yia-Chung Chang, Phys. Rev. B **45**, 9202 (1992).
[16] I. S. Grigor'ev and É. Z. Meĭlikhov (Eds.), *Physical Constants. A Handbook* [in Russian], Énergoatomizdat, Moscow (1991).
[17] S. P. Zimin, Pis'ma Zh. Tekh. Fiz. **21**(24), 46 (1995) [Tech. Phys. Lett. **21**(12), 1015 (1995)].
[18] B. M. Kostishko, A. M. Orlov, and T. G. Emel'yanova, Pis'ma Zh. Tekh. Fiz. **21**(19), 32 (1995) [Sov. Tech. Phys. Lett. **21**(11), 870 (1995)].
[19] E. V. Astrova, A. A. Lebedev, A. D. Remenyuk *et al.*, Fiz. Tekh. Poluprovodn. **29**, 1649 (1995) [Semiconductors **29**, 858 (1995)].
[20] N. Ookubo, J. Appl. Phys. **74**, 6375 (1993).

Translated by P. Shelnitz

Phase measurements of surface electromagnetic waves on silver with excitation through the substrate

Yu. E. Petrov, E. V. Alieva, G. N. Zhizhin, and V. A. Yakovlev

Institute of Spectroscopy, Russian Academy of Sciences, 142092 Troitsk, Moscow District, Russia
(Submitted October 7, 1996)
Zh. Tekh. Fiz. **68**, 64–68 (March 1998)

Surface electromagnetic waves are excited in the visible and near-IR regions of the spectrum, and interference measurements are performed. Their excitation is effected by a helium–neon laser (3.39, 1.15, and 0.63 μm) on the interface between air and a silver film of thickness 100 μm deposited on a substrate in the form of a prism of fused quartz. The exciting radiation is supplied from the substrate side in a regime of total internal reflection in the prism on the edge of the silver film. The wave vector of the surface electromagnetic wave investigated is determined from the results of phase measurements. The dependence of the efficiency of the excitation of surface electromagnetic waves on the angle of incidence of the exciting radiation onto the substrate is investigated. The real part of the dielectric function of the silver film is calculated. © *1998 American Institute of Physics.* [S1063-7842(98)01003-4]

The phase spectroscopy of surface electromagnetic waves (SEWs) was developed to determine the optical constants of metals, insulators, and semiconductor crystals in the mid- and far-IR ranges.[1,2] To excite a surface plasmon– or phonon–polariton mode, the field of an electromagnetic wave must be concentrated near the surface of the sample under investigation.[3] The aperture excitation of radiation is most widely employed in these regions of the spectrum because of its simplicity and universality.[4] However, the attempts to extend this method to the near-IR and visible ranges[5] ran into serious difficulties due to the complexity of the apparatus, the very small gaps (<1 μm), and the overall miniaturization of the experiment.

The edge excitation of radiation was found to be convenient in the near-IR and visible ranges under attenuated total internal reflection (ATR) conditions,[6] which have not hitherto been employed in SEW phase spectroscopy. This technique is carried out in the following manner (Fig. 1). A metal film in the form of a wedge-shaped area is deposited on part of the hypotenuse surface of a prism that is transparent in the spectral range being investigated. A laser beam focused by a lens is directed through the prism at such an angle that total internal reflection takes place from the hypotenuse surface of the prism. As we know,[7] during total internal reflection on a boundary with a less dense medium, the electromagnetic field decays exponentially with increasing distance from the interface, and the reflected ray is displaced somewhat relative to the incident ray. If the boundary of a metal film is placed between the ''entrance'' and ''exit'' points of the ray, the condition for total internal reflection is violated, and the radiation is partially transformed into an SEW and volume radiation, which propagates above the surface of the metal. In addition, as in the case of aperture excitation, the volume and surface waves appearing are coherent to one another. The surface wave excited on the edge of the metal film propagates over its outer surface (the boundary with air) and reaches the opposite edge of the wedge, where it is transformed back into volume radiation, part of which travels into the prism and part of which travels into the space above the prism. We are interested in the latter radiation, which interferes with the volume radiation traveling above the surface and contains information regarding the state of the surface under investigation. Thus, the sample is located in one of the arms of a double-beam interferometer. By moving the photodetector along a circle whose center is located at the point of detachment of the SEW, we can record the angular dependence of the resultant radiated intensity, which, because of the continuous variation of the phase difference between the interfering waves along the trajectory of the detector, gives a characteristic ''interference'' dependence, which can be used to determine both the amplitude and phase relations between the interfering waves. It was used to determine the dependence of the SEW excitation coefficient on the angle of incidence of the radiation onto the hypotenuse surface of the prism for all the wavelengths generated by a helium–neon laser (3.39, 1.15, and 0.63 μm).

The radiated intensities measured at the maxima and minima of the interferogram are equal, respectively, to

$$I_{\max}=I_b+I_s+2\sqrt{I_bI_s}, \tag{1a}$$

$$I_{\min}=I_b+I_s-2\sqrt{I_bI_s}, \tag{1b}$$

where I_s is the intensity of the volume radiation formed at the point of detachment of the SEW from the surface of the metal, and I_b is the intensity of the volume radiation formed at the point of excitation of the surface wave.

In the case where the spatial distributions of I_s and I_b vary only slightly between neighboring maxima and minima of the interference curve, and $I_b>I_s$, it follows from (1a) and (1b) that

$$I_s=(\sqrt{I_{\max}}-\sqrt{I_{\min}})^2.$$

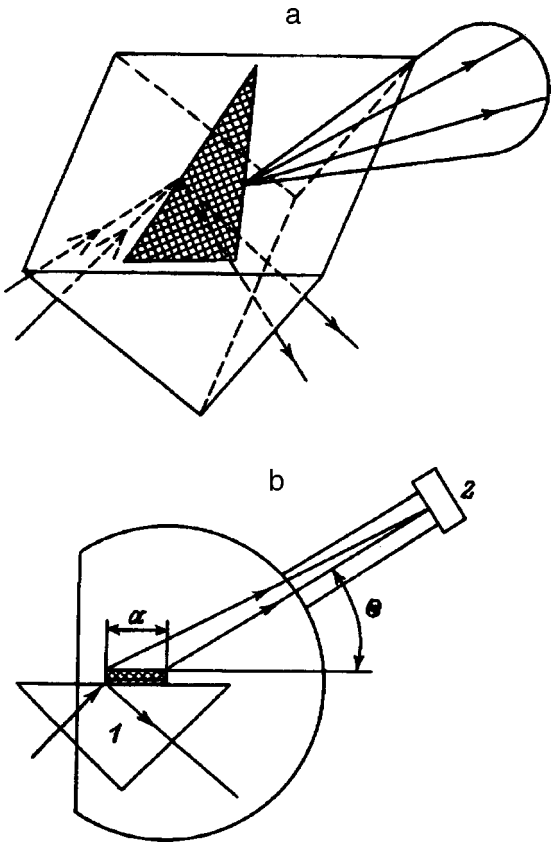

FIG. 1. a: Prism with a deposited metallic wedge; b: view from above: *1*—fused quartz crystal, *2*—radiation detector.

Integrating the dependence of I_s obtained over the angle Θ, we obtain a quantity, which is proportional to the SEW excitation coefficient, $\gamma = I_{s0}/I_0$, where I_{s0} is the intensity of the SEW at the excitation point, and I_0 is the intensity of the laser radiation incident to the prism.

By turning the prism relative to the incident beam, we obtain the dependence of the SEW excitation coefficient on the angle of incidence of the radiation onto the working (hypotenuse) surface of the prism according to the method described above. In addition, the angular dependence of the radiated intensity permits the determination of the phase relations between the interfering waves. The condition for an interference extremum has the form

$$an' + r - \sqrt{(a + r\ \cos\ \Theta)^2 + r^2\ \sin^2\ \Theta} = (m + \Delta m)\lambda, \tag{2}$$

where (Fig. 1) m is the number of the extremum, which is an integer for a maximum and a half integer for a minimum, Δm is the total additional phase shift between the interfering waves appearing upon the excitation and detachment of the SEW, n' is the real part of the effective refractive index of the SEW, a is the length of the path traversed by the SEW over the metal film, r is the distance between the point of detachment of the SEW from the sample and the detector, and Θ is the angle between the ray traveling from the point of detachment of the SEW to the detector and the plane of the metal film.

After obtaining the values of Θ corresponding to known values of m from the interferogram, we can use formula (2) to determine n' and a. It is convenient to solve this problem graphically by constructing a plot of the dependence of the parameter

$$q = \sqrt{(a + r\ \cos\ \Theta)^2 + r^2\ \sin^2\ \Theta} - r$$

on $(m + \Delta m)\lambda/a$. The straight line obtained has an intercept on the vertical axis equal to $n' - 1$, and a can be determined from its slope. However, the number of the extremum is not always known. For example, in our experiments in the visible region the optical difference between the paths of the interfering beams reaches 10–20 wavelengths for the characteristic values $a = 0.1$–0.25 mm. In addition, Δm is an unknown quantity. The determination of these quantities requires several interferograms recorded for different values of a. They are depicted as a family of parallel straight lines on the graph of $q(m)$. By selecting m for each straight line and varying the single parameter Δm for all the straight lines, we can minimize the difference between the straight lines obtained. The straight line thus obtained also specifies m and Δm. In our experiment the interferograms were fed directly into a computer, where the procedure described above was carried out by a program written in BASIC.

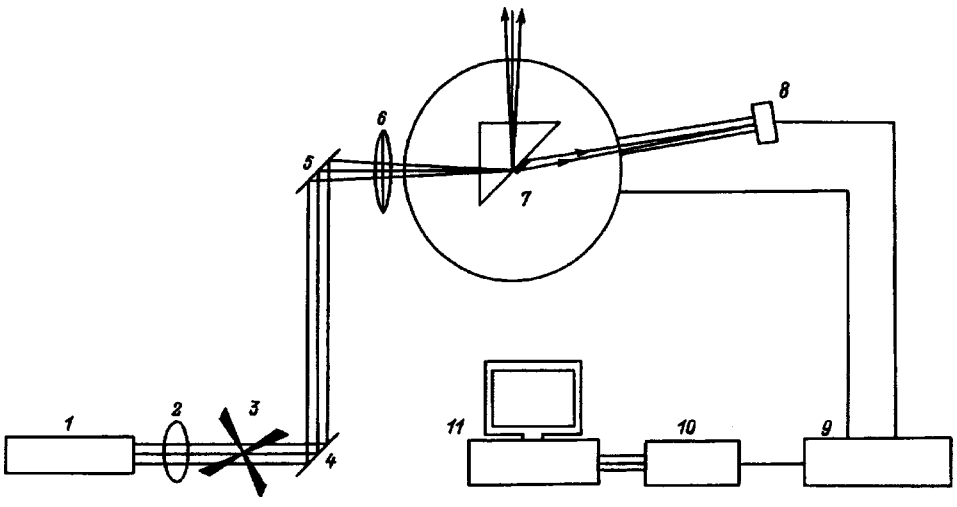

FIG. 2. Diagram of the experimental apparatus: *1*—helium–neon laser; *2*—phase shifter; *3*—400 Hz modulator; *4*, *5*—metallic mirrors; *6*—focusing lens; *7*—goniometer; *8*—detector; *9*—selective amplifier; *10*—analog-to-digital converter; *11*—computer.

A diagram of the experimental apparatus is shown in Fig. 2. Polarized radiation from a continuous He–Ne laser (with wavelengths equal to 0.63, 1.15, and 3.39 μm) is interrupted at a frequency of 400 Hz by a sector disk fastened to the rotating axle of a hysteresis motor. The beam focused by a lens impinges on a prism fastened to the rotating stage of goniometer in such a manner that the laser light impinges on the working surface of the prism at an angle exceeding the angle for total internal reflection. The detector is fastened to the movable arm of the goniometer. The point at which the SEW detaches from the surface of the sample coincides with the rotation axis of the detector. The accuracy of the measurement of the rotation angle of the detector in our experiment was 0.1°. After selective amplification and analog-to-digital conversion, the interferograms, i.e., the angular dependences of the radiated intensity, are fed into a computer, where they are used to calculate the value of n', which permits determination of the real part of the dielectric function Re ε for the metal investigated (silver).

The silver films investigated in the present work were deposited by thermal evaporation in a vacuum with a residual pressure equal to 2×10^{-5} Torr, and the evaporation rate was 1–2 nm/s. The mass thickness of the film was determined using a quartz microbalance and was equal to 100 nm. Each film was deposited on the surface of a prism of KI fused quartz. The dimensions of the working surface were 15×20 mm.

To enable the recording of a series of interferograms at different values of the distance a traversed by the SEW along the metal surface, the SEW was excited in the direction transverse to the wedge. The parameter a can be varied by displacing the point of excitation of the SEW by moving the prism perpendicularly to the incident beam. Since the propagation length of the SEW on the silver film decreases abruptly as the frequency increases, a separate sample was prepared for the experiments at each wavelength, and a film was deposited on it using a mask in the shape of a wedge with a width $\approx0.1-0.3$ mm for the 0.63 μm radiation, $\approx0.3-1$ mm for the 1.15 μm radiation, and $\approx2-5$ mm for the 3.39 μm radiation. In the case of $\lambda=0.63$ μm it should be taken into account that the width of the metal film becomes less than the diameter of the focused radiation beam (200 μm) because of the short propagation length of the SEW. Consequently, we can expect the appearance of a third source that makes a contribution to the interferogram, viz., the beam refracted on the second boundary of the metal film. To clear up this question we recorded interferograms in both

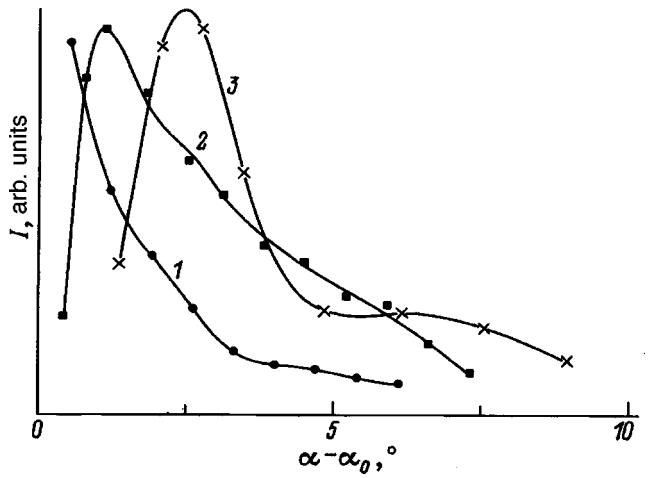

FIG. 3. Dependence of the effective SEW excitation coefficient I on the angle $\alpha-\alpha_0$. λ, μm: *1*—3.39, *2*—1.15, *3*—0.63.

TABLE I.

λ, μm	$\alpha-\alpha_0$ (calc.), deg	$\alpha-\alpha_0$ (exper.), deg
0.63	1.7	2.6
1.15	0.45	1.2
3.39	0.05	-

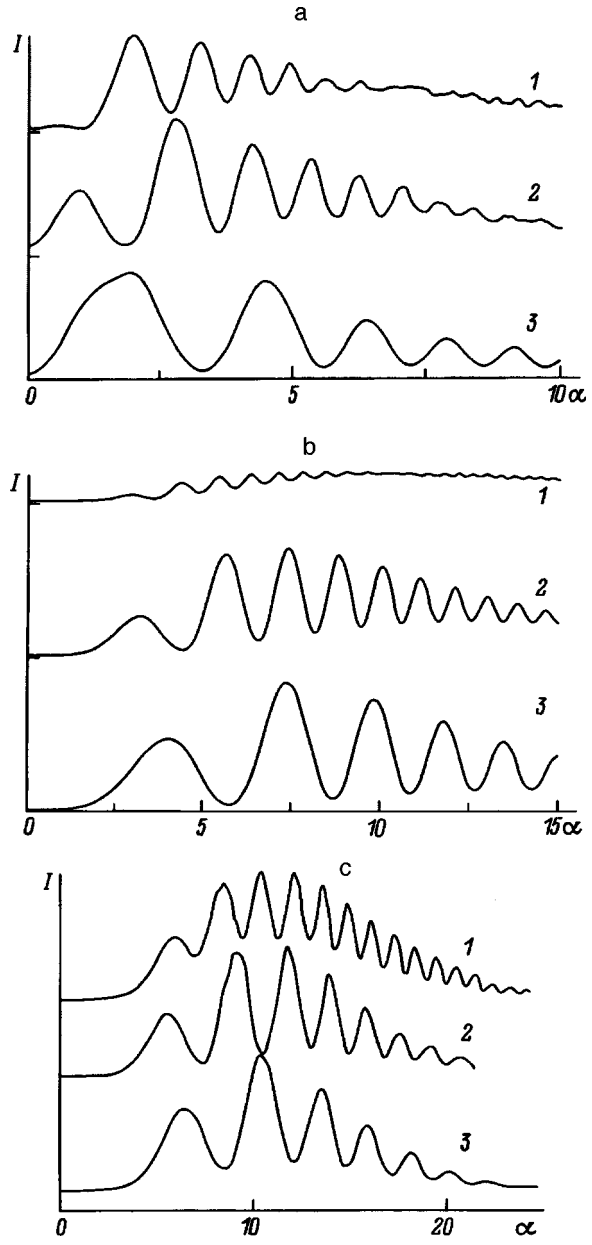

FIG. 4. Typical interferograms. a: $\lambda=0.63$ μm; a, μm: *1*—110, *2*—75, *3*—55; b: $\lambda=1.15$, μm; a, μm: *1*—703, *2*—329, *3*—179; c: $\lambda=3.39$ μm; a, μm: *1*—3, *2*—2, *3*—1.

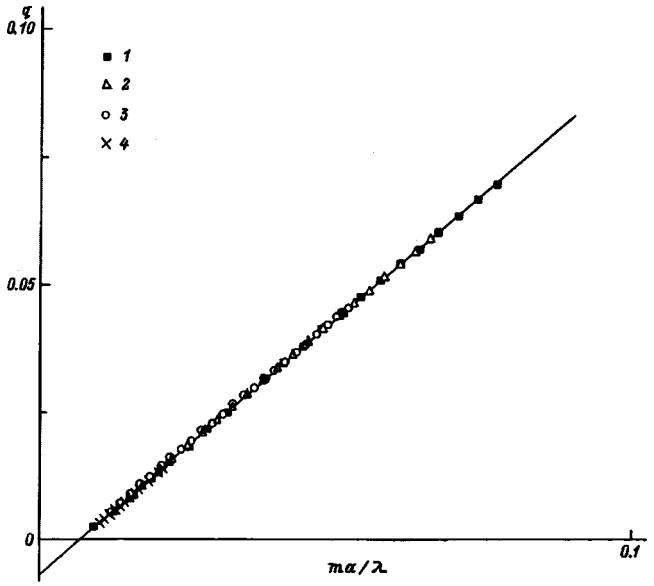

FIG. 5. Graphical determination of Δn for a silver film with a thickness of 100 nm. $\lambda = 1.15$ μm; a, μm: *1*—179, *2*—227, *3*—329, *4*—703.

p and s polarizations. Since the SEW is excited only in p-polarized light,[3] the appearance of interference on the angular dependence of the radiated intensity in the case of s polarization can be caused only by this third source. It was found that in s-polarized light an interference pattern is noticeable only at angles of incidence of the exciting radiation α that are close to the critical value (α_0). The parasitic beam can be suppressed completely by increasing this angle by 1–2°. In this case the beam divergence did not exceed 0.2°.

Figure 3 presents the dependence of the SEW excitation coefficient on the angle of incidence of the exciting beam. As we know, the volume wave is transformed into a surface wave most efficiently in the case of matching of the impedances of the exciting wave and the SEW formed.[8] The values of $\alpha - \alpha_0$ corresponding to the maximum SEW excitation coefficient, which we obtained by simple calculations using the dielectric function,[3] and the values determined experimentally in the present work are presented in Table I.

As can be seen from Table I, the experimental values of the angles corresponding to maximum excitation (in the case of $\lambda = 3.39$ μm the value could not be determined because of the closeness of α to α_0) significantly exceed the calculated values. The reason for this is possibly the imperfect shape of the edge of the metal film on which the surface wave is excited. The SEW is excited on an edge of a film whose thickness drops smoothly to zero over a characteristic distance of the order of several microns, which significantly exceeds the wavelength of the exciting radiation. Therefore, the SEW is actually excited on a portion of the surface of a film of small thickness, for which the value of n', as our calculations show, is greater than that for a thick film.[3] This apparently leads to the difference between the experimental and calculated values of the angles corresponding to maximum excitation of the SEW.

Typical interferograms obtained in the present work are presented in Fig. 4. The corresponding dependence of q on the ordinal number of the extremum for the series of measured interferograms at $\lambda = 1.15$ μm is shown in Fig. 5, which, as we see, confirms the linear dependence of q on m established by Eq. (1). Using the procedure described above, we obtained the values for the real part of the effective index of the SEWs on silver (Table II, column 2).

TABLE II.

λ, μm	$\Delta n = n' - 1$	Re ε
3.39	$(8.2 \pm 1) \times 10^{-4}$	-600
1.15	$(7.3 \pm 0.3) \times 10^{-3}$	-70
0.63	$(3.2 \pm 0.03) \times 10^{-2}$	-16

To test the results obtained, the dependence of the reflection coefficient on the angle of incidence was measured on the same samples for p-polarized radiation at $\lambda = 3.39$ μm. The value calculated from the optical constants of the metal obtained $\Delta n(3.39\ \mu\text{m}) = (8 \pm 2) \times 10^{-4}$ coincides to within the experimental error with the value obtained by SEW spectroscopy. On the air–metal interface $n' = \sqrt{\varepsilon/(\varepsilon + 1)}$, where ε is the complex dielectric function of the metal.[3] Since Re $\varepsilon \gg$ Im ε for silver in the near-IR range, we can write

$$\text{Re } \varepsilon \approx \frac{-n'^2}{n'^2 - 1}.$$

The results obtained, which are presented in Table II (column 3), are close to the available literature data for sputtered silver films.[9] Similarly prepared films were previously studied by SEW phase spectroscopy with aperture excitation.[5] The SEW propagation parameters presented in Ref. 5 agree well with the data obtained in the present work, but the new scheme for exciting SEWs in the interferometer that we used permits improvement of the accuracy of the measurements.

This work was performed with partial support from the Russian Fund for Fundamental Research (Grants Nos. 95-02-04194 and 95-02-04195).

[1] E. V. Alieva, L. A. Kuzik, F. A. Pudonin *et al.*, Fiz. Tverd. Tela (Leningrad) **34**, 3233 (1992) [Sov. Phys. Solid State **34**, 1730 (1992)].
[2] V. Vaĭchkauskas, G. N. Zhizhin, and V. A. Yakovlev, Fiz. Tverd. Tela (Leningrad) **32**, 1833 (1990) [Sov. Phys. Solid State **32**, 1066 (1990)].
[3] *Surface Polaritons: Electromagnetic Waves at Surfaces and Interfaces*, V. M. Agranovich and D. L. Mills (Eds.), North-Holland, Amsterdam (1982).
[4] A. F. Goncharov, G. N. Zhizhin, S. A. Kiselev *et al.*, Phys. Lett. A **133**, 163 (1988).
[5] E. V. Alieva, V. A. Yakovlev, V. I. Silin, and A. Volkov, Opt. Commun. **96**, 218 (1993).
[6] Y. J. Chabal and A. J. Sievers, Appl. Phys. Lett. **32**, 90 (1978).
[7] N. J. Harrick, *Internal Reflection Spectroscopy* [Interscience, New York (1967); Mir, Moscow (1970)].
[8] V. V. Shevchenko, *Continuous Transitions in Open Waveguides* [Golem Press, Boulder, Colo. (1971); Nauka, Moscow (1969)].
[9] M. A. Ordal, L. L. Long, R. G. Bell *et al.*, Appl. Opt. **22**, 1099 (1983).

Translated by P. Shelnitz

Field evaporation of a Hf–Mo alloy

M. V. Loginov and V. N. Shrednik

A. F. Ioffe Physicotechnical Institute, Russian Academy of Sciences, 194021 St. Petersburg, Russia
(Submitted November 27, 1996)
Zh. Tekh. Fiz. **68**, 69–73 (March 1998)

The field evaporation of a Hf–Mo alloy (15 wt. % Hf) is investigated using a time-of-flight atom probe. A moderately heated tip detects an impurity of Hf and Mo oxides on the surface. Thermofield microprotrusions grown at $T=1440-1850$ K in an electric field (retarding to electrons) of intensity $E=(3.2-5)\times 10^7$ V/cm are analyzed at room temperature and above. © *1998 American Institute of Physics.* [S1063-7842(98)01103-9]

INTRODUCTION

Field evaporation[1] as applied to new materials is interesting in itself, being a result of an interaction of a strong electric field with a solid. At the same time, it underlies the creation of promising point ion sources for nanotechnologies.[2] A thin (fine) ion beam could be used for deposition on a substrate and for writing or drawing on the nanometer scale. In the case of low-temperature (cold) field evaporation, the tip, i.e., the source of the material, becomes dull with use and must be sharpened (preferably *in situ*), as in the case of writing with a pencil. If the source operates in a high-temperature (hot) evaporation field,[3] the ion flux forms during its operation and can differ with respect to its stability, geometric properties, and ionic composition.[2] All this determines the quality of the ''pen'' or ''marker'' for writing on the nanometer scale. Its quality can be influenced by utilizing the special features of hot field evaporation. This has been demonstrated in the case of several refractory metals: W, Mo, Ir, and Pt.[3–6] Alloys would be interesting in this context, since their employment would diversify the evaporated components and, in addition, would facilitate the formation of thin ion beams of some materials and thereby lower, for example, the working temperatures and fields.

While the ordinary cold field evaporation of alloys has been studied repeatedly,[7] mainly for analytical purposes, their hot field evaporation has not been studied at all. On the other hand, even when a regime of cold field evaporation was employed, the method of ''sharpening the pencil'' by growing thermofield microprotrusions, for example, was likewise scarcely considered in reference to alloys. Only one study in which such microprotrusions were grown on the basis of a Si{110}–W adsorption system can be noted.[8] However, a detailed study of the field evaporation of silicides from microprotrusions has been conducted quite recently.[9]

After selecting a Hf–Mo alloy (15 wt. % Hf) as a convenient and useful model, we studied two new problems in the present work: the cold field evaporation of thermofield microprotrusions grown on tips made from this alloy and the hot (high-temperature) field evaporation of this alloy. It should be noted that the conditions for crystal growth in a field and the composition of the corresponding growth formations, as well as the composition and geometry of the ion beams (especially in the case of hot field evaporation), are all of physical interest in themselves in the scarcely studied case of alloys even without regard to the problem of creating a nanometer writer.

EXPERIMENTAL METHOD

Atom probe microanalysis,[7] which employs a mass spectrometer combined with a field emission microscope, is a suitable method for the problems posed. In the present work we employed a field electron microscope, a field ion desorption microscope, and mass analysis of ions which have passed through the probe opening in a microchannel image amplifier. The time-of-flight atom probe of moderate resolution used in this work (its resolution was about 30) was described in detail in Ref. 10. The need to heat the tip required the inclusion of a heated arch, to which the tip was welded, in its electrical circuit. The tip could be heated at the moment when a high voltage (either constant or pulsed) was supplied to it. Tip temperatures in the range from room temperature to 2030 K were used in the investigation of field evaporation. In the pyrometric region the temperature was determined using a Piro optical micropyrometer, and in the nonpyrometric region it was determined from an extrapolation graph. The temperature was measured in the form of the heating current in the arch. Under high-temperature conditions it is difficult to avoid field evaporation at the constant (base) voltage. Satisfactory correct mass spectra with a selective character could be obtained only with a high contrast between the evaporation rates during the application of the pulsed voltage and at the base voltage. Values of the contrast (i.e., the ratio between these rates) from 10^4 to 10^6 can be considered sufficient, although, of course, not all the atoms evaporated from the surface are analyzed in this case.

The field-emission characteristic of the object was used to estimate the intensities of the working electric fields from the measured voltages. Experience showed that the hafnium in our alloy behaves as a surface-active material, being concentrated in the surface and near-surface layers. Therefore, in our estimates the work function φ of the surface was set equal to the value for hafnium, $\varphi=3.5$ eV (Ref. 11). The residual pressure under working conditions was about 10^{-8} Torr. The main components of the residual gas (nitro-

gen, carbon dioxide, and, despite the preliminary heating of the system, water) were detected. However, they could not influence the character of the growth and emission processes taking place at high temperatures.

RESULTS OF EXPERIMENTS AND DISCUSSION

a) Growth conditions and composition of the thermofield microprotrusions. The tips of the Hf–Mo alloy were heated to $T=1400-1650$ K in the absence of an electric field to clean the surface. The use of higher temperatures was undesirable, since it led to blunting of the tips and, accordingly, to an increase in the working voltages V (the latter were restricted to the $+20$ kV level for a constant voltage and 5.6 kV for a pulsed voltage). A moderately heated tip prepared from a Hf(15%)–Mo(85%) alloy contained surface irregularities that could not be removed by such heating. The electron emission image contained a set of bright spots, which were not always symmetrically arranged. In view of the high Hf content on the surface, it can be assumed that these spots are similar in nature to the contaminants on a Zr surface (an analog of Hf) described by Müller,[12] which cannot be removed by heating. We analyzed the mass spectra for cold (at ~ 300 K) field evaporation from these spots and discovered that they contain not only metallic Hf^{+++}, Hf^{++}, Mo^{+}, Mo^{++}, Hf_2^{+}, $HfMo^{+}$, $(HfMo)^{++}$, $(HfMo)^{+++}$, Hf^{+}, and other such ions, but also oxide HfO_2^{+++}, HfO^{++}, MoO^{+}, MoO_3^{+++}, $HfMoO_3^{+++}$, $HfMoO_2^{++}$, and $HfMoO_3^{4+}$ ions. The corresponding spectra from the dark area (outside the bright spots) contained practically the same set of ions, but the relative amplitudes of the peaks corresponding to the ions containing Mo (Mo^{+}, Mo^{++}, MoO^{+++}, MoO^{+}, $(HfMo)^{+++}$, and Hf_2Mo^{++}) were appreciably higher than in the spectra from the bright, strongly electron-emitting spots. Thus, the hafnium oxides were unquestionably the main thermostable surface contaminants.

The growth of thermofield microprotrusions on such a surface required heating the tip to a temperature T from 1440 to 1850 K (usually for 1 min) in the presence of a positive electric field of intensity $F=3.2\times10^7-5.0\times10^7$ V/cm. The voltage of negative polarity needed to observe the electron emission image of fixed brightness was usually lowered by a factor of 2 as a result of such treatment. In the case of high temperatures (1850 and 2030 K), the images of growing microprotrusions in ions of the host material could be observed on the screen of the field ion desorption microscope. At $T=1440$ K and moderate growth fields the desorption images of microprotrusions were observed considerably less frequently and were significantly duller. To ''quench'' the microprotrusions grown, the heating was first switched off, and only then was the voltage removed. The competitive growth and evaporation processes decayed with different rates as the cooling proceeded, and these differences could, in principle, alter the geometry and composition of the apices of the cooled microprotrusions. Therefore, we cautiously refer to estimation of the fields from the field-emission characteristics, rather than to measurements. The initial evaporating intensities of the base field (E_b) and the total (base+pulsed) field (F_p) were varied in the range from 1.1×10^8 to 1.8×10^8 V/cm for E_b and from 1.44×10^8 2.4×10^8 V/cm for F_p in accordance with the sharpness of the apex of the microprotrusion. The ratio of the amplitude of the pulsed voltage to the magnitude of the total voltage was equal to 0.25 when the six spectra of the series discussed below were obtained and 0.235 in only one case. As the field evaporation proceeded, the microprotrusions frequently became blunt, and the corresponding field intensities decreased by 15–20% at constant values of V_b and V_p by the end of the experiment. All the spectra of this series were obtained with a tip at room temperature.

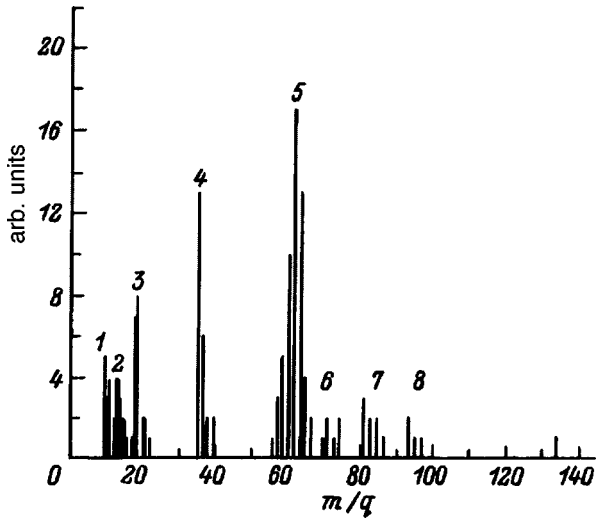

FIG. 1. Field evaporation spectrum of a thermofield microprotrusion obtained for a tip at room temperature. *1*—C^+, *2*—N^+, *3*—H_2O^+, *4*—Mo^{+++}, *5*—Hf^{+++}, *6*—$HfMo^{4+}$, *7*—$HfMoO_3^{4+}$, *8*—$HfMo^{+++}$. The residual pressure is 10^{-8} Torr, $V_b=12$ kV, and the amplitude of the applied pulses is 4 kV.

A typical spectrum of the ''cold'' field evaporation of a thermofield microprotrusion from the alloy investigated is shown in Fig. 1. The two strongest peaks correspond to triply charged Hf and Mo ions, the Hf peak being appreciably stronger. There are peaks for the residual gases and some impurities (C^+, N^+, and H_2O^+), as well as peaks with $m/q=72$, 81, and 93 (their presumable assignments are shown in the figure). According to our estimates, as the spectrum in Fig. 1 was obtained, E_b decreased from a value of 1.66×10^8 to 1.35×10^8 V/cm, and F_p decreased from 2.22×10^8 to 1.8×10^8 V/cm. This follows, for example, from the dependence of the accumulation of the ions detected n on the number of evaporating pulses N (Fig. 2). The mean effective evaporation rate during the action of an evaporating pulse up to the 230th pulse is about 2×10^7 ions/s, but from the 230th to 900th pulse it is 1.1×10^7 ions/s. The character of this dependence suggests that evaporation (which took place mainly at the base voltage) of a monatomic layer at the apex of the microprotrusion is completed in the first period (up to the 230th pulse) (the probe opening was aimed at the image of the microprotrusion and covered its central portion). As the evaporation of the first layer is completed, the evaporation rate increases. The second layer passing beneath the probe opening is evaporated more slowly, especially at the beginning. If it is assumed that the microprotrusion was in

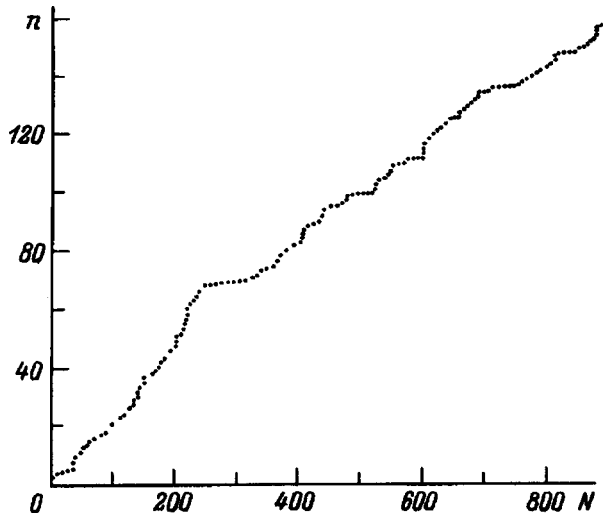

FIG. 2. Accumulation curve of the number of ions detected as a function of the cumulative number of voltage pulses for the spectrum in Fig. 1.

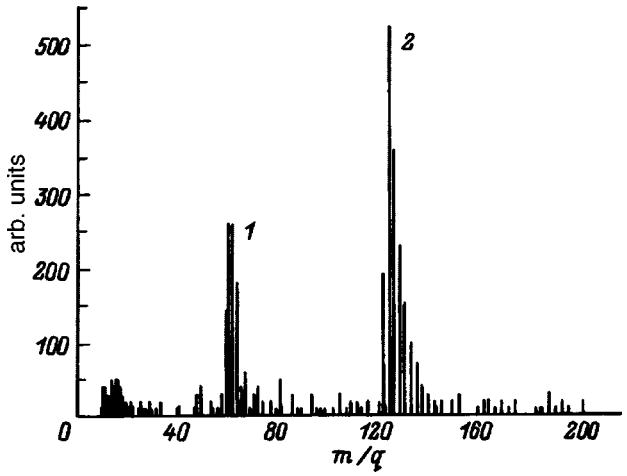

FIG. 3. High-temperature field evaporation spectrum of a microprotrusion obtained for a tip temperature equal to 1400 K. *1*—Hf^{+++}, *2*—Hf_2^{+++}. The residual pressure equals 10^{-8}, $V_B=12$ kV, and the amplitude of the applied pulses is 4 kV.

equilibrium with respect to the ponderomotive and capillary forces and that its diameter at the apex was no more than 300 Å,[13] an upper, probably overestimated, estimate of the number of atoms projected onto the probe opening would be 10^4 atoms. This permits estimation of the upper limit of the evaporation rate at the base voltage: 40 ions/s in the first period up to the 230th pulse and 15 ions/s in the second period. Accordingly, the contrast ω between the evaporation rates during the action of a pulse and at the base voltage is $5-7\times10^5$ or more. In the case of the other spectra of this series, ω lies in the range 10^5-10^6, according to similar estimates. The most pronounced peaks in the spectra are the peaks corresponding to Hf^{+++} and Mo^{+++} (which sometimes change places along the intensity scale), as well as $HfMo^{4+}$ ($m/q=71-72$). The other appreciable peaks include peaks corresponding to Hf^{++}, Mo^{++}, and $HfMoO_3^{4+}$ ($m/q=80-81$). In the initial experiments with an inadequately cleaned tip, the intensity of the peak for HfO^{++} was appreciable. The general conclusion from this series of experiments is that the thermofield microprotrusions growing on the alloy investigated are strongly enriched with hafnium. The microprotrusions can be grown repeatedly with reproducible results. Depending on their initial sharpness, they allow the cold evaporation of from several to tens of monatomic layers at a single voltage setting (i.e., without appreciable blunting). A fairly refractory material, viz., hafnium (with some molybdenum as an impurity), can be deposited by field evaporation at moderate fields for cold evaporation in the range $1.1-1.8\times10^8$ V/cm.

b) High-temperature field evaporation of the Hf–Mo alloy. The appearance of the image of a microprotrusion in the host ions on the screen of the field ion desorption microscope can easily be achieved by raising the temperature and increasing the field accelerating the positive ions. Such images were observed for our alloy at $T>1300-1350$ K in fields equal to $5-6\times10^7$ V/cm or more. At the smallest values of T and F the microprotrusion spots were dull and locally stable. At the highest values of F (up to 9×10^7 V/cm at $T=1440$ K) and especially at the maximum values of T (1850 K in our experiments) there were many spots, and they were bright and mobile.

A definite base voltage V_b was established after growing a microprotrusion which evaporates ions *in situ*, and then a desirable regime, for example, evaporation from a locally stable microprotrusion (toward which the probe opening or diaphragm was aimed) or from a large set of neighboring microprotrusions, which intermittently passed beneath the probe opening, was selected by varying T. An evaporation rate contrast sufficient for obtaining satisfactory selective evaporation spectra with a low noise level and clearly separated mass peaks was attained by varying the amplitude of the pulsed voltage. In most of the experiments of this series the ratio $V_p(V_p+V_b)$ was equal to 0.33, which was sufficient. In a few cases a value of 0.25 or (to cover all possibilities) 0.41 was used.

One of the typical and statistically reliable spectra of the hot field evaporation of the HfMo alloy is presented in Fig. 3. The spectrum contains two pronounced peaks corresponding to Hf_2^{+++} and Hf^{+++}. The field intensities at the base voltage and during the application of a pulse were estimated as 6×10^7 and 8×10^7 V/cm, respectively. The temperature of the tip was about 1400 K. Figure 4 displays a pulse accumulation curve of all the ions detected for the case of the spectrum in Fig. 3. The very characteristic curve in Fig. 4 attests to the nonuniformity in the collection of the ions: on the steep segments of the curve the mean effective evaporation rate reaches 6×10^7 ions/s during the application of a pulse, but there are less steep segments and even pauses in the collection of ions. It follows from the form of the curve that the moving microprotrusions passed at least three times (in the steep segments) exactly under the probe opening as they were rapidly evaporated. At other times only their edges were opposite the probe opening, or (in the pauses) they bypassed it. The small fluctuations on the curve are associated with fluctuations of the evaporation of the microprotrusions. The passage of the microprotrusions through the probe opening zone is demonstrated even more clearly by the ac-

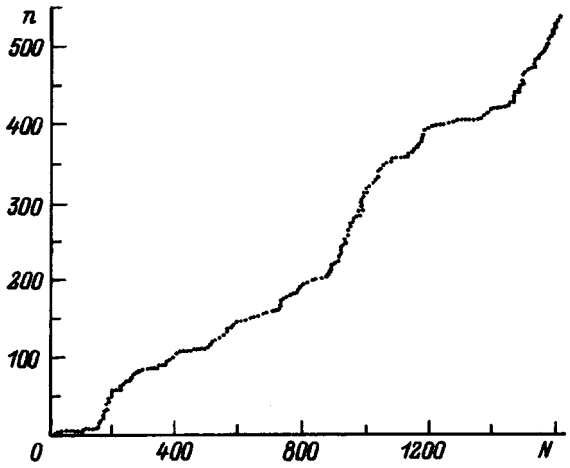

FIG. 4. Accumulation curve of the number of ions detected as a function of the cumulative number of voltage pulses for the case of the spectrum in Fig. 3.

cumulation curve for another spectrum (Fig. 5), where five steps, which are associated with the passage of the emitting spot through the probe opening zone, are clearly displayed. The spectrum corresponding to Fig. 5 was obtained at $T=1440$ K for the higher field intensities $E_b=9\times10^7-1.35\times10^8$ V/cm and $V_p/V_p+V_b=0.33$. In this case, too, there are two peaks for the Hf^{+++} and Hf_2^{+++} ions, but the peak for the dimer is lower than the peak corresponding to the monomer.

An analysis of 12 hot field evaporation spectra showed that the main components in the spectra are the Hf^{+++} and Hf_2^{+++} ions and that the peak for the monomer Hf^{+++} takes first place in cases of very strong fields. The polymeric cluster ions are characteristic of evaporation at high temperatures. For example, at 900 K the Hf_2^{+++} ion is not yet observed (and the Hf^{+++} peak is the most intense peak in the spectrum), while at $T=1325-1850$ K the Hf_2^{+++} peak is always present and is almost always the strongest peak. The other ions observed in the spectra are $HfMo^{++}$, Hf^{++}, and Hf_2Mo^{+++} (at 1325 K and relatively low evaporation rates during a pulse equal to 4.5×10^7 ions/s). At $T=1620-1660$ K, apart from the Hf^{+++} and Hf_2^{+++} ions mentioned above, the spectrum displays a strong peak corresponding to $HfMo_2^{+++}$ ions, which is sometimes the highest peak in the spectrum. At the highest temperature used, $T=1850$ K, peaks for Hf_2^{+++}, Hf_3^{4+}, Hf^{+++}, and $HfMo_2^{+++}$ are noticeable in order of decreasing intensities above the ''noise'' level. At high temperatures (1600–1850 K) evaporation rates during a pulse from 10^8 to 2×10^8 ion/s were typical, while in the range $T=1300-1440$ K the values varied from 4.5×10^7 to 8×10^7 ions/s.

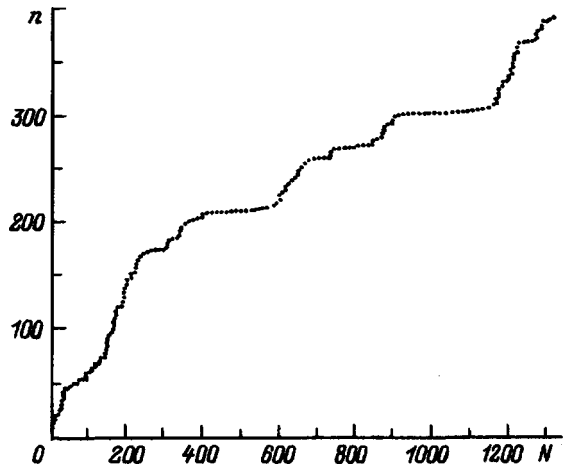

FIG. 5. Ion accumulation curve $n(N)$ for the hot field evaporation spectrum of a Hf–Mo alloy obtained for 1440 K, $V_b+V_p=(8+4)$ kV, and relatively high evaporating fields (up to 1.35×10^8 V/cm).

Thus, in a regime of hot field evaporation an alloy containing less than 10 at. % Hf preferentially supplies Hf in ion fluxes. The stationary ion currents (evaporation at the base voltage) are regulated by varying T and V_b and can apparently range from 10^5-10^6 ions/s from one spot[3] to appreciably smaller values. The selection of relatively weak currents is apparently more convenient for use in nanotechnologies, since a microprotrusion is locally stabilized under those conditions. At stationary currents less than 10^3 ions/s it becomes difficult to observe the images of spots on the screen of the field ion desorption microscope. However, by following the accumulation rate of the ions, we can see that microprotrusions exist and can move. On the other hand, the accumulation curves attest to appreciable local stabilization of a microprotrusion when $n(N)$ curves rise with small fluctuations, have a constant mean slope, and correspond to times measured in tens and hundreds of seconds.[1)] We observed such stable ion emission during a period from 150 to 400 s in half of the cases studied. The stable emission of ions detected during a pulse corresponds to stable stationary emission. While at high T (1620–1660 K) the observed stability is presumably only apparent (due to the numerous rapidly moving microprotrusions), at 1300–1400 K such stability definitely corresponds to prolonged emission from a single stationary microprotrusion. By adjusting T and V, we can extend the temporally and spatially stable emission to significantly greater times.

This work was carried out as part of the Physics of Solid-State Nanostructures State Program (Project No. 2-002, ''Flomaster'').

[1)]The pulse repetition rate is 1 Hz; therefore, the value of N on the horizontal axis on the graphs of the accumulation curves (Figs. 2, 4, and 5) also corresponds to the time in seconds.

[1] E. W. Müller and T. T. Tsong, *Field Ion Microscopy, Field Ionization, and Field Evaporation* [Pergamon Press, Oxford (1973); Nauka, Moscow (1980)].
[2] O. L. Golubev, E. L. Kontorovich, V. N. Shrednik, and Yu. A. Vlasov, in *Nanostructures: Physics and Technology. Abstracts of Invited Lectures and Contributed Papers. International Symposium*, St. Petersburg, (1994), pp. 223–234.
[3] Yu. A. Vlasov, V. G. Pavlov, and V. N. Shrednik, Pis'ma Zh. Tekh. Fiz. **12**(9), 548 (1986) [Sov. Tech. Phys. Lett. **12**(5), 224 (1986)].
[4] Yu. A. Vlasov, O. L. Golubev, and V. N. Shrednik, J. Phys., Colloque **49**, C6-131 (1988).
[5] O. L. Golubev, E. L. Kontorovich, and V. N. Shrednik, in *Eighth International Vacuum Microelectronics Conference, Portland, Oregon. Technical Digest* (1995), p. 447–449.

[6] O. L. Golubev, E. L. Kontorovich, and V. N. Shrednik, Zh. Tekh. Fiz. **66**(3), 97 (1996) [Tech. Phys. **41**, 284 (1996)].
[7] M. K. Miller and G. D. W. Smith, *Atom Probe Microanalysis: Principles and Applications to Materials Problems* [Materials Research Society, Pittsburgh, Pa. (1989); Mir, Moscow (1993)].
[8] V. G. Butenko, Yu. A. Vlasov, O. L. Golubev, and V. N. Shrednik, Surf. Sci. **266**, 165 (1992).
[9] M. V. Loginov and V. N. Shrednik, Zh. Tekh. Fiz. **67**(9), 102 (1997) [Tech. Phys. **42**, 1075 (1997)].
[10] M. V. Loginov, O. G. Savel'ev, and V. N. Shrednik, Zh. Tekh. Fiz. **64**(8), 123 (1994) [Tech. Phys. **39**, 811 (1994)].
[11] V. O. Fomenko and I. A. Podchernyaeva, *Emission and Adsorption Properties of Substances and Materials (A Handbook)* [in Russian], Atomizdat, Moscow (1975).
[12] E. W. Müller, Ergeb. Exakten Naturwiss. **27**, 290 (1953).
[13] Yu. A. Vlasov, O. L. Golubev, and V. N. Shrednik, Izv. Akad. Nauk SSSR, Ser. Fiz. **52**, 1538 (1988).

Translated by P. Shelnitz

Visualization of strains of diffusely scattering surfaces in the optical treatment of photographs of projected fringes using spatial filtering

A. M. Lyalikov

Ya. Kupala Grodno State University, 230023 Grodno, Belarus
(Submitted February 21, 1996; resubmitted December 16, 1996)
Zh. Tekh. Fiz. **68**, 74–78 (March 1998)

A method for visualizing deformed regions on diffusely scattering surfaces is proposed. The method is based on the spatial filtering of a wave diffracted on a photograph of projected fringes. The particular features of the visualization of strains for the cases of both planar and nonplanar surfaces are considered. The results of experimental testing of the method in a visualization of the strains of a flat aluminum plate are presented. © *1998 American Institute of Physics.* [S1063-7842(98)01203-3]

INTRODUCTION

Holographic interferometry is considered the most sensitive contactless testing method for studying small displacements and strains of a surface.[1,2] However, in many cases holographic interferometry is too sensitive for investigating real objects. Speckle photography and speckle holography, which permit regulation of the measurement sensitivity over a fairly broad range, are preferable methods for visualizing comparatively large displacements of diffusely scattering objects.[3–5] Fringe projection and the application of meshes to the diffusely scattering surface under investigation should be assigned to a separate group of methods for visualizing surface displacements and strains.[6,7] Unlike the foregoing methods, these methods do not require coherent light sources. In addition, fringe projection techniques are preferable for investigating normal surface displacements exceeding tens of microns.

Despite the differences in the implementation of the methods just cited for investigating diffusely scattering objects, they all require the introduction of a spatial carrier frequency in the recording stage, as well as utilization of the phenomenon of diffraction and spatial filtering in the stage of visualizing regions with displacements and strains on the surface under investigation.[8]

When flat plates, beams, etc. are investigated, the main information on the surface strains and stresses is provided by the first derivatives $\partial\omega/\partial x$ and $\partial\omega/\partial y$ of the normal displacement $\omega(x,y)$, the $0x$ and $0y$ axes lying in the plane of the surface under investigation.[7] The fringes of a double-exposure hologram observed normal to a plate after reconstruction are essentially lines of constant normal displacement $\omega(x,y)$. The moiré fringes observed when a deformed planar surface is visualized by fringe projection also describe the normal displacements of the surface investigated. The simplest method for differentiating displacement data is the optical differentiation of interferograms or moiré patterns.[7,9] Optical differentiation employing either the optical shearing of displacement patterns or the superposition of interferograms is applicable here in real time.[10]

In the present work the possibility of visualizing deformed regions of diffusely scattering surfaces is demonstrated on the basis of the optical treatment of photographs of projected fringes using spatial filtering.

The optical treatment of double-exposure holograms and speckle photographs using spatial filtering has been employed previously for the subtraction of images and for extracting information on the deformation and translational displacement of the object under investigation.[5,11–13]

We shall examine the optical treatment of photographs of projected fringes in monochromatic light for the case of a single photograph and for a pair of photographs oriented in optically conjugate planes.

OPTICAL TREATMENT OF A SINGLE PHOTOGRAPH

Let us assume that the object of investigation is a planar, diffusely scattering surface. After deformation, its surface differs from the planar situation. To simplify the mathematical manipulations, we assume that the optical axis of the photographic system used to record the photograph of the projected fringes is normal to the planar surface under investigation, that the linear magnification of the photographing system is equal to unity, and that the $x0y$ plane is parallel to both the planar surface under investigation and the recording plane of the photograph of projected fringes. If, for example, the projected fringes are oriented parallel to the $0x$ axis, in this case the amplitude transmission of the photograph of projected fringes can be represented in the form[7,14]

$$\tau(x,y)\sim\left\{1+\cos\left[\frac{2\pi y}{T}+\Phi(x,y)\right]\right\}^{-\gamma/2}, \tag{1}$$

where T is the period of the fringes observed in the region of the planar surface of the object and γ is the contrast coefficient of the photographic emulsion.

In (1) the phase $\Phi(x,y)$ is defined as

$$\Phi(x,y)=\frac{2\pi\omega(x,y)\tan\Theta}{T}, \tag{2}$$

where $\omega(x,y)$ is the normal displacement of the surface under investigation as a consequence of deformation of the object and Θ is the angle between the projected planes of the

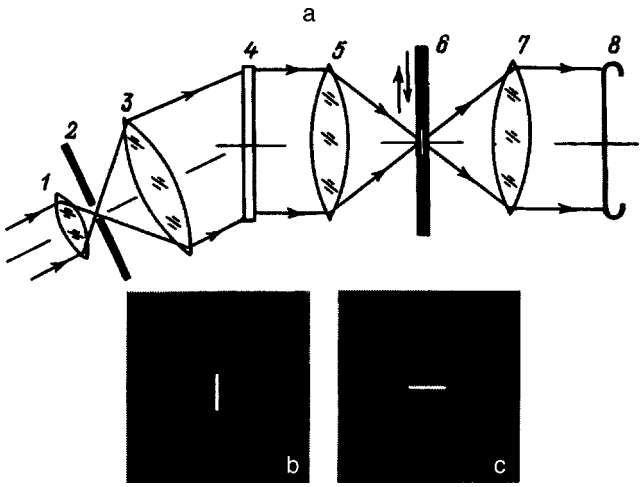

FIG. 1. Optical scheme of the apparatus for the optical treatment of photographs of projected fringes (a) and orientation of the visualizing slit diaphragm for the visualization of $\partial\omega/\partial x$ (b) and $\partial\omega/\partial y$ (c).

shadows creating the system of fringes on the object and a normal to the plane of the surface of the object.

As was noted in Ref. 14, the form of expression (1) for the amplitude transmission of a photograph of projected fringes corresponds to the amplitude transmission of a hologram of a phase object recorded with planar wave fronts, where $\Phi(x,y)$ describes the variation of the phase of the plane wave caused by the phase object. Drawing such an analogy between the amplitude transmissions of a photograph of projected fringes and a hologram of a phase object permitted the use of the methods for extracting information on the phase distribution, which have been developed to a high level in the holographic interferometry of phase objects, to visualize, for example, the relief of a diffusely scattering surface.[14,15]

It is seen from (2) that it is easy to go from derivatives of the phase $\Phi(x,y)$ to $\partial\omega/\partial x$ and $\partial\omega/\partial y$, which are of interest to us and specify the strains of the diffusely scattering surface under investigation. Because the variation of the intensity along the field in a wave diffracted on a photograph of projected fringes is more significant than the variation in a wave reconstructed from a hologram of a phase object, only the shadow methods,[16,17] for which the nonuniformity of the intensity in the wave does not influence the measured values of the derivatives of the phase $\Phi(x,y)$, can be chosen for quantitatively estimating the derivative of the phase $\Phi(x,y)$. Thus, shadow methods with a visualizing diaphragm in the form of a diffraction grating, a wire, or a slit, which performs spatial filtering in the Fourier plane of the objective, can be employed to quantitatively evaluate $\partial\omega/\partial x$ and $\partial\omega/\partial y$. In our opinion, of the types of spatial filters just cited, preference should be given to the slit as the most universal filter, which permits easy regulation of the width of the spectrum of spatial frequencies isolated.[18]

Figure 1a presents the optical scheme of an apparatus for the optical treatment of photographs of projected fringes, which permits the visualization of deformed regions of the diffusely scattering surface under investigation. A photograph of projected fringes *4* is illuminated by a collimated light beam from a point light source, which is formed in the rear focal plane of a microobjective *1* and is cut out by a circular diaphragm *2*, which has a small diameter equal to $\sim 10\ \mu$m. Microobjective *1* and objective *3* form a telescopic system. When the photograph *4* is illuminated by monochromatic light with a wavelength λ, we assume that the condition $\cos\alpha_0 = n\lambda/T$ is satisfied, where α_0 is the angle between the wave propagation direction and the $0y$ axis, and $n = 1,2,3,\ldots$. In this case the wave diffracted in the nth order propagates along a normal to the photograph *4*. The phase of the diffracted wave is defined as $[n\Phi(x,y)]$. This wave is focused by objective *5* and is obstructed in the Fourier plane of the latter by narrow slit diaphragm *6*, which is followed by objective *7*. The waves diffracted into other orders are obstructed by the opaque part of a visualizing diaphragm *6*.

Using the analogy between the case of the optical treatment of a photograph of form (1) under consideration and the shadow methods for investigating a wave front reconstructed by a hologram of a phase object, we can relate $\partial\omega/\partial x$ and $\partial\omega/\partial y$ to the displacements l_x and l_y of the image of a point source in the Fourier plane of objective *5*:

$$\frac{\partial\omega}{\partial x} \approx \frac{Tl_x}{f\lambda \tan\Theta}, \tag{3}$$

$$\frac{\partial\omega}{\partial y} \approx \frac{Tl_y}{f\lambda \tan\Theta}, \tag{4}$$

where f is the focal distance of objective *5*, and l_x and l_y are measured along the $0x$ and $0y$ axes, respectively.

Figure 1 presents the orientations of the slit diaphragm for visualizing the corresponding surface-displacement derivatives: $\partial\omega/\partial x$ (Fig. 1b) and $\partial\omega/\partial y$ (Fig. 1c). The edges of the slit are oriented strictly parallel to the $0y$ axis in the former case and to the $0x$ axis in the latter case.

The measurements of the first derivatives $\partial\omega/\partial x$ and $\partial\omega/\partial y$, which characterize the strains of the diffusely scattering surface, are performed in the following manner. Visualization of only the regions of the image of the surface under investigation where $\partial\omega/\partial x = 0$ for orientation of the visualizing slit diaphragm in Fig. 1b and where $\partial\omega/\partial y = 0$ for orientation of the diaphragm in Fig. 1c in plane *8* is achieved by moving the visualizing slit diaphragm *6*. In these cases only undeformed regions of the surface under investigation are illuminated in the observation plane *8*. Then, the deformed regions of the surface under investigation are visualized by discretely displacing the visualizing slit in the direction perpendicular to its edges. A series of patterns which visualize the deformed regions of the surface in plane *8* is thus obtained, and the values of the first derivatives $\partial\omega/\partial x$ and $\partial\omega/\partial y$ are determined from the measured displacements l_x and l_y of the visualizing slit relative to the position for visualizing the undeformed regions of the surface.

OPTICAL TREATMENT OF A PAIR OF PHOTOGRAPHS

The method described above for visualizing the deformed regions of a diffusely scattering surface is suitable only for the case in which the surface was planar before

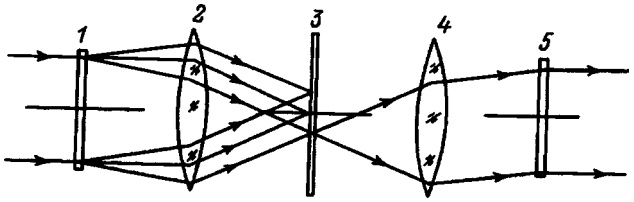

FIG. 2. Optical scheme for treating a pair of photographs of projected fringes.

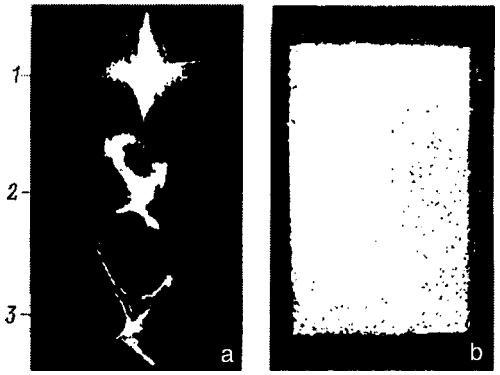

FIG. 3. Portion of the diffraction spectrum (a) and pattern observed in the visualization plane with complete isolation of the +1 diffraction order by a wide slit (b). *1*—Zeroth order, *2*—+1 order, *3*—+2 order.

deformation. In the case of a nonplanar surface, the visualization of regions with constant values of the first derivatives of the normal displacement requires consideration of the original shape of the relief or, more precisely, the first derivatives of the deviation $L(x,y)$ of the relief of the surface under investigation from a planar reference surface, i.e., $\partial L/\partial x$ and $\partial L/\partial y$.

The influence of the first derivatives of the deviation of the relief of the surface under investigation from a planar reference surface on the visualization of a deformed region of a nonplanar surface can be compared with the influence of the aberrations of a system for recording holograms of a phase object when the angles of deflection of light rays by the phase object are visualized.[18] Clearly, if the conditions

$$\left|\frac{\partial\omega}{\partial x}\right| \gg \left|\frac{\partial L}{\partial x}\right| \quad \text{and} \quad \left|\frac{\partial\omega}{\partial y}\right| \gg \left|\frac{\partial L}{\partial y}\right|, \tag{5}$$

hold, the deviation $L(x,y)$ of the surface relief from the plane can be neglected when strains are visualized.

Figure 2 presents an optical scheme for treating photographs of projected fringes, which permits subtraction of the influence of the relief of the nonplanar surface under investigation.

We assume that a pair of photographs of projected fringes has been recorded before and after deformation of a nonplanar, diffusely scattering surface. The amplitude transmissions of such photographs are described by (1), the phases for the first and second photographs being equal, respectively, to

$$\Phi_1(x,y) = \frac{2\pi L(x,y)\tan\Theta}{T}, \tag{6}$$

$$\Phi_2(x,y) = \frac{2\pi[L(x,y)+\omega(x,y)]\tan\Theta}{T}. \tag{7}$$

To eliminate the influence of $L(x,y)$ on the shape of the wave front under investigation, the two photographs are oriented in optically conjugate planes *1* and *5* (Fig. 2). Optical phase conjugation of the photographs is ensured by telescopic system *2*, *4* with onefold magnification.

When the first photograph *1* is illuminated along the normal in the optical treatment scheme under consideration, it can be shown[15] that a wave will propagate along the normal to the second photograph *5* with a phase specified by the difference $\{n[\Phi_2(x,y)-\Phi(x,y)]\}$, where n is the diffraction order isolated in the Fourier plane of objective *2* by circular filtering diaphragm *3*. In this case, according to (6) and (7), the phase of the wave is determined only by the displacement $\omega(x,y)$ due to deformation of the nonplanar surface under investigation.

To visualize the strains of nonplanar surfaces, the optical scheme of the apparatus in Fig. 1a is supplemented by a scheme for treating a pair of optically conjugate photographs instead of photograph *4* (Fig. 2). It should be noted here that the optical axes of the illumination and reception systems of the apparatus, unlike those in the case of the treatment of a single photograph, coincide. This should be taken into account in experimentally implementing the method.

Formulas (3) and (4) are used to determine the values of $\partial\omega/\partial x$ and $\partial\omega/\partial y$ in the visualized regions of the image of a nonplanar surface from the known values of the displacements of the visualizing slit l_x and l_y relative to the exactly oriented position.

The errors in the measurement of $\partial\omega/\partial x$ and $\partial\omega/\partial y$ in the optical treatment of both a single photograph and a pair of photographs of projected fringes can be estimated in analogy to the estimation of the resolving power of a monochromator[19,20] because of the virtual equivalence of the optical schemes. The error in the measurement of the first derivatives of the normal surface displacement is determined by the error in the determination of the spatial coordinate of the position of the slit relative to the exactly oriented position, i.e., δl_x and δl_y. The error in the determination of the coordinates is influenced by the finite width of the image of the point light source. This is attributed both to the diffraction phenomena due to the finite width of the light beams and to the aberrations of the optical elements of the system for the optical treatment of the photographs. In the case of a wide slit in the visualizing diaphragm, the diffraction phenomena, as well as the aberrations of the optical system can be neglected. In this case the accuracy of the measurements of $\partial\omega/\partial x$ and $\partial\omega/\partial y$ is determined by the width of the visualizing slit Δl. It is clear from simple arguments that the spatial coordinate in the Fourier plane of the objective cannot be measured more accurately than Δl. In this case the errors in the measurement of $\partial\omega/\partial x$ and $\partial\omega/\partial y$ are given by the expression

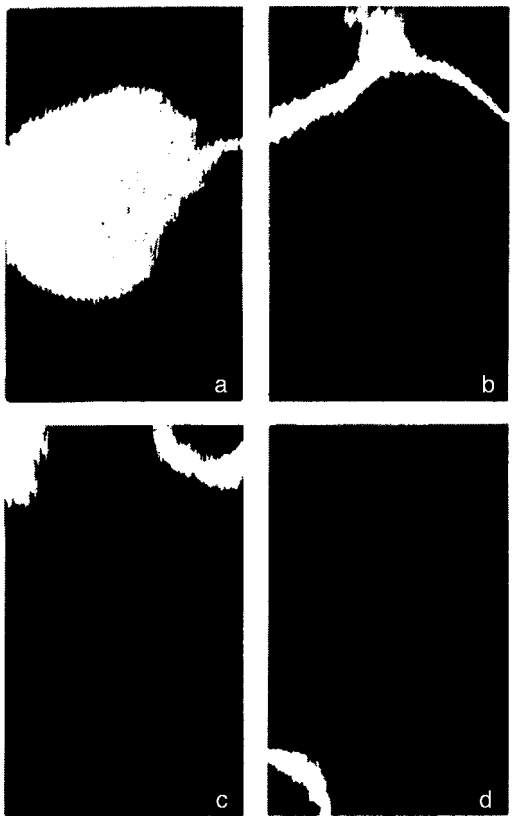

FIG. 4. Patterns visualizing deformed regions of a thin aluminum plate with different values of $\partial\omega/\partial y$.

$$\delta(\partial\omega/\partial x)=\delta(\partial\omega/\partial y)\approx\frac{T\Delta l}{n\lambda f\,\tan\Theta}. \tag{8}$$

It is seen from (8) that the error in the measurements of $\partial\omega/\partial x$ and $\partial\omega/\partial y$ is inversely proportional to the selected diffraction order n of the wave diffracted on the photographs of projected fringes being treated.

EXPERIMENTAL TESTING

The method developed for visualizing the strains of diffusely scattering surfaces as a result of the optical treatment of photographs of projected fringes was experimentally tested in the visualization of deformed regions of a flat rectangular aluminum plate, which had undergone large strains.

The photographs of projected fringes were recorded by projecting a system of interference fringes formed in a Mach–Zehnder interferometer upon the illumination of the latter by coherent light from a helium-neon laser onto the plate under investigation. The projected fringes were oriented perpendicularly to the $0y$ axis. The photographs were recorded on the Mikratizopan high-resolution photographic emulsion by a Zenit camera with a Gelios-44M objective at a relative aperture of 1:8. The optical axis of the photographic system coincided with a normal to the planar undeformed surface of the plate. The period of the visualized projected fringes on the deformed regions of the object was equal to 0.12 mm. When the photograph of projected fringes was optically treated according to the scheme shown in Fig. 1a, an LGN-125 helium-neon laser served as the coherent light source. Figure 3a presents a portion of the diffraction spectrum observed in the Fourier plane of objective *5* (Fig. 1a). The brightest diffraction order corresponds to a directly transmitted wave, i.e., to a wave diffracted into the zeroth order. Figure 3b presents the pattern observed in plane *8* (Fig. 1a) when the $+1$ diffraction order is completely isolated by a broad slit in the filtering plane *6*. This pattern demonstrates the practically uniform illumination of the entire image of the surface of the plate investigated.

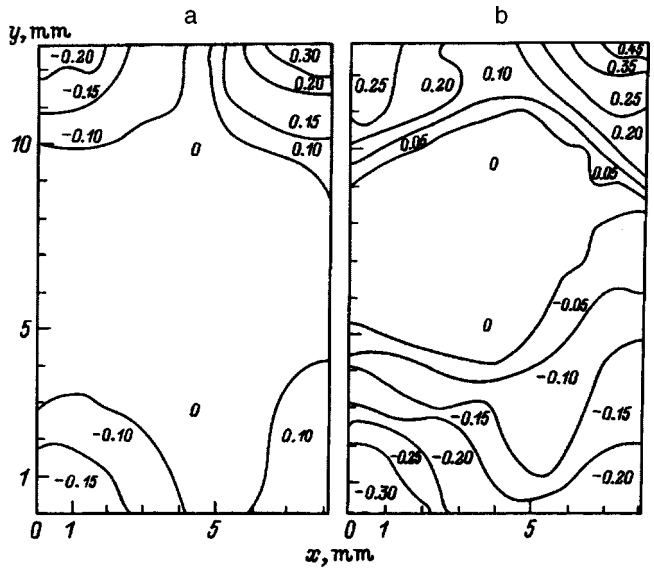

FIG. 5. Isolines of $\partial\omega/\partial x$ (a) and $\partial\omega/\partial y$ (b) for the aluminum plate investigated.

The deformed regions of the plate investigated were visualized by discretely scanning the $+1$ diffraction maximum by a narrow slit with a width of 50 μm. The scanning step was 50 μm. Figure 4 presents the patterns observed in plane *8* (Fig. 1a), which visualize regions of the image of the plate under investigation with different degrees of strain. The derivative $\partial\omega/\partial y$ equals 0 (a), 0.10 (b), and 0.25 (c,d). The pattern shown in Fig. 4a corresponds to visualization of an undeformed region of the plate investigated. Figure 5 presents patterns of the isolines of the deformed plate investigated with constant values of $\partial\omega/\partial x$ (a) and $\partial\omega/\partial y$ (b). The graphs were constructed from series of photographs which visualize deformed regions of the image of the plate.

Thus, the method considered permits not only visualization of the deformed regions of the diffusing scattering surfaces investigated, but also quantitative evaluation of the degree of strain.

[1] B. P. Hidebrand and K. A. Halnes, Appl. Opt. **5**, 595 (1966).
[2] E. B. Aleksandrov and A. M. Bonch-Bruevich, Zh. Tekh. Fiz. **37**, 360 (1967) [Sov. Phys. Tech. Phys. **12**, 258 (1967)].
[3] N. G. Vlasov, in *Proceedings of the 5th All-Union Seminar on Holography* [in Russian], LIYaF, Leningrad (1973), pp. 293–303.
[4] N. G. Vlasov, Yu. P. Presnyakov, and S. N. Smirnova, Zh. Tekh. Fiz. **43**, 1104 (1973) [Sov. Phys. Tech. Phys. **18**, 706 (1973)].
[5] I. S. Klimenko, *Holography of Focused Images and Speckle Interferometry* [in Russian], Nauka, Moscow (1985).
[6] R. K. Erf (Ed.), *Holographic Nondestructive Testing*, Academic Press [New York (1974); Mashinostroenie, Moscow (1979)].

[7] C. M. Vest, *Holographic Interferometry* [Wiley, New York (1979); Mir, Moscow (1982)].
[8] N. G. Vlasov and G. V. Skrotskiĭ, in *Proceedings of the 6th All-Union Seminar on Holography* [in Russian], LIYaF, Leningrad (1974), pp. 165–175.
[9] K. Patorski and M. Kujawinska, Appl. Opt. **24**, 3041 (1985).
[10] K. Patorski, D. Post, R. Cramek, and Y. Cuo, Appl. Opt. **26**, 1977 (1987).
[11] E. Archbold and A. E. Ennos, Opt. Acta **19**, 253 (1972).
[12] I. S. Klimenko, V. P. Ryabukho, B. V. Fedulyaev, and N. V. Lokhova, Zh. Tekh. Fiz. **53**, 888 (1983) [Sov. Phys. Tech. Phys. **28**, 568 (1983)].
[13] I. S. Klimenko and V. P. Ryabukho, in *Practical Topics in Holography. Proceedings of the 14th All-Union Seminar on Holography* [in Russian], LIYaF, Leningrad (1982), pp. 62–79.
[14] A. M. Lyalikov, Opt. Spektrosk. **74**, 865 (1993) [Opt. Spectrosc. **74**, 516 (1993)].
[15] A. M. Lyalikov, Opt. Spektrosk. **77**, 959 (1994) [Opt. Spectrosc. **77**, 863 (1994)].
[16] Yu. I. Ostrovsky, M. M. Butusov, and G. V. Ostrovskaya, *Interferometry by Holography* [Springer-Verlag, Berlin–New York (1980); Nauka, Moscow (1977)].
[17] A. K. Beketova, A. F. Belozerov, A. I. Berezkin *et al.*, *Holographic Interferometry of Phase Objects* [in Russian], Nauka, Leningrad (1979).
[18] A. M. Lyalikov, Opt. Spektrosk. **78**, 524 (1995) [Opt. Spectrosc. **78**, 473 (1995)].
[19] K. I. Tarasov, *Spectral Devices* [in Russian], Mashinostroenie, Moscow (1977).
[20] I. V. Skokov, *Optical Spectral Devices* [in Russian], Mashinostroenie, Moscow (1984).

Translated by P. Shelnitz

BRIEF COMMUNICATIONS

Use of the surface ionization of organic molecules for investigating some questions in geochemistry

O. K. Fomin and A. A. Khomichenko

Institute of Geology, Karelian Science Center, Russian Academy of Sciences, 185610 Petrozavodsk, Russia
(Submitted June 4, 1996; resubmitted April 2, 1997)
Zh. Tekh. Fiz. **68**, 79–81 (March 1998)

The possibility of using the surface ionization of organic molecules to investigate the organic matter in carbonaceous minerals is tested. It is shown in the example of shungite that the pyrolysis of such compounds releases organic molecules or radicals into the gas phase that are capable of being ionized on the surface of oxidized tungsten. © *1998 American Institute of Physics.* [S1063-7842(98)01303-8]

INTRODUCTION

The scientific and practical significance of the surface ionization of organic molecules on a number of different metals in vacuum[1–4] or in an atmosphere of air[5,6] became clear immediately after its discovery. A search for efficient ionizers and classes of organic compounds that are capable of being ionized on the surfaces of heated solids began. The first experiments showed that for the ionization of organic molecules upon contact with a surface, the latter must have both a large work function and catalytic properties.[7–9] This called for a search for efficient emitters,[10,11] and the ability of organic molecules to generate ions with a fairly high efficiency on hot oxidized molybdenum under the conditions of an air environment[6,8] created a promising new area in which this phenomenon can be utilized, viz., the detection of organic compounds in air.[12,13]

A great deal of work has been performed in searching for classes of organic compounds that are capable of being ionized on the surfaces of oxidized metals.[14–20] These studies formed the foundation for the extensive use of the surface ionization of organic compounds in scientific research. The surface ionization of organic compounds has been employed in physics, physical chemistry, analytical chemistry, and industrial ecology.[16,17] The discovery of the surface ionization of organometallic compounds[18,20] opened up new areas for using the surface ionization of organic compounds as a method of scientific research. For example, in geochemistry investigations of the chemical species and the mechanisms for the transport of metals in nature are of great interest.[21] Resolving these questions should help to solve several problems in geology, for example, ore formation. The problems of the formation and genesis of carbonaceous minerals (coal, shale, etc.) are no less important for geology. One of the ways to solve these problems is to find so-called biomarkers, i.e., organic compounds of biological origin. Biomarkers include compounds with fairly low ionization potentials (nitrogen- and sulfur-containing compounds and condensed aromatic compounds). The content of these substances in natural minerals is generally very small, and here the surface ionization of organic compounds with its unique surface and selectivity can be very useful.

To test the possibilities of the surface ionization of organic compounds in finding and identifying organic compounds in geological objects, we carried out a search for organic compounds which have fairly low ionization potentials in shungite—a carbonaceous material which has a long ($\sim 1.9\times 10^9$ years) and complex history.[22]

EXPERIMENT

Shungite of the first kind (the Shunga deposit, Karelia) was selected as the object of investigation. The experiments were carried out on an MI1201T mass spectrometer with the use of a two-ribbon ion source. The ion currents were measured by an electrometer using an electron multiplier with an open entrance as a preamplifier. The principal technical characteristics of the version of the instruments used were as follows: mass range, 1–300 a.m.u.; resolution, 600; sensitivity in the detection of ion currents, 10^{-18} A; stability of the ribbon heating currents, $\pm 0.05\%$; ribbon material, tantalum (vaporizer) and oxidized tungsten (ionizer); dimensions of the ribbons, $18\times 0.8\times 0.03$ mm. The shungite samples were ground in an agate mortar, and the powder obtained was used to prepare a suspension in triply distilled water (the last distillation step was carried out in a quartz apparatus). Five drops of the finely dispersed suspension were successfully applied to the vaporizer ribbon with intermediate drying in air at a temperature of about 100 °C. A blank sample was prepared in a similar manner: five drops of water were applied to the ribbon serving as the vaporizer in the blank experiment. The mass spectra were recorded at an ionizer temperature equal to ~ 430 °C, the temperature of the vaporizer being gradually raised from $t_{\min}$, which corresponds to radiative heating of the vaporizer from the ionizing ribbon, to $t_{\max}=1200$ °C by stepwise variation of the ribbon heating current in 0.4 A steps. In each vaporizer heating step, the mass spectrum was recorded in the range $m/e = 1-300$ a.m.u. The temperature of the ribbons was deter-

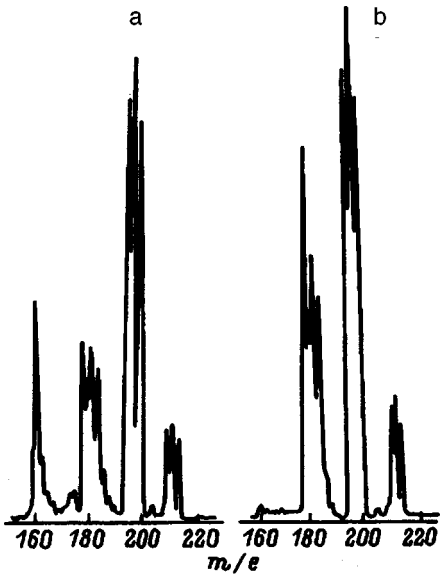

FIG. 1. Mass spectra of the organic compounds formed during the high-temperature pyrolysis of shungite in a vacuum. t_{vap}: a—890, b—1000 °C.

mined from the ribbon heating current below 800 °C and was measured by an optical pyrometer above 800 °C. The experiments were repeated with distilled water.

RESULTS AND DISCUSSION

The mass spectra obtained with a shungite sample and an oxidized tungsten ionizer contained not only lines for ions of alkali and alkaline-earth metals, whose main source was the ribbon material, but also groups of lines that are not observed in the blank experiment. The corresponding fragments of the mass spectra obtained at two vaporizer temperatures are presented in Fig. 1. It follows from these spectra that at temperatures near 1000 °C complicated fragmentation reactions of the residues of organic matter take place in shungite. The products of this fragmentation can thus be detected at the time of their release by surface-ionization mass spectrometry, apparently because of their low ionization potentials. The group of lines in the range $m/e = 158-166$ a.m.u. can be observed only in a narrow temperature range near $t_{vap} \sim 900$ °C, and the remaining groups of lines remain in the mass spectrum up to $t_{vap} = 1100$ °C, at which their intensity begins to decrease appreciably with time. The character of the dependence of the most intense line from these three groups on the vaporizer temperature is shown in Fig. 2. The intensities of the remaining lines vary in a similar manner.

Because of the inadequacy of the data on the surface ionization of organic molecules, it is difficult to precisely identify the compounds responsible for the mass spectrum observed in our case. However, the current ideas regarding the chemical nature of biomarkers and the characteristics of the mass spectrum that we obtained in the mass range 178–214 allow us to advance the following hypothesis regarding the nature of the molecules responsible for the mass spectrum and the processes taking place in shungite at temperatures above 800 °C: the pyrolysis of the organic matter in

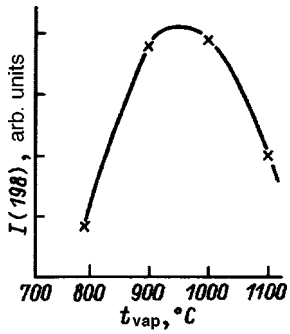

FIG. 2. Dependence of the intensity of the line with $m/e = 178$ on the vaporizer temperature.

shungite is accompanied by the release of light particles (H, H_2, H_2O, CO, CO_2, and hydrocarbon particles up to C_4) and the formation of phenanthrene and its derivatives, which have sufficiently low ionization potentials to be efficiently ionized on heated oxidized tungsten. The presence of the phenanthrene ion ($m/e = 178$) in the mass spectrum suggests that the biomarkers found in shungite can be steroids.

The results obtained should be regarded as preliminary findings for the investigation of problems concerning the organic matter in carbon-containing rocks using the surface ionization of organic compounds. They are intended to illustrate the prospects of the surface ionization of organic compounds as a method for investigating geochemical problems associated with the presence of organic compounds in rocks. We plan to expand our investigations of shungites using this method in the future.

[1] G. H. Pelmer, *Advances in Mass Spectrometry*, Pergamon Press, London and other cities (1959), p. 89.
[2] E. I. Agishev and Yu. I. Belyakov, Zh. Tekh. Fiz. **30**, 223 (1960) [Sov. Phys. Tech. Phys. **5**, 201 (1960)].
[3] É. Ya. Zandberg and N. I. Ionov, Dokl. Akad. Nauk SSSR **141**, 139 (1961).
[4] O. K. Fomin, M. V. Tikhomirov, and N. N. Tunitskiĭ, Zh. Tekh. Fiz. **34**, 1441 (1964) [Sov. Phys. Tech. Phys. **9**, 763 (1964)].
[5] O. K. Fomin and M. V. Tikhomirov, Zh. Fiz. Khim. **38**, 725 (1964) [Russ. J. Phys. Chem. **38**, 383 (1964)].
[6] O. K. Fomin and M. V. Tikhomirov, Zh. Fiz. Khim. **38**, 813 (1964) [Russ. J. Phys. Chem. **38**, 444 (1964)].
[7] S. S. Stroeva, L. A. Rudnitskiĭ, O. K. Fomin *et al.*, Kinet. Katal. **5**, 355 (1964).
[8] O. K. Fomin, M. V. Tikhomirov, and N. N. Tunitskiĭ, Kinet. Katal. **6**, 634 (1965) [Kinet. Catal. **6**, 565 (1965)].
[9] O. K. Fomin and M. V. Tikhomirov, Kinet. Katal. **6**, 764 (1965) [Kinet. Çatal. **6**, 687 (1965)].
[10] É. Ya. Zandberg, U. Kh. Rasulev, and Sh. M. Khalikov, Zh. Tekh. Fiz. **46**, 832 (1976) [Sov. Phys. Tech. Phys. **21**, 483 (1976)].
[11] F. T. Ishii, Int. J. Mass Spectrom. Ion Processes **87**(11), 51 (1989).
[12] O. K. Fomin, in *Gas Chromatography* [in Russian], NIITEKhIM, Moscow (1964), pp. 65–72.
[13] O. K. Fomin, N. N. Tunitskiĭ, and M. V. Tikhomirov, Inventor's Certificate (USSR) No. 179509 [in Russian]; Byull. Izobret., No. 5, (1966).
[14] É. Ya. Zandberg and U. Kh. Rasulev, Usp. Khim. **51**, 1425 (1982).
[15] A. Ya. Nezdyurov, V. I. Paleev, and D. A. Ponomarev, Teor. Éksp. Khim., No. 2, 180 (1986).
[16] É. Ya. Zandberg, in *Surface Methods of Ionization in Mass Spectrometry* [in Russian], Ufa, (1986), pp. 5–26.
[17] É. Ya. Zandberg, Zh. Tekh. Fiz. **65**(9), 1 (1995) [Tech. Phys. **40**, 865 (1995)].
[18] V. I. Paleev, Teor. Éksp. Khim. **19**, 59 (1983).
[19] F. T. Ishii, Chem. Phys. Lett. **163**, 69 (1989).

[20] F. T. Ishii, Int. J. Mass Spectrom. Ion Processes **104**, 129 (1991).
[21] E. Yu. Buslaeva and M. I. Novgorodova, *Organometallic Compounds in the Problem of the Migration of Ore Silver* [in Russian], Nauka, Moscow (1989).
[22] M. M. Filippov, A. I. Golubev, P. V. Medvedev *et al.*, *Organic Matter in Shungite-Bearing Rocks in Karelia (Genesis, Evolution, and Methods of Study)* [in Russian], Karel'skiĭ Nauchnyĭ Tsentr Ross. Akad. Nauk, Petrozavodsk (1994).

Translated by P. Shelnitz

Theorem on the kinetic energy in an elastic continuum with defects

Yu. V. Grinyaev and N. V. Chertova

Institute of the Physics and Strength and Materials Engineering, Siberian Branch of the Russian Academy of Sciences, 634048 Tomsk, Russia

(Submitted April 8, 1997)
Zh. Tekh. Fiz. **68**, 82–83 (March 1998)

An expression of the theorem on the kinetic energy for an elastic continuum with dislocations is derived on the basis of the dynamical equations of a gauge model of the medium. This relation shows that the work performed by internal surface stresses in the volume is redistributed between the work performed by the effective stresses at the rates of the effective elastic distortions and plastic distortions. In phenomenological theories of plasticity the latter quantity, representing the rate of energy dissipation, governs the dissipative processes. An expression is obtained which relates the rate of energy dissipation with the self-energy density of the field of the defects and the energy flux of the defects. © *1998 American Institute of Physics.* [S1063-7842(98)02902-X]

According to Ref. 1, one of the most important consequences of the dynamical equations of motion of a medium is the kinetic energy theorem. We shall obtain and analyze a similar relation for an elastic continuum with dislocations, which is described in a gauge approach.[2,3] The simplest Lagrangian of the gauge model has the form

$$L=\rho D_0\mathbf{u}D_0\mathbf{u}-D\mathbf{u}:C:D\mathbf{u}+BI:I-S\alpha:\alpha, \tag{1}$$

where

$$D_0\mathbf{u}=\frac{\partial\mathbf{u}^{\mathrm{el}}}{\partial t}+\mathbf{v}, \quad D\mathbf{u}=\nabla\mathbf{u}^{\mathrm{el}}+\beta^{\mathrm{el}\,D},$$

$$I=\frac{\partial\beta^{\mathrm{el}\,D}}{\partial t}-\nabla\mathbf{v}, \quad \alpha=\nabla\times\beta^{\mathrm{el}\,D}.$$

In these expressions ρ is the density of the medium; C is a rank-four tensor of the elastic constants; $\mathbf{u}^{\mathrm{el}}$ is the vector of elastic displacements; $\mathbf{v}$ is the velocity of the material points, which are due to the motion of the defects; $\beta^{\mathrm{el}D}$ is an incompatible elastic distortion; α and I are the dislocation density and dislocation flux tensors; and, B and S are new constants of the theory. Here and below a colon designates a scalar contraction with respect to the first and second indices and $\times$ denotes a vector product. Varying the Lagrangian (1) with respect to the independent variables $\mathbf{u}^{\mathrm{el}}$, $\beta^{\mathrm{el}\,D}$, and $\mathbf{v}$, we obtain the dynamical equations of the medium[2,3] in the form

$$\nabla\cdot\sigma=\frac{\partial}{\partial t}\rho\mathbf{V}, \tag{2}$$

$$B\nabla\cdot I=-\rho\mathbf{V}, \tag{3}$$

$$S\nabla\times\alpha=-B\frac{\partial I}{\partial t}-\sigma. \tag{4}$$

Here $\sigma=C:D\mathbf{u}$ is the tensor of effective stresses, and $\mathbf{V}=D_0\mathbf{u}$ is the total velocity of the elastic continuum with defects. Equations (3) and (4), supplemented by the well-known continuity equations[4,5]

$$\nabla\times I=\frac{\partial\alpha}{\partial t}, \tag{5}$$

$$\nabla\cdot\alpha=0, \tag{6}$$

comprise a complete system of field equations of a dislocation ensemble. The dynamic equation of equilibrium (2) is a compatibility condition for the system. Let us form a scalar product of this equation and the velocity $\mathbf{V}$ and integrate over the volume W of the body bounded by the surface S

$$\int_W(\nabla\cdot\sigma)\cdot\mathbf{V}dW=\int_W\left(\frac{\partial}{\partial t}\rho\mathbf{V}\right)\cdot\mathbf{V}dW. \tag{7}$$

Using the equality

$$\nabla\cdot(\sigma\cdot\mathbf{V})=(\nabla\cdot\sigma)\mathbf{V}+\sigma:\nabla\mathbf{V}, \tag{8}$$

we write Eq. (7) in the form

$$\int_W\nabla\cdot(\sigma\cdot\mathbf{V})dW=\int_W\left[\sigma\cdot\nabla\mathbf{V}+\frac{\partial}{\partial t}\frac{\rho V^2}{2}\right]dW \tag{9}$$

or

$$\int_S\mathbf{n}\cdot\sigma\cdot\mathbf{V}dS=\int_W\left[\sigma:\nabla\mathbf{V}+\frac{\partial}{\partial t}\frac{\rho V^2}{2}\right]dW, \tag{10}$$

where $\mathbf{n}$ is the outer normal to the surface S.

If we now introduce the vector of surface forces

$$\mathbf{t}=\mathbf{n}\cdot\sigma, \tag{11}$$

then the left-hand side of the equality (10) will represent the rate of change of the work performed by the surface forces

$$\int_S\mathbf{t}\cdot\mathbf{V}dS=\int_W\left[\sigma:\nabla\mathbf{V}+\frac{\partial}{\partial t}\frac{\rho V^2}{2}\right]dW. \tag{12}$$

The first term on the right-hand side of Eq. (10) determines the rate of change of the work performed by the internal surface stresses in the bulk. Since

$$\nabla \mathbf{V} = \frac{\partial}{\partial t} \nabla \mathbf{u}^{\mathrm{el}} + \nabla \mathbf{v} \tag{13}$$

and at the same time, according to Ref. 6,

$$\nabla \mathbf{v} = \frac{\partial \beta^{\mathrm{el}\,D}}{\partial t} + \frac{\partial \beta^{\mathrm{pl}\,D}}{\partial t} = \frac{\partial \beta^{\mathrm{el}\,d}}{\partial t} - I,$$

where $\beta^{\mathrm{pl}\,D}$ is an incompatible plastic distortion due to the defects, and the rate of change of the work performed by the internal surface stresses in the bulk can be written in the form

$$\int_W \sigma : \nabla \mathbf{V} dW = \int_W \sigma : \frac{\partial B}{\partial t} dW - \int_W \sigma : I dW. \tag{14}$$

Here $\beta = Du$ represents the effective stresses of the distortion, and the corresponding integral in Eq. (14) represents the work performed by the effective stresses at the rates of elastic distortions. The second integral is most interesting. It expresses the work performed by the effective stresses at the rates of the plastic distortions. In phenomenological theories of plasticity the dissipation of energy is described by this quantity, which determines the rate of energy dissipation on plastic distortions. Summing Eqs. (10)–(14), we obtain finally the expression

$$\frac{\partial}{\partial t} \int_W \rho \frac{V^2}{2} dW = \int_S \mathbf{t} \cdot \mathbf{V} dS + \int_W \sigma : \frac{\partial \beta}{\partial t} dW - \int_W \sigma : I dW, \tag{15}$$

which shows that the rate of change of the kinetic energy of a finite individual volume of an elastic continuum with dislocations is determined by the rate of change of the work performed by the external and internal surface forces and by the rate of dissipation of energy. Therefore, in the gauge theory of the medium, in contrast to the phenomenological theories of plasticity, a term describing the dissipation of energy appears automatically in the expression of the kinetic energy theorem without any physical assumptions. To determine how the rate of dissipation of energy is related with the characteristics of the dislocation ensemble, let us examine the last integral on the right-hand side in Eq. (14) in greater detail, substituting the expression for σ from the field equation (4),

$$\int_W \sigma : I dW = -\int_W \left(S \nabla \times \alpha + B \frac{\partial}{\partial t} I \right) : I dW. \tag{16}$$

Let us add to this expression the integral, which is identically equal to zero, from Eq. (3), scalar-contracting it twice with α,

$$S \int_W \left(\nabla \times I + B \frac{\partial \alpha}{\partial t} \right) : \alpha dW. \tag{17}$$

Using the identity

$$\nabla \cdot (\alpha \times I) = (\nabla \times \alpha) : I - (\nabla \times I) : \alpha,$$

we finally obtain the expression

$$\int_W \sigma : \beta^{\mathrm{pl}\,D} dW = \frac{\partial}{\partial t} \int_W \frac{S\alpha^2 + BI^2}{2} dW + S \int_S dS \cdot (\alpha \times I), \tag{18}$$

which shows that the rate of energy dissipation in an elastic continuum with dislocations is determined by the rate of change of the self-energy of the field of defects and the energy flux of the field of the defects. The quantity $\alpha \times I$, which determines the energy flux of the field of defects, is similar to the Poynting vector in electrodynamics.

In closing, we note that the expression for the kinetic energy theorem[1] contains, besides an increment to the work performed by the external and internal surface forces, an increment to the work performed by the body forces (internal and external), which likewise can be taken into account in the initial model (1) and obtained in expression (15).

[1] L. I. Sedov, *A Course in Continuum Mechanics* (translation of 1st Russian edition), Wolters-Noordhoff, Groningen, 1971–1972 [cited Russian original, Nauka, Moscow, 1987, Vol. 1].
[2] A. Kadić and D. Edelen, *A Gauge Theory of Dislocations and Disclinations*, Springer-Verlag, Berlin, 1983 [Russian translation, Mir, Moscow, 1987].
[3] Yu. V. Grinyaev and N. V. Chertova, Izv. Vyssh. Uchebn. Zaved. Radiofiz. **2**, 34 (1990).
[4] L. D. Landau and E. M. Lifshitz, *Theory of Elasticity*, Pergamon Press, New York, 1986; Nauka, Moscow, 1987.
[5] A. M. Kosevich, *Crystal Lattice Theory* [in Russian], Vysshaya Shkola, Kharkov, 1988.
[6] Yu. V. Grinyaev and N. V. Chertova, Pis'ma Zh. Tekh. Fiz. **22**(10), 34 (1996) [Tech. Phys. Lett. **22**, 391 (1996)].

Translated by M. E. Alferieff

One- and two-front states of equilibrium in a thin superconducting film

A. S. Rudyĭ

Istituto per la ricerca di base Castello Principe Pignatelli, 1-86075 Monteroduni (IS), Molise, Italy
(Submitted May 19, 1997; resubmitted August 4, 1997)
Zh. Tekh. Fiz. **68**, 84–87 (March 1998)

Two-phase states of equilibrium of a thin superconducting film carrying a current under conditions of convective heat exchange at the free surface of the film are studied. It is shown that for a classical superconductor the two-phase state of the film remains a single-front state over a wide range of parameters of the system. For high-T_c superconductors there exists a maximum value of the Steckl number above which weakly nonequilibrium stationary states can only be multifront states. The solutions of the boundary-value problem modeling a two-front state of equilibrium are investigated, and the conditions under which they obtain are examined. © *1998 American Institute of Physics.* [S1063-7842(98)03002-5]

1. The main factor limiting the sensitivity of superconducting IR detectors is thermal noise—primarily fluctuations of the temperature of the cooling liquid. W. Franzen proposed a nonisothermal bolometer, which is not so critically dependent on thermostatting accuracy.[1] A free superconducting film, part of which is in a normal state, can be used as a nonisothermal bolometer. In this connection it is of interest to analyze the two-phase states of a superconducting film over a wide range of thermophysical and electrophysical parameters.

The two-phase states of equilibrium of a thin superconducting film carrying a current were studied in Ref. 2. The main results of this work reduce to the following. The state of the system under study is determined by the control parameter $\sigma=\sigma_0/(1-\varepsilon\sigma_0)$, where $\varepsilon=\beta T_c$, σ_0 is the Steckl number, β is the temperature coefficient of the resistance of the film, and T_c is the difference between the critical temperature and the thermostat temperature. Above the critical value of the control parameter σ_c, the superconducting state is metastable, and a region of normal phase can form at the center of the film. The position of the phase boundary ξ_b in the general case is given by the condition

$$\coth[\sqrt{2\mathrm{Bi}_n(1-\varepsilon\sigma_0)}(1-\xi_b)]\coth\sqrt{\mathrm{Bi}_s}\xi_b = \frac{(1+\varepsilon)\sigma_0-1}{\sqrt{1-\varepsilon\sigma_0}}\sqrt{\frac{\lambda_n}{\lambda_s}}, \tag{1}$$

where $\mathrm{Bi}=\alpha l^2/h\lambda$, α is the heat-transfer coefficient, l and h are, respectively, the length and thickness of the superconductor, and λ_s and λ_n are the thermal conductivity of the superconducting and normal phases.

In the special case of a classical superconductor the parameter ε is so small that $\sigma_0 \ll 1/\varepsilon$ almost always. In Ref. 2 it was shown for this case that there exist two nonuniform states of equilibrium $\xi_b^{(1)}$ and $\xi_b^{(2)}$, where $\xi_b^{(1)}<\xi_b^{(2)}$, of which the state $\xi_b^{(1)}$ turned out to be stable.

2. For high-T_c superconductors $1/\varepsilon$ and σ_0 are comparable quantities, so that the cases $\sigma_0<1/\varepsilon$ and $\sigma_0>1/\varepsilon$ should be distinguished. If $\sigma_0\in[0,1/\varepsilon]$, then the situation is similar to that studied in Ref. 2 for a classical superconductor (Fig. 1a). Qualitative changes occur for $\sigma_0>1/\varepsilon$, when the coordinate of the phase boundary is determined by the condition

$$\cot[\sqrt{2\mathrm{Bi}_n(\varepsilon\sigma_0-1)}(1-\xi_b)]\coth\sqrt{\mathrm{Bi}_s}\xi_b = \frac{(1+\varepsilon)\sigma_0-1}{\sqrt{\varepsilon\sigma_0-1}}\sqrt{\frac{\lambda_n}{\lambda_s}}. \tag{2}$$

If the phase boundary $\xi_b^{(2)}$ of the unstable state approaches 1 asymptotically, as shown in Fig. 1b, then the boundary of the stable state $\xi_b^{(1)}\to 0$ as $\sigma_0\to\sigma_{c1}$. This result can be easily explained, taking account of the fact that as $\sigma_0\to\sigma_{c1}=1/\varepsilon+\pi^2/8\varepsilon\mathrm{Bi}_n$, the temperature of the normal phase

$$\Theta_n(\xi)=1+\left(\frac{(1+\varepsilon)\sigma_0-1}{\varepsilon\sigma_0-1}\right)\times\left[\frac{\cos\sqrt{2\mathrm{Bi}_n(\varepsilon\sigma_0-1)}(1-\xi)}{\cos\sqrt{2\mathrm{Bi}_n(\varepsilon\sigma_0-1)}(1-\xi_b)}-1\right] \tag{3}$$

approaches ∞. Therefore, σ_{c1} is the maximum (in the approximation studied) value of the Steckl number for a high-T_c superconductor.

Nonetheless, above σ_{c1} with $\sigma_0=\sigma_{c2}$ a new stationary state (Fig. 1b) that does not correspond to the conditions of the problem posed in Ref. 2 appears near the stability boundary. Indeed, in the formulation of the boundary-value problem it was assumed that the temperature of the normal phase is a monotonic function of the coordinate. Nonmonotonicity of the temperature, provided that it is symmetric with respect to the center of the film, would signify the possibility of multifront states of equilibrium forming. Since now the temperature (3) is periodic and therefore is not always a monotonic function of the spatial variable, Eq. (2) must be supplemented by the requirement of monotonicity:

$$\Theta_n'(\xi)>0, \quad \xi\in[\xi_b,1]. \tag{4}$$

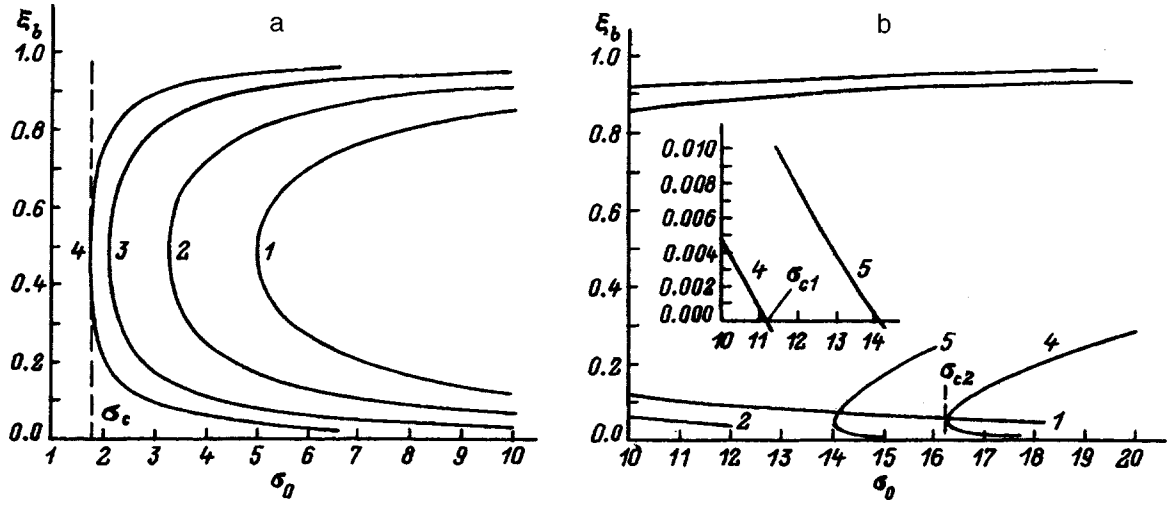

FIG. 1. Structure of the separation of the phase plane of a high-T_c superconducting film with $\varepsilon=0.1$. a—$\sigma_0<1/\varepsilon$: Below the first critical value of the Steckl number σ_c the state of the film is uniform, above σ_c the superconducting state is metastable and a normal-phase region, whose boundary as a function of the Steckl number is represented by the curves *1*–*5*, corresponding to Bi=0.5, 1, 3, 10, 15, can form at the center of the film; b—$\sigma_0>1/\varepsilon$, σ_{c1}—second critical value of the Steckl number, which determines the physical boundaries of the nonuniform state of a linear system.

From the latter equation follows the equation for the separatrix

$$\xi_b=1-\frac{\pi}{\sqrt{2\mathrm{Bi}_n(\varepsilon\sigma_0-1)}}, \tag{5}$$

which separates the phase plane into a region of the single-front (we have in mind the number of fronts on the segment studied) and multifront states (Fig. 2). Therefore if states of equilibrium exist above σ_{c2}, then they can only be multi-front states. However, this does not mean that multifront states cannot arise below σ_{c2} or σ_{c1}.

3. Let us examine the simplest case of a two-front state of equilibrium, when the center of the film is in a superconducting state. In view of the symmetry of the temperature field, we shall formulate the boundary-value problem only for the positive semiaxis, placing the origin of coordinates at the center of the film (Fig. 3),

$$\Theta_{s1}''(\xi)-2\mathrm{Bi}_s\Theta_{s1}(\xi)=0,$$

$$\Theta_n''(\xi)-\varkappa\Theta_n(\xi)+K=0,$$

$$\Theta_{s2}''(\xi)-2\mathrm{Bi}_s\Theta_{s2}(\xi)=0,$$

$$\Theta_{s1}(\xi_1)=\Theta_n(\xi_1)=1;\quad \lambda_s\Theta_{s1}'(\xi_1)=\lambda_n\Theta_n'(\xi_1),$$

$$\Theta_n(\xi_2)=\Theta_{s2}(\xi_2)=1;\quad \lambda_n\Theta_n'(\xi_2)=\lambda_s\Theta_{s2}'(\xi_2),$$

$$\Theta_{s1}'(\xi)|_{\xi=0}=0;\quad \Theta_{s2}(1)=0. \tag{6}$$

Here Θ_{s1}, Θ_{s2}, and Θ_n are the temperatures, normalized to T_c, of the superconducting regions and the normal phase,

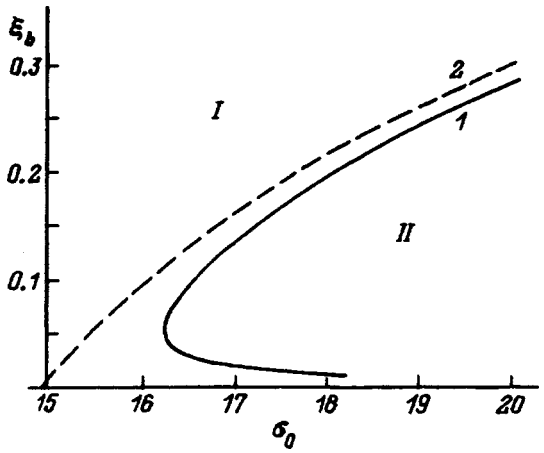

FIG. 2. Coordinate of the phase boundary versus the Steckl number *1* and the separatrix *2*, dividing the phase plane into regions of single-front (*I*) and multifront (*II*) states of equilibrium for Bi=10.

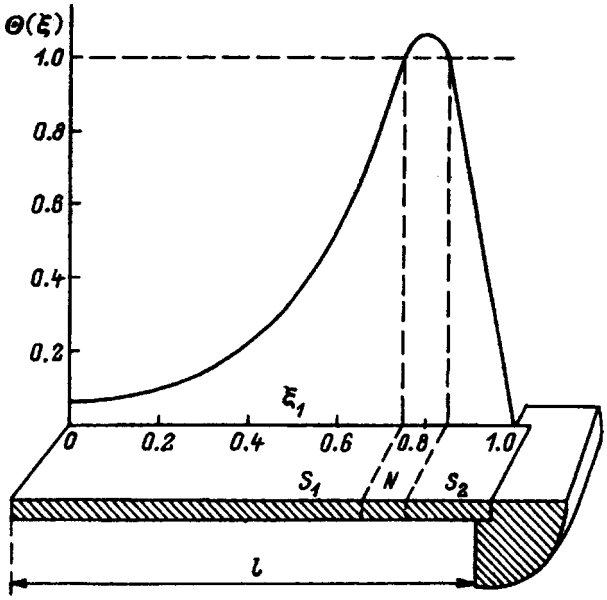

FIG. 3. Thin superconducting film in a two-phase stationary state with two phase boundaries on the segment studied. The temperature field of the film corresponds to curves *1* in Fig. 4b.

respectively, and ξ_1 and ξ_2 are the coordinates of the phase boundaries. The solutions of the boundary-value problem (6) have the form

$$\Theta_{s1}(\xi)=\frac{\cosh\sqrt{2\mathrm{Bi}_s}\xi}{\cosh\sqrt{2\mathrm{Bi}_s}\xi_1},$$

$$\Theta_n(\xi)=(1-\sigma)\mathrm{Re}\left\{[1-\exp\sqrt{\varkappa}(\xi_1-\xi_2)]\times\frac{\sinh\sqrt{\varkappa}(\xi-\xi_1)}{\sinh\sqrt{\varkappa}(\xi_2-\xi_1)}\right\}+(1-\sigma)\times\mathrm{Re}[1-\exp\sqrt{\varkappa}(\xi_1-\xi_2)]+\sigma,$$

$$\varkappa=2\mathrm{Bi}_n(1-\varepsilon\sigma_0),$$

$$\Theta_{s2}(\xi)=\frac{\sinh\sqrt{2\mathrm{Bi}_s}(1-\xi)}{\sinh\sqrt{2\mathrm{Bi}_s}(1-\xi_2)}. \tag{7}$$

The conditions of continuity of the heat flux lead to the following relations between the coordinates of the phase boundaries:

$$f(\xi_1,\xi_2)\equiv\lambda_s\sqrt{2\mathrm{Bi}_s}\tanh\sqrt{2\mathrm{Bi}_s}\xi_1-\lambda_n(1-\sigma)\times\mathrm{Re}\sqrt{\varkappa}\left[\frac{1-\exp\sqrt{\varkappa}(\xi_1-\xi_2)}{\sinh\sqrt{\varkappa}(\xi_2-\xi_1)}-1\right]=0, \tag{8}$$

$$\varphi(\xi_1,\xi_2)\equiv\lambda_s\sqrt{2\mathrm{Bi}_s}\coth\sqrt{2\mathrm{Bi}_s}(1-\xi_2)-\lambda_n(\sigma-1)\times\mathrm{Re}\sqrt{\varkappa}\{[1-\exp\sqrt{\varkappa}(\xi_1-\xi_2)]\times\coth\sqrt{\varkappa}(\xi_2-\xi_1)-\exp\sqrt{\varkappa}(\xi_1-\xi_2)\}=0. \tag{9}$$

As one can see from the plots (Fig. 4) of the implicit functions $f(\xi_1,\xi_2)=0$ and $\varphi(\xi_1,\xi_2)=0$, the conditions (8) and (9) are incompatible in the regions $\sigma_0<1/\varepsilon$ and $\sigma_0>1/\varepsilon$ (Fig. 4a). However, for large values of Bi the curves *1* and *2* approach so close to each other (dashed line in Fig. 4b) that they are virtually impossible to distinguish when solving Eqs. (8) and (9) by numerical methods. This means that the size of the normal region for large Bi becomes constant, and the region itself becomes delocalized.

In a real situation the normal phase will remain localized for any value of Bi, since even a very small change in the parameters of heat exchange can cause the conditions (8) and (9) to be satisfied. For example, the heat-transfer coefficient should be somewhat lower at the edges of the film in direct proximity to the thermostat (Fig. 3) than at the center. One can see from Fig. 4b that for $\mathrm{Bi}_{s1}=\mathrm{Bi}_n>\mathrm{Bi}_{s2}$ the conditions (8) and (9) are compatible, i.e., two-front states of equilibrium are possible. The temperature field of one state, where the superconducting phase occupies a small region at the thermostatted edge of the film, is shown in Fig. 3.

4. In summary, the two-phase state of equilibrium of a thin film of a classical superconductor under constant conditions of heat transfer at the free surface remains a single-front state in a wide range of values of the parameters of the system. For high-T_c superconductors there exists a limit above which the slightly nonequilibrium (in the thermodynamic sense) stationary states can only be multifront states. For the formation of two-front states in the case of both high-T_c and traditional superconductors it is sufficient for the coefficients in the equations (6) to depend on the spatial variable, specifically, it is sufficient for the parameter Bi to be a piecewise-continuous function of the coordinate.

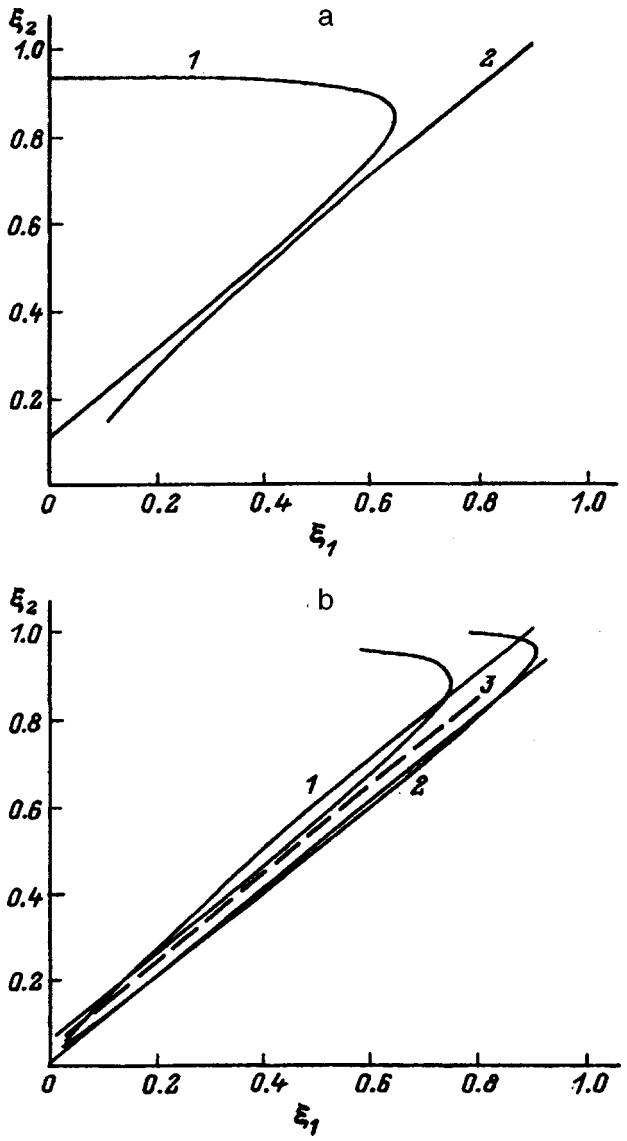

FIG. 4. Implicit functions $f(\xi_1,\xi_2)=0$ and $\varphi(\xi_1,\xi_2)=0$ with $\varepsilon=0.1$. a—$\mathrm{Bi}=10$, the plots of the functions (*1* and *2*) with $\sigma_0=5$ and 20 are virtually indistinguishable; b—plots of the same functions with $\mathrm{Bi}_{s1}=\mathrm{Bi}_n=10$, $\mathrm{Bi}_{s2}=3.6$, $\sigma_0=5$ (*1*), $\mathrm{Bi}_{s1}=\mathrm{Bi}_n=10$, $\mathrm{Bi}_{s2}=3.6$, $\sigma_0=20$ (*2*); $\mathrm{Bi}_{s1}=\mathrm{Bi}_n=\mathrm{Bi}_{s2}=50$, $\sigma_0=5$ (*3*).

[1] W. Franzen, J. Opt. Soc. Am. **53**, 596 (1963).
[2] A. S. Rudyĭ, Pis'ma Zh. Tekh. Fiz. **22**(9), 85 (1996) [Tech. Phys. Lett. **22**, 382 (1996)].

Translated by M. E. Alferieff

Photophoresis of aerosol particles in a resonance radiation field

V. V. Levdanskiĭ

Academic Science Complex, A. V. Lykov Institute of Heat and Mass Transfer, Belarus Academy of Sciences, 220072 Minsk, Belarus.

(Submitted February 7, 1996)
Zh. Tekh. Fiz. **68**, 88–89 (March 1998)

The additional force exerted by a gas on an aerosol particle on account of the change in recoil momentum of the gas molecules on the surface of the particle in a resonance radiation field is analyzed. [S1063-7842(98)01403-2]

The problem of controlling the motion of aerosol particles is of crucial importance for numerous areas of modern technology (the preparation of high-purity substances, the fabrication of microelectronics elements, ecological concerns, etc.). This has led to a search for new methods to influence the motion of aerosol particles. The use of resonance (particularly laser) radiation can be effective here.

It is known that the character of the interaction of gas molecules with a surface can be altered significantly in a resonance radiation field. Such changes, in turn, give rise to new components of the force exerted by the gas phase on aerosol particles.[1,2] In this paper we examine the possibility of the appearance of a new component of the photophoretic force due to a change in the normal momentum transferred by gas molecules to the surface of an aerosol particle in a resonance radiation field. Let us consider a spherical particle of radius R, on which radiation with a flux density J impinges. We next assume that a free-molecule flow regime, in which the mean free path of the molecules is much greater than the radius of the particle, is realized. The distribution of the molecules moving away from the surface is assumed to be diffuse. For the absolute value of the force acting on the particle we can write the expression

$$F = 2\pi R^2 \left| \int_0^{\pi} P_s \cos\theta \sin\theta d\theta \right|, \tag{1}$$

where P_s is the pressure of the gas at the surface of the particle, and θ is the angle between the axis passing through the center of the particle in the direction parallel to the radiation flux and a normal to the surface.

The value of P_s is determined by the momentum transferred to the aerosol particle during collisions of gas molecules with its surface and by the recoil momentum of the gas molecules moving away from the surface. Under the assumption that the first of these components of P_s is constant, a contribution to F will be made only by the recoil pressure P_d of the gas molecules moving away from the surface of the particle, which can differ on different portions of its surface due to the nonuniform heating of the particle (the classical variant of photophoresis). However, in the case of the action of resonance radiation on a disperse system in air, such a difference in the values of P_d can also appear even when the temperature of the surface of the aerosol particle is constant, particularly when there is asymmetry of the sticking coefficients of the gas molecules on the particle surface relative to the direction of the incident radiation. We note that such asymmetry can be caused by a difference between the flux densities of the excited gas molecules impinging on opposite sides of the aerosol particle relative to the radiation source and by a difference between the sticking coefficients for excited and unexcited molecules. This situation can arise in the case of nonuniform illumination of the aerosol particle (when its radius is sufficiently large) or when the radiation frequency is detuned from the resonance frequency of the gas molecules, in which case only molecules moving in a definite direction will be excited because of the Doppler effect (velocity-selective excitation of molecules[3]). The latter case is especially significant for small (relative to the wavelength of the radiation) particles, as well as transparent particles with a sufficiently high thermal conductivity. Under such conditions the heating of the particle by radiation will be nearly uniform and the classical component of the photophoretic force associated with nonuniform heating of the particle can be neglected. The fraction of excited molecules can be found from the system of kinetic equations for the transitions of resonant molecules from the ground state to an excited state (and in the opposite direction). For simplicity, we consider a two-level system. These equations now have the form[4]

$$\frac{dn_1}{dt} = (n_2 - n_1)\frac{J\sigma}{h\nu} + \frac{n_2}{t_\nu}, \tag{2}$$

$$\frac{dn_2}{dt} = (n_1 - n_2)\frac{J\sigma}{h\nu} - \frac{n_2}{t_\nu}, \tag{3}$$

where n_2 and n_1 are, respectively, the densities of the excited and unexcited molecules, t_ν is the relaxation time of the excited molecules, J is the radiated intensity, ν is the radiation frequency, h is Planck's constant, and σ is the cross section of the radiation-induced transitions of the molecules, which depends on the direction of motion of the molecules because of the Doppler effect when the radiation frequency is detuned away from the resonance frequency of the gas molecules.

Assuming that the heating of the particle by radiation is uniform, for its temperature T_s we have

$$T_s = T_g + k_1 J/4k_T, \tag{4}$$

where T_g is the temperature of the gas, k_I is the efficiency factor for the absorption of radiation by the particle, and k_T is the effective heat-transfer coefficient.

We next assume that the excited and unexcited molecules are characterized by different sticking coefficients on the surface of the aerosol particle. For simplicity, we also assume that only the molecules sticking to the surface of the particle take the temperature of the latter, while the nonsticking molecules are reflected elastically (without energy transfer) from it. Under the assumption of a Maxwellian velocity distribution function for the molecules impinging on the surface of the aerosol particle and the molecules moving away from it, as well as with consideration of the difference in σ for gas molecules characterized by oppositely directed projections of the velocity onto the direction of the radiation flux (for simplicity we assume that σ is nonzero only for one of the directions of these projections), in the stationary case we obtain the following expression for F from (1)–(4):

$$F=\frac{P}{2}\pi R^2\frac{J\sigma}{h\nu}t_\nu\left(1+2\frac{J\sigma}{h\nu}t_\nu\right)^{-1}|\alpha-\alpha'| \times\left[\left(1+\frac{k_1 J}{4k_T T_g}\right)^{1/2}-1\right], \tag{5}$$

where P is the pressure of the gas, and α and α' are, respectively, the sticking coefficients for unexcited and excited gas molecules.

It follows from (5) that for F to be nonzero, the resonance and thermal effects (excitation of gas molecules and heating of the particle by radiation) must occur simultaneously. If phase transformations (evaporation and condensation) take place on the surface of the particle, F will not be equal to zero even in the case of equality between the temperatures of the particle and the gas. In this case a difference between the condensation coefficients of the excited and unexcited molecules is sufficient by itself. In the steady-state approximation F can be estimated as

$$F=\frac{P}{2}\pi R^2\frac{J\sigma}{h\nu}t_\nu\left(1+2\frac{J\sigma}{h\nu}t_\nu\right)^{-1}|\alpha_c-\alpha_c'|,$$

where α_c and α_c' have the meaning of the condensation coefficients for the unexcited and excited molecules, and the radius of the aerosol particle R depends in this case on the time and is determined by the resultant flux of molecules into the particle.

We note that unlike the case of an impermeable surface considered above, here asymmetry of the recoil pressure appears because of the molecules that impinge on the surface of the particle and condense on it, while the molecules moving away (evaporating) from the surface do not make a contribution to the resultant force under the assumptions stipulated above.

[1] V. V. Levdanskiĭ, in *Abstracts of the 14th All-Union Conference on Current Topics in the Physics of Aerodispersion Systems* [in Russian], Odessa (1986), Vol. 1, p. 165.
[2] V. I. Roldugin, in *Abstracts of the 14th All-Union Conference on Current Topics in the Physics of Areodispersion Systems* [in Russian], Odessa, (1986), Vol. 1, p. 116.
[3] F. Kh. Gel'mukhanov and A. M. Shalagin, Pis'ma Zh. Éksp. Teor. Fiz. **29**, 773 (1979) [JETP **29**, 711 (1979)].
[4] N. V. Karlov and B. S. Luk'yanchuk, Kvantovaya Elektron. (Moscow) **8**, 1509 (1981) [Sov. J. Quantum Electron. **11**, 909 (1981)].

Translated by P. Shelnitz